STUDIES ON BIOACTIVE GLASS MATERIALS FOR BROAD SPECTRUM APPLICATIONS

Thesis Submitted to

DELHI TECHNOLOGICAL UNIVERSITY

For the Award of the Degree of

DOCTOR OF PHILOSOPHY

Submitted By

HIMANSH GOEL

2K17/PhD/AC/02

Under the Guidance of

Dr. Deenan Santhiya

Department of Applied Chemistry

Delhi Technological University

Shahbad Daulatpur, Main Bawana Road,

Delhi- 110042, INDIA

October 2022

DELHI TECHNOLOGICAL UNIVERSITY

(Formerly Delhi College of Engineering)

Department of Applied Chemistry

Shahbad Daulatpur, Bawana Road, Delhi- 110042, India

DECLARATION

This is to declare that the research work embodied in this thesis entitled **"Studies on Bioactive Glass Materials for Broad Spectrum Applications"** submitted to the Delhi Technological University **is an original work and carried out by me for the degree of Doctor of Philosophy** under the supervision of **Dr. Deenan Santhiya**, **Assistant Professor**, Department of Applied Chemistry. This thesis is a contribution to my original research work. The extent of information derived from the existing literature has been indicated in the body of the thesis at appropriate places giving the source of information. Every effort has been made to make sure that the scientific contributions of others are appropriately cited. To the best of my knowledge, this research work has not been submitted in part or full for award of any degree or diploma in Delhi Technological University or in any other university/institution.

Date:

Himansh Goel
Research Scholar
Reg. No. 2K17/PhD/AC/02

DELHI TECHNOLOGICAL UNIVERSITY

(Formerly Delhi College of Engineering)

Shahbad Daulatpur, Bawana Road Delhi- 110042, India

CERTIFICATE

This is to certify that the thesis entitled **"Studies on Bioactive Glass Materials for Broad Spectrum Applications"** submitted to the Delhi Technological University, Delhi-110042, in fulfillment of the requirement for the award of the degree of **Doctor of Philosophy** has been carried out by the candidate, **Mr. Himansh Goel**, (Reg. No. 2K17/PhD/AC/02) under the supervision of **Dr. Deenan Santhiya**, **Assistant Professor**, Department of Applied Chemistry. It is further certified that the work embodied in this thesis has neither partially nor fully been submitted to any other university or institution for the award of any degree or diploma.

Dr. Deenan Santhiya
Supervisor
Department of Applied Chemistry
Delhi Technological University, Delhi

Prof. S. G. Warkar
Head of the Department
Department of Applied Chemistry
Delhi Technological University, Delhi.

DEDICATED TO

MY PARENTS & FAMILY...

Acknowledgment

"I am blessed with everything I need. I am working hard towards everything I want, and most of all, I appreciate & Thank God for what I have."

I would like to thank the Almighty God for the successful completion of my research work.

Coming to the end of my Ph.D., I pour out my thoughts and hope that reflect the deep gratitude I hold for people that have made it possible for me to surmount this hurdle and achieve my dream.

The life of a Ph.D student is anchored by their supervisor and I am extremely fortunate to have ***Dr. Deenan Santhiya*** *as my mentor, an individual with years of experience and possibly the most encouraging person I have come across in my educational years. She is not only the person behind innumerable success stories of her doctoral students but also the one who established a pioneering research ethics amongst young researchers. A life filled with such scholarly achievements is only possible when the person is immensely talented and truly committed to their cause. I have witnessed her humility in response to gratitude, strength in face of adversity, decisiveness in matters of dilemma and undistinguished love for science at every step. Her scientific aptitude and clarity of even complex concepts helped me in testing times of research while her ability to motivate students to discover their hidden talents has introduced me to my own strengths. Her extensive generosity taught me the value of being generous, and her promptness taught me the value of time management. Her concept of "work hard, play hard" has been inspiring throughout the duration of my association with her. I am incredibly fortunate to have been trained and introduced to the world of research under her guidance.*

I am extremely grateful to ***Professor S. G. Warkar*** *(Head, Department of Applied Chemistry) for providing the necessary research facilities and an excellent working environment in the department. His work exhibits the ideal fusion of punctuality, enthusiasm, commitment, organization, and excellent administrative abilities. We are fortunate to have a visionary like him in our department. I*

would also like to thank our former Head, ***Professor Archana Rani****, who helped me in the initial days of my research and stood by my side in all difficult times.*

I would also like to thank Professor D. Kumar, Professor R. C. Sharma, Professor R. K. Gupta, Professor Anil Kumar, Professor Ram Singh, Professor Roli Purwar, Dr. Richa Srivastava, Dr. Manish Jain, Dr. Raminder Kaur, Dr. Saurabh Mehta, and Dr. Poonam, faculty members, Department of Applied Chemistry, DTU for their time-to-time valuable support.

No word and no language is ever adequate to express my heartfelt admiration for my respected ***parents, Mrs. Vinny Goel (Mother), Mr. Chand Kishore Goel (Father) and My younger brother (Adv. Yuganter Goel),*** *who have been pillars of inspiration for my academic expedition and I am thankful for their blessings and unconditional love, without which I would have failed to complete this work.*

For efficaciously accomplishing a project, a healthy environment is a must.

- *I am grateful to all my labmates and deepest thanks to* ***Dr. Meenakshi Gautam*** *for her help and support whenever needed and for being such a good friend.*
- *I sincerely thank all my colleagues in* ***Kingfa Science and Technology (India) Ltd.*** *and my deepest thanks to Sun Yajie, S. Shanmugasundaram, and Divya Lakshmi T. They provided excellent help throughout the last days of thesis compilation, which allowed me to remain focused and finish my thesis without being distracted.*
- *I thank all the non-teaching and official staff of the Department of Applied Chemistry for their obligatory help whenever needed.*
- *I am grateful to* ***Prof. Jai Prakash Saini*** *(Vice Chancellor) and* ***Prof. Yogesh Singh*** *(former Vice Chancellor) of Delhi Technological University for giving me this opportunity to conduct my research work.*

- *I must also thank CIF-Delhi Technological University, USIC-University of Delhi, AIRF-Jawaharlal Nehru University, CIF-IIT Delhi, SAIF-AIIMS Delhi and CNMS-Jain University Bangalore for providing various instrumentation facilities.*
- *Finally, I must thank all those, whom I have failed to mention specifically and personally, but they have helped me in various ways during this work.*

Thank you so much!!!!!

(Himansh Goel)

OVERVIEW OF THESIS

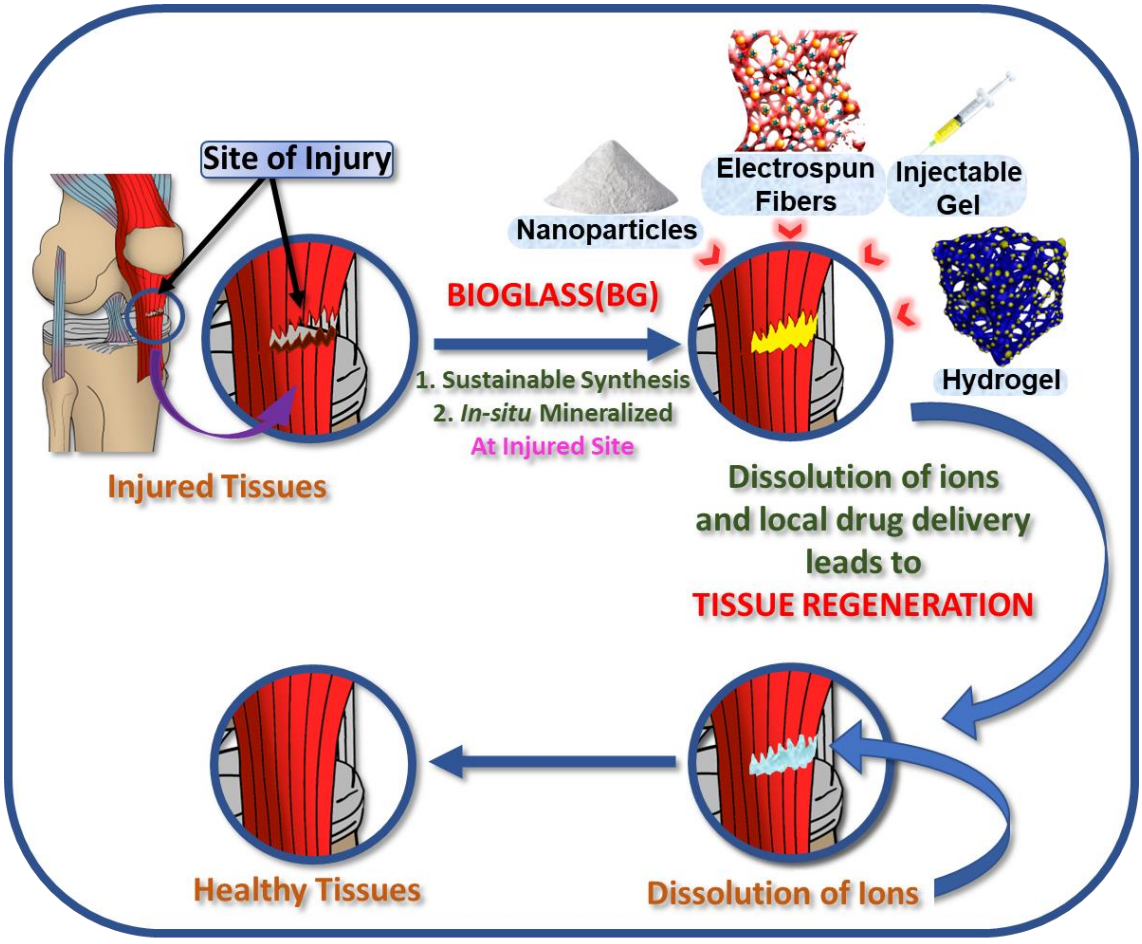

ABSTRACT

The function of biomaterials is to replace infected, injured or damage tissues. The first used biomaterials are bioinert, thus minimizing the formation of scar tissue at implant-tissue interface. Bioglass was discovered by Dr. Larry Hench in 1969, which has the capability to bond with bone without encapsulated by fibrous tissues. It has been discovered that bioglass has a far higher bonding capacity than any other biomaterial. Its ability to form hydroxyapatite with body fluid makes it undefendable compared to virgin hydroxyapatite crystals. In addition to providing a surface for cell development, the presence of Si ions acts as a catalyst to speed up cellular proliferation. Recently, it has been discovered that bioglass is not only a good candidate for hard tissue regeneration but can also be used beyond bone regeneration such as soft tissue engineering applications. Since the late 1960s, many techniques have been developed and used to create bioglass, including the melt-quench method, the sol-gel method, flame spray synthesis, microwave synthesis, and others. Apart from these methods, a new cost effective, green synthetic route called bioinspired route has been reported by Santhiya *et al* in 2013. This approach was developed on admiring naturally synthesized nano-structured materials such as silica in diatoms by the guidance of bio macromolecular templates. In last two decades, the bio-inspired synthesis of nanostructured ceramic oxides below 100 °C has been well established using organic templates. Santhiya *et al*. explored the effect of various templates on the textural and morphological properties of the bioglass particles. In the present investigation, the bio-medical application of bioglass materials as inorganic-organic hybrid composites are explored. Herein, bioinspired method was adopted for *in-situ* mineralization of bioglass particles. Initially, the bioglass particles were synthesized using small molecules i.e., a

monomer instead of high molecular weight synthetic polymers. Further, we have developed a new sustainable green synthetic method for the synthesis of bioglass particles directly utilising a natural plant extract as both a template and a source of a few inorganic metal ions.

In this thesis, considering the huge importance of bioactive glass hybrid materials for both soft and hard tissue engineering applications, various *in-situ* mineralized bioactive glass hybrid materials are synthesized and characterized in detail. This thesis has been summarized in 6 chapters.

Chapter 1 provides a general overview on soft and hard tissue engineering, generations of biomaterials, bioactive glass as third generation biomaterial and application of bioglass beyond bone regeneration. Additionally, a thorough overview of studies on the synthesis of bioactive glass and the mechanism of bioactivity in simulated body fluid is reviewed in detail. Bioactive glass hybrid materials' significance in biological applications is briefly discussed.

Chapter 2 explains the fundamentals of numerous methods used to characterise bioglass materials. These tools help us to determine their structural, morphological, thermal and mechanical properties like size, charge, surface area, surface functional groups, morphology, and molecular structure.

In **Chapter 3,** bioinspired synthesis method for mesoporous L-lysine-bioactive glass (LBG) hybrid xerogels at ambient conditions was discussed in details. L-lysine molecules were incorporated in bioactive glass (BG) network through physiochemical interaction. The step-wise addition of various BG precursors with L-lysine took place at its three pKa (2.18, 8.94, 10.54) and pI (9.74) values respectively. These LBG hybrid xerogels were thoroughly characterized before and after interaction with simulated body

fluid (SBF). Interestingly, elemental analysis on xerogels reported 45S5 composition for inorganic contents of LBG_8.94 and LBG_9.74. In contrast, LBG_2.18 and LBG_10.54 contained higher SiO_2 and corroborating discrete bioactivity behaviour of xerogels. Nitrogen sorption analysis confirmed the mesoporous nature of all four LBG xerogels with different pore size, pore volume and surface area. Importantly, distinctively controlled 7-Dehydrocholesterol release pattern of each LBG xerogels highlighted the importance of their tuneable textural property. Reported viscoelastic nature of freshly prepared LBG xerogels by rheological analysis promised its non-invasive injectability. These new generation materials not only promise to serve nutrients for cell growth but also contain tailored textural as well as rheological characteristics for targeted bone engineering applications.

In Chapter 4, we report for the first time, BGNPs synthesized using *Trigonella foenum-graecum* (TFG) leaf extract (TFGL_EX). Bioactive glass nanoparticles (BGNPs) have been reported in various biomedical applications such as tissue engineering, dental and bone repair, drug and gene delivery, tumour therapy and skincare. The requirement of sustainable synthesis methods is pertinent for large-scale manufacture of such popular materials. Currently, green synthesis methods have gained popularity in various nanoparticle synthesis as it is considered environmentally benign with minimal waste generation. To our knowledge, we report synthesis of BGNPs for the first time using *Trigonella foenum-graecum* (TFG) leaf extract (TFGL_EX). The TFGL_EX can be used both as a template and precursor for synthesizing BGNPs. The influence of the leaf extract on the composition, particle size and porosity of BGNPs has been determined using characterization techniques like ICP-MS, HR-TEM and nitrogen sorption analysis. Further, bioactivity and biocompatibility of the synthesized BGNPs could be successfully demonstrated through *in-vitro* studies in Simulated Body

Fluid (SBF) and on model bone cell line, respectively. Native BGNPs as well as model antibacterial drug loaded counterparts demonstrates significant antibacterial properties and sustained drug release profiles. Overall, the study reports a sustainable property-dependent synthesis methodology for BGNPs by utilizing organic and inorganic constitutes of TFGL_EX.

In **chapter 5**, we address the design of a novel collagen/pectin (CP) hybrid composite hydrogel (CPBG) containing *in-situ* mineralized bioactive glass (BG) particles to simulate an integrative 3D cell environment. Systematic analysis of the CP sol revealed that collagen and pectin molecules interacted despite having comparable net negative charges through the mechanism of surface patch binding interaction. FTIR and TGA analysis confirmed this associative interaction resulting in the formation of a hybrid crosslinked network with the BG nanoparticles acting as pseudo crosslink junctions. SEM, EDX and TEM results confirmed uniform mineralization of BG particles, and their synergetic interaction with the network. The *in-vitro* bioactivity tests on CPBG indicated the formation of bone-like hydroxyapatite ($Ca_{10}(PO_4)_6(OH)_2$) microcrystals on its surface after interaction with simulated body fluid. This hydrogel was tested against *Candida albicans* when infused with the model antifungal medication amphotericin-B (AmB). The AmB release kinetics of the hydrogel followed the Fickian diffusion release mechanism demonstrating direct proportionality to gel swelling behaviour. Rheological analysis revealed the viscoelastic compatibility of CPBG for mechanical load bearing applications. Cell viability tests indicated appreciable compatibility of the hydrogel against U2OS and HaCaT cell lines. FDA/PI on the hydrogel portrayed preferential U2OS cell adhesion on hydrophobic hydroxyapatite layer compared to hydrophilic surfaces, thereby promising the regeneration of both soft and hard tissues.

In Chapter 6, ultrafine fibers and a bioactive glass mineralized fibrous mat of gelatin-pectin blends were produced by electrospinning in an aqueous phase. Herein, the gelatin-pectin blend was used as a template for the *in-situ* mineralization of bioactive glass particles during electrospinning of gelatin-pectin based hybrid composite fiber matrix. Additionally, *in-situ* mineralized bioactive glass along with the fibrous mat served as a site for 7-dehydrocholesterol, i.e., a vitamin-D precursor. This engineered fibrous mat resulted in the sustained release of the drug, which is essential for fortifying the neo regenerated bones. The fibrous mat also exhibited excellent bioactivity in simulated body fluid. Additionally, hybrid composite fibre mat displayed cell proliferation on the surface of fibrous mat and had outstanding cytocompatibility with osteoblast cells.

LIST OF PUBLICATIONS

- Nidhi Gupta, **Himansh Goel**, Deenan Santhiya, Chandra Mohan Srivastava, Sarita Mishra, and Pragya Rai. "Aqueous-Phased Electrospun Bioactive Glass Mineralized Gelatin/Pectin Hybrid Composite Fiber Matrix For 7-Dehydrocholesterol Delivery.**"ChemistrySelect"** 5, no. 14 (2020): 4364-4370. **(SCIE indexed) (Impact Factor: 2.307)**
- **Himansh Goel,** Nidhi Gupta, Deenan Santhiya, Namit Dey, Himadri B. Bohidar, and Aditi Bhattacharya. "Bioactivity reinforced surface patch bound collagen-pectin hydrogel. **"International Journal of Biological Macromolecules"** 174 (2021): 240-253. **(SCIE indexed) (Impact Factor: 8.025)**
- **Himansh Goel,** and Deenan Santhiya. "Effect of pH on bio-inspired synthesis of L-Lysine templated bioactive glass hybrid xerogels for tailored textural and rheological properties.**" Materials Chemistry and Physics"** 281 (2022): 125828. **(SCIE indexed) (Impact Factor: 4.778).**
- **Himansh Goel,** and Deenan Santhiya. "Role of Trigonella foenum-graecum Leaf Extract in Tailoring the Synthesis and Properties of Bioactive Glass Nanoparticles". **" Sustainable Materials and Technologies"** 33 (2022): e00485. **(SCIE indexed) (Impact Factor: 10.681).**

CONTENT

List of Figures

List of Tables

List of Abbreviations and Symbols

AFM	Atomic force microscope
AmB	Amphotericin-B
AOAC	Association of official analytical chemists
AR	Analytical reagent
ASTM	American society for testing and materials
BET	Brunauer–Emmett–Teller
BG	Bioactive glass
BGNP	Bioactive glass nanoparticle
BGNPs	Bioactive glass nanoparticles
BJH	Barrett–Joyner–Halenda
BO	Bridging oxygen
C	Collagen
Ca	Calcium
Ca^{2+}	Calcium ion
CaAc	Calcium acetate
CHA	Carbonated hydroxyapatite
CHNSO	Carbon, Hydrogen, Nitrogen, Sulphur and Oxygen analysis
CP	Collagen/pectin blend
CPBG	Collagen/pectin control hydrogel containing *in-situ* mineralized bioactive glass
CPCa	Collagen/pectin control hydrogel containing calcium acetate
CTAB	Cetyltrimethyl ammonium bromide

CT-DNA	Calf thymus deoxyribonucleic acid
Cu	Copper
DMEM	Dulbecco's Modified Eagle's Medium
E. coli	Escherichia coli
EBC	Equilibrium buffer content
ECM	Extracellular matrix
EDAX	Energy dispersive X-ray analysis
Fe	Iron
Fe^{2+}	Iron (II) ion
FE-SEM	Field emission scanning electron microscope
FTIR	Fourier transform infrared spectroscopy
FWHM	Full width at half-maximum (β)
G	Gelatin
GC	Gas chromatography
GP	Gelatin-pectin fiber
GPBG	Gelatin-pectin hybrid composite fibers containing *in-situ* mineralized bioactive glass particles
GPBGD	7-dehydrocholesterol containing GPBG
HaCaT	Adult keratinocyte cell line
HAP	Hydroxyapatite
HCA	Hydroxycarbonate apatite
HCl	Hydrochloric acid
HR-TEM	High-resolution transmission electron microscopy
ICDD	International centre for diffraction data
ICP-MS	Inductively coupled plasma mass spectrometry

IS	Indian standards
IUPAC	International union of pure and applied chemistry
JCPDS	Joint committee on powder diffraction standard
K	Potassium
LBG	L-lysine-bioactive glass hybrid xerogel
LBG_10.54	LBG xerogels obtained at pH 10.54
LBG_2.18	LBG xerogels obtained at pH 2.18
LBG_8.94	LBG xerogels obtained at pH 8.94
LBG_9.74	LBG xerogels obtained at pI 9.74
LDH	Lactate dehydrogenase assay
MBG	Mesoporous bioactive glass
MTT	3-(4,5-Dimethylthiazol-2-yl)-2,5-diphenyltetrazolium bromide
Na	Sodium
NaAc	Sodium acetate
NaOH	Sodium hydroxide
NBO	Non bridging oxygen
NH2	Amine group
NH_3^+	Ammonium ion
P	Pectin
PBS	Phosphate buffer saline
pI	Isoelectric point
S. aureus	Staphylococcus aureus
SBF	Simulated body fluid
SEM	Scanning electron microscopy
tan δ	Loss tangent

TEM	Transmission electron microscope
TEOS	Tetraethyl orthosilicate
TEP	Triethyl phosphate
TFG	Trigonella foenum-graecum
TFGL_BG1	Green synthesis of TFGL-BGNPs using only TEOS as precursor
TFGL_BG2	Bio-inspired synthesis of TFG-BGNPs as per 45S5 Bioglass composition
TFGL_BG2 _CAL	Calcination of TFG_BG2
TFGL_EX	Trigonella foenum-graecum leaf extract
TGA	Thermogravimetric analysis
U2OS	human osteoblast-like osteosarcoma cell line
XRD	X-Ray Diffraction
%	Percentage
Å	Angstrom
cc	Cubic centimetre
cm	Centimetre
d	Inter-planar spacing
D	buffer diffusion coefficient
dS/dt	swelling kinetic analysis
EE%	Entrapment efficiency
emu	Electromagnetic unit
eV	Electron-volt
G'	Storage modulus
G"	Loss modulus

gm	Gram
h	Hour
Hz	Hertz
K	Kelvin
kD	Kilo dalton
KJ	Kilojoule
kV	Kilo Volts
M	Molar
mA	Milliampere
mg	Milligram
mg	Magnesium
MHz	Megahertz
min	Minutes
mL	millilitre
mM	Millimolar
mm	Millimetre
Mpa	Mega pascal
MW	Molecular weight
nm	Nanometer
oC	Degree Celsius
Pa	Pascal
v/v	Volume per volume
w/v	Weight per volume
wt.	Weight
λ	X - ray wavelength

λmax	wavelength
***μ*g**	Microgram
μm	Micrometre
ω	angular frequency
θ	Diffraction angle

CHAPTER 1

Introduction

CHAPTER 1

Introduction

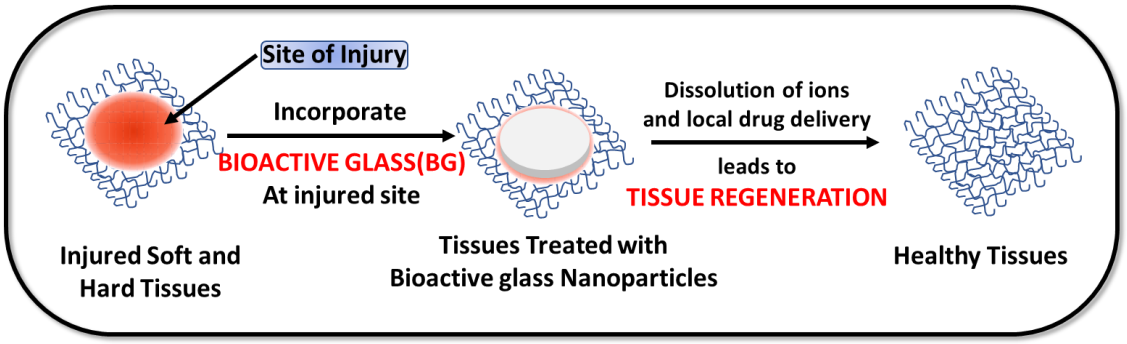

1.1.Introduction:

Bone is a rigid organ which provides structural support to the body, protect various organs of the body, produce red and white blood cells and store minerals.[1] Currently, most of the people are suffering from bone diseases due to injuries and ageing such as fracture, low bone density, osteoporosis, osteoarthritis, Paget's disease, osteogenesis imperfecta and many more which makes the bones weak and brittle more likely to break.[2] These are caused by poor nutrition, genetics, or problems with the rate of bone growth or rebuilding.[3] The natural process of bone regeneration is very much effective against minor fractures or small bone defects. However, the challenges such as poor vascularity or large bone tissue loss arise with an increase in the number of fractures or poor healing due to various diseases associated with bone.[4,5] Even after the huge advancement in the field of biomedical engineering, surgery remains the only option for the treatment of bone disease and bone injuries, which leads to the risk of infection, allergic reaction to anaesthesia and prosthetic joint, bleeding, blood clots, delayed skin healing, instability or stiffness in the joints, damage to the nerves and

blood vessels, dislocation or loosening of the artificial joint and many more.[6,7] In addition to this, high treatment cost, prolonged operative time and prolonged healing duration raise the possibility of nosocomephobia and tomophobia inside the patient. Apart from this, diabetes mellitus and glucocorticoid treatment, delays the optimal bone repairing process.[8–10] At the end, there is a need of advance procedures for bone treatment.

Moreover, musculoskeletal system is mainly consisting of bones, muscles, cartilage, tendon, ligament and other connective tissues that work combinedly to bind and support various organs together.[11] The point where the soft tissues such as tendon, ligament, cartilage etc. meet the hard tissue i.e., bone create a bone tissue interface. This interface exists over a distance of less than 1 mm and is majorly responsible for transmission of load between highly dissimilar tissues without creating stress concentration that would cause tissue damage.[12] Due to outsized divergence in elastic stiffness, these interfaces are the critical points for injury, damage or long-term degradation. Additionally, due to their micro size, high degree of variance in mechanical properties, composition, and cell phenotype, these interfaces are among the most challenging tissues to regenerate. Many of the homogenous tissues involved in these interfaces can be replicated by various tissue engineering techniques. But, the most challenging situation is to replicate both soft and hard tissue simultaneously and biomimetic fixation of these soft tissue engineered grafts with the bone to re-establish the normal process of musculoskeletal system.[12] Thus, it is important in tissue engineering to recreate the structure-function correlation at native tissue interface and enable engineered tissues to perform the same physiological functions as their natural counterparts.

This chapter provides a brief credential view on bioactive glass, a hard and soft tissue regenerating biomaterial. The various synthetic methods involved in the synthesis of

bioactive glass materials, their properties and specific biomedical applications have been discussed in detail. In addition, the effect of various synthesis parameters, composition, size and method of synthesis on the materials solubility, degradability and bioactivity in physiological body fluid is discussed in detail. Moreover, the studies related to bioactive glass as third generation material and advances in bioactive glass has been thoroughly reviewed.

1.2. Biomaterials:

Materials that can be engineered to recapitulate the biological system as well as the architecture of the native tissue for various therapeutic purposes are known as biomaterials. It is important for a biomaterial not to trigger any toxic response after implantation. The definition of biomaterial has been significantly changed over past decades considering the requirement of modern tissue engineering capabilities. These changes are well categorized under three different generations. Biomaterials can be used to treat, grow, repair or replace various soft and hard tissues of the body. In order to employed as a perfect biomaterial for various regenerative medical applications, it must be non-cytotoxic, biodegradable, bioactive and osteoconductive in nature.[13] Numerous biomaterials have been used as bone substitute including hydroxyapatite, calcium phosphate, calcium silicate as well as Bioactive glass 45S5 and other bioactive glasses.

Hydroxyapatite is itself a main component of bone structure contributing 70 % in bone weight. It is used for bone regeneration because of its ability to stimulate osteoconduction (enable attachment and encourage bone cell growth) and osteoinduction (actively promote the production of new bone cells).[14] **Tricalcium phosphate** is also used due to having similar structure and chemical composition as that

of inorganic content of native bone. Besides having the ability of osteoconduction and osteoinduction, it also favours growth of vascular tissues which provide integration with host tissue without the formation of scar tissues. Tricalcium phosphate is generally found in two crystalline forms i.e., α-form and β-form. α-form is less dense, more brittle, high heat of formation and a metastable phase, so considered as less relevant for bone tissue engineering applications. β-form has low heat of formation and having good structural, mechanical and biological properties. It is mostly used as biomaterial. Dicalcium phosphate is not considered for bone regeneration application because of its brittle nature and high rate of *in-vivo* resorption.[15] **Calcium silicate** is also a good candidate due to its superior biocompatibility and mechanical properties. It also shows excellent bioactivity and faster degradation comparing to other phosphate-based materials. Further, the release of Si ion helps to stimulate cellular proliferation. It also induces *in-vivo* bone tissue formation and provide support for cell adhesion.[16] In comparison to these biomaterials, **Bioglass** exhibit extraordinary properties, making it a prime choice for use in bone tissue engineering application. It has the ability to form hydroxyapatite crystals naturally by exchanging ions with body fluid which results in strong bond and natural interaction with native bone. Compared to other bioactive ceramics, it has the capacity to connect with bone more quickly without harming the health or tissues of living organism.[17]

1.2.1. Generations of Biomaterials for Bone Tissue Regeneration:

Different type of biomaterials as a bone substitution material are well known from late centuries and was categorized under three different generations **(Fig 1.1)**.[18–20]

Historically, the purpose of **first-generation** biomaterials was to replace diseased, damaged or aging tissues. Therefore, the physical property of the selected material has

to match with the replaced tissue with minimum toxic response i.e., it has to be bioinert, corrosion-resistant, nontoxic. It does not trigger any reaction in the host, neither rejected nor recognized. The characteristic of 'Bio inert' tissue response leads to the formation of non-adherent fibrous capsules at the material-host interface.

The **second-generation** biomaterials are bioactive i.e., they have the ability to bond with the living tissues so that they can interact with the biological environment to enhance the biological response and are bioresorbable i.e., they can degradation while new tissue regenerates and heals. Bioactive glasses as a bone regenerating material comes under the second-generation biomaterials. On interaction with the wound site of bone, bioactive glass particles lead to the dissolution of ions which result in healthy bone **(Fig 1.2)**.

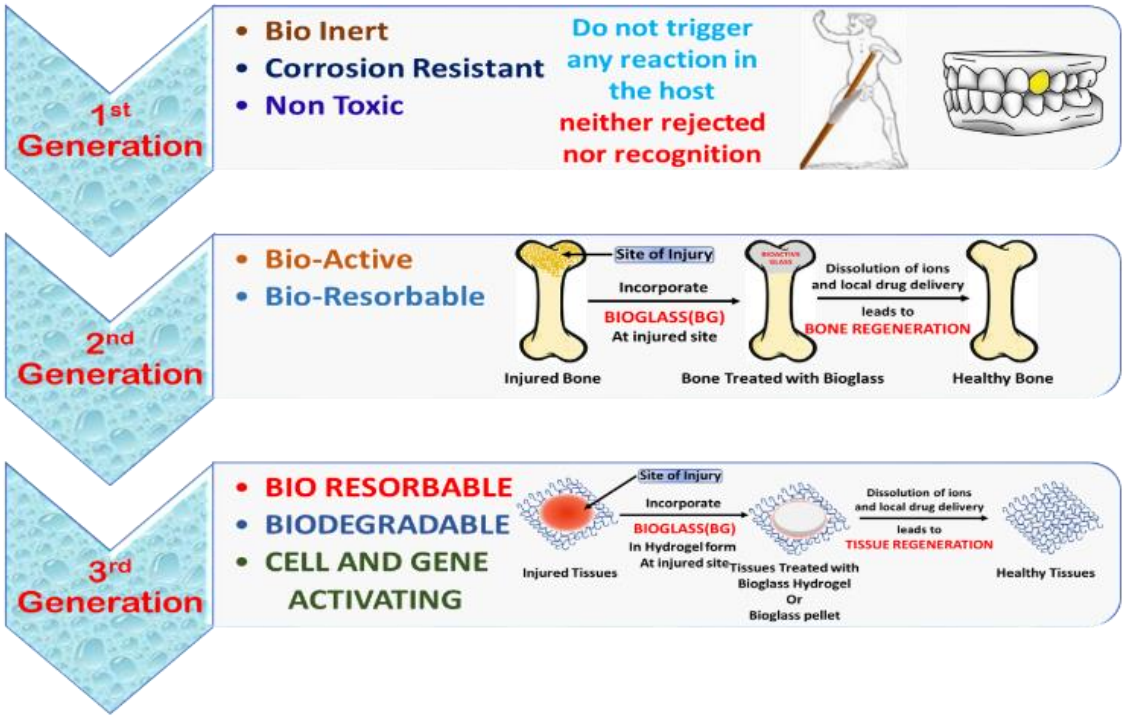

Fig. 1.1: Schematic diagram showing different generations of biomaterial.

The **third-generation biomaterials** are bioresorbable, biodegradable and also have the ability for cell and gene activation. Due to three-dimensional porous structures, they are

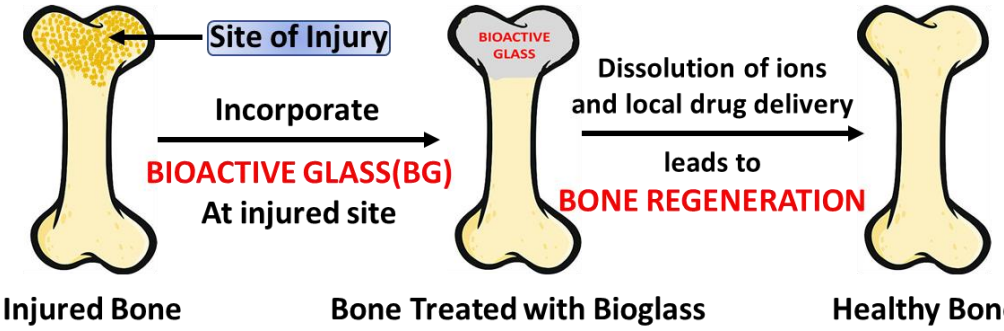

Fig. 1.2: Schematic diagram showing Bioactive Glass as bone regeneration biomaterial.

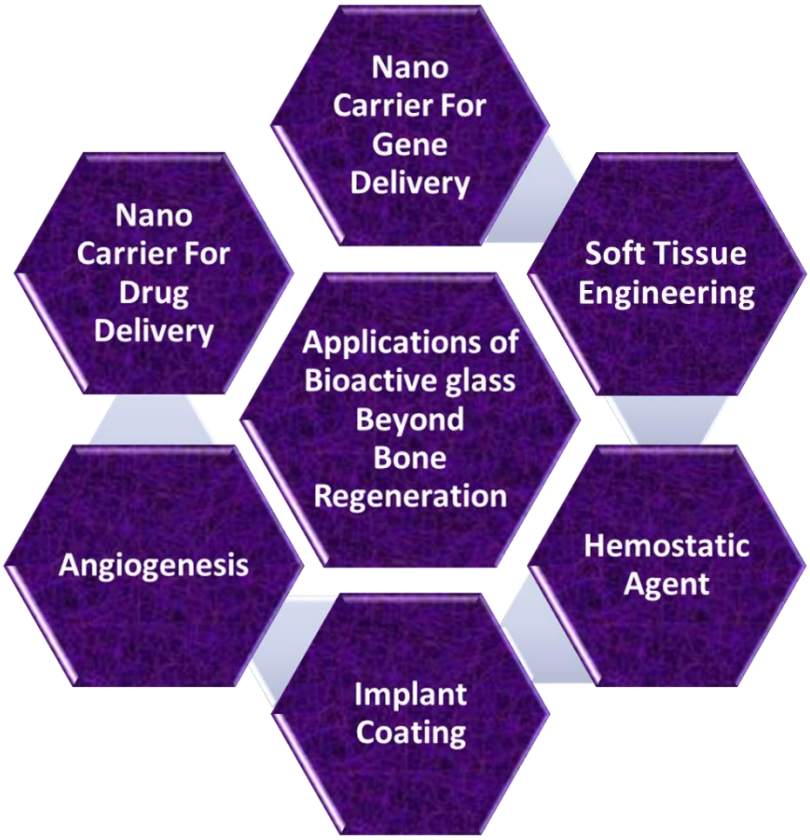

Fig. 1.3: Schematic diagram showing Bioactive Glass as third-generation biomaterials. (modified)[21]

able to activate genes that stimulate regeneration of living tissue. For these biomaterials, the concept of bioactivity and biodegradability is combined in such a way that the bioactive materials are being made more bio-resorbable and bio-resorbable polymers are made more bioactive. These are the biomaterials that directly induce cell growth and differentiation through their specific interactions with cell integrins.

The role of bioactive glass as third-generation biomaterials can be extended to different applications as shown in **Fig. 1.3**.[22]

1.3. Bioactive Glass:

Bioactive glasses are novel material for bone regeneration applications. It is the first biodegradable bioactive ceramics which has the capability to bond with bone without encapsulated by fibrous tissues.[23] They are different from conventional glasses and are used in orthopaedic treatment. Bioactive glasses contain calcium and phosphate ions which are present in a proportion that is similar to the bone hydroxyapatite.[3] These glasses bond to the tissue and are biocompatible. They have a wide range of medical applications and are currently used as bone grafts, scaffolds and coating material in orthopaedics.[19] The beauty of bioactive glass is that, its structure can be manipulated in different ways to suit the desired biomedical application. In the structure of bioactive glass **(Fig. 1.4)**, silica has been used as the major component of the glass composition. Silicate glasses comprise an amorphous network structure based on SiO_4 tetrahedron, which is linked to each other at the oxygen centres. Silicate glasses have an open structure of silica due to the presence of non–bridging oxygen ions attached with silicon. Addition of network modifiers such as Na^+, Ca^{2+} also causes the opening of silica network structures.[24,25] These ions replace bridging oxygens of the network with non–bridging oxygens, hence opening of the glass structure. The number of modifier ion–oxygen bonds and non–bridging oxygen bonds determines several properties of the corresponding glass. In the case of bioactive glasses, each silica tetrahedron contains more than 2.6 number of non-bridging oxygen ions, which is necessary for bioactivity.[26] The composition of bioactive glass is different from the traditional soda-lime-silica glasses that consist of more than 65 wt. % of silica. Basic components required for a glass to obtain bioactivity are SiO_2, Na_2O, CaO and

P_2O_5.[24–26] The amount of SiO_2 should be in between 45 and 60 wt. %, Na_2O and CaO content must be high and a high CaO/P_2O_5 ratio. Higher content of SiO_2 decreases the dissolution rate of the glass ions from the surface, leading to a decrease of bioactivity. Very low content of silica also leads to totally dissolvable monomeric SiO_4 units.[23] Silica content also plays an important role to form hydroxyapatite (HAP) upon contact with physiological fluids, thus leading to the chemical attachment to soft/hard tissues. High CaO/P_2O_5 ratio tends to enable the release of ions from the surface of the material when soaked in a body fluid, forming a surface layer of HCA in a very short time span. Bioactivity can be independent of P_2O_5 as phosphate ion is also available in physiological fluids.[23,25,26]

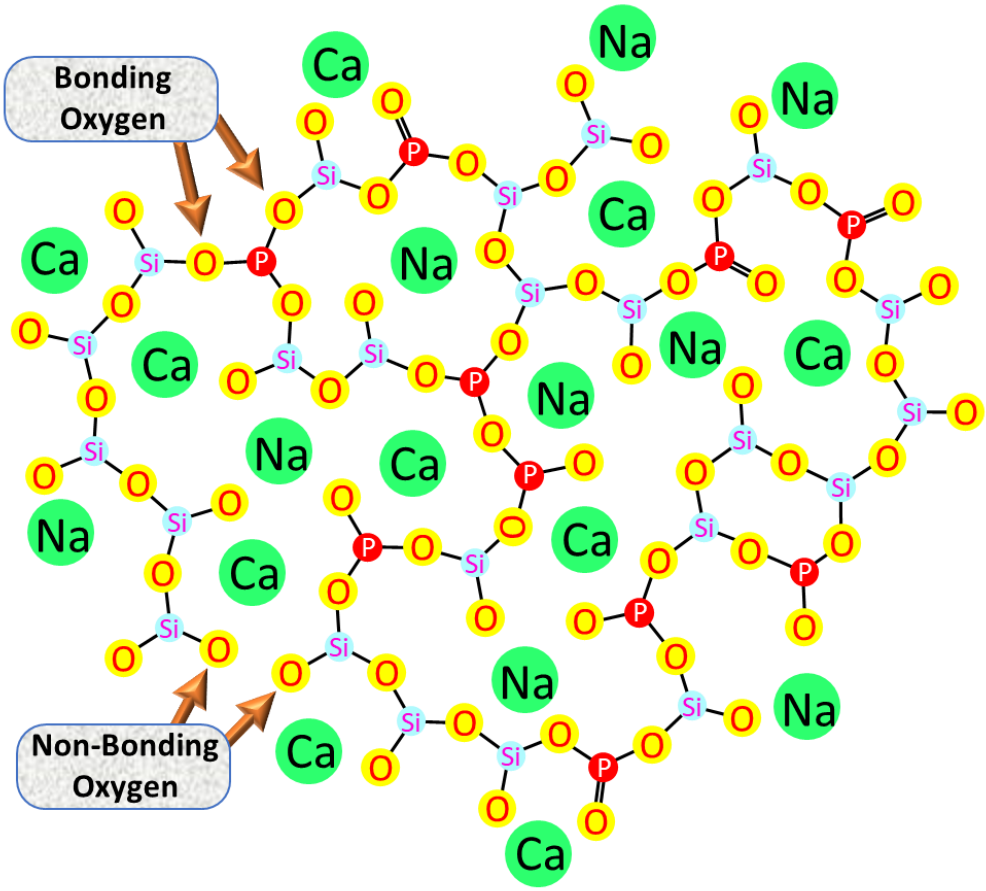

Fig. 1.4: Molecular structure of Bioglass. (modified)[27]

1.4. Bioactive Glass in Soft Tissue Engineering:

Bioactive glasses are used in orthopaedics, dentistry and are developed to treat non-self-healing bone defects because of their high bioactivity. Recently report shows that the dissolution of ions during the bioactivity mechanism to form hydroxyapatite, affects the regeneration of soft tissues too, which inspired the researchers to extend the applications of bioactive glass in soft tissue engineering (**Fig 1.5**).[28,29]

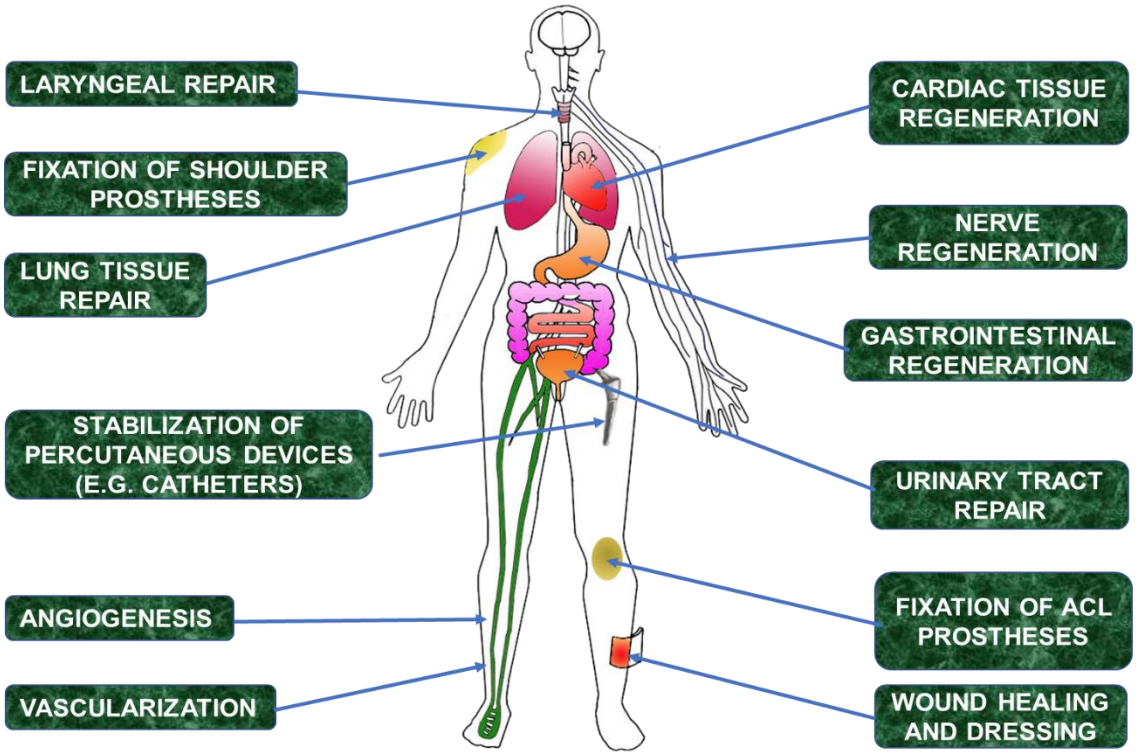

Fig. 1.5: Applications of Bioactive Glass in Soft tissue Engineering.(modified)[29]

1.4.1. Angiogenesis:[30–32]

It is the physiological process through which the new blood vessels from the pre-existing one was formed. It is important for the transport of nutrients and growth factors into the tissue forming site and removal of waste products. It is also important for the survival of cells seeded inside the scaffold. Bioactive glass stimulates the secretion of angiogenic growth factors by fibroblast and significantly increase angiogenesis process.

1.4.2. Cardiac Tissue Regeneration:[33–35]

Bioactive glass molecules loaded with bioactive molecules and exhibit a controlled drug delivery capability could be used as an additive to biodegradable polymers to enhance the mechanical property, biocompatibility and functionality of the cardiac patches.

1.4.3. Haemostatic Agent:[29,36]

It was observed that the interaction of bioactive glass particles with blood decrease the clotting time i.e. the rate of coagulation of the blood increased in contact with the bioactive glass particles.

1.4.4. Wound Healing and Dressing:[29,37]

Due to the haemostatic effect of the bioglass particles, it was observed that the proliferation of connective tissue and wound healing ability was enhanced, so, bioactive glass can be used as a wound dressing material which helps to increase the time for the injured to be transported to the medical faculty.

1.4.5. Nerve Regeneration:[29,38]

Bioactive glasses incorporated with neurotrophic factors with controlled release rate shows enhanced nerve regeneration. It was observed that the Zn doped bioglass show an increase in the proliferation of nerve cells.

1.4.6. Gastrointestinal Regeneration:[36,39]

An oral dose of bioactive glass particles incorporated with omeprazole and hydrotalcite shows decrease in gastric ulcer healing time without significant change to the amount of Si present in blood which also shows that bioglass is not only orally absorbable but

decrease the ulcer healing rate too.

1.4.7. Urinary Tract Repair:[29,36]

Bioactive glass injected to the urinary bladder of a rabbit suffering from incontinence (lack of voluntary control over urination) showed that the particulates were surrounded by the collagen fibers as well as connective tissues and an increase in urethral resistance was observed.

1.4.8. Lung Tissue Engineering:[29,36]

The cell adhesion and cell proliferation property of bioactive glass particles were also found useful in case of lung tissues engineering exhibiting poor regeneration capability.

1.4.9. Laryngeal Repair: [29,36]

Bioactive glass particles can be used for the treatment of paralyzed vocal cord and cancerous vocal cord due to its proven ability to bond with the soft tissue. [37]

1.4.10. Implant Coating:[40–42,42]

The space between the medical devices and the interposed fibrous layer can provide a pathway for the spreading of infectious microorganisms. Bioactive glass coating on the medical devices and catheters was found useful due to its ability to bond with soft tissue, promotes adhesion and cell proliferation. Instead of using Bioactive glass coating, it can also be used as a filler material in between the spaces of the biomedical implants and the tissues.

1.5. Synthesis of Bioactive Glass:

Up to now, various methods have been developed for the synthesis of bioactive glasses and its different composites as follows:[3,26,43,44]

1.5.1. Melt Quench Method (High Temperature Melting):[45,46]

The first bioactive glass, developed by Dr. Larry L. Hench in 1969 is through melt quench method. This method includes melting the mixture of the related precursor oxides at relatively high temperatures around 1300-1600 ºC in a Platinum crucible, then quenching the melt at 25 ºC in order to fabricate amorphous BG. Here, the resulting material is a dense one and the desired particle size is only achieved by means of grinding using ball milling.

For the mass production of bioactive glass, the melt quench technique is more popular and extensively been used as cost-effective procedure due to its following advantages:

1. Fusion of raw materials obtained a viscous liquid, then melt casting by rapid quenching.
2. Formed glass is free from strains and fractures
3. It is easy to dope various active ions in bioactive glass network
4. Composites are flexible because batch calculations are nonstoichiometric. ;
5. Achievement of large structures compared to a single crystal;
6. Achievement of the highly flexible geometrical shape of glass;
7. well-known synthesis strategies.

Apart from the following advantages, there are many downsides for this technique.

1. The resulting mixture is a dense one without any porosity.
2. The total surface area relies especially on the particle size which can be only achieved by means of grinding. Therefore, it is also been difficult to achieve homogenous particle size of desired textural properties.
3. High temperature furnace around 1300-1600 ºC is been used for the melting of the precursor oxides.

4. At very high temperature treatment, various volatile component such as P_2O_5 is been evaporated.
5. Only a few studies have been reported for antibacterial studies or drug delivery application of melt quench bioactive glasses due to their non-porous nature.

Due to these draw backs of melt quench method, there is a scope for researchers to explore new techniques for the bioactive glass particle synthesis.

1.5.2. Sol-Gel Derived Bioactive Glasses:[43–45]

A new alternative route for the synthesis of bioglass particles has been developed in early 1990's by Li et al, using sol-gel approach. They develop $60SiO_2$-$36CaO$-$4P_2O_5$ composition of bioactive glass and found that the rate of formation of hydroxycarbonate apatite (HCA) is more as compared to melt-quench method. It can be understood that the accelerated bioactivity and quicker rate of HCA formation is due to the mesopore structure and high surface area, which provides the increased rate of dissolution. Remarkably, the sol-gel synthesized glasses possess high surface area, typically in the range of 200 m^2/g to 1000 m^2/g. Whereas melt-quinch derived bioactive glass possess surface area less than 50 m^2/g. This is because, a higher firing temperature in the synthesis process generally leads to decrease in surface area and porosity, which ultimately affects the bioactivity.

Using sol-gel method, bioglass glass can be obtained at low temperature with characteristic properties. From last few decades sol-gel method is been widely used to synthesize bioactive glass particles having enhanced compositional range and superior bioactivity. The sol-gel derived glasses contain a porous network structure that is inherent to this synthesis method, whereas the melt-derived glasses are made of rigid matrix. Using this technique, different glass systems have been synthesized with high

amount of silica and the fast rate of HCA formation noticed. An important difference between sol-gel and melt-derived glass composition lies in the textural properties. The large differences in the textural properties depends on the different physical parameters like temperature, surfactant, and time maintained during synthesis. By controlling these parameters, various textural characteristics like surface area, pore size, pore volume and pore size distribution can be significantly controlled. Subsequently, the mesostructured materials can be achieved with desired properties.

Furthermore, during an in-vivo experiment on a trabecular rabbit, it has been observed that the particles formed using melt-quench method leaves large size residual particles even after the bioactivity whereas such particles not been observed with sol-gel derived bioglass. Moreover, due to the porous structure of bioactive glass, during bioactivity, various biological moieties can pass through it providing structural stability and creating indistinguishable environment between glass structure and host-tissue in physiological environment. In addition, using sol-gel method, various metal ions can be used as dopant for enhancing the inherent properties of the formed bioactive glass. For example, research groups fabricated the bioactive glass network with the Ag^{+} doping for inherent anti-microbial properties.

Apart from numerous pros of sol-gel method over melt-quench method along with its wide applicability, there are many limitations too. The formed particles are of irregular shape along with certain amount of agglomeration. Further, the method requires costly and toxic organic solvents, synthetic organic templates and harsh inorganic acids/bases which follows complicated organometallic synthetic strategies to obtained the desired textural properties. Moreover, sol-gel method has prolonged synthesis period need for the densification of the gel network. At the end sol-gel derived products need to be calcined at high temperature to get porous microstructure. Therefore, there is need of

some environment friendly techniques for the bioactive glass synthesis.

1.5.3. Flame Spray Synthesis of Bioactive Glass:[47,48]

This method is a cost-effective and scalable process for the production of BG nanoparticles. In addition, this procedure ensures the distribution of narrow particle size with low product contamination risk. The flame spray synthesis method is one of the most effective techniques that is based on the gas phase. This technique works on the principle of fabrication of molecular nuclei from either chemical reactions or condensation followed by growth via coalescence in high-temperature regions during process duration. This technique also utilizes metalorganic precursors to generate nanoparticles at temperatures above 1000°C, where the metalorganic precursors are ignited in a flame. The organic components of the liquid precursors are completely ignited and oxidization of the metal components is achieved to fabricate the nanoparticles. The rapid cooling, short residence times as well as the high-temperature atmosphere in the flame reactor leads to the formation of metastable polymorphs directly after the generation of the particles. The fast quenching can retain the materials amorphous state depending on the composite. As mentioned, the benefits of flame spray fabrication are associated with the confirmed scalability of the method, the facile introduction of dopants, and the favourite availability of various nanoparticle compositions. Therefore, it has been interesting for numerous researchers.

1.5.4. Microwave Synthesis:[46,49]

The heating process by means of microwave is the recent aspects nowadays through which the interaction of microwaves with specimen has been taken into account to optimize the synthesis conditions for proper sintering and calcinations to take place. Microwaves are electromagnetic (EM) waves having wavelength and frequency in the range from 1m to 1mm and 300 MHz to 300 GHz, respectively. When the specimen is

exposed to incident microwave radiation, it partially gets reflected (R), absorbed (A) or transmitted (T) depending upon the dielectric properties of material like permittivity and permeability; which is a function of composition, and size of the specimens. The absorbed portion of the incident microwave, heats the material by polarization of the atomic/ molecular structure or through magnetic dipole movement [21]. This technique can furnish the yield of formed BG particles with superior purity in much shorter time. The microwave-assisted technique is widely used for nanomaterial synthesis. The microwave sintering advantages contain enhanced sintered body density and decreased grain sizes at lower temperatures of sintering as well as significantly faster heating rates over conventional strategies. Furthermore, microwave sintering provides mechanical characteristics owing to finer microstructures obtained at equivalent sintering temperatures to conventional resistance heating.

Apart from various advantages, the microwave synthesis method has several disadvantages. Some materials absorb microwaves much more readily than others which narrows the use of the microwave for a wide range of products. It also leads to uneven heating of the material, leading to unreproducible results. Regular control of microwaves is also needed; otherwise, with time heating rate may surpass the solvent boiling point, causing build-up pressure which may lead to an explosion. Further, an increase in material heat may also lead to unexpected side reactions leading to unwanted products forming. Additionally, till knows it is impossible to expand this method at the industrial level due to the lack of an industrial microwave reactor that can produce several tons of material.[50,51]

1.5.5. Bio-Inspired Synthesis:[52–55]

First time, a new approach based on bio-inspired route has been developed by Santhiya *et al* in 2013.[53] Herein, bioactive glass-ceramic was synthesized using CT-DNA as

template at atmospheric conditions with exceptional textural properties, good biocompatibility and it serve as an effective biomaterial for bone tissue engineering. The obtained bioactive glass particles possessed a new type of crystalline phase $(Na_{0.11}Ca_{0.89})(P_{0.11}Si_{0.89})O_3$, different from the earlier observations on 45S5.[53]

Bio-inspired route was developed on admiring naturally produced nano-structured materials such as silica in diatoms by using bio macromolecular templates.[56] Materials produced through biological synthesis have a very high purity and a unique functionality that was created through natural selection. Examples of naturally occurring materials with exceptional mechanical qualities includes shells, bones, and teeth. These are composite materials made up of both inorganic and organic materials. Organic molecules are well known to retain their originality and to induce crystallization of inorganic molecules from the solution phase in ambient conditions. The organic molecules serve as surface directing agent and regulate the shape and growth of the inorganic part of the composite. Many research groups are intensively investigating the interactions between inorganic and organic substances and the influence that one type of substance has on the other.[53] The used organic molecules are mostly synthetic polymers, proteins, carbohydrates and henceforth. These polymers have different number and nature of binding sites which can absorb metal ions stereo-selectively by multipoint bonding. Hence each different type of organic template has unique ability to bind with inorganic molecules and produce particles of different textural and morphological properties.

In this thesis we have used bioinspired method for synthesizing bioactive glass particles. The major advantages of this method are synthesis of bioactive glass at ambient conditions without any compromise in mechanical strength and bioactivity using an organic biodegradable surface directing agent. Chosen bio-inspired

methodology is aqueous based and comprises of few simple cheaper, eco-friendly steps along with the omission for calcination. Special attention is paid to the nano-level of particle synthesis, as at this particular level the surface to volume ratio increases leading more surface area to make strong contact with the bone and with the possibility of getting injected easily to the targeted site of delivery. The porous nature of the synthesized bioactive glass will be utilized in loading the therapeutic molecule and their release kinetics will be studied.

For the synthesis of bioglass particles using the bioinspired route as directed by Santhiya *et al.*[53] Initially, 10 mM tris(hydroxymethyl) aminomethane buffer (Trizma buffer) at pH 8.0 was prepared by dissolving 0.60 g\L trizma HCl and 0.74 g\L trizma base in Milli-Q water. Further, the required amount of surface directing agent was added in 100mL of 10mM Trizma buffer, followed by the addition of the bioglass precursors namely tetraethyl orthosilicate (9.29g), triethyl phosphate (1.0g), sodium acetate (6.36g), and calcium acetate (4.21g), at an interval of 30 minutes with constant stirring at ambient conditions in a silicone oil bath for 24 h. After 24 h formation of precipitate will be observed. It will be then centrifuged, washed with Milli-Q water and dried at 40°C in an air oven for 48 h and preserved in a desiccator for further use. Before characterization, each batch of the bioactive glass samples was lyophilized.

1.6. Bioactivity Analysis:

The rate of bone growth and bone bonding ability is very much crucial to understand the bioactivity and biocompatibility of the bioactive glass and it mainly depends on the rate of dissolution of silica network. The bone-bonding ability of a material is often evaluated by examining the ability of apatite to form on its surface in a simulated body fluid (SBF) with ion concentrations nearly equal to those of human blood plasma.[52,57] It is proven in the literature, that the ability of BGNPs to form apatite in

SBF is in correlation with the *in-vivo* bone bonding ability of BGNPs. Various novel bioactive materials have been developed on the bases on bioactivity analysis in SBF. This technique, to study bioactivity not only saves the animals sacrificed for *in-vivo* studies but also remarkably reduce the time required to setup the animal experiment procedure.[58,59]

The simulated bodily fluid (SBF) is a solution maintained under mild pH and physiological temperature conditions with ion concentration similar to that of human blood plasma. Kokubo *et al.*[58] invented SBF in order to assess the alterations on the surface of a bioactive glass ceramic as shown in **Table 1.1**.

Table 1.1: The ionic concentration of Human blood plasma compare to that of simulated body fluid is as follows:

Formulation	**Na^+**	**K^+**	**Mg^{2+}**	**Ca^{2+}**	**Cl^-**	**HCO_3^-**	**HPO_4^{2-}**	**SO_4^{2-}**
Human Blood plasma (mM)	142.0	5.0	1.5	2.5	103.0	27.0	1.0	0.5
Simulated Body Fluid (mM)	142.0	5.0	1.5	2.5	147.8	4.2	1.0	0.5

1.6.1. Bioactivity Mechanism of Bioactive Glass:

There are two stages for the bioactivity of bioactive glasses. First, Bone bonding is attributed to the formation of an HCA layer, which interacts with collagen fibrils of damaged bone to form a bond **(Fig. 1.6**).[23,26] Once the HCA layer has formed, the next stage is the adsorption of biological moieties, macrophages which helps in cell differentiation and cell proliferation results in the generation of healthy hard and soft tissues (**Fig. 1.7**).[58]

There are five proposed steps for HCA layer formation in body fluid *in-vivo* or in simulated body fluid (SBF) *in-vitro*.[26]

1. Initially, H^+ ions from the surrounding physiologically simulated body fluid (SBF), rapidly exchange with alkali and alkaline earth cations like Na^+ and Ca^{2+} ions, forming silanol linkages (Si-OH) on the glass-solution interface:

$$\mathbf{Si–O–Na^+ + H^+ \rightarrow Si–OH + Na^+(aq.)}$$

$$\mathbf{Si\text{-}O\text{-}Ca^{2+}\text{-}O\text{-}Si + 2H^+ \rightarrow 2Si\text{-}OH + Ca^{2+}(aq.)}$$

   Herein, the pH of the solution increases and a silica-rich region forms near the glass-solution interface. Phosphate is also lost from the glass. Due to superior textural properties, the ion exchange kinetics response mechanism has been purposefully improved. The accessible porosity, increased surface area, and higher material reactivity of BGNPs material, among other textural traits, all contribute to the acceleration of surface reaction processes. As compared to conventional bioactive glasses, the higher surface interactions of mesoporous BGNPs ultimately result in an additional intensive ions-exchange followed by better H^+ ions exchange from the physiological solution.

2. The second stage deals with the formation of high density of silanols (Si-OH) groups at the glass-surface interface in mesoporous BGNPs whereas in the case of conventional BG the content of Si-OH formed is very less. Due to high local pH, OH^- ions from the solution attack the silica glass network results in the breakage of Si–O–Si bonds. Soluble silica is also lost in the form of $Si(OH)_4$ to the solution, leaving more Si–OH (silanol) at the glass–solution interface:

$$\mathbf{2(Si—O—Si) + H_2O \rightarrow 2Si—OH}$$

3. In this stage, repolymerization of Si-OH groups took place to form silica-rich layer near the glass–solution interface:

$$\mathbf{Si—OH + OH—Si \rightarrow —Si—O—Si— + H_2O}$$

4. Migration of Ca^{2+} and PO_4^{3-}groups to the surface of glass from the solution, forming Amorphous calcium phosphate (ACP) ($CaO–P_2O_5$) rich layer on the top of the silica-rich layer. In the case of Mesoporous bioglass BGNPs this deposition is intense compare to the conventional bioglass material due to high surface area and high concentration of surface silanol groups.
5. In the final stage, incorporation of hydroxyls ions and carbonate ions from the solution leads to the devitrification of ACP which results in the formation of hydroxycarbonate apatite (HCA) layer onto the surface. Furthermore, it has been noticed that outstanding textural characteristics of mesoporous bioglass than conventional bioglass particles leads to the time deviation for HCA precipitation. Hence, the higher surface area and mesoporosity of the bioglass are responsible for accelerating the HCA crystal growth at relatively shorter duration then conventional BGNPs.

After the formation of HCA crystals, second stage is the adsorption of biological moieties, macrophages which helps in cell differentiation and cell proliferation results in the generation of healthy hard and soft tissues **(Fig. 1.7)**.[17,22] SBF solution composition is mainly consist of ionic concentrations but lack proteins like collagen and fibronectin. It leads to the glass dissolution and hap deposition but for *in-vitro* cell analysis to study the osteoblast cell adhesion on HAP surface, cell culture media consist of protein serum is required. Cell culture analysis enables one to show the impact of BG on active cells by monitoring the timely growth of cells directly in contact with the glass sample. It is been noticed that 45S5 bioglass shows better results for *in-vitro* cell-

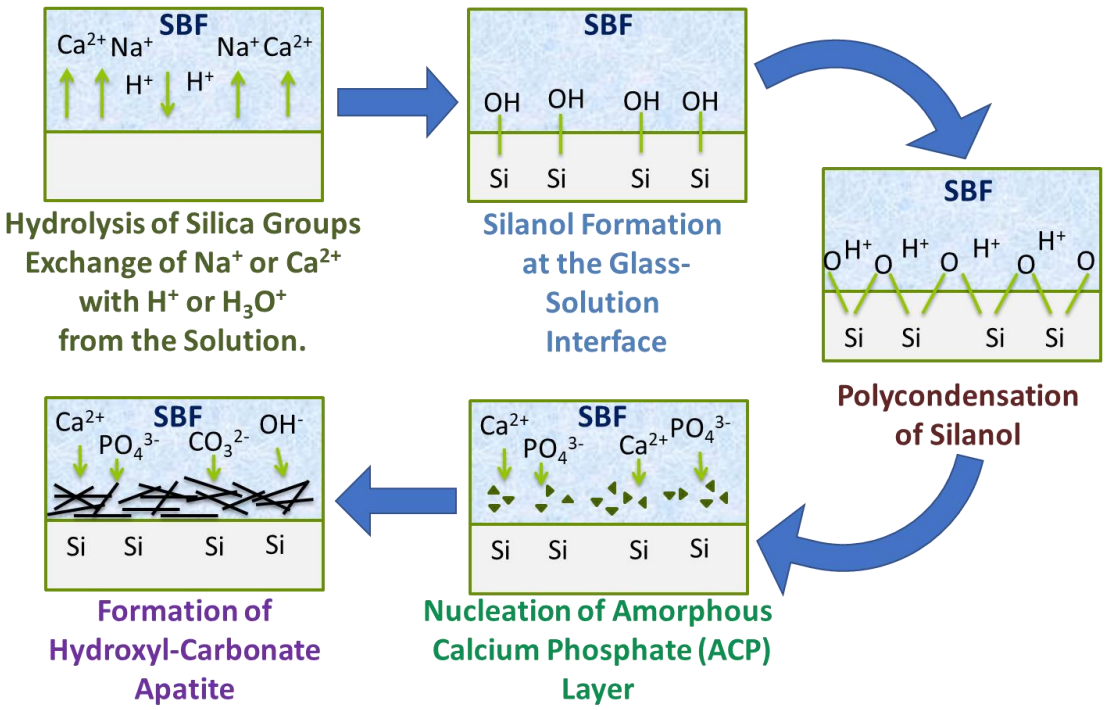

Fig. 1.6: Mechanism of Hydroxyapatite layer formation on Bioactive Glass surface when treated with simulated body fluid (SBF).(modified)[63]

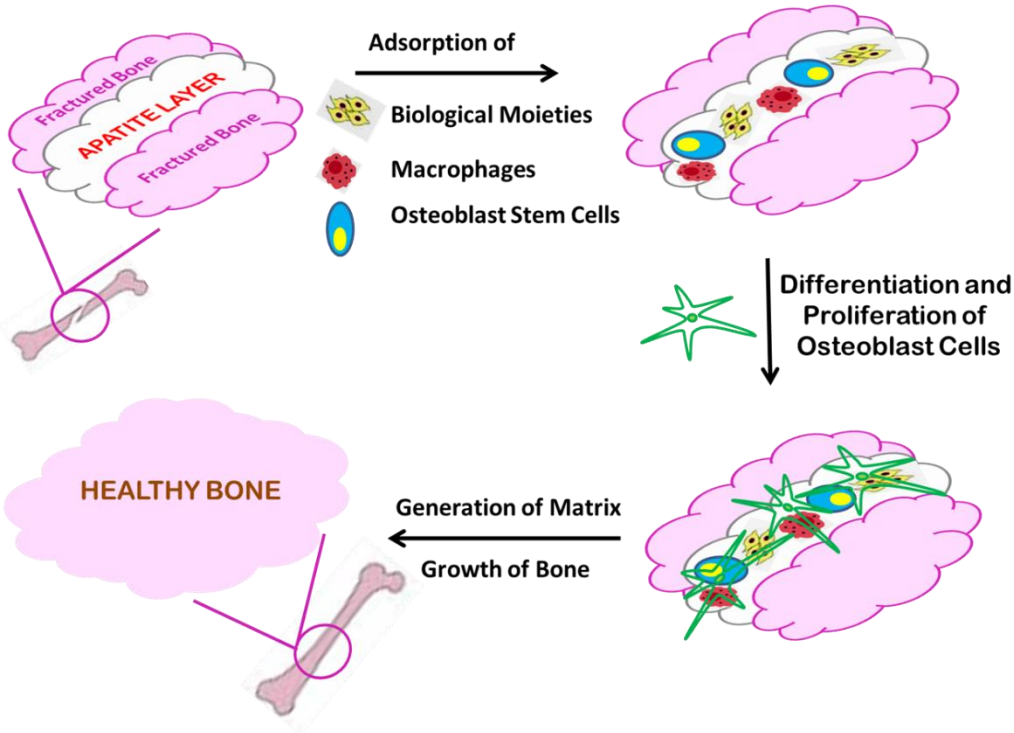

Fig. 1.7: Sequence of interfacial reactions between bone & bioactive glass.

cycling which results in quick cellular proliferation compare to other compositions of bioactive glasses. 45S5 bioglass leads to the formation of the mineralized tissue in a comparatively short-time interval with high concentration of cell population, irrespective of the glass network structure polymerization. It has been observed that various network modifiers such as Na^+ and Ca^{2+}, shows noticeable influence on cellular proliferation and differentiation.[60,61] It is also been noticed that the bioglass glass composition mainly 45S5 show better bone bonding ability and degradability compare to the synthetic HAP particles.[62]

1.7.Advances in Bioactive Glass:

1.7.1. Bone Graft Substitute:

A bone graft can be used to replace lose or damage bone resulted due to an infection, disease, or trauma. As a synthetic bone graft, BG has been used in clinical situations for more than a decade. It is available as a product named Novabone for orthopaedic surgery[64] and as PerioGlas for maxillofacial surgery.[65] In 2005, FDA also approved the use of 45S5 bioglass for various bone engineering applications due to its osteostimulation and osteoconductive functions.[66] It is been reported in the literature that bioglass scaffolds can be used as bone graft material due to their low inflammatory response and high resorption rate. In multiple long-term studies, bioactive glasses as bone graft material shows outstanding bone healing abilities.

1.7.2. Bone regeneration application:

A shift to tissue regeneration from tissue replacement is needed as per current scenario of biomedical application. Bioactive glasses are well known for their inherent bone regeneration ability, due to the dissolution of ions when interacted with body fluid.[29,34] It is been found that the bioactive glass particles on interaction with body

fluid exchange ions which result in subsequent deposition of hydroxyapatite crystals leads to the regeneration of bone naturally. In comparison to non-porous materials, porosity confirms enhanced bioactivity, which in turn increases cellular proliferation.[3] Additionally, the materials bioactivity is further increased by the pores organised orderly.

1.7.3. Drug Delivery applications:

The application of bioactive glass particles as third generation biomaterial is extended beyond bone regeneration. New generation bioactive glass particles have mesoporous nature and high surface area due to nano size in nature. Therefore, they work as a good cargo carrier for various drug delivery applications. It has been found in the literature that for mesoporous bioactive glass nanoparticles, mostly drug release occurs through Fickian diffusion mechanism and can be controlled for slow and steady drug release kinetics compare to conventional bioactive glass materials.[66] To prevent infection at wound site, bioactive glass particles are incorporated with various anti-bacterial drugs such as gentamicin[67], ampicillin[68], amoxicillin[69] and hence forth. Moreover, therapeutic molecules like anti-inflammatory drugs[70], anti-cancerous drugs[71] and osteogenic drugs are also been studies. Targeted therapeutic delivery application to improve angiogenesis, osteogenesis and bone related gene expressions are some of the important application of mesoporous bioactive glass nanoparticles. Moreover, by tailoring the surface of nanoparticles some hydrophobic drugs can also be incorporated for various applications.

1.7.4. Therapeutic Ions Doping:

The structure of bioglass consists of various network formers and network modifiers. It is interesting to note that these network modifiers can be replaced or new ions can be

added as per the clinical applications without interfering the bioactivity of bioactive glass particles. Various therapeutic ions can be doped in bioactive glass network as per the medication needed. Silver, copper, selenium, strontium, magnesium, iron, cobalt, zinc, and many more are doped in bioactive glass network as seen in the literature.[72–74] Silver, cerium, gallium dopped particles show inherent antibacterial effect. Cobalt doping is used for anti-cancerous activity. Europium is used for biolabeling. Iron doped particles show magnetic properties for various medical applications. Further, ion doping also helps to enhance the mechanical, thermal and biophysical properties of bioactive glass particles. Ions such as lithium, boron, cerium, gallium shows increase in osteogenesis and osteoinductive properties.[75]

Before this thesis, from our lab, the first thesis on mesoporous bioactive glass nanoparticles was submitted by Dr. Nidhi Gupta entitled **"Pluripotent Bioactive Glass Material for Bone Regenerative Applications."** Dr. Nidhi Gupta, under the supervision of Dr. Deenan Santhiya, used a bio-inspired route at ambient conditions for the synthesis of bioglass particles, using different organic surface directing agents, namely, polyamido amine (PAMAM) dendrimer, cetyl trimethyl ammonium bromide (CTAB), folic acid, cellulose and its derivatives mainly, aminated cellulose and methylcellulose. Interestingly, textural tunability has been observed in the bioactive glass material with the corresponding templates. This tunability directly affects the materials bioactive nature, biological response for osteogenesis, viscoelastic response of the material and henceforth. She explored the bioglass as a third-generation biomaterial, i.e., beyond usual bone regeneration towards plasmid DNA and co-antibiotic delivery against osteomyelitis. Herein, the structural, morphological and textural characteristics of bioactive glass nanoparticles have been explored. The applications of formed bioglass nanoparticles were tested for gene, antibiotics and therapeutic ions delivery.

Interestingly, due to the highly fragile and low mechanical strength of bioactive glass, there is vast research scope to synthesize inorganic-organic hybrid composite bioactive glass materials with enhanced textural and, morphological properties. Considering the immense requirement of hybrid bioactive glass materials in soft and hard tissue engineering, an initiative has been made to investigate the *in-situ* mineralization of bioactive glass using organic molecules for various soft and hard tissue regeneration as discussed in successive chapters.

RESEARCH SCOPE

On the bases on current research literature interest reported till date, following are the major possibilities that need to be explored in the field of bioactive glass materials for hard and soft tissue engineering.

1. Sustainable synthetic methodologies for the synthesis of bioactive glass materials are to be refined for industrial scale production.
2. A new class of bioactive glass materials such as inorganic - organic hybrids (small molecule and natural extract) does not exist till date.
3. Major studies focus on the bioactive glass as a bone regenerative material and in bone tissue engineering applications.
4. Studies related to soft tissue regeneration especially tendons and ligaments (connective tissues) using bioactive glass are very less.
5. Studies focus on simultaneous regeneration of soft and hard tissues are in infantry.

MAJOR OBJECTIVES

In this investigation, considering the said research scope and importance of bioactive glass particles for various biomedical applications, the following major objectives are proposed.

- Novel strategies to synthesize bioactive glass materials for soft and hard tissue engineering.
    - Synthesis of bioactive glass material using small molecules.
    - Synthesis of bioactive glass using plant extract.
- Applications of bioactive glass materials for soft and hard tissue engineering.
    - *In-situ* mineralization of bioactive glass particles in bio-polymers based hydrogel matrix.
    - In-situ mineralization of bioactive glass in electrospun nanofibers.
- To evaluate the cytocompatibility and *in-vitro* interaction of bioactive glass based material with the bone cells.
- To evaluation the drug delivery application of the bioactive glass based materials.

OUTLINE OF THE THESIS

Chapters included in this thesis **summarises the current literature and results obtained till date as follows:**

Chapter II: In this chapter we briefly explain the principles and analytical methods for various instrumentation techniques used for the characterization of bioglass materials synthesized in the present study.

Chapter III: In this chapter, we discuss the effect of pKa and pI values of L-Lysine for tailoring the textural and rheological properties of bioactive glass hybrid xerogels. Herein, mesoporous L-lysine-bioactive glass (LBG) hybrid xerogels were synthesized by bioinspired method at ambient conditions at different pKa and pI values of L-Lysine. The formed hybrid xerogels was thoroughly investigated for their composition, interaction mechanism between the L-lysine molecules and the bioglass precursors, bioactivity in simulated body fluid, textural properties, rheological properties and drug delivery applications. These formed hybrid xerogels can be tailored for various textural as well as rheological properties for targeted bone engineering applications along with drug delivery applications.

Chapter IV: In this chapter, we explored a sustainable green synthesis for large scale production of bioactive glass particles. Herein, using a simple green approach Bioactive glass particles was successfully synthesized using *Trigonella foenum-graecum* (TFG) leaf extract (TFGL_EX). The TFGL_EX acted both as a template and precursor for the synthesis of BGNPs (TFGL_BG1). In addition, TFGL_BG1 could also show inherent antibacterial property along with sustainable drug release profile. Hence, there is no doubt that TFGL_BG1 is a sustainable property dependent bioglass material for biomedical applications.

Chapter V: In this chapter, we have designed a novel collagen-pectin (CP) composite hydrogel (CPBG) containing *in-situ* mineralized bioactive glass (BG) particles to simulate an integrative 3D cell environment. The formed hydrogel was thoroughly investigated for the surface patch binding of collagen and pectin molecules and their hybrid composite crosslinked network formation with the BGNPs that are acting as a crosslink junction. In addition, the formed hydrogel shows bioactivity, biocompatibility, cellular viability and a good candidate for drug cargo carrier for targeted drug delivery applications. Hence, the hydrogel was proven as a great contender for the regeneration of both soft and hard tissues.

Chapter VI: In this chapter, we have provided a new insight into the *in-situ* mineralization of bioactive glass into gelatin-pectin ultrafine fibers and fibrous mat along with incorporation of 7-dehydrocholesterol i.e., a vitamin D precursor, formed by electrospinning in aqueous phase. The formed fibrous mat exhibit excellent bioactivity, remarkable cytocompatibility and also shows cellular proliferation on its surface. Hence, the engineered fibrous mat act as a promising candidate for the strengthening of the neo regenerated bones.

REFERENCES:

[1] E. Abdel Meguid, Y. Ke, J. Ji, A.H.K. El-Hashash, Stem cells applications in bone and tooth repair and regeneration: New insights, tools, and hopes, J. Cell. Physiol. 233 (2018) 1825–1835. https://doi.org/10.1002/jcp.25940.

[2] A. Kuźnik, A. Październiorniok-Holewa, P. Jewula, N. Kuźnik, Bisphosphonates—much more than only drugs for bone diseases, Eur. J. Pharmacol. 866 (2020) 172773. https://doi.org/https://doi.org/10.1016/j.ejphar.2019.172773.

[3] I. Farooq, Z. Imran, U. Farooq, A. Leghari, H. Ali, Bioactive glass: a material for the future, World J Dent. 3 (2012) 199–201. https://doi.org/10.5005/jp-journals-10015-1156.

[4] L. Li, H. Lu, Y. Zhao, J. Luo, L. Yang, W. Liu, Q. He, Functionalized cell-free scaffolds for bone defect repair inspired by self-healing of bone fractures: A review and new perspectives, Mater. Sci. Eng. C. 98 (2019) 1241–1251. https://doi.org/10.1016/j.msec.2019.01.075.

[5] M. Haffner-Luntzer, K.D. Hankenson, A. Ignatius, R. Pfeifer, B.A. Khader, F. Hildebrand, M. Van Griensven, H. Pape, M. Lehmicke, Review of animal models of comorbidities in fracture-healing research, J. Orthop. Res. 37 (2019) 2491–2498. https://doi.org/10.1002/jor.24454.

[6] C. Wan, S.R. Gilbert, Y. Wang, X. Cao, X. Shen, G. Ramaswamy, K.A. Jacobsen, Z.S. Alaql, A.W. Eberhardt, L.C. Gerstenfeld, Activation of the hypoxia-inducible factor-1α pathway accelerates bone regeneration, Proc. Natl. Acad. Sci. 105 (2008) 686–691. https://doi.org/10.1073/pnas.0708474105.

[7] A.A. El-Rashidy, J.A. Roether, L. Harhaus, U. Kneser, A.R. Boccaccini, Regenerating bone with bioactive glass scaffolds: A review of in vivo studies in bone defect models, Acta Biomater. 62 (2017) 1–28. https://doi.org/10.1016/j.

actbio.2017.08.030.

[8] F. Paladini, M. Pollini, Antimicrobial silver nanoparticles for wound healing application: progress and future trends, Materials (Basel). 12 (2019) 2540. https://doi.org/10.3390%2Fma12162540.

[9] P. Kostenuik, F.M. Mirza, Fracture healing physiology and the quest for therapies for delayed healing and nonunion, J. Orthop. Res. 35 (2017) 213–223. https://doi.org/10.1002/jor.23460.

[10] N.A.P. van Gestel, J. Geurts, D.J.W. Hulsen, B. van Rietbergen, S. Hofmann, J.J. Arts, Clinical applications of S53P4 bioactive glass in bone healing and osteomyelitic treatment: a literature review, Biomed Res. Int. 2015 (2015). https://doi.org/10.1155/2015/684826.

[11] D. Bakhshayesh, A. Rahmani, N. Asadi, A. Alihemmati, H. Tayefi Nasrabadi, A. Montaseri, S. Davaran, S. Saghati, A. Akbarzadeh, A. Abedelahi, An overview of advanced biocompatible and biomimetic materials for creation of replacement structures in the musculoskeletal systems: focusing on cartilage tissue engineering, J. Biol. Eng. 13 (2019) 1–21. https://doi.org/10.1186/s13036-019-0209-9.

[12] O.E. Armitage, M.L. Oyen, Hard-soft tissue interface engineering, in: Eng. Miner. Load Bear. Tissues, Springer, 2015: pp. 187–204. https://doi.org/10.1007/978-3-319-22345-2_11.

[13] H.J. Haugen, S.P. Lyngstadaas, F. Rossi, G. Perale, Bone grafts: which is the ideal biomaterial?, J. Clin. Periodontol. 46 (2019) 92–102. https://doi.org/10.1111/jcpe.13058.

[14] H. Shi, Z. Zhou, W. Li, Y. Fan, Z. Li, J. Wei, Hydroxyapatite based materials for bone tissue engineering: A brief and comprehensive introduction, Crystals. 11

(2021) 149. https://doi.org/10.3390/cryst11020149.

[15] M. Bohner, B.L.G. Santoni, N. Döbelin, β-tricalcium phosphate for bone substitution: Synthesis and properties, Acta Biomater. 113 (2020) 23–41. https://doi.org/10.1016/j.actbio.2020.06.022.

[16] P. Srinath, P. Abdul Azeem, K. Venugopal Reddy, Review on calcium silicate-based bioceramics in bone tissue engineering, Int. J. Appl. Ceram. Technol. 17 (2020) 2450–2464. https://doi.org/10.1111/ijac.13577.

[17] R.G. Ribas, V.M. Schatkoski, T.L. do Amaral Montanheiro, B.R.C. de Menezes, C. Stegemann, D.M.G. Leite, G.P. Thim, Current advances in bone tissue engineering concerning ceramic and bioglass scaffolds: A review, Ceram. Int. 45 (2019) 21051–21061. https://doi.org/10.1016/J.CERAMINT.2019.07.096.

[18] X. Yu, X. Tang, S. V Gohil, C.T. Laurencin, Biomaterials for bone regenerative engineering, Adv. Healthc. Mater. 4 (2015) 1268–1285. https://doi.org/10.1002/adhm.201400760

[19] A.J. Salinas, P. Esbrit, M. Vallet-Regí, A tissue engineering approach based on the use of bioceramics for bone repair, Biomater. Sci. 1 (2013) 40–51. https://doi.org/10.1039/C2BM00071G.

[20] H. Qu, H. Fu, Z. Han, Y. Sun, Biomaterials for bone tissue engineering scaffolds: A review, RSC Adv. 9 (2019) 26252–26262. https://doi.org/10.1039/C9RA05214C.

[21] N. Gupta, D. Santhiya, 3 - Mesoporous bioactive glass and its applications, in: H. Ylänen (Ed.), Bioact. Glas. (Second Ed., Second Edi, Woodhead Publishing, 2018: pp. 63–85. https://doi.org/10.1016/B978-0-08-100936-9.00003-4.

[22] S. Sarin, A. Rekhi, Bioactive glass: A potential next generation biomaterial, SRM J. Res. Dent. Sci. 7 (2016) 27. https://doi.org/10.4103/0976-433X.176482.

[23] L.L. Hench, The story of Bioglass®, J. Mater. Sci. Mater. Med. 17 (2006) 967–978. https://doi.org/10.1007/s10856-006-0432-z.

[24] J.R. JONES, 12 - Bioactive glass, in: T. Kokubo (Ed.), Bioceram. Their Clin. Appl., Woodhead Publishing, 2008: pp. 266–283. https://doi.org/10.1533/9781845694227.2.266.

[25] D.S. Brauer, Bioactive glasses—structure and properties, Angew. Chemie Int. Ed. 54 (2015) 4160–4181. https://doi.org/10.1002/anie.201405310.

[26] J.R. Jones, Reprint of: Review of bioactive glass: From Hench to hybrids, Acta Biomater. 23 (2015) S53–S82. https://doi.org/10.1016/j.actbio.2015.07.019.

[27] K. Deshmukh, T. Kovářík, T. Křenek, D. Docheva, T. Stich, J. Pola, Recent advances and future perspectives of sol–gel derived porous bioactive glasses: a review, RSC Adv. 10 (2020) 33782–33835. https://doi.org/10.1039/D0RA04287K.

[28] F. Baino, G. Novajra, V. Miguez-Pacheco, A.R. Boccaccini, C. Vitale-Brovarone, Bioactive glasses: Special applications outside the skeletal system, J. Non. Cryst. Solids. 432 (2016) 15–30. https://doi.org/10.1016/j.jnoncrysol.2015.02.015.

[29] V. Miguez-Pacheco, L.L. Hench, A.R. Boccaccini, Bioactive glasses beyond bone and teeth: Emerging applications in contact with soft tissues, Acta Biomater. 13 (2015) 1–15. https://doi.org/10.1016/j.actbio.2014.11.004.

[30] L. Cui, J. Liang, H. Liu, K. Zhang, J. Li, Nanomaterials for angiogenesis in skin tissue engineering, Tissue Eng. Part B Rev. 26 (2020) 203–216. https://doi.org/10.1089/ten.teb.2019.0337.

[31] S. Kargozar, F. Baino, S. Hamzehlou, R.G. Hill, M. Mozafari, Bioactive glasses: sprouting angiogenesis in tissue engineering, Trends Biotechnol. 36 (2018) 430–

444. https://doi.org/10.1016/j.tibtech.2017.12.003.

[32] J. Crush, A. Hussain, K.T.M. Seah, W.S. Khan, Bioactive glass: methods for assessing angiogenesis and osteogenesis, Front. Cell Dev. Biol. (2021) 1523. https://doi.org/10.3389/fcell.2021.643781.

[33] K. Zheng, B. Sui, K. Ilyas, A.R. Boccaccini, Porous bioactive glass micro-and nanospheres with controlled morphology: Developments, properties and emerging biomedical applications, Mater. Horizons. 8 (2021) 300–335. https:// doi.org/10.1039/D0MH01498B.

[34] F. Baino, Bioactive glasses–when glass science and technology meet regenerative medicine, Ceram. Int. 44 (2018) 14953–14966. https://doi.org /10.1016/J.CERAMINT.2018.05.180.

[35] S. Kargozar, R.K. Singh, H.-W. Kim, F. Baino, "Hard" ceramics for "Soft" tissue engineering: Paradox or opportunity?, Acta Biomater. 115 (2020) 1–28. https:// doi.org/10.1016/j.actbio.2020.08.014.

[36] S. Kargozar, S. Hamzehlou, F. Baino, Can bioactive glasses be useful to accelerate the healing of epithelial tissues?, Mater. Sci. Eng. C. 97 (2019) 1009–1020. https://doi.org/10.1016/j.msec.2019.01.028.

[37] T. Mehrabi, A.S. Mesgar, Z. Mohammadi, Bioactive glasses: a promising therapeutic ion release strategy for enhancing wound healing, ACS Biomater. Sci. Eng. 6 (2020) 5399–5430. https://doi.org/10.1021/acsbiomaterials.0c00528.

[38] S. Kargozar, M. Mozafari, M. Ghenaatgar-Kasbi, F. Baino, Bioactive glasses and glass/polymer composites for neuroregeneration: should we be hopeful?, Appl. Sci. 10 (2020) 3421. https://doi.org/10.3390/app10103421.

[39] S. Majumdar, S. Gupta, S. Krishnamurthy, Multifarious applications of bioactive glasses in soft tissue engineering, Biomater. Sci. 9 (2021) 8111–8147. https://

doi.org/10.1039/D1BM01104A.

[40] R. Sergi, D. Bellucci, V. Cannillo, A comprehensive review of bioactive glass coatings: State of the art, challenges and future perspectives, Coatings. 10 (2020) 757. https://doi.org/10.3390/coatings10080757.

[41] H.R. Fernandes, A. Gaddam, A. Rebelo, D. Brazete, G.E. Stan, J.M.F. Ferreira, Bioactive glasses and glass-ceramics for healthcare applications in bone regeneration and tissue engineering, Materials (Basel). 11 (2018) 2530. https:// doi.org/10.3390/ma11122530.

[42] N.O. Joy-anne, Y. Su, X. Lu, P.-H. Kuo, J. Du, D. Zhu, Bioactive glass coatings on metallic implants for biomedical applications, Bioact. Mater. 4 (2019) 261–270. https://doi.org/10.1016/j.bioactmat.2019.09.002.

[43] K. Zheng, A.R. Boccaccini, Sol-gel processing of bioactive glass nanoparticles: A review, Adv. Colloid Interface Sci. 249 (2017) 363–373. https://doi.org/ 10.1016/j.cis.2017.03.008.

[44] M. Montazerian, E. Dutra Zanotto, History and trends of bioactive glass-ceramics, J. Biomed. Mater. Res. Part A. 104 (2016) 1231–1249. https:// doi.org/10.1002/jbm.a.35639.

[45] G. Kaur, G. Pickrell, N. Sriranganathan, V. Kumar, D. Homa, Review and the state of the art: sol–gel and melt quenched bioactive glasses for tissue engineering, J. Biomed. Mater. Res. Part B Appl. Biomater. 104 (2016) 1248–1275. https://doi.org/10.1002/jbm.b.33443.

[46] M. Dziadek, B. Zagrajczuk, P. Jelen, Z. Olejniczak, K. Cholewa-Kowalska, Structural variations of bioactive glasses obtained by different synthesis routes, Ceram. Int. 42 (2016) 14700–14709. http://dx.doi.org/10.1016/j.ceramint. 2016.06.095.

[47] M.E. Taygun, A.R. Boccaccini, Nanoscaled bioactive glass particles and nanofibers, in: Bioact. Glas., Elsevier, 2018: pp. 235–283. https://doi.org/10.1016/B978-0-08-100936-9.00012-5.

[48] B. Garrido, S. Dosta, I.G. Cano, Bioactive glass coatings obtained by thermal spray: Current status and future challenges, Boletín La Soc. Española Cerámica y Vidr. (2021). https://doi.org/10.1016/j.bsecv.2021.04.001.

[49] H. Khalid, F. Suhaib, S. Zahid, S. Ahmed, A. Jamal, M. Kaleem, A.S. Khan, Microwave-assisted synthesis and in vitro osteogenic analysis of novel bioactive glass fibers for biomedical and dental applications., Biomed. Mater. 14 (2018) 15005. https://doi.org/10.1088/1748-605X/aae3f0.

[50] A.K. Sharma, S. Gupta, Microwave Processing of Biomaterials for Orthopedic Implants: Challenges and Possibilities, JOM. 72 (2020) 1211–1228. https://doi.org/10.1007/s11837-020-04003-z.

[51] N. Wang, J.Y.H. Fuh, S.T. Dheen, A. Senthil Kumar, Synthesis methods of functionalized nanoparticles: a review, Bio-Design Manuf. 4 (2021) 379–404. https://doi.org/10.1007/s42242-020-00106-3.

[52] N. Gupta, D. Santhiya, A. Aditya, Tailored smart bioactive glass nanoassembly for dual antibiotic: In vitro sustained release against osteomyelitis, J. Mater. Chem. B. 4 (2016) 7605–7619. https://doi.org/10.1039/c6tb01528j.

[53] D. Santhiya, H.K. Alajangi, F. Anjum, S. Murugavel, M. Ganguli, Bio-inspired synthesis of microporous bioactive glass-ceramic using CT-DNA as a template, J. Mater. Chem. B. 1 (2013) 6329. https://doi.org/10.1039/c3tb21212b.

[54] N. Gupta, D. Santhiya, A. Aditya, K. Badra, Dendrimer templated bioactive glass-ceramic nanovehicle for gene delivery applications, RSC Adv. 5 (2015) 56794–56807. https://doi.org/10.1039/c5ra04441c.

[55] N. Gupta, D. Santhiya, Role of cellulose functionality in bio-inspired synthesis of nano bioactive glass, Mater. Sci. Eng. C. 75 (2017) 1206–1213. https://doi.org/10.1016/j.msec.2017.03.026.

[56] L.P. Bauermann, J. Bill, F. Aldinger, Bio-inspired syntheses of ZnO-protein composites, Int. J. Mater. Res. 98 (2007) 879–883. https://doi.org/doi:10.3139/146.101536.

[57] N. Gupta, D. Santhiya, A. Aditya, K. Badra, Dendrimer templated bioactive glass-ceramic nanovehicle for gene delivery applications, RSC Adv. 5 (2015). https://doi.org/10.1039/c5ra04441c.

[58] T. Kokubo, H. Takadama, How useful is SBF in predicting in vivo bone bioactivity?, Biomaterials. 27 (2006) 2907–2915. https://doi.org/10.1016/j.biomaterials.2006.01.017.

[59] T. Kokubo, Bioactive glass ceramics: properties and applications, Biomaterials. 12 (1991) 155–163. https://doi.org/10.1016/0142-9612(91)90194-F.

[60] M. Łączka, K. Cholewa-Kowalska, A.M. Osyczka, Bioactivity and osteoinductivity of glasses and glassceramics and their material determinants, Ceram. Int. 42 (2016) 14313–14325. http://dx.doi.org/10.1016%2Fj.ceramint.2016.06.077.

[61] H. Arstila, E. Vedel, L. Hupa, M. Hupa, Factors affecting crystallization of bioactive glasses, J. Eur. Ceram. Soc. 27 (2007) 1543–1546. http://dx.doi.org/10.1016/j.jeurceramsoc.2006.04.017

[62] M. Rizwan, M. Hamdi, W.J. Basirun, Bioglass® 45S5-based composites for bone tissue engineering and functional applications, J. Biomed. Mater. Res. - Part A. (2017). https://doi.org/10.1002/jbm.a.36156.

[63] H. Eckert, Structural characterization of bioactive glasses by solid state NMR, J.

Sol-Gel Sci. Technol. 88 (2018) 263–295. https://link.springer.com/article/10.1007/s10971-018-4795-7.

[64] J. Madison, J.N. Oliver, D. Zhu, Bioactive glasses in orthopedic applications, in: Racing Surf., Springer, 2020: pp. 557–575. https://doi.org/10.1007/978-3-030-34471-9_21.

[65] V.V. Dam, H.A. Trinh, D. Rokaya, D.H. Trinh, Bone Augmentation for Implant Placement: Recent Advances, Int. J. Dent. 2022 (2022). https://doi.org/10.1155/2022/8900940.

[66] F. Baino, S. Hamzehlou, S. Kargozar, Bioactive glasses: where are we and where are we going?, J. Funct. Biomater. 9 (2018) 25. https://doi.org/10.3390%2Fjfb9010025.

[67] A. Escobar, N.E. Muzzio, P. Andreozzi, S. Libertone, E. Tasca, O. Azzaroni, M. Grzelczak, S.E. Moya, Antibacterial layer-by-layer films of poly (acrylic acid)–gentamicin complexes with a combined burst and sustainable release of gentamicin, Adv. Mater. Interfaces. 6 (2019) 1901373. https://doi.org/10.1002/admi.201901373.

[68] S. Gupta, S. Majumdar, S. Krishnamurthy, Bioactive glass: A multifunctional delivery system, J. Control. Release. 335 (2021) 481–497. https://doi.org/10.1016/j.jconrel.2021.05.043.

[69] Z. Tabia, K. El Mabrouk, M. Bricha, K. Nouneh, Mesoporous bioactive glass nanoparticles doped with magnesium: drug delivery and acellular in vitro bioactivity, RSC Adv. 9 (2019) 12232–12246. https://doi.org/10.1039/C9RA01133A.

[70] K. Zheng, E. Torre, A. Bari, N. Taccardi, C. Cassinelli, M. Morra, S. Fiorilli, C. Vitale-Brovarone, G. Iviglia, A.R. Boccaccini, Antioxidant mesoporous Ce-

doped bioactive glass nanoparticles with anti-inflammatory and pro-osteogenic activities, Mater. Today Bio. 5 (2020) 100041. https://doi.org/10.1016/j.mtbio.2020.100041.

[71] M.S.U. Rahman, M.A. Tahir, S. Noreen, M. Yasir, I. Ahmad, M.B. Khan, K.W. Ali, M. Shoaib, A. Bahadur, S. Iqbal, Magnetic mesoporous bioactive glass for synergetic use in bone regeneration, hyperthermia treatment, and controlled drug delivery, RSC Adv. 10 (2020) 21413–21419. https://doi.org/10.1039/C9RA09349D.

[72] N. Gupta, D. Santhiya, S. Murugavel, A. Kumar, A. Aditya, M. Ganguli, S. Gupta, Effects of transition metal ion dopants (Ag, Cu and Fe) on the structural, mechanical and antibacterial properties of bioactive glass, Colloids Surfaces A Physicochem. Eng. Asp. 538 (2018) 393–403. https://doi.org/10.1016/j.colsurfa.2017.11.023.

[73] G. Kaur, O.P. Pandey, K. Singh, D. Homa, B. Scott, G. Pickrell, A review of bioactive glasses: Their structure, properties, fabrication and apatite formation, J. Biomed. Mater. Res. - Part A. 102 (2014) 254–274. https://doi.org/10.1002/jbm.a.34690.

[74] G. Gautam, S. Kumar, K. Kumar, Processing of biomaterials for bone tissue engineering: State of the art, Mater. Today Proc. 50 (2022) 2206–2217. https://doi.org/10.1016/j.matpr.2021.09.459.

[75] R. Eivazzadeh-Keihan, K.K. Chenab, R. Taheri-Ledari, J. Mosafer, S.M. Hashemi, A. Mokhtarzadeh, A. Maleki, M.R. Hamblin, Recent advances in the application of mesoporous silica-based nanomaterials for bone tissue engineering, Mater. Sci. Eng. C. 107 (2020) 110267. https://doi.org/10.1016%2Fj.msec.2019.110267.

CHAPTER 2

Characterization Techniques

CHAPTER 2

Characterization Techniques

Characterization tools are one of the most important parts of material-based research. We can analyze the physiochemical properties of the materials using a huge variety of scientific approaches. The principles and analytical procedures of various instrumentation techniques used for the characterization of materials are discussed in detail. Additionally, we provided a briefing on the characterization tools used to determine size, charge, surface area, surface functional groups, morphology, and molecular structure.

2.1. FOR STRUCTURAL DETERMINATION

2.1.1. X-Ray Diffraction (XRD) Analysis:[1–5]

A non-destructive analytical method known as X-ray diffraction analysis (XRD) offers thorough details about the crystallographic structure, chemical composition and physical characteristics of a substance. It is generally used to determine the material crystalline phase, atomic spacing, and the size of unit cells. Instead of measuring elemental composition, it essentially examines structural crystalline parameters. X-rays are electromagnetic radiations with shorter wavelengths, resulting from the deceleration of electrically charged particles with sufficient energy. XRD works when incident X-rays are used to bombard the material and then the intensities of diffracted ray and scattering angles of the reflected X-rays that leaves the material are measured. Diffracted X-rays intensity is then detected, processed, counted and plotted against various angles of their diffraction to display a diffraction pattern. Due to the specific chemistry and atomic

organization of the substance, each phase of the material generates a distinct diffraction pattern. The pattern of the diffracted signal would be impacted by flaws in the sample material. In this instance, the sample heterogeneous composition, crystal structural imperfections, micro stains and crystallite size can be the reason for imperfection in the sample. XRD is dependent on the constructive interference of monochromatic X-rays and a crystalline sample when conditions satisfy Bragg's law:

$$2d_{hkl} \sin\theta = n\lambda \qquad (2.1)$$

Here, $\boldsymbol{\theta}$ is the angles of incidence; variable $\mathbf{d_{hkl}}$ stands for the lattice spacing of a particular hkl plane; **λ** is the incident X-ray wavelength (Cu Kα, λ = 1.541 Å); **n** is the order of diffraction.

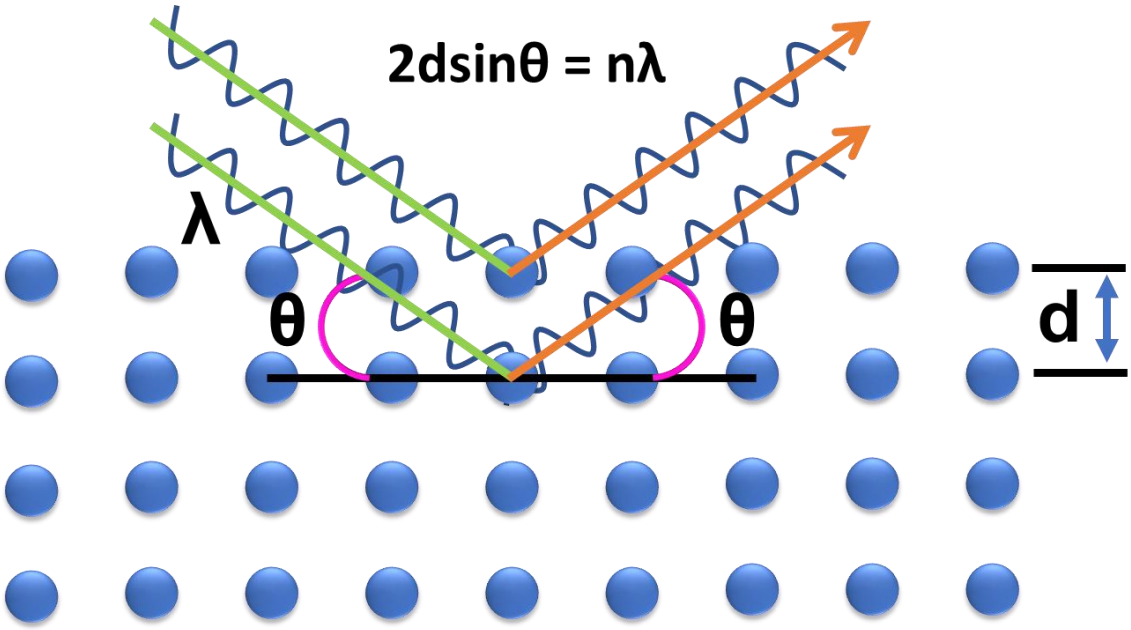

Fig. 2.1: Principle of X-ray diffraction (modified).[1]

In brief, this law establishes the relationship between the lattice spacing, diffraction angle, and electromagnetic radiation wavelength in a crystalline sample **(Fig. 2.1)**. Each mineral has a specific set of unique d-spacings, hence converting the diffraction peaks to d-spacings enables mineral identification. Typically, this is done by comparing the d-

spacing values to the available standard reference patterns at ICDD (International Centre for Diffraction Data). The peaks of the XRD pattern are crucial for determining both the phases and the characteristics properties of the material. In this instance, the peak FWHM would reflect the average crystalline size of a nanoparticle, where sharp peaks indicate crystallites of larger sizes and broad peaks indicate crystallites of smaller sizes. In XRD, the Debye-Scherrer formula helps to relate the broadening of a peak in a diffraction pattern to the size of subatomic particles or crystallites in a material. The mean size of coherently diffracting domains was calculated by the Debye-Scherrer equation, which can be written as:

$$\tau = \frac{K\lambda}{\beta cos\theta} \tag{2.2}$$

Here, **τ** represents the average size of the crystalline domains, which may be smaller or equal to the size of crystals present in the material; **K** is a dimensionless shape factor with a value close to unity. The shape factor has a typical value of about 0.9 but varies with the actual shape of the crystallite; **λ** is the X-ray wavelength (Cu Kα, λ = 0.1541 nm); **β** stands for full width at half maxima (FWHM) for the diffracting domain, after subtracting the instrumental line broadening (in radians); **θ** is the Bragg's angle (in radian).

Instrument specification:

To evaluate the crystalline and amorphous nature of the powder sample, X-ray diffraction experiments were performed using Rigaku Miniflex-II operating at 20 KV and 10 mA using Cu-Kα radiation. XRD patterns were collected at 25 °C in the 2θ range of 10° to 70° with step sizes of 0.02° and a counting time of 6 s per step unless otherwise stated.

2.1.2. Fourier Transform Infrared (FTIR) Spectroscopy:[6–11]

Atoms that are connected by chemical bonds form molecules. These chemical bonds and atoms are constantly moving. These movements consist of two parts: stretching and

bending vibrations **(Fig.2.2)**. The masses of the atoms, the strength of their chemical bonds and their geometric configurations all affect the vibrational spectrum. Infrared spectroscopy using the Fourier transform, often known as FTIR spectroscopy, is highly considered as a crucial analytical method for identifying these types of vibrations. It is among the non-destructive methods for examining the atomic composition of many classes of materials. Detailed information about the rotational and vibrational behaviour related to chemical bonding and molecular structure is provided by FTIR. It is more accurate and sensitive than other IR techniques.

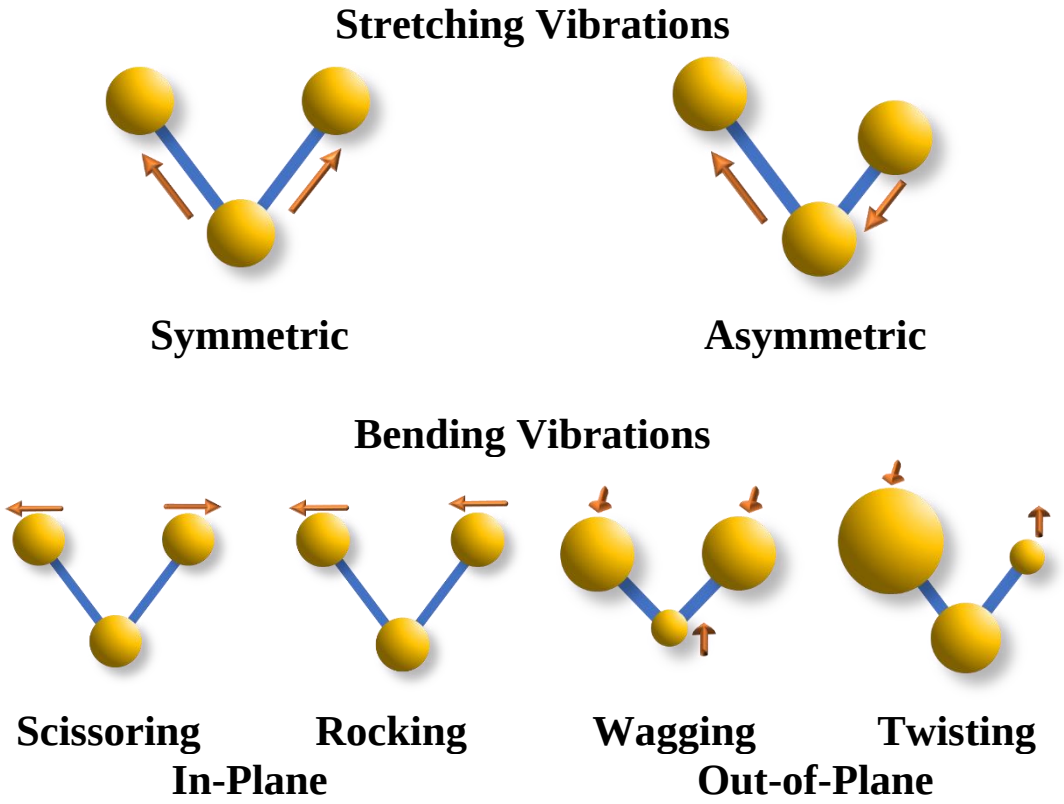

Fig. 2.2: Illustrate common molecules vibrations and rotation modes observed in IR spectrum (modified).[6]

It is possible for infrared radiation to interact with a vibrating molecule when the electric field vector of infrared radiation oscillates at the same frequency as the molecular dipole moment. Therefore, it is possible to confirm that a molecule depends on being IR active

if the normal vibration modulates the molecular dipole moment and the equation is satisfied:

$$\frac{d\mu}{dq} \neq 0 \qquad (2.3)$$

Where **μ** = molecular dipole moment; **q** = normal coordinate which describes atomic motion during normal vibrational motion.

The chemical bonds in a substance can absorb a certain amount of energy (**hν**) from an IR light source to enter a vibrationally excited state (**h**: Planck's constant, 6.626 x 10^{-34} Js; **ν**: frequency). The energy differential between the vibrational levels for ground and excited states determines the frequency of an absorption band. The signal produced at the detector is a spectrum that serves as a molecular "fingerprint" of the sample that is unique for various chemical structures (molecules). All bonds in a molecule have a dipole moment that absorbs IR at particular wave numbers, resulting in quantized excited vibrational states. It is interesting to note that an absorption peak only appears for vibrations that change the dipole moment. A bond or combination of bonds in a molecule can be identified by an observable absorption band (peak) at a certain wavelength.

"Fourier-transform infrared spectroscopy" refers to the mathematical procedure, namely Fourier transform, used to turn the raw data obtained from interferograms, decoded into distinguishable spectra. Vibrational spectroscopy used to get the infrared spectrum shows patterns that reveal structural information. "Michelson interferometer" is the most frequently used interferometer **(Fig. 2.3).** It has three active parts, including a beam splitter, a moving mirror, and a stationary mirror. Here, the mirrors are maintained perpendicular and vertical to one another. The beam from the source of infrared radiation is aligned, allowed to enter an interferometer, and collides on a beam splitter, a semi-reflecting apparatus. The beam is divided into two beams by the beam splitter. One beam

is then reflected off through a stationary mirror, while the other is reflected off through a moving mirror.

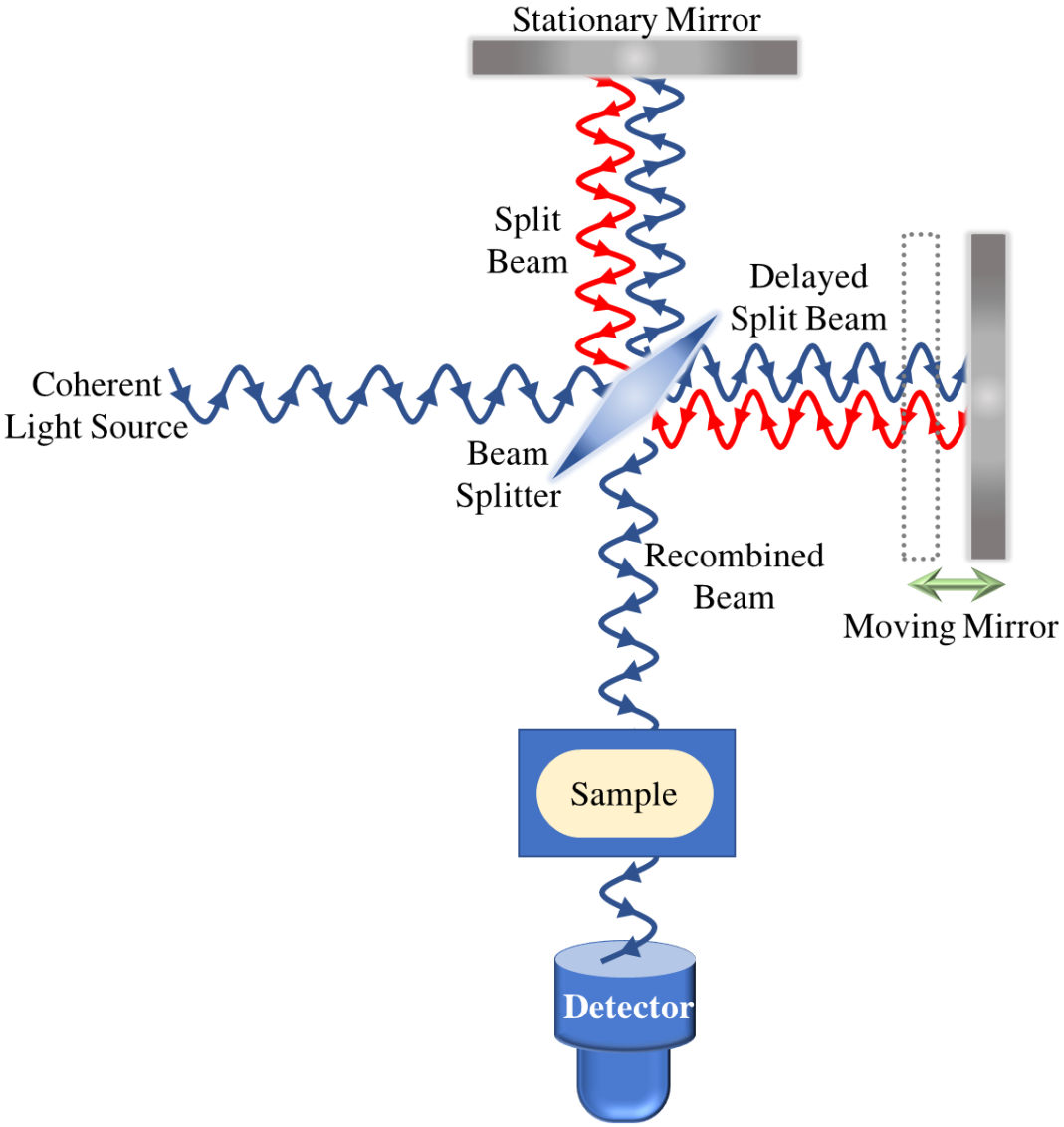

Fig. 2.3: Illustrates common molecules vibration and rotation modes observed in IR spectrum (modified).[11]

Then, at a beam splitter, where an optical path difference is introduced between the two beams, both of these beams are recombined. The added route difference is what causes constructive and destructive interference to occur. As a result, the Fourier transform may be used to reassemble the as-derived spectra by measuring the signal strength at different discrete positions of the moving mirror. Then, as the IR beam passes through the

interferometer, the interferometer's job is to encode the data using a sophisticated mathematical tool called the Fourier transformation in order to retrieve the needed information. In this scenario, some infrared radiation is absorbed by the sample and some radiation passes through, i.e., gets transmitted. Finally, between transmittance/absorbance versus wave number, IR spectra has been plotted.

Instrument specification

To record the FTIR spectra of powdered bioactive glass nanoparticles, dried materials were completely pulverized, blended with potassium bromide at a 1:100 ratio, and pelleted. All these spectra were recorded using Perkin Elmer (Model spectrum 2) spectrometer operating in the spectral range of 4000–400 cm^{-1} with the resolution of 1 cm^{-1}. FTIR spectra of the reaction mixture for each of the successively added precursor interactions with the template were examined for the interaction studies of bioactive glass synthesis using the ATR mode of the spectrometer.

2.1.3. Raman Spectroscopy:[12–16]

The Nobel Prize-winning Physicist Sir C. V. Raman made the discovery that light wavelength changes when it interacts and deflects with a transparent substance. The Raman effect, the name given to this light scattering, was discovered and opened the door for modern Raman spectroscopy. Raman spectroscopy relies on the scattering of monochromatic light, often from a laser source. When monochromatic radiation with wave number υ_o strikes a material like a molecule or a crystal, most of the radiation is transmitted unchanged, but some scattering of the radiation also takes place. Analysis of the scattered radiation frequency content would reveal pairs of new wavenumbers of the kind $\upsilon_S = \upsilon_o \pm \upsilon_m$ in addition to the wave number υ_o associated with the incident radiation. The wave numbers υ_m are found to exist principally in the ranges associated to transitions

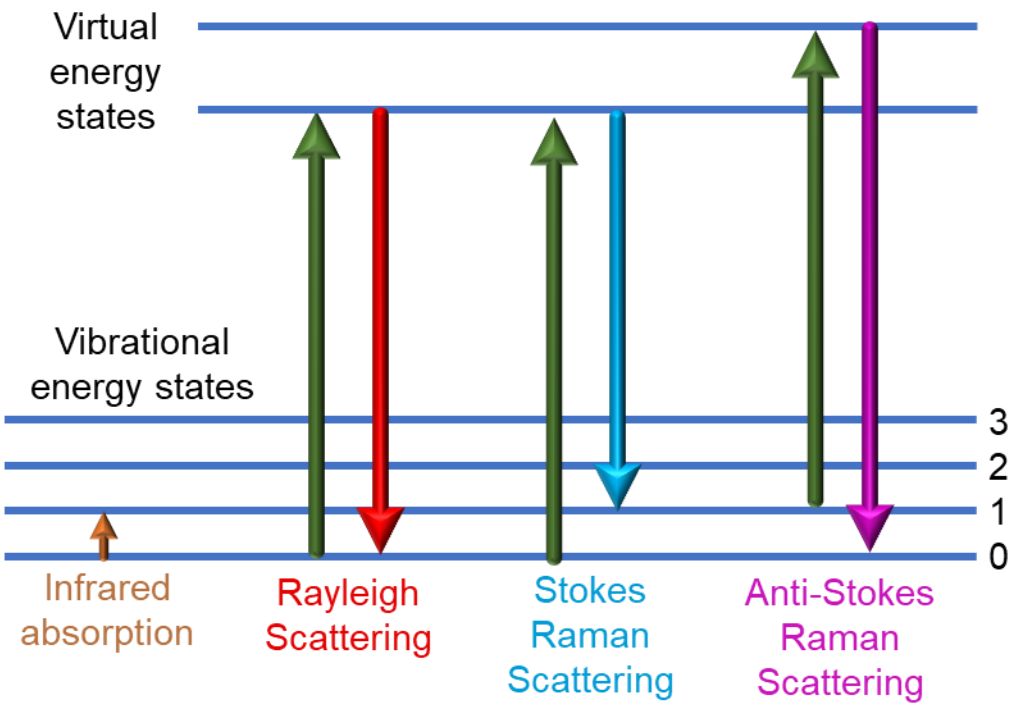

Fig. 2.4: Energy level diagram representing quanta of energy **υo** hit the molecule, an elastic impact scatters the quantum **υ_o** known as Rayleigh scattering**,** inelastic impact scatter quanta which have energies smaller or larger by the amount of the vibrational energy **υ_m** knows as raman scattering (modified).[17]

between rotational, vibrational, and electronic levels in molecular systems. This type of radiation scattering with a change in wavenumbers (or frequency) is referred to as Raman Scattering. It is possible to analyze solid, liquid, and gaseous samples using Raman spectroscopy. Molecular polarizability (α), is used to determine the Raman effect, which is based on molecule deformations in an electric field (E). The laser beam can be viewed as an oscillating electromagnetic wave with electrical vector "E". When it interacts with the sample, it creates an electric dipole moment **P = αE**, which causes molecules to deform periodically. As a result of this periodic deformation, molecules begin to vibrate at a specific frequency **υ_m**. Nuclear displacement is the term used to describe the amplitude of vibration, also called monochromatic laser light with frequency υ_o excites molecules and transforms them into oscillating dipoles. As shown in **Fig. 2.4**. Such oscillating dipoles emit light of three different frequencies.

1. A photon with the frequency υ_o is absorbed by a molecule without any Raman-active modes. When the excited molecule returns to its initial vibrational state and emits light at the same frequency υ_o as that of the source of excitation, **elastic rayleigh scattering** is the name given to this kind of interaction.

2. Raman-active molecules that are at the time of interaction in the ground vibrational state absorb a photon with frequency υ_o. When the molecule is returned to the ground vibration state, the frequency of scattered light is lowered to $\upsilon_o - \upsilon_m$ as a result of a portion of the photon's energy is transferred to the Raman active mode with frequency υ_m; this Raman frequency is known as the **Stokes frequency** or simply **stokes**.

3. A Raman active molecule that is already in the excited vibrational state at the time of interaction absorbs a photon of frequency υ_o. The molecule returns to its ground vibrational state and releases excess energy from the excited Raman active mode, increasing the frequency of scattered light to $\boldsymbol{\upsilon_o + \upsilon_m}$. **Anti-Stokes frequency**, or simply **anti-Stokes**, is the name given to this Raman frequency.

Elastic Rayleigh scattering occurs to around 99.999 % of all incident photons in spontaneous Raman. For practical purposes of molecular characterization, this kind of signal is meaningless. A Raman signal with frequencies $\upsilon_o \pm \upsilon_m$ is produced by an inelastic portion of incident light which is only about 0.001% of incident light. In order to identify spontaneous Raman scattering from the more common Rayleigh scattering, specific steps should be performed because it is relatively faint. To lessen Rayleigh scattering and produce high-quality Raman spectra, techniques including notch filters, tunable filters, laser stop apertures, double and triple spectrometric systems are used. Typically, a Raman system comprises four main components as shown in **Fig 2.5**:

1. excitation source (laser).

2. sample illumination system and light collection optics.

3. wavelength selector (filter or spectrophotometer).

4. detector (photodiode array, CCD or PMT).

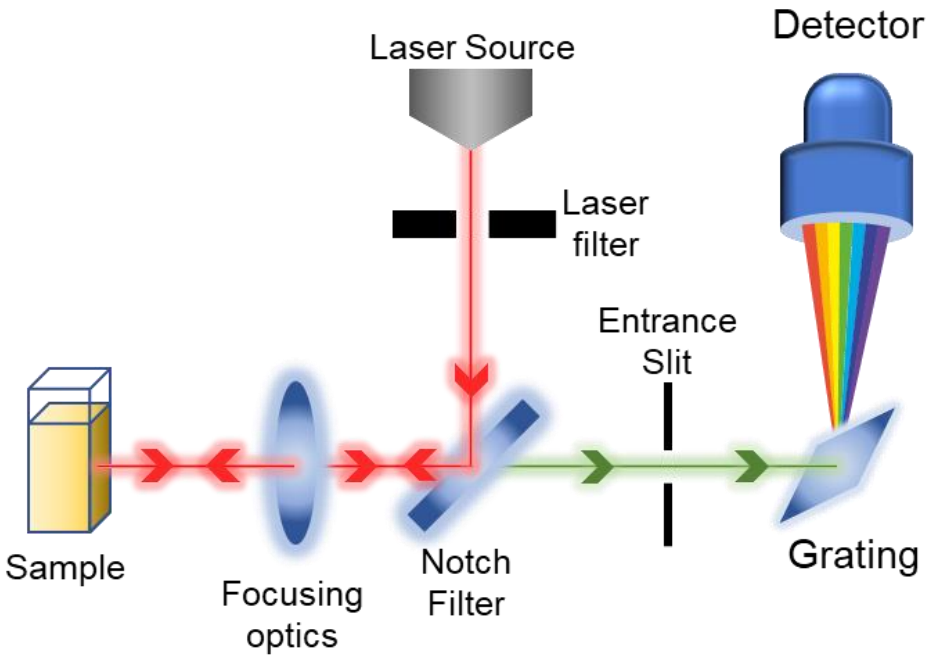

Fig. 2.5: Schematic diagram of main components in a Raman spectrometer (modified).[18]

A laser beam in the ultraviolet (UV), visible (VIS), or near-infrared (NIR) range is typically used to illuminate a sample. To acquire the Raman spectrum of a material, the scattered light is collected using a lens and transmitted via an interference filter or spectrophotometer. More specifically, the main issue here is not Rayleigh scattering but rather the possibility that, in the close vicinity of the laser wavelength, the intensity of stray light from Rayleigh scattering may significantly surpass the intensity of the usable Raman signal. Cutting off the Spectral range close to the laser line, where the stray light has the most substantial impact, will often alleviate the issue. People utilize commercially available interference (notch) filters to block the laser line spectral region between 80 cm^{-}

[1] to 120 cm^{-1}. However, it does not allow for the identification of low-frequency Raman modes in the range below 100 cm^{-1}, despite being effective at removing stray light. In the spectrometer, stray light is produced mainly through light dispersion on gratings and relies highly on grating quality. Holographic gratings, which often have fewer manufacturing flaws in their structure, are frequently used in Raman spectrometers. Holographic gratings typically create stray photons roughly an order of magnitude less bright than those produced by ruled gratings with the same groove density. Another method of reducing Stray light is to use numerous stages of dispersion. Raman spectra can be acquired using double or triple spectrometers without the need for notch filters. Raman-active modes with frequency as low as 3 cm^{-1} to 5 cm^{-1} exist in such systems and can be detected effectively. In the past, single-point detectors like photon-counting photomultiplier tubes (PMT) were the most common. It took a long time to obtain a single raman spectrum using a PMT detector in wavenumber scanning mode, which slowed down any study or commercial activity based on the raman analysis technique. To detect the dispersed light, currently, researchers are frequently utilizing multi-channel detectors like photodiode arrays (PDA) or, more frequently, charge-coupled devices (CCD). Modern CCD detectors sensitivity and performance are advancing quickly. CCD is increasingly becoming the preferred detector for Raman spectroscopy.

Instrument Specification

A custom-built Raman spectrometer outfitted with a SPEX TRIAX 550 monochromator, a liquid nitrogen-cooled CCD, and a 532 nm excitation of a frequency-doubled Nd:YAG solid state laser (model GDLM-5015 l, Photop Suwtech Inc., China) was used to record the raman spectra. The sample's laser had an 8mW output, and a spectrum acquisition took two minutes with a 2 cm^{-1} spectral resolution.

2.1.4. Thermogravimetric (TGA) Analysis:[19–21]

TGA is an analytical method for assessing thermal stability of the compound. It is based on the idea of calculating the mass change of a sample over time or as a function of temperature while the sample is being subjected to a controlled temperature program in a controlled environment. This measurement offers data on chemical and physical events, such as chemisorption, thermal breakdown, and solid-gas reactions (such as oxidation or reduction), as well as phase transitions, absorption, adsorption, and desorption. Many additional measurements can be derived from mass, temperature and time, which are base measurement parameters. TGA generally comes in three varieties:

Isothermal or static thermogravimetry: This method records the sample weight as a function of time at a constant temperature.

Quasistatic thermogravimetry: By this method, the sample is heated to a constant weight at progressively higher temperature.

Dynamic thermogravimetry: This method involves heating the sample in a setting where the temperature changes in a predetermined way, typically at a linear pace. This kind of TGA is generally preferred.

TGA operates on the principle that when the sample is heated at a controlled pace in a certain environment (air, N_2, O_2, CO_2, He, Ar and so forth), with the change in temperature or time, the substance weight change was noted. For a substance with a known beginning weight, the temperature is raised steadily, and at various time intervals, the weight changes are noted as a function of temperature. Then the thermogravimetric curve or thermogram has been plotted, showing weight change vs temperature. In order to do a TGA analysis, a sample is heated up progressively inside of a furnace while an analytical balance is used to weigh it outside of the furnace. If a heat event results in the

loss of a volatile component, mass loss is detected in TGA. Mass losses occur during chemical processes like burning but not during physical processes like melting. To demonstrate thermal transitions in the material, such as the loss of solvent and plasticizers in polymers, water of hydration in inorganic materials, and finally, material disintegration, the weight of the sample is plotted versus temperature or time.

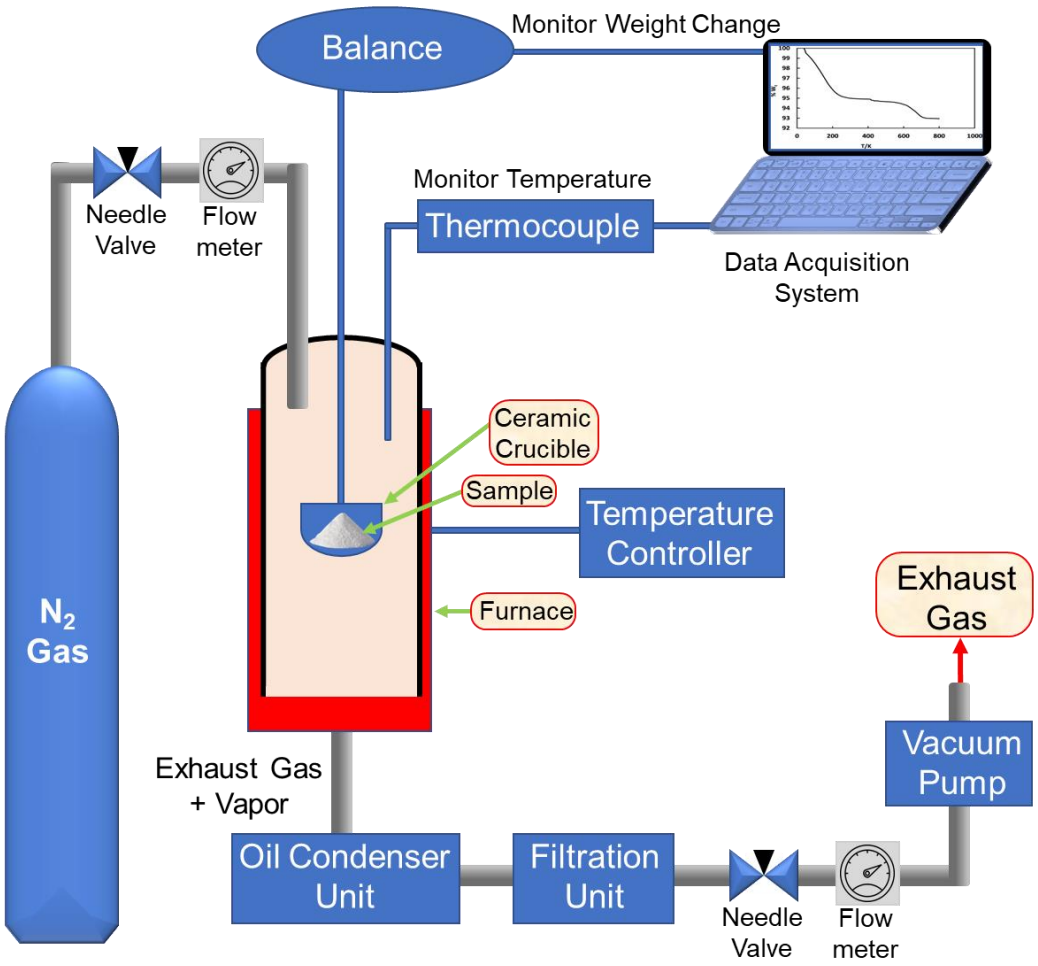

Fig. 2.6: Schematic illustration for the TGA instrument. (modified)[22]

Fig. 2.6 depicts a schematic example of the TGA instrument. A precision balance supports a sample pan that is the main component of a TGA. Throughout the experiment, the pan in the furnace is heated or cooled. The experiment keeps track of the sample mass. In most cases, weight percentage is monitored while the temperature is raised at a constant rate. During the thermal reaction in TGA, which is often conducted under an

inert environment, particularly N_2 gas, the temperature typically approaches 1000 °C. This sample purge gas regulates the sample environment. This gas, which passes over the sample and leaves through an exhaust, may be inert or reactive. The amount of water, solvent, plasticizer, decarboxylation, pyrolysis, oxidation, decomposition, weight percent filler, the metallic catalytic residue left on carbon nanotubes, and ash loss can all be measured using this equipment. The majority of these measurables involve heating and TGA also offers a temperature-mass-percentage relationship graph. If the substance is thermally stable, there won't be any observable mass change and no slope in the TGA plot. This method is also employed to estimate the polymers heat stability.

Instrument specification

The thermal stability of BG samples was investigated using Perkin Elmer thermogravimetric analyzer (Model TGA 4000). About 5 mg of sample material was used. Herein, samples were heated from room temperature to 800 °C at a heating rate of 10 °C/min under a nitrogen atmosphere by maintaining a nitrogen flow rate of 20 mL/min.

2.1.5. Nitrogen Sorption Analysis:[23–26]

Nitrogen sorption analysis explains the physical adsorption (physisorption) of gas molecules on the surface of solid specimens. In honor of Stephen Brunauer, Paul Hugh Emmett and Edward Teller, who first published the theory behind the multi-molecular adsorption process, it is also known as "BET" surface area analysis. The BET method is essentially just an extension of the Langmuir theory that emphasizes the monolayer adsorption of gas molecules and correlates the physically essential properties of the materials, such as specific surface area, total pore volume, average pore diameter, and its pore size distribution. **Fig. 2.7.** depicts the fundamental schematic diagram of monolayer

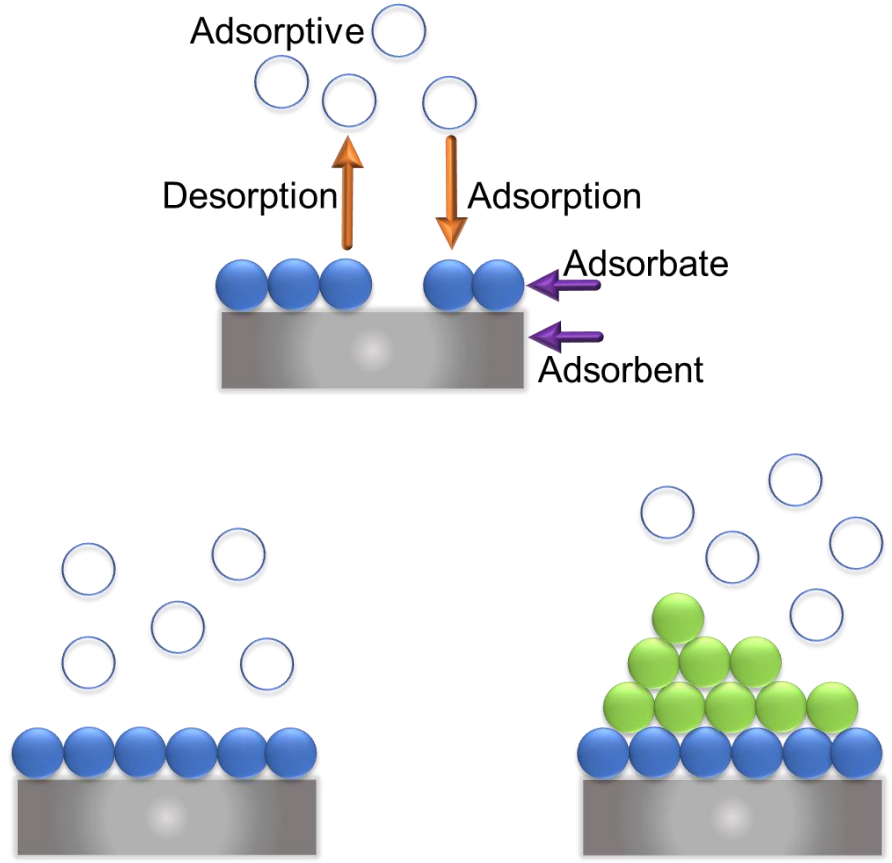

Monolayer Adsorption

The heat of adsorption for the first monolayer is significantly higher than that for the following layers. Typical of cases of chemisorption.

Multilayer Adsorption

The heat of condensation in the following layers is similar to the heat of adsorption in the first monolayer. frequently noticed during Physisorption.

Fig 2.7: Schematic diagram of monolayer and multilayer adsorption processes (modified).[23]

and multilayer adsorption. The term "adsorption" describes how some adsorbate molecules are strengthened onto the adsorbent, causing a layer to form on the adsorbed surface. Desorption is the term used to describe the escape of adsorbed molecules from the adsorbent. The following set of assumptions for BET theory needs to be addressed in order to enable the confident application of the acquired data:

- There are no preferential sorption sites since the material surface is homogeneous and the adsorption happens uniformly throughout the entire surface.
- After adsorption, every single molecule function as a single sorption site for other gas molecules. No further intermolecular interactions are taken into account, including lateral contacts between molecules that are adsorbed, interactions between molecules in the gas phase and non-sorption interactions between molecules in the gas and adsorbed phases.
- At a particular vapour pressure, the rate of adsorption should be equal to the rate of desorption with no discernible change in the number of molecules that are adsorbed.
- Energy must be provided in order for the reaction to proceed because the rate of the reaction is constrained by kinetic constraints rather than diffusion restrictions. For the surface adsorption layer, the required energy is equal to the heat of adsorption. Additionally, each additional layer is viewed as a condensed liquid that needs the same amount of energy for heat of condensation.
- The quantity of adsorbed layers allows the sample to be entirely encircled by condensed liquid-phase adsorbent as the saturation pressure (P_O) is been approached.

There are two groups of adsorption processes based on the strength of the interactions:

Physisorption: Depending on the porosity of the material, a certain number of condensable gas molecules will be absorbed into the adsorbent whenever the gas approaches or comes into contact with it. Physical adsorption, also known as physisorption, is the process by which certain gas molecules partially penetrate a solid but remain on an adsorbent surface. These gas molecules form weak Van der Waals

connections with the surface (the adsorbent).

Chemisorption: It is also known as chemical adsorption and is distinguished by having a high interaction potential that frequently results in high heat of adsorption that is close to those required to form chemical bonds. It typically occurs at temperatures greater than the adsorbate critical temperature due to the arrangement of chemical bonding. Because of the chemical interaction between the adsorbate and a particular spot on the surface, the adsorbed molecules are localized on the surface.

Adsorption is the method through which an amount of adsorbate molecules or vapours are adsorbed on an adsorbent at a fixed temperature (T) in order to forecast morphological changes and pore architecture. The relationship between the weights of adsorbed molecules and rising gas pressure has also been examined and is known as an adsorption isotherm. Desorption isotherm refers to the process by which a certain amount of adsorbate molecules has been separated from the adsorbent surface. In monolayer adsorption, every gas molecule that has been adsorbed is in direct touch with the absorbent's surface layer. The adsorption space can support more than one layer of molecules in multilayers, preventing all adsorbed molecules from coming into direct touch with the adsorbent surface layer. Capillary condensation is the "process by which multilayer adsorption from the vapour phase into porous media proceeds to the point at which pore gaps get filled with condensed liquid from the vapour phase". The three categories of pore diameters are determined by the IUPAC categorization:

Micropore: These are the pores whose pore diameter is < 2 nm.

Mesopore: Pores with a size between 2 nm to 50 nm behave in a mesoporous manner.

Macropore: Macropore is generally termed with pore diameter > 50 nm.

Fig. 2.8 illustrates various isotherm types from the preliminary analysis, created by deBoer, codified by Brunauer *et al*., and subsequently appended by Gregg and Sing.

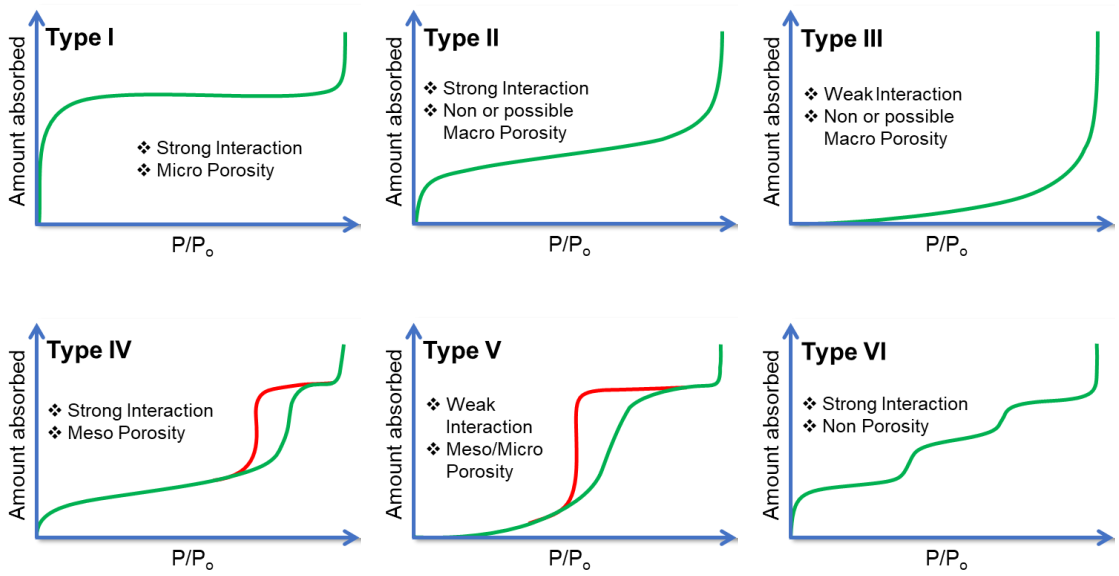

Fig. 2.8: Pictorial representation of different types of isotherms (modified).[24]

According to the classification frequently employed in literature, these are numbered I to VI and have the following interpretations:

Type I: Microporous specimens with pore diameters that don't exceed any adsorbate molecular diameters result in this type of isotherm. Since pores are thus small, a gas molecule inside them fights off the overlapping potential from their walls, which increases the amount of material that is adsorbed at relatively low pressures. Pores get packed with condensed adsorbate at greater pressures, creating a plateau zone. The presented isotherm shows that the exposed surface almost completely overlaps the micropores and the pores are in the range of the microporous region.

Type II: This type of isotherm is typically seen whenever an adsorption happens on a specimen with pores that are in the nano-meter range or larger than micropores. Herein, when the inflection point of the adsorbed monolayer is reached, increase in relative pressure follows and the subsequent higher layers are finished until the saturation of the adsorbed layers approaches infinite.

Type III: The idea of heat of adsorption best describes this type of isotherm. The heat of adsorption is lower than the heat of liquefaction of the adsorbate molecules. Because the adsorbate interacts with an adsorbed layer more favourably than it does with the adsorbent surface, therefore supplementary adsorption is made easier.

Type IV: In this case, by showing the pore condensation in conjunction with hysteresis actions between the adsorption-desorption layer, an isotherm illustrates the unique nature of mesoporous materials.

Type V: The survival of mesopores in which phase transformation (similar to pore condensation) may occur is indicated whenever the isothermic branch diverges from type IV curves by nearly vertical centre of the adsorption-desorption branches.

Type VI: It describes the chemisorption process and provides the multilayer adsorbate in steps. At low temperatures, the adsorbed layers in this case become more pronounced.

Hysteresis loops characteristics: The four unique types of the hysteresis loops (H1-H4) (as depicted in **Fig. 2.9**) are described and listed below using an IUPAC classification.

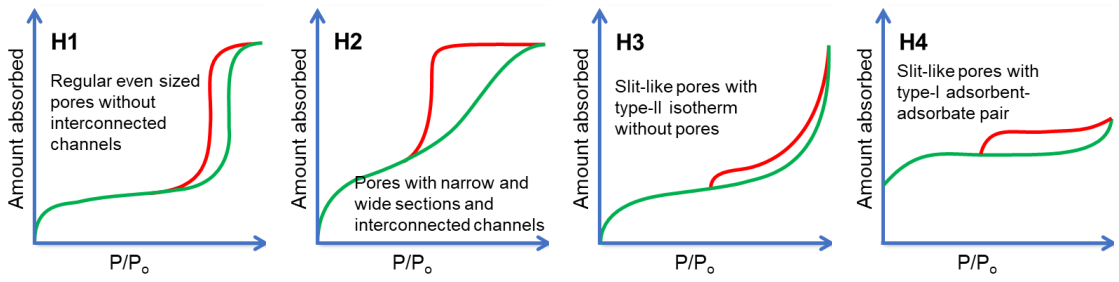

Fig. 2.9: Graphical representation of characterization of hysteresis loops (modified).[25]

H1 type: The H1 type has regular even sized pores exclusive of unified channels and is distinguished by having nearly two parallel and vertical adsorption-desorption layers.

H2 type: Two branches, one with sloping adsorption layers and the other with vertical desorption layers, are used to describe it. The pores that are shown by the H2 type hysteresis loop is both fine and broad section and potential unified regions are revealed.

H3 type: Sloping adsorption-desorption branches that cover very broad regions of P/Po with a basic type II isotherm are used to identify the H3 type of hysteresis loop. Additionally, it reveals the slit-like pores for which the coupled pair of adsorbent and adsorbate results in a type II isotherm without pores.

H4 type: It shows a type I isotherm with an oversized range for the hysteresis loop and denotes slit-like pores for a type I coupled pair of adsorbent and adsorbate.

Instrument specification

The Textural characteristics of various BG materials was determined by nitrogen adsorption-desorption analysis at -196 °C using Microtrac BEL (Model BELSORP-max), Japan and with nitrogen as adsorptive gas (N_2, cross-sectional area 0.162 nm^2). As per the standard nitrogen sorption protocol, before analysis, xerogels were degassed under vacuum at 200 °C for 6 h. The surface area was determined using the Brunauer–Emmett–Teller (BET) equation on the nitrogen adsorption data obtained. The pore-size distribution was determined by the Barrett–Joyner–Halenda (BJH) method applied to the desorption branch of the isotherm.

2.1.6. Zetasizer:[27–29]

Using the Dynamic Light Scattering (DLS) method, Zetasizer Instruments detect the particle size of dispersed systems from sub-nanometer to several micrometres in diameter. DLS technique is the most commonly used for particle size analysis in the nanometre range. DLS measures the hydrodynamic radius (D_h) of a molecule rather than the exact particle size. The basic principle of DLS is based upon the Brownian motion among dispersed particles. When dispersed in a liquid, particles move irregularly in all directions. The fundamental principle behind Brownian motion is that solvent molecules and particles constantly collide. Thus, particle movement is brought about by the energy

that is transmitted during these collisions. Smaller particles are more affected since the energy transmission is more or less constant. Because of this, smaller particles move more quickly and larger particles show slower motion **(Fig 2.10)**.

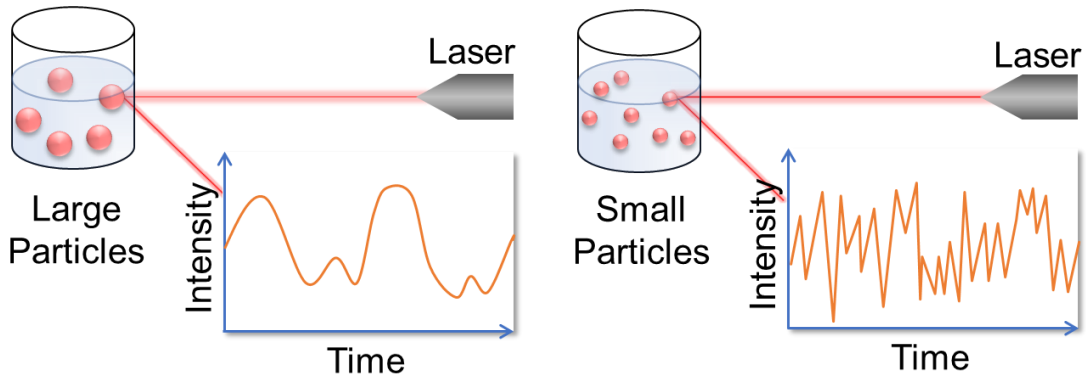

Fig. 2.10: Principle of Zeta sizer (modified).[30]

The Stokes-Einstein equation provides the relationship between the particle speed and its size. **(Eq. 2.4)**.

$$D_h = \frac{k_B T}{3\pi\eta D_t} \tag{2.4}$$

Where: $\mathbf{D_h}$ is the hydrodynamic diameter of the suspended Nanoparticles; $\mathbf{D_t}$ is the translational diffusion coefficient (we find this by dynamic light scattering); $\mathbf{k_B}$ is Boltzmann's constant; **T** is thermodynamic temperature; **η** is dynamic viscosity. The translational diffusion coefficient D_t determines the particle's speed. Furthermore, as both the temperature and the dispersant's viscosity directly impact particle mobility, they are both included in the equation. The particles movement must entirely depend on Brownian motion to satisfy the Stokes-Einstein equation. If no random movement occurs due to sedimentation or precipitation, inaccurate results may be produced. As a result, the beginning of sedimentation denotes the maximum size for DLS measurements. In contrast, the signal-to-noise ratio determines the lower size limit. Small particles don't scatter light very much, which results in a weak measuring signal.

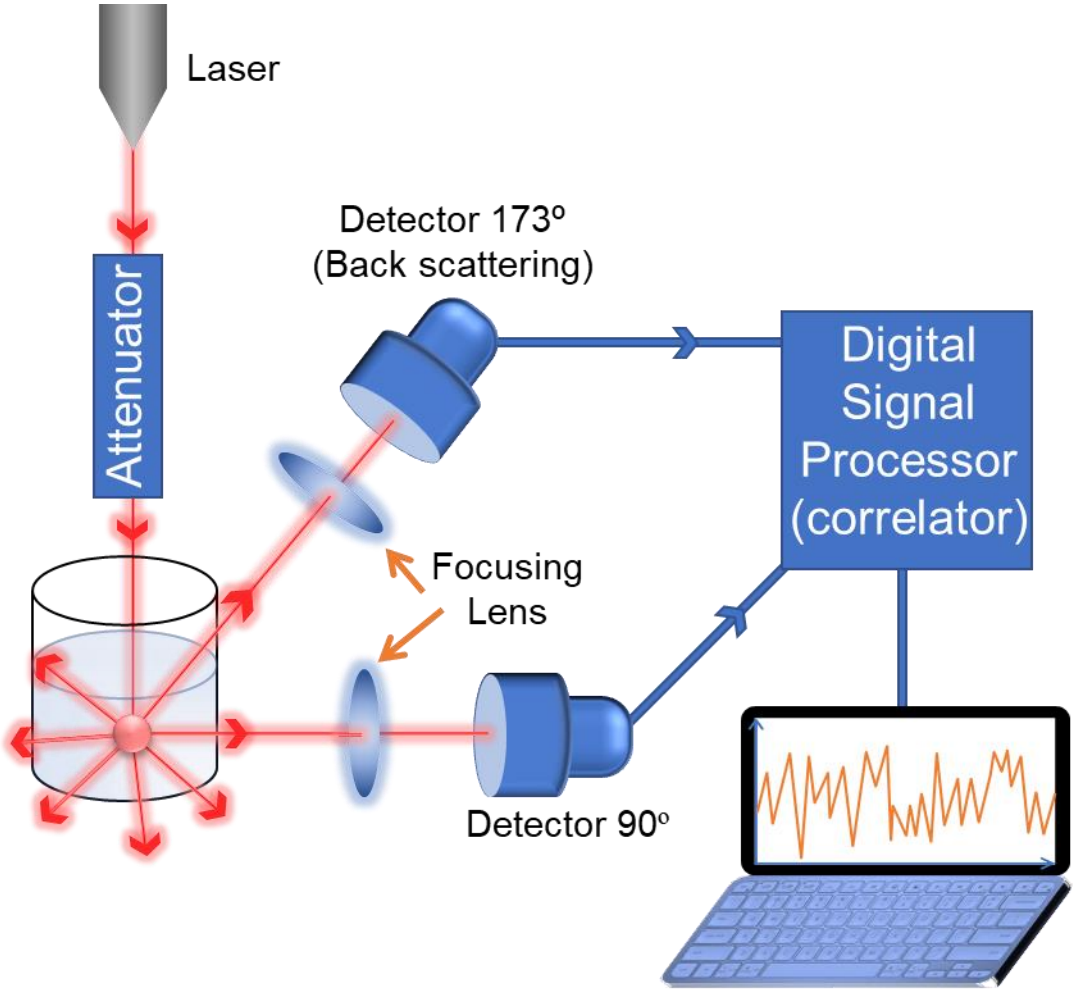

Fig. 2.11: Schematic illustration for the basic components of DLS instrument (modified).[31]

The basic setup of a DLS instrument is shown in **Fig. 2.11**. A laser targets the sample inside a cuvette with a single frequency. The incoming laser light is scattered widely by the particles in the sample. The Stokes-Einstein equation uses the signal from the scattered light, which is monitored over time at a specific angle, to calculate the diffusion coefficient and particle size. There are two detection angles for particle size measurements in modern DLS equipment. Depending upon the sample turbidity, side scattering (90°) or backscattering (173°) is preferable. Aggregation can be observed at a forward angle of 15°.

Instrument specification

Hydrodynamic radii of the BG samples were measured using Zetasizer (Model ZSP, Malvern Instruments, UK). An average of 3 readings were taken for each sample.

2.1.7. Zeta Potential:[31–33]

Zeta potential, or ζ potential, is referred to as electrokinetic potential in colloidal systems. It is a method of analysis used to determine the surface charge of nanoparticles in colloidal solution. The Stern layer is a thin liquid layer that forms when a charged particle surface attracts and firmly binds to the opposite charge ions from the solution. As the

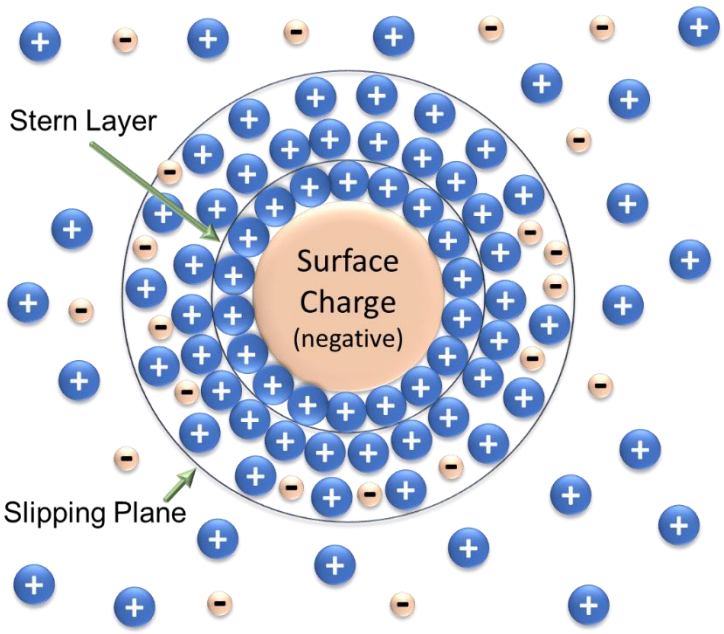

Fig. 2.12: Schematic representation of a negatively charged particle in contact with liquid shows the electrical double layer (modified).[32]

particle diffuses in solution, it will also be connected by a diffuse outer layer made up of loosely associated ions, resulting in the formation of an electrical double layer **(Fig. 2.12)**. Zeta Potential is known as the electrical potential difference between this double layer and a point in the continuous phase away from the interface. Zeta potential is the

difference in the potential between the mobile dispersion medium and the stationary layer of the dispersion medium that is associated to the dispersed particle. It is calculated by measuring the velocity of the charged particles as they move through the sample solution toward the electrode in the presence of an external electric field. Zeta potential readings usually fall between +100 and –100 mV. Zeta potential provides an estimation for colloidal stability. The medium pH is the main factor that influences the zeta potential value. Ionic strength, concentration of any additives, and temperature can be further considered. Zeta potential signifies both the short-term and the long-term stability of the emulsions. For example, nanocrystals with large positive or negative zeta potential indicate their good physical stability for nanosuspensions due to high electrostatic repulsion between the individual particles. Generally, it is considered that the zeta potential value outside the range of –30 mV to +30 mV has enough repulsive force to improve colloidal physical stability. On the other hand, a smaller zeta potential value may result in physical instability of the suspension because the attraction forces such as van der Waals attraction acting on the particles results in particle aggregation and flocculation.

Instrument Specification

Zeta-potential values of the BG samples were measured using Zetasizer (Model ZSP, Malvern Instruments, UK). An average of 3 readings were taken for each sample.

2.2. For Morphological and Elemental Analysis:

2.2.1. Electron Microscopy:

The fundamentals of an electron microscope are the utilisation of an accelerated electron beam to visualize the specimen. It can view considerably smaller objects in more detail since it has significantly higher magnification and resolving powers than a light

microscope. The following electron microscopes could be investigated depending on the feature of interest.

2.2.1.1. Scanning Electron Microscope (SEM):[34–36]

Scanning electron microscopy (SEM) is one of the most suitable method for examining and analysing the microstructural morphology of a material. It is used to produce 3D images of the material's surface with high resolution. It is advantageous to understand the specimen structural architecture. It works on the principle that when a concentrated beam of energetic electrons incident on the material surface, it causes a variety of signals to appear at the surface of the specimen. The signals originated due to the exchange of energy during the interaction of the electron beam with the sample revealing details of the sample such as external appearance, chemical composition, and particle alignment and orientation. The resulting signals consist of secondary electrons (SEs), backscattered electrons, auger electrons and characteristic X-rays that contribute to predict various sample-related information. The SEs appear to be quite efficient in extracting information about the sample external morphology. The number of SEs that a detector can detect is typically thought as a function of the angle between the sample surface and focussed electron beam. **Fig. 2.13** displays a schematic diagram of the main components of SEM instrument.

Here, thermionic triod and field emission guns are the two most often employed electron guns for producing electron beams. In a thermionic triod electron gun, cathode is made up of tungsten, which is heated upto 2800 K by passing the current across the filament to generate the concentrated electron beam. At the same time, field emission gun is used in field emission scanning electron microscope (FESEM) to provide higher brightness for the sample surface. It works on the principle of the tunnelling effect, wherein the tungsten

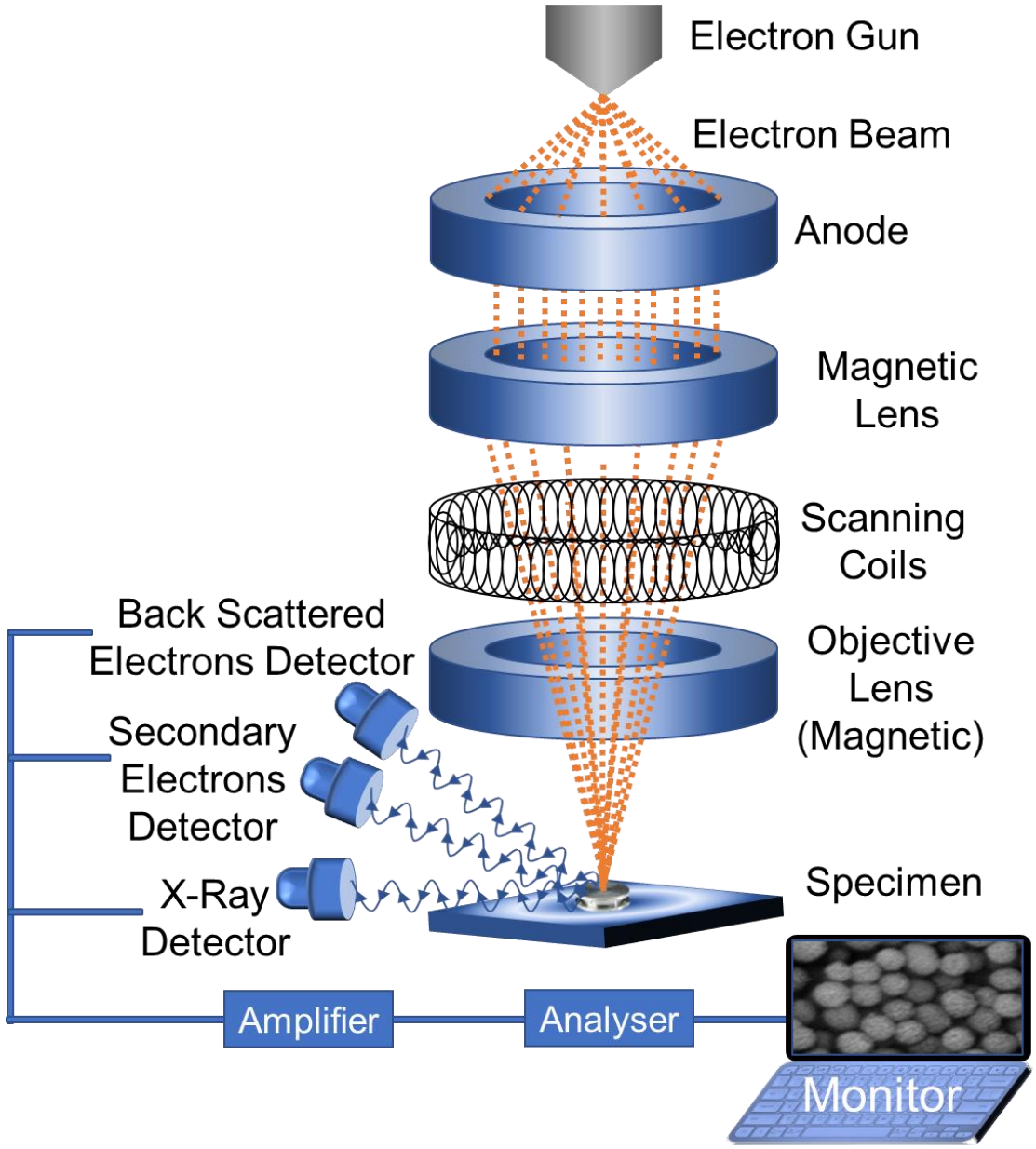

Fig. 2.13: Schematic diagram of the core component of SEM (modified).[34]

filament is exposed to an extremely high electric field (> 109 Vm^{-1}) to enable an electron to escape the metal surface before receiving the amount of energy represented by its work function. This causes the piece of tungsten to emit a lot more electrons, resulting in increasing brightness by a factor of up to 1,000 or more.

Energy Dispersive X-Ray Analysis (EDAX):[35,37,38]

SEM coupled with an energy dispersive X-Ray (EDX) analyzer helps to identify elements

and provide quantifiable information about them. It is one of the most flexible SEM assemblies and used to investigate the X-ray emitted from the sample by simply computing the X-ray energies, as shown in **Fig. 2.13**. It functions as a SEM integrated topography and supports the user in predicting the elemental composition of the unknown materials. When the sample emits X-rays radiations detected by a semiconductor detector, electron-hole pairs are created whose quantity matches the energy of the X-rays. To determine the X-rays energy value, we need to measure the quantity of electron-hole pairs produced. Due to the simultaneous analysis of X-rays from a variety of elements, from Boron (B) and Uranium (U), EDX has its own significance.

Sample Preparation and Instrument specification:

The preparation of the sample is an absolutely critical stage since the sample is intended to interact directly with the extremely high energy electron beam. In order to prevent the charging effect and vacuum compatibility, the probing specimen must be electrically conductive. For non-conductive samples, the specimen surface should be electrically grounded to prevent the build-up of electrostatic charges there. For this aim, a metallic ultra-thin coating of the order of 100 Å to 1000 Å need to be applied to the probing sample surface.

The surface morphology of bioactive glass materials was recorded using field emission scanning electron microscopy (FE-SEM) (Model FEI Quanta 200 F SEM, FEI Company, Netherland). The samples were gold coated and then observed in FE-SEM at an accelerating voltage of 5 kV at required magnifications. To investigate the presence of various metal ions, present in the BG samples, the samples were also subjected to Energy Dispersive X-Ray Analysis (EDAX) operated at the voltage of 20 kV using FEI Quanta 200 F SEM with Oxford-EDS system IE 250 X Max 80, FEI Company, Netherland. The

particle size was also analyzed using ImageJ bundled with 64-bit Java 1.8.0_172 software.

2.2.1.2. Transmission Electron Microscope (TEM):[39–41]

Transmission electron microscopy (TEM) is a technique used to obtain information about the crucial morphological behaviour of the particles and their diverse microstructural length scales. Here, when an electron beam is permitted to interact with the specimen while transmitting through it, it produces an image map, which helps to carry out microstructural studies of the material. The electron beam in a standard TEM is more energetic than that in SEM because here, the transmitted electrons are gathered instead of scattered electrons. As a result, the specimen picture can be magnified about a million times. It is based on the principle that by allowing an electron beam with high kinetic energy to contact with an ultra-thin specimen, usually less than 200 nm thick, an electron beam will ultimately be transmitted and de-accelerated as it passes through the sample. The collection of electrons that were conveyed via energy loss through the sample was then magnified and concentrated onto an imaging device assembly to create an electronic map (or image). It is quite capable of recording the images with a high resolution of the order of 0.45 Å because of the lower wavelength of electrons utilized. The viewer may inspect the specimen with sufficient detail because of the high-resolution photographs, which are 10,000 times more magnified than that of the optical microscope.

Various Components of TEM microscope is shown in **Fig. 2.14**. Here, accelerated electron gun voltage typically ranges from 100 to 200 kV. When the electron beam bombards the sample, the condenser lens's job is to demagnify it, regulate the size of the electron beam spot and also manage the convergence angle. The back focal plane and image plane of the objective lens are where the diffraction pattern and images are created.

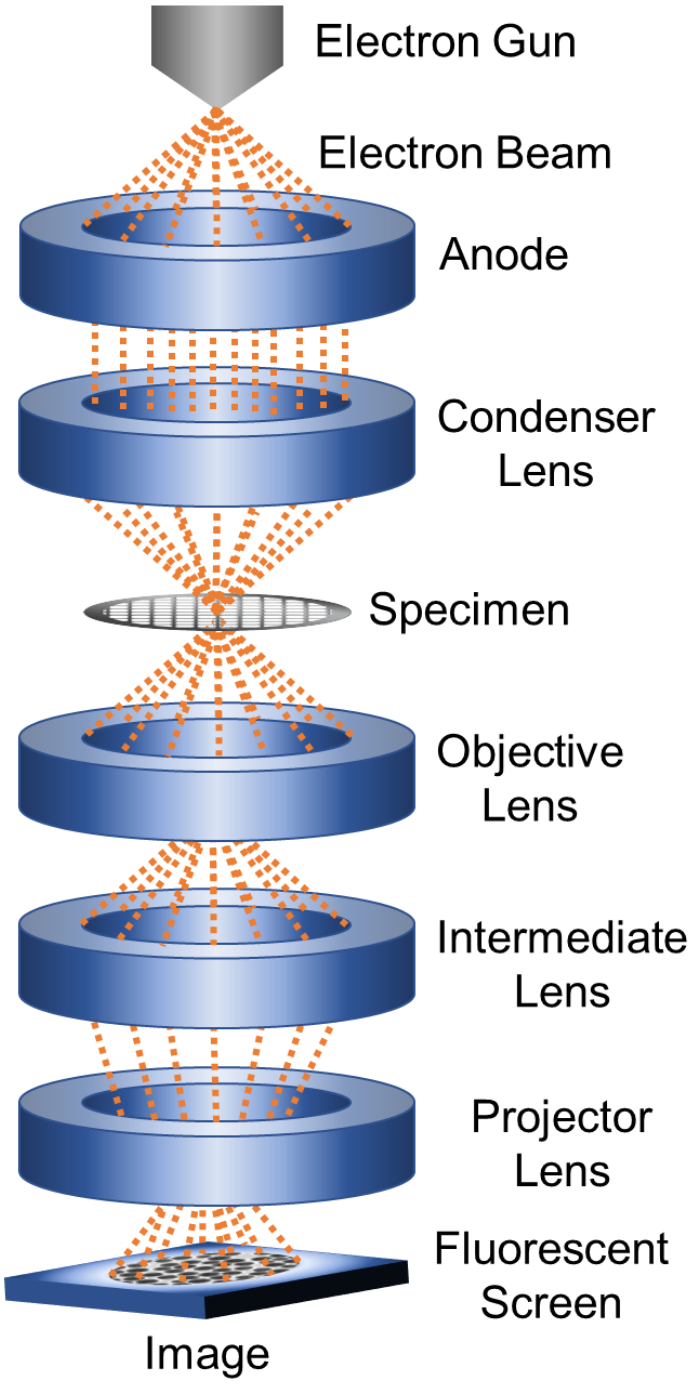

Fig. 2.14: Schematic diagram of the core component of TEM (modified).[39]

If the intermediate lens and projector objective planes are taken back as the focal plane, a diffraction pattern will develop on the screen. The generation of an image on the screen, known as an image mode, occurs when the image plane of the objective lens is taken as the plane of the intermediate lens and projector lens.

Selected Area Electron Diffraction (SAED):[42]

A type of crystallographic study tool called selected area electron diffraction is used to detect the various phases present in the material. Its principle is based on a traveling plane wave (or parallel beam) that is permitted to engage with the sample. Here, a small aperture in the first image plane below the sample allows the user to specify the cross-sectional area of the thin sample from which the diffraction fingerprint is to be recorded. The observed diffraction pattern recorded either in the form of spots or ring pattern on the desired screen. A satisfied diffraction condition is associated with each observed spot, providing details about the specimen crystallography. However, the orientation of the ring pattern resembles the powder diffraction for multiple orientations of multiple crystals.

Sample Preparation Methodology and Instrument Specification:

In order to prepare the sample, it must first be dissolved in the proper solvent, such as ethanol, water, or another substance depending on the sample solubility. After dispersion, the mixture is homogenized using sonication for around 10-15 minutes. With the aid of a pipette, the sonicated sample is loaded onto carbon-coated copper grids (TEM grids) and left to dry for around 30 minutes. For porosity visualization, 1 % uranyl acetate is subsequently used to stain the dried grid. The specimen was then imaged using the mounted grid set up in the TEM sample stage. Further, the particle size has been randomly collected from various areas of the grid. Finally, the average particle size was calculated.

The morphology and selected area electron diffraction (SAED) patterns of the various bioactive glass samples were analyzed using a high-resolution transmission electron microscope (HR-TEM) (Model TALOS S, Thermo Scientific, USA) operating at an accelerating voltage of 200 kV. The diameter of bioactive glass nanoparticles was

calculated by measuring particle sizes using ImageJ bundled with 64-bit Java 1.8.0_172 software.

2.2.2. Atomic Force Microscope (AFM):[43–45]

AFM is the most versatile and high-resolution scanning probe microscope (SPM) with a resolution of fractions of Angstrom. It has more than 1000 times higher resolution when compared to the traditional optical microscope. It is capable of producing a three-dimensional topography using just a single scan. The information is gathered by "feeling" or "touching" the material surface with a mechanical probe. AFM may help characterise

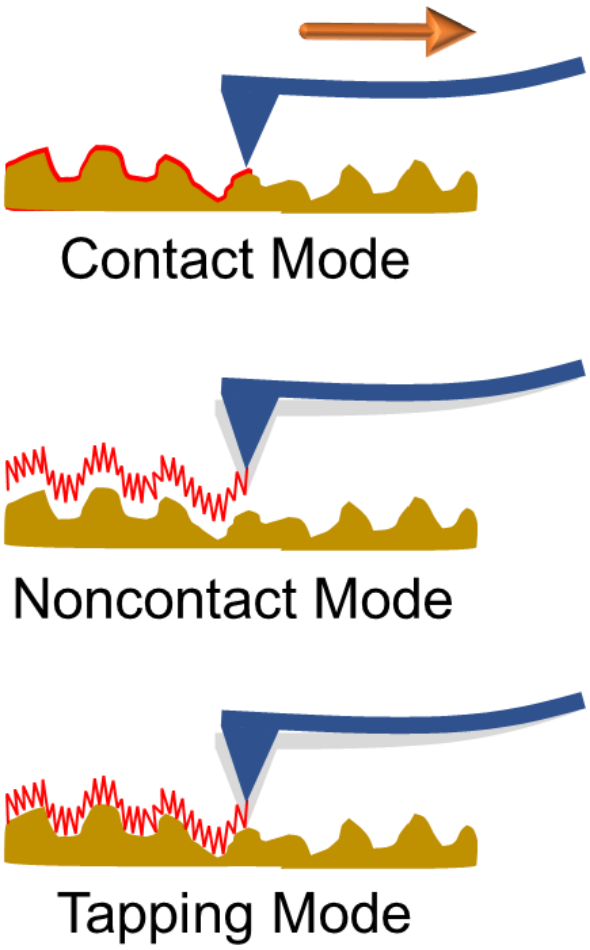

Fig. 2.15: Different modes of operations in an AFM unit (modified).[43]

various materials in various conditions, such as biological serums and vacuum, its nanometre-sharp probe that is capable of delicate interaction with an infinite array of materials. It can measure intermolecular forces and is used to evaluate parameters including height, magnetic force, surface potential, and friction. The fundamental concept behind AFM is that, a small cantilever, which functions as a spring and is linked to a nanoscale tip, bends when it comes into contact with a surface. A split photodetector and a laser diode are used to detect this bending which indicates the interaction force between the tip and the sample. In order to maintain the deflection constant throughout the scanning, the tip is pressed into the surface and an electrical feedback loop monitors the tip-sample interaction force.

An AFM unit typically has three separate operating modes: contact mode, non-contact mode, and tapping mode, as shown in **Fig. 2.15.**

In **contact mode,** the cantilever tip scans the sample while being in close proximity to the surface. It is the most frequently applied technique for measuring surface forces. The higher wear and tip failure rate during scanning provides several challenges with the contact mode.

In **non-contact mode,** the tip typically floats 5–15 nm above the substrate surface. The non-contact mode is employed to examine the dynamics of chromatin.

In **tapping mode,** the cantilever vibrates close to its resonance frequency. The tip subsequently moves up and down in a sinusoidal motion. As its tip approaches the sample, attracting or repulsive interactions slow down its motion. In order to safeguard both the sample surface and the tip from harm, it restricts their contact. However, the tapping mode addresses issues with adhesion, electrostatic forces, friction, tip dealing with rough surfaces, and other challenges through the tapping process. Tapping and

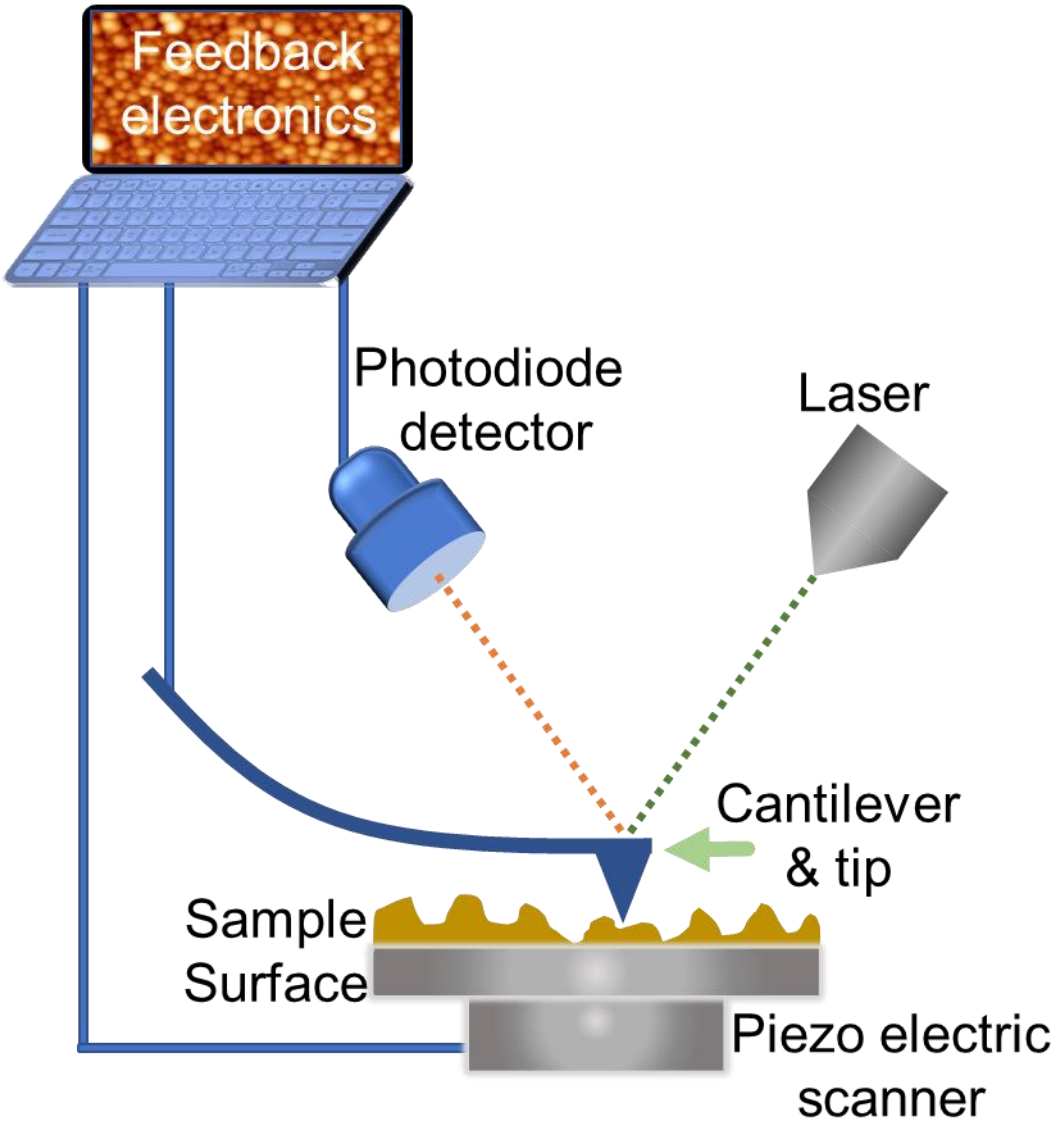

Fig. 2.16: Schematic illustration for various parts of Atomic Force Microscopy (modified).[46]

noncontact modes are frequently employed in biological examinations. The biological substances are soft and delicate; therefore, the sample could be harmed if the tip applies shear stresses to them. High-resolution topography imaging of subcellular structures, as well as soft and delicate biological materials, are visible in tapping mode. These technologies are also helpful for single molecule studies, nanotechnology, and chemical sciences.

As shown in **Fig. 2.16**, AFM instrument consists of an optical head, a moveable scanner,

and a multimode base. The head part contains the alignment knobs, photodiode array, laser and probe, all used to align the system. The probe, which scans the specimen surface at the nanoscale level, is a microscale or nanoscale cantilever with a sharp tip made up of silicon or silicon nitrite at its one end. To make the cantilever tip sharper and improve image resolution of the surfaces at the angstrom level, CNTs can be attached to the tip. However, because the CNT-based AFM tip is so delicate, special precautions must be taken during the mounting and surface scanning. The top of the cantilever constantly reflects a laser beam, which detects the bend as it occurs and determines the cantilever actual position. The sample is put on the movable scanner, which has a piezo tube for controlling the sample mobility. Piezoelectric components offer precision scanning by enabling small and exact movements that may be controlled electronically. The base manages the probe lifting and lowering.

Instrument specification

The topographic images of the gelatin-pectin hybrid composite fibers containing *in-situ* mineralized bioactive glass particles (GPBG) and 7-dehydrocholesterol containing GPBG were obtained along with Raman spectra, recorded through atomic force microscope (AFM) (WITech Project) equipped with Raman spectrometer (WITech Project Raman Imaging) to understand internal structural details. For analysis, tapping mode is used in air, using 225 mm-long silicon cantilevers.

2.2.2. Elemental Analysis:

2.2.2.1. Inductively Coupled Plasma-Mass Spectrometry (ICP-MS):[47–49]

Inductively coupled plasma-mass spectrometry or ICP-MS is one important experimental method for the qualitative and quantitative identification of elements at very low concentrations, typically in the ppm range. It is practically used in many disciplines where

inorganic analytical analysis is necessary. It is a technique for chemical analysis that uses inductively coupled plasma to generate excited atoms and ions that emit electromagnetic radiation with wavelengths specific to a given element in order to estimate the concentration of that element in the sample. The number of atoms in the element is directly proportional to the intensity of emitted radiation.

ICP-MS works on the principle that the sample is introduced into the nebulizer of ICP plasma chamber as an aerosol. The aerosol can be either in the form of aspirating liquid or dissolved solid sample. The sample aerosol is completely desolvated once it is placed inside the plasma chamber. Further, the elements present in the aerosol are subsequently converted into gaseous atoms and then ionized. The ionized atoms radiate energy at a particular wavelength which is then caught and evaluated using a mass spectrometer. Generally, a liquid form of the specimen is required for ICP-MS analysis. However, the sample was delivered to the torch either in a gaseous state or an aerosol form. Therefore,

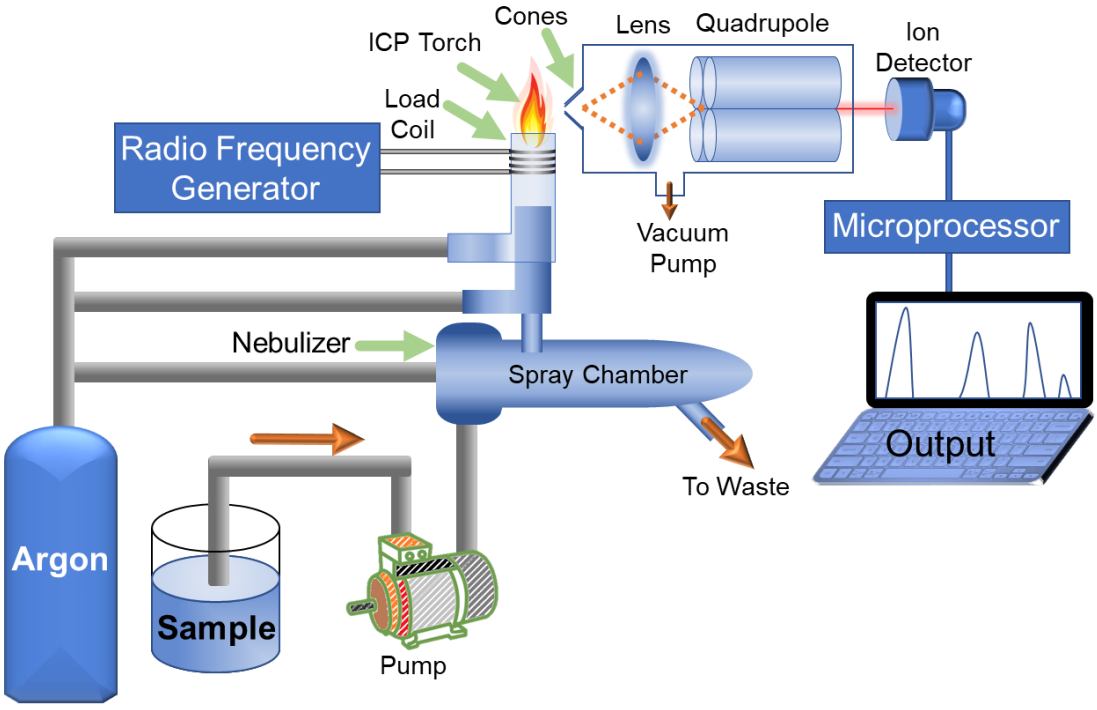

Fig. 2.17: Pictorial representation of inductively coupled plasma-mass spectrometry (ICP-MS) (modified).[50]

liquid samples need to be nebulized. A peristaltic pump transfers the liquid sample from a vial into the nebulizer. In the nebulizer, the liquid droplets are shaped on the needle tip, which has been nebulized in presence of argon gas flowing through a second needle positioned perpendicular to the sample needle. Herein, only a tiny amount of the generated aerosol is dispersed into the torch while the majority portion condenses on the nebulizer wall and is drained out into the waste container. **Fig. 2.17** shows the pictorial representation of inductively coupled plasma-mass spectrometry.

Mass Spectrometer:[51,52]

In mass spectrometer, the scattered ions are typically analyzed based on their mass to charge (m/e) ratio. Except for the signal processor and readout section, the entire instrument component requires low pressure atmospheres. It has unique ability to distinguish between masses and express it in terms of resolution, as illustrated by the equation below:

$$R = \frac{m}{\Delta m} \tag{2.5}$$

Where $\Delta\mathbf{m}$ = mass difference between recently resolved adjacent peaks; **m** = nominal mass of the first peak.

Different components of mass spectrometer are shown in **Fig 2.18.**

Interface: A sampler and skimmer cone are part of an interface through which a small number of free ions generated by plasma are conveyed. Here, ions move from a component at extremely high temperature and atmospheric pressure to a chamber at room temperature.

Electrostatic lenses system: The lens system provides the entry gate to the ions towards the mass analyzer.

Quadrupole section: Four metal rods typically make up the quadrupole section, which divides the ions based on their masses.

An electro-multiplier: It is a precise form of detector that increases the signal strength from colliding ions to produce a pulse that can be analyzed.

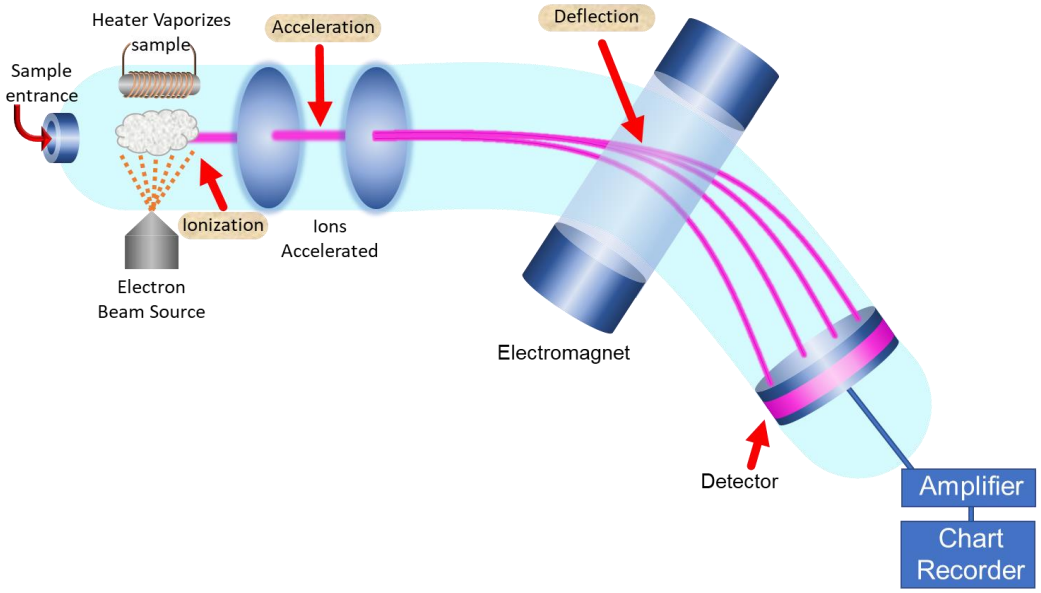

Fig. 2.18: Schematic illustration of different components of Mass spectrometer (modified).[53]

Electronics: In order to acquire a comprehensive spectrum, this section typically counts and sort the pulses in milliseconds by linking them to their respective masses.

Sample Preparation:

As per the standard protocol, BG samples were transferred into separate silica crucible and kept in an incinerator at 900 °C for 24 h. Further, the resulted ash was dissolved in mineral acid such as aqua regia which is then diluted to a known volume. After that, the samples were filtered using a syringe filter and introduced into the ICP plasma chamber as an aerosol. In plasma chamber entire sample was desolvated and converted into gaseous atoms and ionized. The ionized plasma was analyzed using mass spectrometer.

Instrument Specifications:

ICP-MS technique has been employed by using Agilent 7900, ICP-MS, USA, to estimate the atomic % of various elements such as Si, P, Na, Ca and so forth present in the BG samples.

2.2.2.2. CHNSO Analysis:[54]

The CHNSO elemental analysis method, also known as organic elemental analysis or elemental microanalysis, works on the principle of "Duma's method," which entails the complete and instantaneous oxidation of the sample by "flash combustion,". It is used to calculate the amounts of carbon (C), hydrogen (H), nitrogen (N), sulphur (S), and oxygen (O) present in a sample. The combustion products are separated by a chromatographic column before being detected by a thermal conductivity detector (T.C.D.), which produces an output signal proportional to the concentration of the mixture various constituents. It is a trustworthy and economical method that may be performed on a variety of different sample types, including solid, liquid, volatile and viscous substances. It is used to determine the purity and chemical composition of compounds. Analysts can better evaluate the structure of the sample substance by understanding the composition of the organic constituents. In research and for quality assurance, organic molecules are chemically characterised (QC). **Fig. 2.19** shows the schematic illustration for CHNSO analyzer.

Sample Preparation and Instrument Specification:

The amount of incorporated organic molecules in various BG materials were confirmed by estimating the atomic % of C, N and H using CHNSO analyser, Vario Micro Cube, Elementar Analysensysteme, Germany. The experiment was performed as per the standard protocol. Firstly, small quantity of sample was weighted accurately into a tin

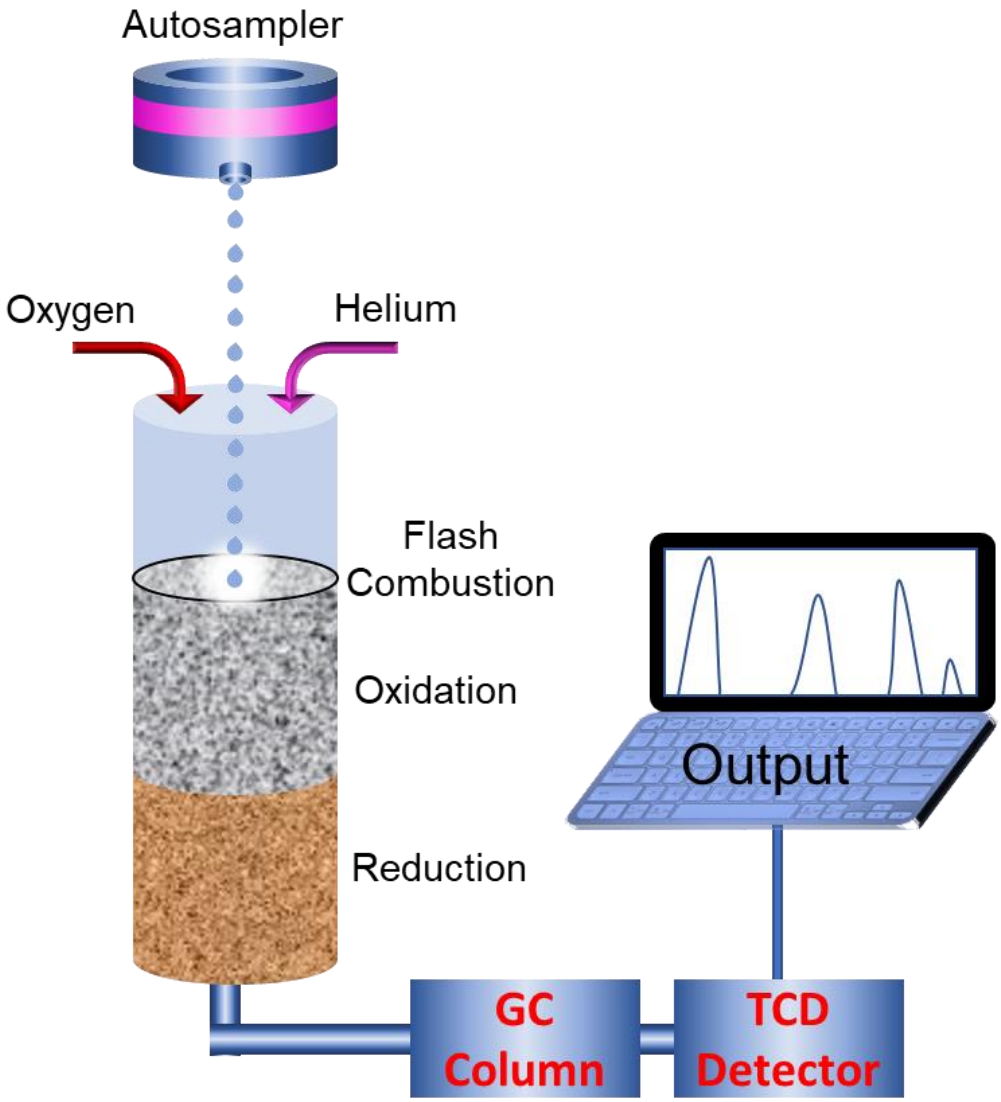

Fig. 2.19: Schematic illustration for CHNSO analyzer (modified).[55]

capsule. Further, the sample was combusted at 1000 °C in the presence of excess oxygen to form CO_2, H_2O and N_XO_Y compounds. The formed N_XO_Y was further reduced to N_2 inside the reduction tube. The final collected gases such as CO_2, H_2O and N_2 were further passed through the Gas chromatography (GC) column to quantify the content of C, H and N inside the sample.

2.3. For Mechanical Properties:

2.3.1. Rheometer:[56,57]

The rheometer is used to evaluate the rheological properties of the material. It measures the viscoelastic properties of the material in a fluid or gel state. The rheometer is generally used to determine the flow of liquid, suspension or slurry in reaction to externally applied forces. It is used for fluids whose viscosity cannot be expressed by a single number, necessitating the configuration and measurement of more parameters than in the case of a viscometer. Rheometers can measure the stress at a known shear rate or the shear rate at known stress to measure viscosity.

Rheometers are of two types: rotational or shear rheometer that modulate the applied shear stress or shear strain; and extensional rheometers that apply extensional stress or extensional strain to the specimen.

Rotational rheometer that regulates the shear strain and shear stress is shown in **Fig 2.20.** Here, the sample is sandwiched between two plates and a direct drive motor is used to provide strain (deformation) to the sample, which decides how much torque (stress) is delivered. Viscosity is calculated as a frequency function by changing the frequency or

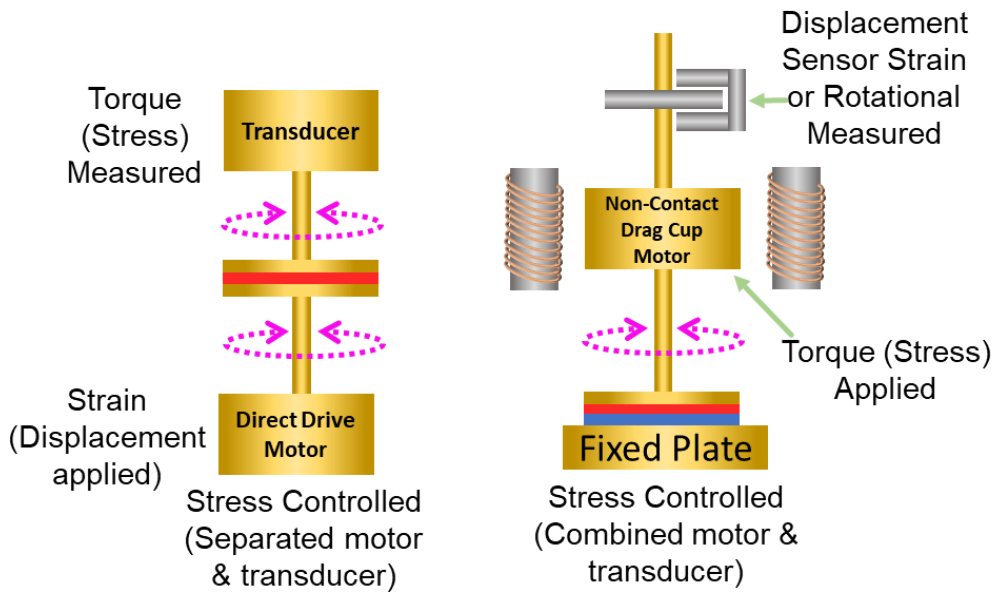

Fig. 2.20: Stress-strain controlled rotational rheometer (modified).[57]

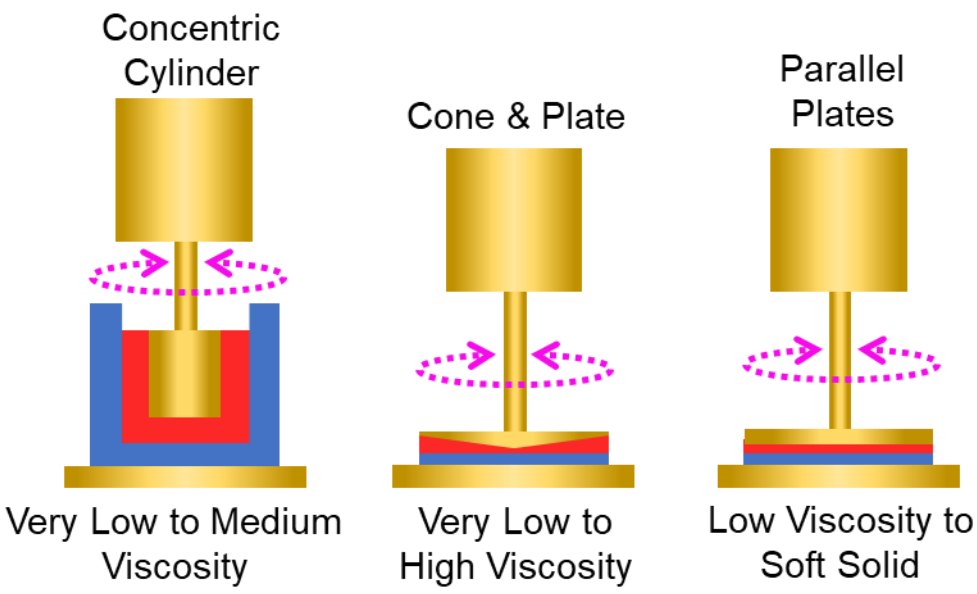

Fig. 2.21: Various rheometer geometry used for rotational or shear type rheometers (modified).[57]

the shear rate. When stress is applied, the sample responds by deforming (strain) that may be measured. Rheometers of the rotational or shear types are often made as strain-controlled or stress-controlled instruments. In a **strain-controlled rotational rheometer**, when a strain is applied, the sample response defines the amount of torque (stress) transferred. This strain (or deformation) can be applied using a sinusoidal oscillatory deformation or at a steady shear rate. It enables you to adjust the frequency or shear rate and measure the viscosity as a function of both. In a **stress-controlled rotating rheometer**, when stress is applied, the material responds by deforming (strain). It helps to record the creep behaviour but in rotational mode. **Fig. 2.21** shows various rheometer geometries used for rotational or shear type rheometers.

Instrument specification

For viscoelastic measurements, rheological characterization has been performed using a stress-controlled Anton Paar Rheometer (Model MCR 702), Austria . The rheometer was equipped with parallel-plate geometry (40 mm). The constant stress of 1 Pa and a

truncation gap of 1 mm were maintained in all the measurements. Rheology experiments were performed to map the viscoelastic profiles of freshly formed gels. The mechanical spectra yielded the storage (G') and loss modulus (G") as a function of angular frequency (ω) in the range of 0.1 rad/s to 100 rad/s as well as shear strain from 0.01 % to 100 %.

2.3.2. Universal Testing Machine (UTM):[58,59]

The word "universal" refers to its adaptability in performing various standard tensile and compression tests on different materials, parts and structures. UTM is frequently used to evaluate material tensile and compressive strengths. Its application can be extended to evaluate bend, peel, and puncture tests. It works on the principle of elongation and deformation. Typically, a hydraulic cylinder is used by this equipment to generate the force. The system pressure helps to determine the applied force, which can be precisely measured. The working cylinder receives oil from the high-pressure oil pump, which results in the upward movement of the piston, the platen and the upper beam (the upper jaw seat), which helps to test the sample for tensile or compression. Tensile tests are conducted between the main machine upper beam and the moving beam, whereas compression test is conducted between the main machine platen and the moving beam. The drive system (elevating motor, sprocket and chain) drives the double screw to revolve synchronously to raise and lower the moving beam, which helps to adjusts the test space. Schematic illustration for universal testing machine is shown in **Fig 2.22.**

In a typical stress-strain curve **(Fig. 2.23a)**, the region from point A to point C depicts the elastic nature of the material. Here the changes are reversible and the changes are instantaneously reversible between point A and B. Beyond point C (proportional limit), the curve deviates from the straight line in the absence of intermolecular slippage and the deformations may eventually be recoverable, but not instantaneously. However,

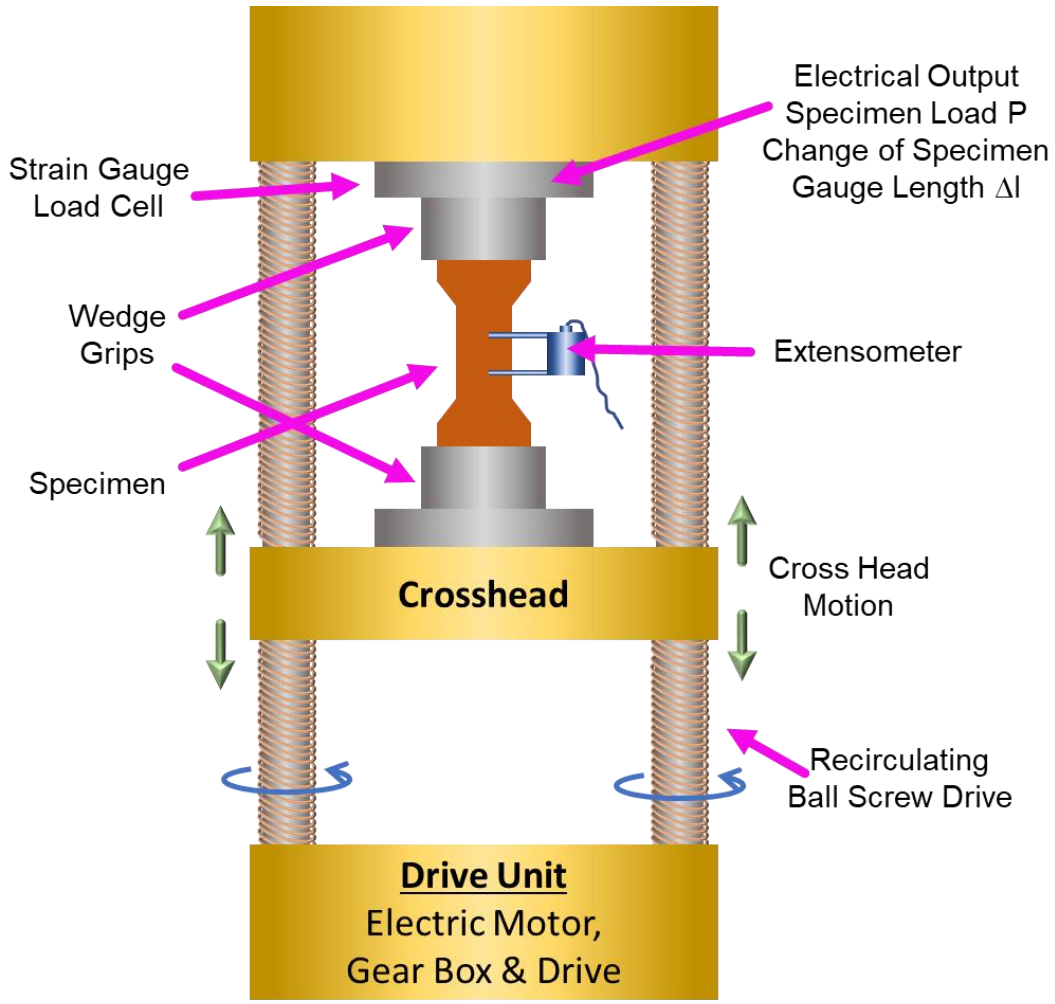

Fig. 2.22: Schematic illustration for universal testing machine (modified).[58]

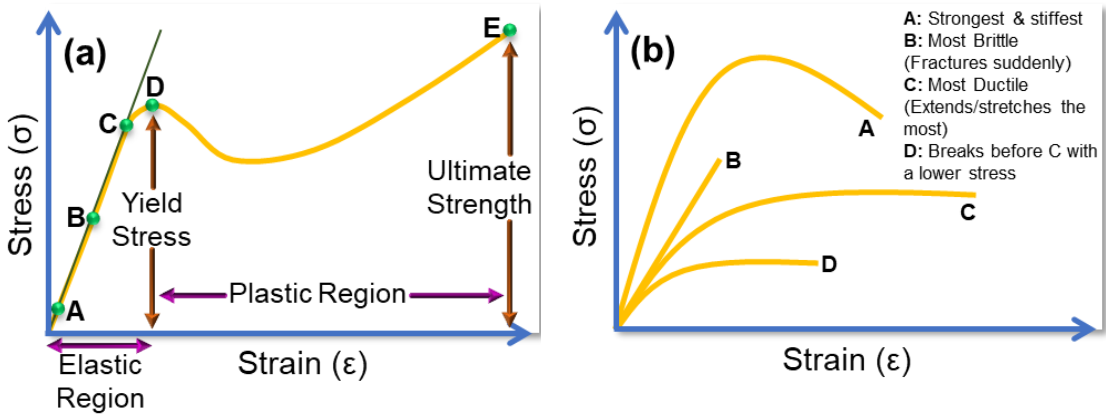

Fig. 2.23: Typical stress-strain curve, (b) Stress-strain curve of different types of materials (modified).[58]

extensions that happen beyond the material yield point D are not recoverable as these deformations occur because of the actual displacement of the molecules from one another. Here the displaced molecules are not able to slip back to their original positions so, a permanent deformation takes place. The region under the stress-strain curve provides details about the material's toughness. The stress-strain curve derived using UTM represents the material's structural and functional characteristics as shown in **Fig. 2.23b**.

Instrument Specification

The mechanical properties of the materials were determined by using Universal Testing Machine (Instron-2700) in tensile mode as per ASTM D 882-02. The strain rate was maintained at 50 mm/min and gauge length was maintained at 20 mm respectively. Various samples were tested and their stress-strain curves were recorded.

2.4. For Biophysical Studies:

2.4.1. Ultraviolet–Visible Spectroscopy:[60,61]

UV-Vis spectroscopy helps to identify pure organic molecules. Numerous compounds have chromophores, which can absorb energies at certain visible or ultraviolet light wavelengths. The principle of UV-Vis Spectroscopy is the idea in which chemical compounds can absorb ultraviolet or visible light, creating unique spectra. The basis of spectroscopy is the interaction of light and matter. A spectrum is created when the substance absorbs the light through excitation and de-excitation processes. The Beer-Lambert law can directly relate the sample concentration to the absorption of spectra produced from these samples at a specific wavelength. UV-Vis spectroscopy is a cheap and simple method that allows sample recovery and excellent discrimination between pure compounds without the requirement for derivatization. A schematic illustration of

UV-Vis spectrometer is shown in **Fig. 2.24.**

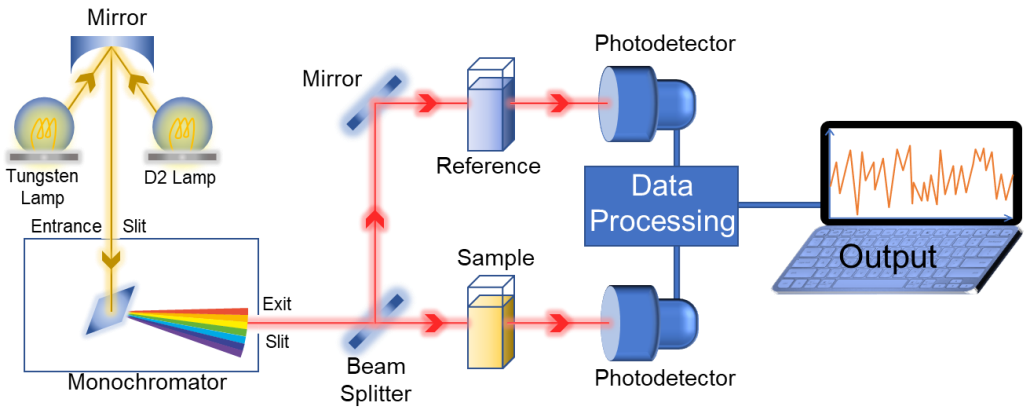

Fig. 2.24: Schematic illustration for different components of UV-Vis spectrometer (modified).[62]

UV-Vis spectroscopy includes absorption and reflectance spectroscopy in the UV-Vis region of the electromagnetic spectrum. The energy of ultraviolet or visible light can be absorbed by molecules carrying π-electrons or non-bonding electrons (n-electrons), which can then be excited to higher anti-bonding molecular orbitals. Compared to IR spectroscopy, which uses vibrational transitions to study molecules, UV-Vis spectroscopy uses electronic transitions to study molecules that occur in the ultraviolet or visible region. UV-Vis spectroscopy is typically used to quantify elemental concentrations in a solution using the Beer-Lambert law:

$$A = Log_{10}\frac{I_o}{I} = \varepsilon CL \qquad (2.5)$$

Where $\boldsymbol{A}$ is the absorbance measured, $\boldsymbol{I_0}$ is the intensity of the incident light at a specific wavelength, $\boldsymbol{I}$ is the intensity of transmitted light, $\boldsymbol{L}$ is the path length through the sample, $\boldsymbol{C}$ is the concentration of the absorbing molecule in the sample, and $\boldsymbol{\varepsilon}$ is a molar absorptivity or extinction coefficient, it is constant for each species and wavelength. According to the law, analyte concentration can be estimated when ε is given, L is fixed, and I_0 and I can be measured. The concentration of the analyte can be calculated more

precisely when a calibration curve for the analyte is available.

Instrument Specification

For drug loading and drug release studies, the supernatant was subjected to determine the unbound drug using UV-Vis (Agilent Technologies Carry 300 UV-Vis) spectrophotometer at the wavelength (λ max) appropriate for the used drug under study.

REFERENCES:

[1] J. Epp, 4 - X-ray diffraction (XRD) techniques for materials characterization, in: G. Hübschen, I. Altpeter, R. Tschuncky, H.-G. Herrmann (Eds.), Mater. Charact. Using Nondestruct. Eval. Methods, Woodhead Publishing, 2016: pp. 81–124. https://doi.org/10.1016/B978-0-08-100040-3.00004-3.

[2] F. Civan, Chapter 18 - Instrumental and Laboratory Techniques for Characterization of Reservoir Rock, in: F. Civan (Ed.), Reserv. Form. Damage (Third Ed., Third Edition, Gulf Professional Publishing, Boston, 2016: pp. 593–611. https://doi.org/10.1016/B978-0-12-801898-9.00018-7.

[3] M. Nasrollahzadeh, M. Atarod, M. Sajjadi, S.M. Sajadi, Z. Issaabadi, Chapter 6 - Plant-Mediated Green Synthesis of Nanostructures: Mechanisms, Characterization, and Applications, in: M. Nasrollahzadeh, S.M. Sajadi, M. Sajjadi, Z. Issaabadi, M. Atarod (Eds.), An Introd. to Green Nanotechnol., Elsevier, 2019: pp. 199–322. https://doi.org/10.1016/B978-0-12-813586-0.00006-7.

[4] C.F. Holder, R.E. Schaak, Tutorial on Powder X-ray Diffraction for Characterizing Nanoscale Materials, ACS Nano. 13 (2019) 7359–7365. https://doi.org/10.1021/acsnano.9b05157.

[5] Y. Waseda, E. Matsubara, K. Shinoda, X-ray diffraction crystallography: introduction, examples and solved problems, Springer Science & Business Media, 2011. ISBN: 978-3-642-16635-8.

[6] J.M. Cameron, C. Bruno, D.R. Parachalil, M.J. Baker, F. Bonnier, H.J. Butler, H.J. Byrne, Chapter 10 - Vibrational spectroscopic analysis and quantification of proteins in human blood plasma and serum, in: Y. Ozaki, M. Baranska, I.K.

Lednev, B.R. Wood (Eds.), Vib. Spectrosc. Protein Res., Academic Press, 2020: pp. 269–314. https://doi.org/10.1016/B978-0-12-818610-7.00010-4.

[7] Z. Cai, F. Li, M. Rong, L. Lin, Q. Yao, Y. Huang, X. Chen, X. Wang, Chapter 1 - Introduction, in: X. Wang, X. Chen (Eds.), Nov. Nanomater. Biomed. Environ. Energy Appl., Elsevier, 2019: pp. 1–36. https://doi.org/10.1016/B978-0-12-814497-8.00001-1.

[8] P.R. Griffiths, J.A. De Haseth, J.D. Winefordner, Fourier Transform Infrared Spectrometry, Wiley, 2007. ISBN: 978-0-471-19404-0

[9] B.C. Smith, Fundamentals of Fourier Transform Infrared Spectroscopy, Taylor \& Francis, 1995. https://doi.org/10.1201/b10777.

[10] B.C. Smith, Introduction to infrared spectroscopy, in: Fundam. Fourier Transform Infrared Spectrosc., CRC Press, 2011: pp. 15–32. https://doi.org/10.1201/b10777.

[11] O.S. Oluwafemi, E.H.M. Sakho, S. Parani, T.C. Lebepe, Chapter Five - Characterization techniques for ternary I–III–VI quantum dots, in: O.S. Oluwafemi, E.H.M. Sakho, S. Parani, T.C. Lebepe (Eds.), Ternary Quantum Dots, Woodhead Publishing, 2021: pp. 117–135. https://doi.org/10.1016/B978-0-12-818303-8.00007-1.

[12] R. Wolthuis, T.C.B. Schut, P.J. Caspers, H.P.J. Buschman, T.J. Römer, H.A. Bruining, G.J. Puppels, Chapter Thirty-Two - Raman Spectroscopic Methods for In Vitro and In Vivo Tissue Characterization, in: W.T. MASON (Ed.), Fluoresc. Lumin. Probes Biol. Act. (Second Ed., Second Edition, Academic Press, London, 1999: pp. 433–455. https://doi.org/10.1016/B978-012447836-7/50034-8.

[13] P.C. Chen, Nonlinear Raman Spectroscopy, Instruments, in: J.C. Lindon, G.E.

Tranter, D.W. Koppenaal (Eds.), Encycl. Spectrosc. Spectrom. (Third Ed., Third Edition, Academic Press, Oxford, 2017: pp. 401–407. https://doi.org/10.1016/B978-0-12-803224-4.00302-2.

[14] G.G. Hammes, Spectroscopy for the biological sciences, John Wiley & Sons, 2005. ISBN: 978-0-471-73354-6.

[15] An {Introduction} into {Raman} {Spectroscopy}, (2021). https://www.news-medical.net/whitepaper/20210511/An-Introduction-into-Raman-Spectroscopy.aspx.

[16] M.-T.I. all rights reserved, Raman {Spectroscopy} \textbar{} {Instrumentation}, {Introduction} & {Principle}, (n.d.). https://www.mt.com/.

[17] K. Liu, Q. Zhao, B. Li, X. Zhao, Raman Spectroscopy: A Novel Technology for Gastric Cancer Diagnosis, Front. Bioeng. Biotechnol. 10 (2022). https://doi.org/10.3389/fbioe.2022.856591.

[18] Micro- {Raman} {Spectroscopy}, (n.d.). https://duffy.princeton.edu/laboratory/raman-spectroscopy/micro-raman-spectroscopy.

[19] P. Gabbott, Principles and Applications of Thermal Analysis, Wiley, 2008. https://doi.org/10.1002/9780470697702.

[20] M. Wagner, Thermal Analysis in Practice: Fundamental Aspects, Hanser, 2018. ISBN: 978-1-56990-643-9.

[21] J.D. Menczel, R.B. Prime, Thermal Analysis of Polymers: Fundamentals and Applications, Wiley, 2014. ISBN: 978-0-471-76917-0.

[22] K. Unapumnuk, T.C. Keener, M. Lu, S.-J. Khang, Pyrolysis Behavior of Tire-Derived Fuels at Different Temperatures and Heating Rates, J. Air \& Waste

Manag. Assoc. 56 (2006) 618–627. https://doi.org/10.1080/10473289.2006.10464481.

[23] S. Lyubchik, A. Lyubchik, O. Lygina, S. Lyubchik, I. Fonseca, Comparison of the Thermodynamic Parameters Estimation for the Adsorption Process of the Metals from Liquid Phase on Activated Carbons, in: J.C. Moreno-Pirajan (Ed.), Thermodynamics, IntechOpen, Rijeka, 2011. https://doi.org/10.5772/19514.

[24] M. Thommes, K. Kaneko, A. V Neimark, J.P. Olivier, F. Rodriguez-Reinoso, J. Rouquerol, K.S.W. Sing, Physisorption of gases, with special reference to the evaluation of surface area and pore size distribution (IUPAC Technical Report), Pure Appl. Chem. 87 (2015) 1051–1069. https://doi.org/doi:10.1515/pac-2014-1117.

[25] W. Wang, P. Liu, M. Zhang, J. Hu, F. Xing, The pore structure of phosphoaluminate cement, (2012). http://dx.doi.org/10.4236/ojcm.2012.23012.

[26] I. Langmuir, The adsorption of gases on plane surfaces of glass, mica and platinum., J. Am. Chem. Soc. 40 (1918) 1361–1403. https://doi.org/10.1021/ja02242a004.

[27] The principles of dynamic light scattering :: Anton {Paar} {Wiki}, (n.d.). https://wiki.anton-paar.com/in-en/the-principles-of-dynamic-light-scattering/.

[28] B.J. Berne, R. Pecora, Dynamic Light Scattering: With Applications to Chemistry, Biology, and Physics, Dover Publications, 2013. https://doi.org/10.1016/0307-4412(77)90025-5

[29] K.S. Schmitz, Introduction to Dynamic Light Scattering by Macromolecules, Elsevier Science, 2012. ISBN: 9780323140355.

[30] 2.4: Dynamic {Light} {Scattering} - {Chemistry} {LibreTexts}, (2016). https://chem.libretexts.org/.

[31] S. Bhattacharjee, DLS and zeta potential – What they are and what they are not?, J. Control. Release. 235 (2016) 337–351. https://doi.org/10.1016/j.jconrel.2016.06.017.

[32] A.J. Shnoudeh, I. Hamad, R.W. Abdo, L. Qadumii, A.Y. Jaber, H.S. Surchi, S.Z. Alkelany, Chapter 15 - Synthesis, Characterization, and Applications of Metal Nanoparticles, in: R.K. Tekade (Ed.), Biomater. Bionanotechnol., Academic Press, 2019: pp. 527–612. https://doi.org/10.1016/B978-0-12-814427-5.00015-9.

[33] G.W. Lu, P. Gao, CHAPTER 3 - Emulsions and Microemulsions for Topical and Transdermal Drug Delivery, in: V.S. Kulkarni (Ed.), Handb. Non-Invasive Drug Deliv. Syst., William Andrew Publishing, Boston, 2010: pp. 59–94. https://doi.org/10.1016/B978-0-8155-2025-2.10003-4.

[34] Scanning {Electron} {Microscope} ({SEM}) - {Bioscience} {Notes}, (2018). https://www.biosciencenotes.com/.

[35] A. Ul-Hamid, A Beginners' Guide to Scanning Electron Microscopy, Springer International Publishing, 2018. http://dx.doi.org/10.1007/978-3-319-98482-7.

[36] H.C. Backer, Scanning Electron Microscopy., Lubrication. 61 (1975) 37–56. https://doi.org/10.1007/978-0-387-49762-4_3.

[37] T. Roodbar Shojaei, S. Soltani, M. Derakhshani, Chapter 6 - Synthesis, properties, and biomedical applications of inorganic bionanomaterials, in: A. Barhoum, J. Jeevanandam, M.K. Danquah (Eds.), Fundam. Bionanomaterials, Elsevier, 2022: pp. 139–174. https://doi.org/10.1016/B978-0-12-824147-9.00006-6.

[38] D. Titus, E. James Jebaseelan Samuel, S.M. Roopan, Chapter 12 - Nanoparticle characterization techniques, in: A.K. Shukla, S. Iravani (Eds.), Green Synth. Charact. Appl. Nanoparticles, Elsevier, 2019: pp. 303–319. https://doi.org/10.1016/B978-0-08-102579-6.00012-5.

[39] Joy, David C. , Ford, Brian J. and Bradbury, Savile. "transmission electron microscope". Encyclopedia Britannica, 23 Sep. 2019, https://www.britannica.com/technology/transmission-electron-microscope. Accessed 11 July 2022, (n.d.).

[40] C.B. Carter, D.B. Williams, Transmission Electron Microscopy: Diffraction, Imaging, and Spectrometry, Springer International Publishing, 2016. https://link.springer.com/book/10.1007/978-3-319-26651-0.

[41] D.B. Williams, C.B. Carter, Transmission Electron Microscopy: A Textbook for Materials Science, Springer US, 2013. https://link.springer.com/book/10.1007/978-0-387-76501-3.

[42] W.F. Tivol, Selected Area Electron Diffraction and its Use in Structure Determination, Micros. Today. 18 (2010) 22–28. https://doi.org/10.1017/S1551929510000441.

[43] R. Asmatulu, W.S. Khan, Chapter 13 - Characterization of electrospun nanofibers, in: R. Asmatulu, W.S. Khan (Eds.), Synth. Appl. Electrospun Nanofibers, Elsevier, 2019: pp. 257–281. https://doi.org/10.1016/B978-0-12-813914-1.00013-4.

[44] S. Palchoudhury, M. Baalousha, J.R. Lead, Chapter 5 - Methods for Measuring Concentration (Mass, Surface Area and Number) of Nanomaterials, in: M. Baalousha, J.R. Lead (Eds.), Charact. Nanomater. Complex Environ. Biol. Media, Elsevier, 2015: pp. 153–181. https://doi.org/10.1016/B978-0-08-099948-7.00005-1.

[45] G.A. Selvan, S. Rachel, T. Gajendran, Chapter 13 - Several assorted characterization methods of nanoparticles, in: R.P. Kumar, B. Bharathiraja (Eds.), Nanomaterials, Academic Press, 2021: pp. 301–308. https://doi.org/10.1016/B978-0-12-822401-4.00040-4.

[46] G.W. Fernando, Chapter 5 - Probing Layered Systems: A Brief Guide to Experimental Techniques, in: G.W. Fernando (Ed.), Met. Multilayers Their Appl., Elsevier, 2008: pp. 111–130. https://doi.org/10.1016/S1570-002X(07)00005-5.

[47] G. Nageswaran, Y.S. Choudhary, S. Jagannathan, Chapter 8 - Inductively Coupled Plasma Mass Spectrometry, in: S. Thomas, R. Thomas, A.K. Zachariah, R.K. Mishra (Eds.), Spectrosc. Methods Nanomater. Charact., Elsevier, 2017: pp. 163–194. https://doi.org/10.1016/B978-0-323-46140-5.00008-X.

[48] C. Jose Chirayil, J. Abraham, R. Kumar Mishra, S.C. George, S. Thomas, Chapter 1 - Instrumental Techniques for the Characterization of Nanoparticles, in: S. Thomas, R. Thomas, A.K. Zachariah, R.K. Mishra (Eds.), Therm. Rheol. Meas. Tech. Nanomater. Charact., Elsevier, 2017: pp. 1–36. https://doi.org/10.1016/B978-0-323-46139-9.00001-3.

[49] H.-C. Lee, Review of inductively coupled plasmas: Nano-applications and bistable hysteresis physics, Appl. Phys. Rev. 5 (2018) 11108. https://doi.org/10.1063/1.5012001.

[50] M. Levine, ICP-OES – ICP Chemistry, ICP-OES Analysis, Strengths and Limitations. Technology Networks (2021). https://www.technologynetworks.com/.

[51] E. De Hoffmann, V. Stroobant, Mass spectrometry: principles and applications, John Wiley & Sons, 2007. ISBN: 978-0-470-03310-4.

[52] C.G. Herbert, R.A.W. Johnstone, Mass Spectrometry Basics, CRC Press, 2002. https://doi.org/10.1201/9781420040340.

[53] R. ten Haaft, Mass Spectrometry and Mass Flow Control; A closer ion them (2021). https://www.bronkhorst.com/.

[54] M. Tabatabaei, H. Ghanavati, Biogas: Fundamentals, Process, and Operation, Springer International Publishing, 2018. https://link.springer.com/book/10.1007/978-3-319-77335-3.

[55] E.C. Ebere, V.E. Ngozi, Microplastics, an emerging concern: A review of analytical techniques for detecting and quantifying microplatics, Anal. Methods Environ. Chem. J. 2 (2019) 13–30. https://doi.org/10.24200/amecj.v2.i2.57.

[56] J. Abraham, T. Sharika, R.K. Mishra, S. Thomas, 14 - Rheological characteristics of nanomaterials and nanocomposites, in: R.K. Mishra, S. Thomas, N. Kalarikkal (Eds.), Micro Nano Fibrillar Compos. (MFCs NFCs) from Polym. Blends, Woodhead Publishing, 2017: pp. 327–350. https://doi.org/10.1016/B978-0-08-101991-7.00014-5.

[57] J. Gotro, Rheology of {Thermosets} {Part} 2: Rheometers - {Polymer} {Innovation}, (2014). https://polymerinnovationblog.com/rheology-thermosets-part-2-rheometers/.

[58] V. Shah, Handbook of Plastics Testing and Failure Analysis, Wiley, 2007. ISBN: 978-1-118-94363-2.

[59] J.R. Davis, Tensile Testing, 2nd Edition, ASM International, 2004. ISBN: 978-0-87170-806-9.

[60] M.L.C. Passos, M.C. Sarraguça, M.L.M.F.S. Saraiva, T. Prasada Rao, V.M. Biju,

Spectrophotometry | Organic Compounds☆, in: P. Worsfold, C. Poole, A. Townshend, M. Miró (Eds.), Encycl. Anal. Sci. (Third Ed., Third Edition, Academic Press, Oxford, 2019: pp. 236–243. https://doi.org/10.1016/B978-0-12-409547-2.14465-8.

[61] H. Wang, P.K. Chu, Chapter 4 - Surface Characterization of Biomaterials, in: A. Bandyopadhyay, S. Bose (Eds.), Charact. Biomater., Academic Press, Oxford, 2013: pp. 105–174. https://doi.org/10.1016/B978-0-12-415800-9.00004-8.

[62] F.S. Rocha, A.J. Gomes, C.N. Lunardi, S. Kaliaguine, G.S. Patience, Experimental methods in chemical engineering: Ultraviolet visible spectroscopy—UV-Vis, Can. J. Chem. Eng. 96 (2018) 2512–2517. https://doi.org/10.1002/cjce.23344.

CHAPTER 3

Effect of pH on Bio-inspired Synthesis of L-Lysine Templated Bioactive Glass Hybrid Xerogels for Tailored Textural and Rheological Properties

CHAPTER 3

Effect of pH on Bio-inspired Synthesis of L-Lysine Templated Bioactive Glass Hybrid Xerogels for Tailored Textural and Rheological Properties

GRAPHICAL ABSTRACT

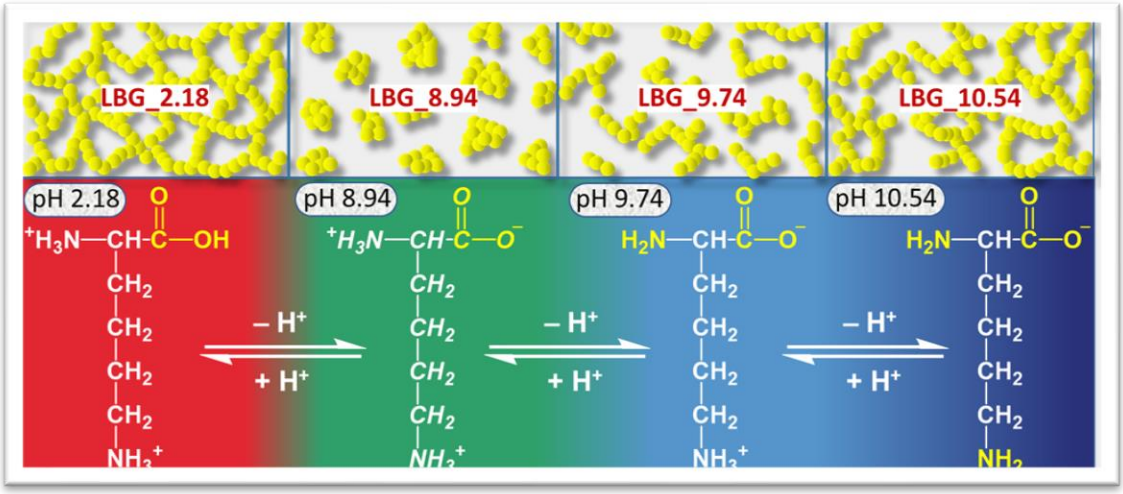

3.1. Introduction:

In recent years, silica based gels (xerogels, aerogels and cryogels) have emerged as an attractive alternative to polymer based hydrogels for diverse biomedical applications [1–3]. Silica based gels are well known for tailorable porosity, better mechanical strength, water absorption, apparent bulk density, degradation and biocompatibility [4–7]. Silica gels are also identified as promising carrier materials for targeted controlled drug delivery with high drug loading efficiency and low processing temperature. These unique attributes sparked tremendous interest in creating a new class of biomaterials favourable for *in-situ* incorporation of drug molecules into the silica matrix [8]. León Albarran et al. [9] encapsulated a derivative of 6-aminoribofuranosil purine (IFC-305) into

nanostructured silica. Herein, silica surface was functionalized with —OH groups by the sol-gel process for liver targeted drug delivery to treat cancer. Tamal Sarkar *et al.* [10] incorporated 5 nm sized spherical and fluorescent carbon dots (CD) into nanocomposite xerogel silica matrix for real-time tracking of drug delivery route. Silica aerogels were reported to be an excellent alternative for artificial heart valve leaflets due to their superior mechanical strength, low inertia and preparation cost [7]. Poly(ε-caprolactone)-silica xerogel hybrids were used as a novel coating material for Titanium implants [11].

It is beyond doubt that hybrid systems combining inorganic-organic materials [12–14] also offer improved osteoconductive functions, elastomeric property, and electroactivity for bone tissue regeneration [8]. Interestingly, current advancements favor these composite materials not only for hard tissue [1], but for soft tissue replacement as well [15]. Hence the scope of making commercially viable silica based materials has considerably increased as a result of persistent requirement of bone repair, replacement, or regeneration treatments. In this context, 60S-PEG hybrid xerogels synthesized by Wei Liu *et al* [16] exhibited properties of bone regeneration materials. As a result of nanoscale interaction between the organic and inorganic components (i.e 60S silica and PEG), the hybrid xerogel exhibited improved mechanical and apatite forming ability (or bioactivity). Importantly, mesoporosity observed in these xerogels was found suitable for cell growth and osteogenesis. Apatite layer formation on ternary bioactive glasses (SiO_2-CaO-P_2O_5) xerogel and aerogel on immersion in SBF has been reported by Dalila Ksouri *et al.* [17]. The studies mentioned above employ sol–gel method for synthesizing xerogels, which has limitations like prolonged synthesis period (approximately 1 week) [18]. In addition, synthesis of class I and class II silica based hybrids by sol–gel method requires costly and toxic chemicals such as organic solvents and metal alkoxides which follows complicated organometallic synthetic strategies [19]. At the end sol-gel derived

products need to be calcined at high temperature to get porous microstructure [19].

Bio-inspired route was developed on admiring naturally synthesized nano-structured materials such as silica in diatoms by the guidance of bio macromolecular templates [20,21]. In last two decades, the bio-inspired synthesis for nanostructured ceramic oxides below 100 °C was well established using organic templates[22,23]. Currently, hybrid materials are also being obtained by this method [24]. In this study, mesoporous L-lysine-bioactive glass hybrid (LBG) xerogels were first time synthesized using L-lysine as a template by bio-inspired method. The template, L-lysine used in this study is an essential amino acid. It plays an indispensable role in carnitine production, a nutrient found in most cells of human body. Importantly, the amino acid is responsible for converting fatty acids into energy and also help to lower cholesterol. The essential amino acid also plays a vital role in the formation of collagen. It also helps in curing osteoporosis by helping the body to absorb calcium to prevent the bone loss [25]. The synthesis of bioactive glass hybrid materials was carried out using tetraethyl orthosilicate (TEOS) as a precursor for silica network in aqueous medium containing L-lysine molecules. Interestingly, the rates of hydrolysis and polycondensation of TEOS is well known to determine the structure and instantaneous properties of the resulting silica network. These rates majorly depend on the pH of the reaction medium [26,27]. Herein, hydrolysis and polycondensation of TEOS was directed by pH dependent charge characteristic of L-lysine molecules. In detail, the reaction media were maintained at various pH values equal to three pKa values (2.18, 8.94, 10.54) and pI value (9.74) of L-lysine to tune its charge characteristics and hydrolysis of TEOS. Novelty of the synthetic procedure lies in the *in-situ* incorporation of therapeutic monomer L-lysine, which tailors the porosity of bioactive glass network. The present study also aims for economic green synthetic method to obtain a new class of viscoelastic mesoporous bioactive glass materials by avoiding polymer templates. The

importance of LBG textural properties in drug delivery applications was evaluated by loading and release of 7-dehydrocholesterol, a precursor to vitamin D as a model drug. The resulted xerogels at pKa_1 (2.18), pKa_2 (8.94), pKa_3 (10.54) and pI (9.74) were thoroughly characterized by Inductively Coupled Plasma Mass Spectrometry (ICP-MS), Carbon, Hydrogen, Nitrogen, Sulphur, or Oxygen Analysis (CHNSO), Fourier Transform Infrared Spectroscopy (FTIR), X-Ray Diffraction (XRD), Thermogravimetric Analysis (TGA), Field Emission Scanning Electron Microscope (FE-SEM), High-Resolution Transmission Electron Microscopy (HR-TEM), Nitrogen Sorption Analysis and Rheometer. Also, *in-vitro* bone-bonding abilities of xerogels were understood by interacting with simulated body fluid (SBF) solution.

3.2. Experimental Section:

3.2.1. Materials:

L-lysine, tetraethyl orthosilicate (TEOS), triethyl phosphate (TEP), sodium acetate (NaAc) and calcium acetate monohydrate (CaAc), were obtained from Sigma, USA. 7-dehydrocholesterol and Hank's Balanced Salt solution (simulated body fluid (SBF)) were also purchased from Sigma, USA and used for *in-vitro* bioactivity test. Milli-Q water was used for all experiments. All reagents used in these experiments were of analytical reagent (AR) grade of high purity. All experiments were performed at 25 °C unless otherwise stated and in triplicates for error analysis.

3.2.2. Bio-inspired synthesis of L-Lysine-Bioactive glass hybrid (LBG) xerogels:

Initially, 1 mg/ml L-Lysine solution was prepared in Milli-Q water. Further, the solution's pH was adjusted to its pKa values i.e., 2.18, 8.94, 10.54 using HCl and NaOH solutions. L-lysine solution in Milli-Q water showed the pH equal to its isoelectric point (pI) i.e., 9.74. Further, for the synthesis of LBG xerogels at pI and various pKa values of L-lysine,

required BG precursors, namely TEOS (9.29 g), TEP (1.0 g), NaAc (6.36 g) and CaAc (4.21 g), which were sequentially added into the corresponding L-lysine solutions (100 ml). Herein, for every precursor an interval of 30 min was maintained **(Fig. 3.1)** and kept for stirring overnight as per the procedure reported by Santhiya *et. al.,* [28,29] centrifuged and washed with distilled water to remove unreacted components. The obtained LBG xerogels were named as LBG_2.18, LBG_8.94, as well as LBG_10.54 and LBG_9.74 as

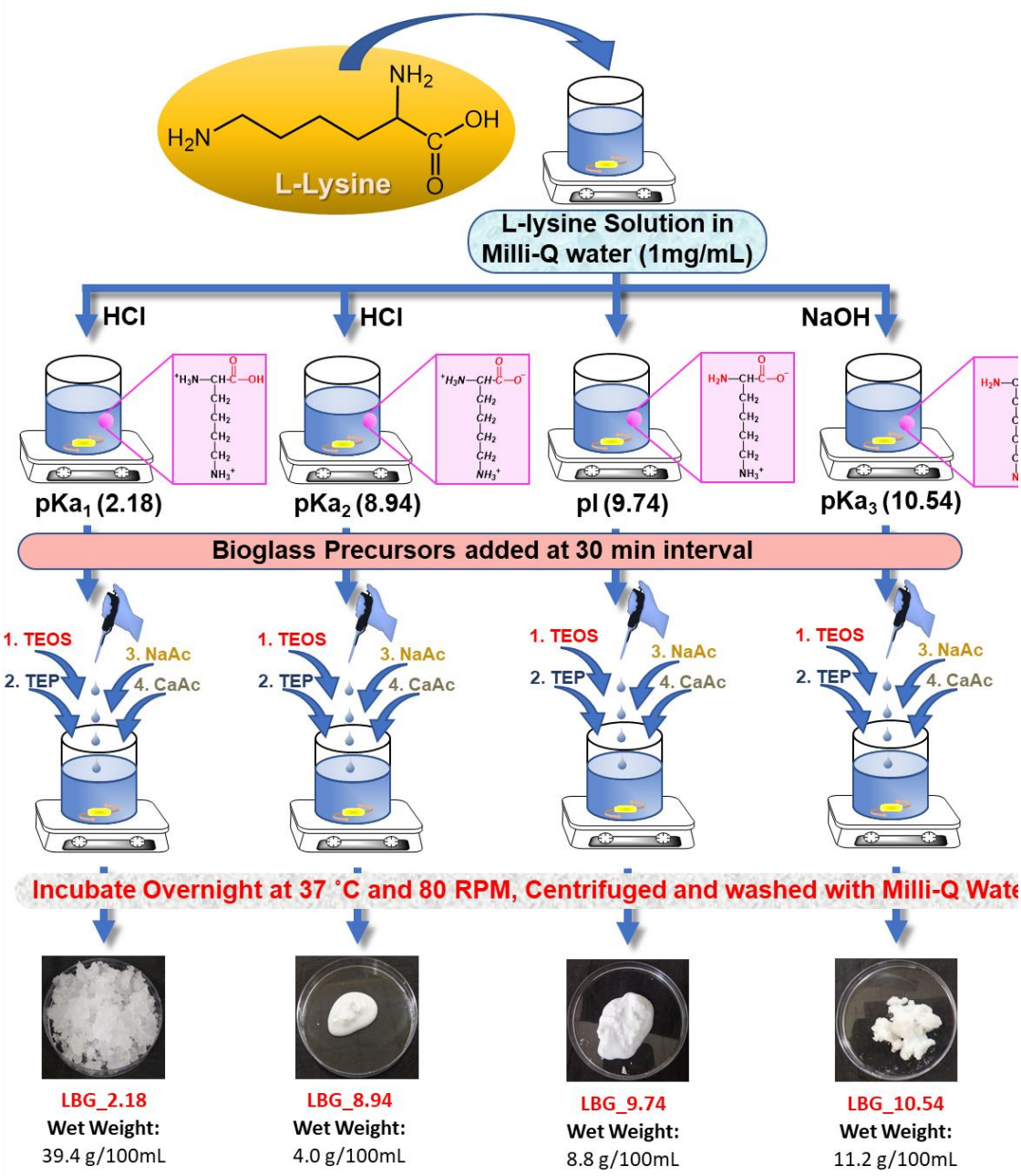

Fig. 3.1: Schematic illustration for the synthesis of LBG xerogels.

per various pKa and pI values of L-Lysine, respectively. The wet weight of the xerogels were observed to be 39.4 g/100 ml for LBG_2.18, 4 g/ml for LBG_8.94, 8.8 g/100 ml for LBG_9.74 and 11.2 g/100 ml for LBG_10.54. Further, samples were dried at 40 °C in an air oven for 48 h and preserved in a vacuum desiccator. In the absence of L-lysine, corresponding blank samples were also prepared. Herein, it is pertinent to mention that in the absence of L-lysine, BG gels were obtained only at pH 2.18 and pH 10.54. These blank gels are captioned as BG_2.18 and BG_10.54, preserved and subjected to characterization similar to LBG samples.

3.2.3. Characterization of LBG xerogels:

A detailed explanation for sample preparation and instrument specification for characterization tools used for LBG xerogel analysis was already discussed in Chapter 2. The atomic % of various elements such as Si, P, Na and Ca present in the LBG xerogels were estimated using ICP-MS analysis as described in section 2.2.3.1. The amount of incorporated L-lysine in various LBG xerogels were confirmed by estimating the atomic % of C, N and H using CHNSO analyzer as described in section 2.2.3.2. FTIR spectrum was recorded for every addition of bioactive glass precursors using ATR mode of the spectrometer. In addition, the FTIR analysis of various LBG powders was carried out as described in section 2.1.1. The crystallographic structure of LBG xerogels were analyzed using XRD as described in Section 2.1.2. The thermal stability of LBG xerogels were investigated using TGA as described in Section 2.1.4. The surface morphology of various LBG xerogels was recorded using FE-SEM, HR-TEM and SAED pattern analysis as described in Section 2.2.1.1. and 2.2.1.2. Further, the particle size was analyzed using ImageJ bundled with 64-bit Java 1.8.0_172 software. The porosity of various LBG xerogels was determined by nitrogen adsorption-desorption analysis as described in

Section 2.1.5. Pre-formed LBG xerogels were used for the rheological characterization using Rheometer as described in Section 2.4.1.

3.2.3.1. Drug Loading:

7-Dehydrocholesterol was loaded by immersing the LBG xerogels (25 mg/ml) in 7-Dehydrocholesterol solution (25 mg/ml) for 4 h and 24 h at 37 °C and 120 rpm, centrifuged and dried. To determine the nutrient entrapment efficiency (EE%) the amount of unbound drug was detected in the supernatant using UV-Vis (Agilent Technologies Carry 300 UV-Vis) spectrophotometer at the wavelength (λmax)— of 285 nm [31]. Experiment was performed in triplicate and amount of loaded drug was determined according to the equation:

$$EE\ (\%) = \frac{Total\ Amount\ of\ Drug - \ Amount\ of\ Unbound\ Drug}{Total\ Amount\ of\ Drug}\ X\ 100$$

3.2.3.2. Drug Release Studies:

The LBG xerogels were immersed in SBF solution at a concentration of 1 mg/mL using Erlenmeyer flasks. Then the flasks containing xerogels were shaken at 80 rpm in a water shaker bath at 37 °C. Further, at pre-determined intervals, 1 mL of solution was pipetted out from each flask and subjected to quantitative analysis using UV-visible Spectroscopy to determine the release content of 7-Dehydrocholesterol in SBF at a characteristic wavelength of 285 nm [31]. The amount of drug released was plotted against time. Experiments were conducted in triplicates with required volume corrections.

3.2.3.3. *In-vitro* Bioactivity Test:

In-vitro bioactivity of various LBG xerogels was monitored by the formation of bone-like hydroxyapatite (HAP) on bioactive glass surface as per the procedure described by

Kokubo et al. [32]. Bioactive glass hybrids were immersed in SBF at a concentration of 1 mg/mL. Further, samples were incubated at 37 °C under sterile conditions. The SBF solution was changed for every 3 days to avoid a decrease in its cationic concentration., Otherwise, it may decrease the ease of hydroxyapatite formation. After pre-determined interval of time, the samples were removed, washed with milli-Q water thrice and dried in air oven at 40 °C. They were further characterized using FTIR, XRD and FE-SEM analysis.

3.3. Results and Discussion:

3.3.1. FTIR Analysis:

The step-wise interaction mechanism of BG precursors (TEOS **(step 1)**, TEP **(step2)**, NaAc **(step 3)** and CaAc **(step 4)**) with L-lysine molecules was investigated during the synthesis of LBG xerogels. Herein, FTIR spectrum was recorded for each BG precursor added to L-lysine solution at its pI (9.74) and different pKa values (pKa_1 2.18, pKa_2 8.94 and pKa_3 10.54) (**Fig 3.2a-d**).

At pKa_1 (2.18), L-lysine showed only two peaks at 1635 cm^{-1} and 667 cm^{-1} corresponding to **—**C=O stretching and —N—H wagging, respectively (**Fig 3.2a (L-lysine_2.18)**). In **Step 1,** addition of TEOS (**Fig 3.2a (Step 1)**) shifted **—**C=O stretching peak of L-lysine to slightly higher wavenumber (from 1635 cm^{-1} to 1639 cm^{-1}) possibly due to weak physical interactions. Further, new peaks observed at 1086 cm^{-1} (C—O stretching, Si—O—C stretching, Si—O—Si asymmetric stretching), 1045 cm^{-1} (Si—O^- stretching) and 957 cm^{-1} (Si—O—Si, Si—O—H, Si—O—C) indicates hydrolysis and condensation of TEOS and its interaction with L-lysine through carboxylic acid group. A new peak at higher wavenumber for —N—H wagging of L-lysine emerged at 877 cm^{-1} in addition 667 cm^{-1}. On adding TEP (**Fig 3.2a (Step 2)**), unlike step 1 no new peaks

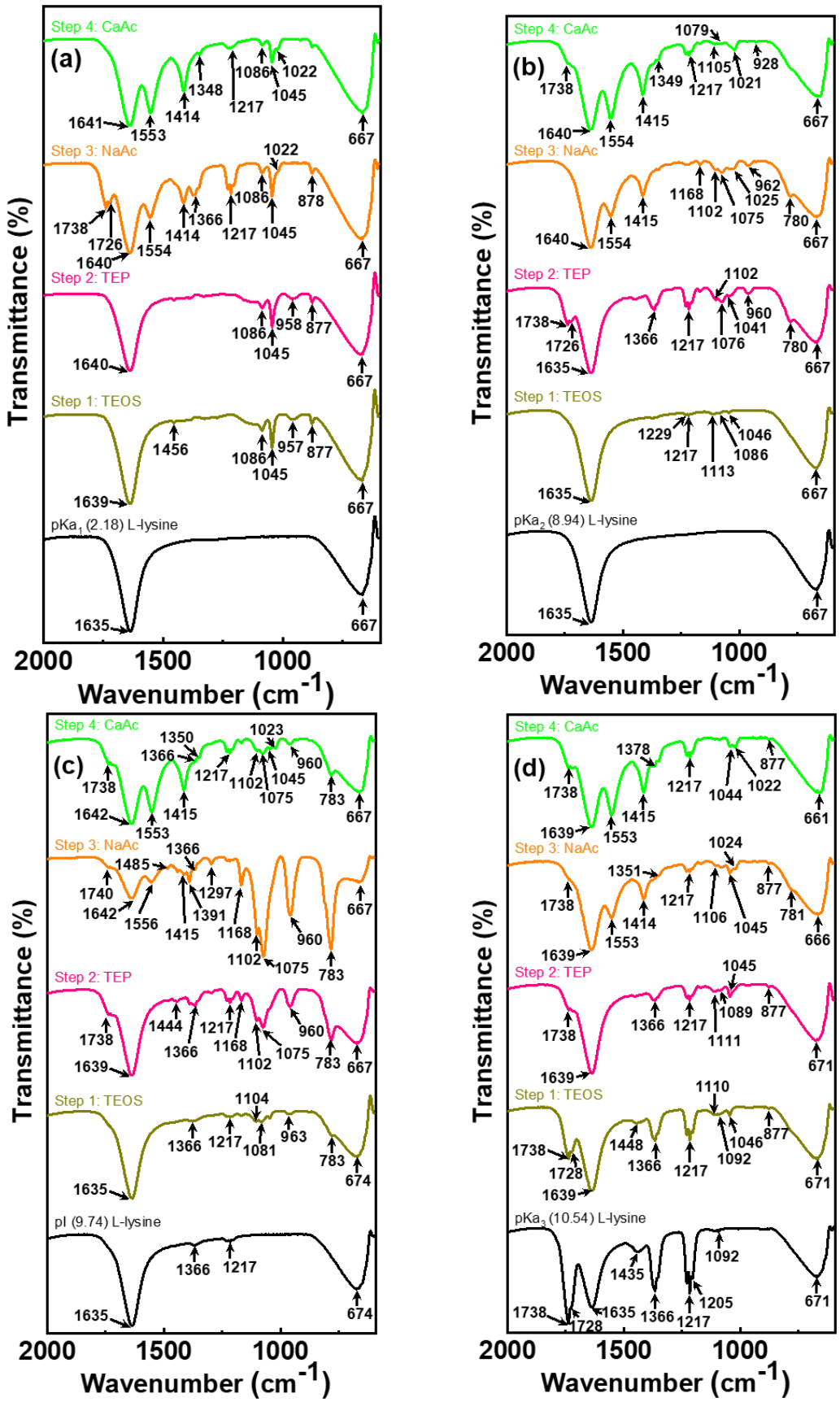

Fig. 3.2 (a-d): Step-wise FTIR spectrum during the synthesis of **(a)** LBG_2.18, **(b)** LBG_8.94, **(c)** LBG_9.74 and **(d)** LBG_10.54 xerogels.

or shift of existing peaks could be observed. This indicates no probable interactions between TEP with L-lysine and SiO_2 network. Post addition of NaAc (**Fig 3.2a (Step 3)**), along with the characteristic C=O stretching peak at 1640 cm^{-1}, additional peaks were observed in the form of a doublet at higher wavenumbers (1738 cm^{-1} and 1726 cm^{-1}) and a singlet at 1554 cm^{-1}. While the doublet may be attributed to chemical interaction of L-lysine with BG precursors, the singlet may have appeared as a result of —OH bending of carboxylic group of L-lysine and silanol groups (Si—OH) from SiO_2 network. It is noteworthy that peaks appearing in the range of 1260 cm^{-1} to 1180 cm^{-1} due to P—H bending, P=O stretching and at 1022 cm^{-1} due to P—H bending, P—O—C were reported comparing to previous step 2. As observed in step 1 and step 2 **(Fig 3.2a)**, peaks at 877 cm^{-1} and 667 cm^{-1} due to —N—H wagging were also seen in step 3. On addition of CaAc (**Fig 3.2a (Step 4)**), most of the peaks of step 3 (**Fig 3.2a)** were retained with the disappearance of few peaks around 1730 cm^{-1} (C=O stretching) and 1366 cm^{-1} (C—H stretching) probably due to completion of bioactive glass network formation through interaction of BG precursors with L-lysine. Based on **Fig 3.2a**, it can be concluded that at pKa_1, bioactive glass precursors interact with carboxylic group (—COOH) of L-lysine through chemical as well as physical interaction. Due to rapid hydrolysis and condensation of TEOS at highly acidic environment [26,27], its interaction with L-lysine is instantaneous.

At pKa_2 (pH 8.94), L-lysine solution (**Fig 3.2b (L-lysine_8.94)**) shows similar peaks as at pKa_1 (**Fig 3.2a (L-lysine_2.18**). In step 1, due to the addition of TEOS (**Fig 3.2b (Step 1))**, peaks with very weak intensity could be observed in the range of 1400 cm^{-1} to 1020 cm^{-1} indicating feeble interaction of TEOS with L-lysine due to its slow hydrolysis at pH 8.94 [27]. Addition of TEP (**Fig 3.2b (Step 2)**) originated a variety of new peaks.

Notably, peaks appearing at 1738 cm^{-1} and 1726 cm^{-1} confirmed the chemical interaction of C=O group of L-lysine with added precursors. Peaks at 780 cm^{-1} and 667 cm^{-1} uniquely observed at pKa_2 indicates the presence of —N—H wagging from —NH_3^+ group of L-lysine. In **Step 3 (Fig 3.2b),** on addition of NaAc, —C=O stretching peak at 1635 cm^{-1} **(Fig 3.2b (Step 2))** shift to slightly higher wavenumber at 1640 cm^{-1} due to weak physical interaction with the BG precursors. A noticeable new peak appeared at 1554 cm^{-1} due to —OH bending of silanol groups (Si—OH) of SiO_2 network. On addition of CaAc (**Fig 3.2b (Step 4)**), peak seen in **Fig 3.2b (Step 2)** at 1738 cm^{-1} reappeared indicating the interaction of Ca^{2+} ion with the carboxylate ion (COO^- group) of L-lysine at pKa_2. Peaks at 1105 cm^{-1} and 1079 cm^{-1} showed a slight decrease in intensity and a shift towards higher wavenumber compared to **Fig 3.2b (Step 3).** These results indicate the interaction of Ca^{2+} ions with the phosphate and SiO_2 group of bioactive glass network.

At pI (9.74) (Fig 3.2c L-lysine_9.74), the conversion of NH_3^+ group attached to the α-carbon of L-lysine to NH_2 group was reported by appearance of new peaks at 1366 cm^{-1} (C—H rocking) and 1217 cm^{-1} (C—N stretching, C—O stretching) compared to previous observations (**Fig 3.2a (L-lysine_2.18) and 3.2b (L-lysine_8.74))**. In addition, peak at 667 cm^{-1} due to —N—H wagging was shifted to higher wavenumber at 674 cm^{-1}. On addition of TEOS **(Fig 3.2c (Step 1))** and TEP **(Fig 3.2c (Step 2))** peaks observed were more or less similar compare to pKa_2 (8.94) **(Fig 3.2b (Step 1 and Step 2))**, except the peak at 674 cm^{-1}**(Fig 3.2c (Step 1))** shifted to 667 cm^{-1} **(Fig 3.2c (Step 2))** conforming interaction of BG precursors to N—H bond of L-lysine. When NaAc was added **(Fig 3.2c (Step 3)),** peaks in the range of 1500 cm^{-1} to 1340 cm^{-1} were uniquely present. Intensity of the peaks in the range of 1250 cm^{-1} to 900 cm^{-1} increased drastically, highest compare to that observed in case of various pKa values. Such an observation indicates that addition

of mono-cationic network modifier (Na^+ ions) distorts the silica network and results in formation of non-bridging oxygen (SiO^-) together with the surface active silanols (Si-OH) groups. Further, due to the addition of CaAc (**Fig 3.2c (Step 4))**, the increased intensity of peaks in step 3 (**Fig 3.2c Step 3)** decreased indicating the replacement of Na^+ by Ca^{2+} from non-bridging oxygens of bioactive glass network.

At pKa_3 (10.54) L-lysine solution (**Fig 3.2d (L-lysine_10.54)**) showed a completely different FTIR spectrum compared to other PKa and pI values. This could be due to conversion of ammonium ion (NH_3^+) to amine group (NH_2) as well as change in net surface charge on L-lysine as -1. Stepwise addition of other precursors TEOS (**Fig 3.2d (Step 1)**), TEP (**Fig 3.2d (Step 2)**), NaAc (**Fig 3.2d (Step 3)**) and CaAc (**Fig 3.2d (Step 4)**) showed more or less similar observations from previous cases. Overall, it can be concluded that, the interaction of bioactive glass precursor was observed at both the carboxylate group as well as amine group of L-lysine at pI and pKa_3 values and participation of L-lysine in bioactive glass network formation is clearly evidenced.

The FTIR spectra of dry LBG xerogels (**Fig 3.3(a))** portrayed most of the characteristic L-lysine peaks with significant shift indicating its interaction with the bioactive glass network. In addition, for LBG_2.18 **(Fig 3.3a)** peaks originated in the range of 990 cm^{-1}—900 cm^{-1} was reported due to the P—O—C, P—O—Si, P—H stretching and peak at 623 cm^{-1}(P—O bending) showed the participation of the phosphate group in the silicate network. Some of the characteristic bioactive glass peaks observed at 1061 cm^{-1} (Si—O—Si, Si—O—C, Si—O^- stretching), 797 cm^{-1}, 700 cm^{-1}— 600 cm^{-1} (Si—O—Si) and 470 cm^{-1} (Si—O—Si) confirmed bioactive glass formation [33,34]. More or less similar results were reported for LBG_8.94, LBG_9.74 and LBG_10.54. Interestingly, additional peaks observed at 878 cm^{-1} and 744 cm^{-1} for —N—H wagging in the case of

LBG_10.54 (**Fig 3.3a**) indicated interaction of bioactive glass network with the amine group of L-lysine.

3.3.2. X-Ray Diffraction Analysis (XRD):

LBG xerogels at various pKa and pI values were investigated through XRD analysis (**Fig 3.3b**). For LBG_2.18 (**Fig 3.3b**), XRD shows sharp intense diffraction maxima at 2θ values as: 10.94° (100), 16.02° (-101), 22.80° (200), 25.32° (-201), 27.16° (201), 28.66° (210), 29.84° (-220), 31.20° (-1-12), 32.64° (121), 33.96° (-310), 35.88° (-301), 44.86° (302), 48.70° (3-31) which indicate the crystalline nature of the xerogel. The reported diffraction maxima corresponds to

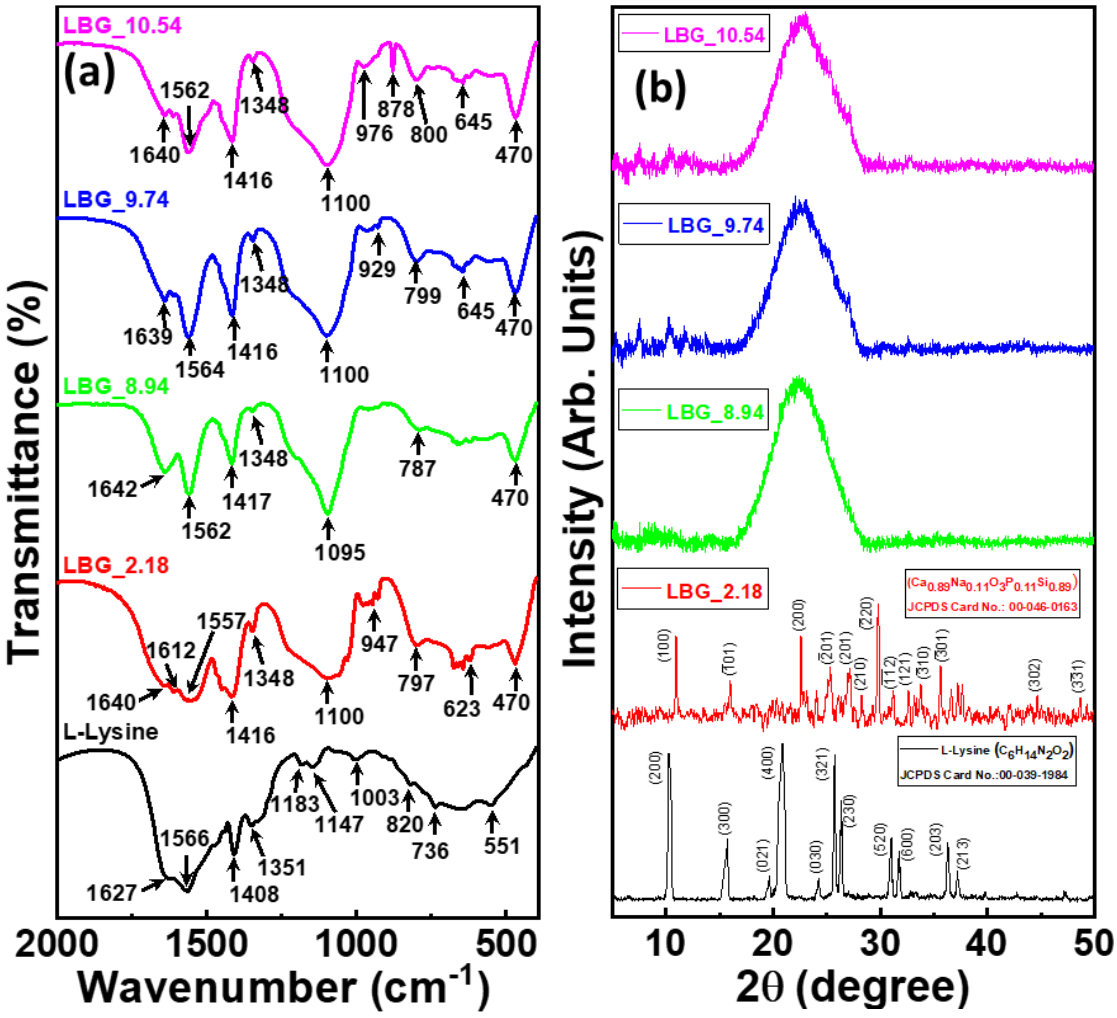

Fig. 3.3: (a)FTIR and **(b)** XRD spectra of L-lysine and LBG xerogels.

$Ca_{0.89}Na_{0.11}O_3P_{0.11}Si_{0.89}$ phase of JCPDS file No. 00-046-0163 and is reported for bioactive glass elsewhere [28,29,35]. The mean size of coherently diffracting domains of LBG_2.18 nanocrystals was calculated as 49.6 ± 1.2 nm by the Debye-Scherrer equation [30]. In contrast, XRD pattern (**Fig 3.3b**) of LBG_8.94, LBG_9.74 and LBG_10.54 showed only a broad hump in 2θ range of 15° to 30° indicating their amorphous nature.

3.3.3. Thermogravimetric Analysis (TGA):

Fig 3.4 portrays TGA thermograms of L-lysine and various LBG xerogels. The initial weight loss (7.6 %) at 65 °C was followed by a gradual weight loss of 28 % till 376 °C for L-lysine. This is due to the evaporation of surface and sorbed water respectively. Additionally, second weight loss observed from 376 °C to 475 °C (90 %) indicated decomposition of L-lysine molecules. At 659 °C, 100 % weight loss of L-lysine was reported. The weight loss due to evaporation of surface water was reported around 90 °C for LBG_2.18 (24 %) and LBG_9.74 (14 %) while for LBG_10.54 (18%), it was at 80 °C. Further, a gradual weight loss is reported upto 344 °C for LBG_9.74 as well as LBG_10.54 and upto 374 °C for LBG_2.18. Herein, the gradual weight loss is attributed to the evaporation of sorbed water into the pores of LBG xerogels. Interestingly, in case of LBG_2.18 highest temperature (374 °C) was required to remove the water content compared to other xerogels. The observation indicates the existence of water molecules inside the BG network. A sharp dip showing around 50% weight loss for xerogels LBG_2.18, LBG_9.74 and LBG_10.54 above 420 °C indicated the decomposition of bounded L-lysine from the bioactive glass network. This confirms the retention of L-lysine molecules in LBG xerogels. The temperature upto which L-lysine decomposes was noticed for LBG_9.74 as 499 °C, LBG_10.54 as 460 °C and LBG_2.18 as 424 °C. The reported higher temperature for decomposition of L-lysine from LBG_9.74 and

LBG_10.54 indicates a strong interaction between the BG network and L-lysine through carboxylate and amino groups compared to LBG_2.18.

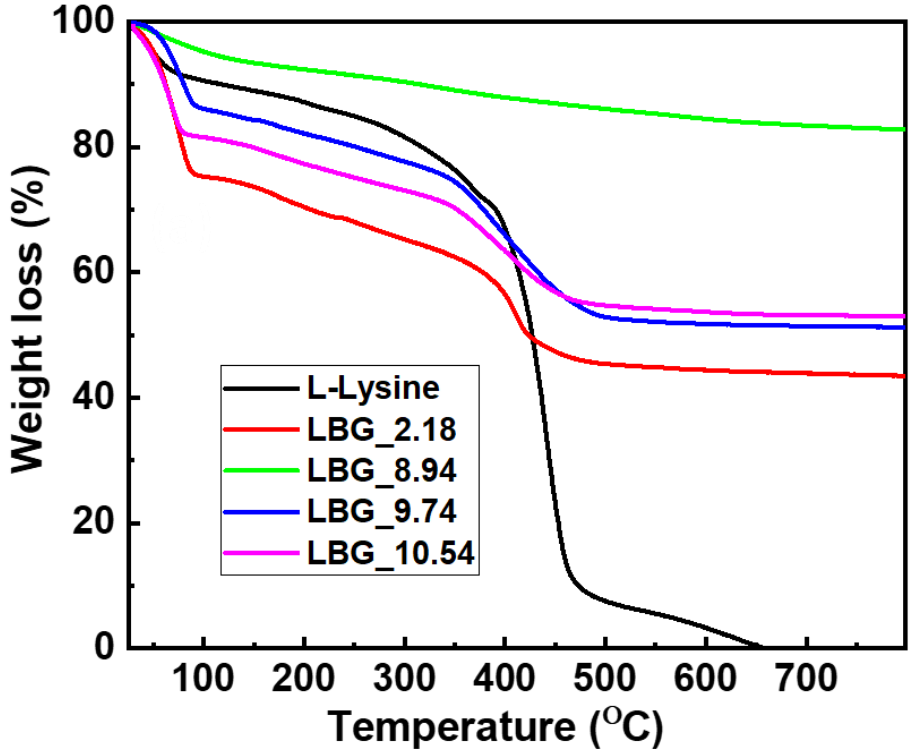

Fig. 3.4: Thermogravimetric analysis of L-lysine and LBG xerogels

These observations are in good agreement with FTIR data (**Fig 3.2**). The residual weight at 800 °C observed for LBG_10.54 (54 %), LBG_9.74 (51 %) and LBG_2.18 (44 %) indicated minimum thermal stability of LBG_2.18. The decrease in thermal stability of LBG_2.18 is due to the existence of more surface silanol groups (Si—OH) as observed from FTIR analysis **(Fig 3.3a)**. Interestingly, for LBG_8.94, minimal weight loss was observed due to water loss as well as L-lysine decomposition. Further the residual weight (83 %) obtained at 800 °C was the maximum for LBG_8.94 compared to other xerogels indicating its highest thermal stability. The observation also revealed that at pH 8.94, slow hydrolysis of bioactive glass precursor (TEOS) results in molecular level interaction between L-lysine and BG precursors. Such interactions between template - BG precursors ultimately leads to the nucleation of LBG nanoparticles as we evidenced in

our earlier reports through bioinspired route [29].

3.3.4 Elemental Analysis:

The compositions of these LBG hybrids were analyzed using ICP-MS (for Si, P, Ca and Na) and CHNSO (for C, N and H) and results are portrayed in **Table 3.1 and Table 3.2**. As per the analysis 33.8 ± 1.6 w/w %, 52.3 ± 1.7 w/w %, 35.5 ± 1.1 w/w % and 36.8 ± 1.4 w/w % were inorganic contents (Si, P, Ca and Na) of LBG_2.18, LBG_8.94, LBG_9.74 and LBG_10.54 respectively. And 31.2 ± 0.8 w/w %, 9.3 ± 0.8 w/w %, 30.8 ± 1.3 w/w % and 26.6 ± 0.7 w/w % were of organic contents (C, N and H) reported from LBG_2.18, LBG_8.94, LBG_9.74 and LBG_10.54 respectively. These observations are in more or less good agreement with the residual weights observed in TGA analysis **(Fig. 3.4).** These findings confirm the existence of L-lysine molecule in bioactive glass network. Interestingly, observed mole % of inorganic contents **(Table 3.2)** of the reported xerogels revealed more or less similar composition to 45S5 bioglass for LBG_8.94 and

Table 3.1: Elemental composition of various LBG xerogels using ICP-MS (for Si, P, Ca and Na) and CHNSO (for C, N and O).

	Various Elements	**Experimental Values (w/w %)**			
		LBG_2.18	**LBG_8.94**	**LBG_9.74**	**LBG_10.54**
CHNSO	**Carbon (C)**	19.9 ± 0.4	5.8 ± 0.8	19.4 ± 1.2	16.6 ± 0.5
	Nitrogen (N)	7.7 ± 0.3	2.2 ± 0.2	7.5 ± 0.4	6.4 ± 0.5
	Hydrogen (H)	3.9 ± 0.6	1.1 ± 0.1	3.8 ± 0.3	3.2 ± 0.2
	Total Organic Content	31.2 ± 0.8	9.3 ± 0.8	30.8 ± 1.3	26.6 ± 0.7
ICP-MS	**Silicon (Si)**	12.5 ± 1.1	18.6 ± 0.7	12.7 ± 0.5	13.9 ± 1.0
	Phosphorous (P)	1.6 ± 0.4	2.3 ± 0.2	1.6 ± 0.4	1.7 ± 0.1
	Calcium (Ca)	10.4 ± 0.6	15.4 ± 0.9	10.6 ± 0.6	11.6 ± 0.8
	Sodium (Na)	10.8 ± 0.9	16.0 ± 1.3	11.0 ± 0.7	12.0 ± 0.6
	Total Inorganic Content	33.8 ± 1.6	52.3 ± 1.7	35.5 ± 1.1	36.8 ± 1.4

Table 3.2: Comparative inorganic chemical composition in mole % of various LBG xerogels with 45S5 bioglass.

	Calculated (mole %)	**Observed (mole %)**			
Units	**45S5**	**LBG_2.18 (mole %)**	**LBG_8.94 (mole %)**	**LBG_9.74 (mole %)**	**LBG_10.54 (mole %)**
SiO_2	46.1	55.0 ± 1.1	45.6 ± 1.3	45.8 ± 1.2	59.4 ± 1.4
P_2O_5	2.6	2.3 ± 0.1	2.7 ± 1.0	2.6 ± 0.3	2.8 ± 0.2
CaO	26.9	21.7 ± 1.0	26.9 ± 1.3	25.4 ± 1.1	20.0 ± 0.6
Na_2O	24.3	20.5 ± 1.1	24.5 ± 1.4	25.0 ± 1.2	17.1 ± 0.4
Total	100.0	99.5 ± 1.8	99.7 ± 2.5	98.8 ± 2.0	99.2 ± 1.6

LBG_9.74. On the other hand, mole % of SiO_2 was found be higher for LBG_2.18 (55.0 ± 1.1 mole %) and LBG_10.54 (59.4 ± 1.4 mole %) compare to other inorganic components of xerogels due to the rapid hydrolysis of TEOS.

3.3.5. Morphological Analysis:

FE-SEM analysis revealed the particle size and morphology of bioactive glass xerogels (LBG_2.18, LBG_8.94, LBG_9.74 and LBG_10.54) **(Fig 3.5(a-d) and Fig 3.6)**. For LBG_2.18 **(Fig 3.5a)**, nanoparticle embedded denser surface morphology was observed with mean particle size 73.4 ± 14.0 nm. Herein, observed size of embedded particles in LBG_2.18 matrix higher than the mean size of coherently diffracting domains (49.6 ± 1.2 nm **Fig 3.3b**) calculated by the Debye-Scherrer equation [30]. Whereas, with increase in L-lysine pH to 8.94 and pH 9.74 individual nanoparticles are reported with increase in particle size 66.8 ± 14.3 nm (LBG_8.94) to 124.9 ± 28.7 nm (LBG_9.74). Herein, size of nanoparticles was analysed by image J analysis software **(Fig 3.6)**. Once again, surface

morphology became denser in case of LBG_10.54 with particle size 84.4 ± 18.0 nm. These observations indicated variations in the morphology of LBG xerogels which are primarily dependant on the rate of hydrolysis and condensation of TEOS. The rapid hydrolysis and condensation of TEOS at extreme acidic (pKa_1 2.18) and alkaline (pKa_3 10.54) pH values lead to denser surface morphology due to the extended BG network. In contrast, slower TEOS hydrolysis might favour L-lysine-TEOS molecular-molecular interaction and results in nanosized LBG particles.

Interestingly, reported higher particle size of LBG_9.74 indicated faster TEOS hydrolysis at pH 9.74 compared to LBG_8.94 at pH 8.94. EDAX analysis (data not shown) revealed the existence of Si, P, Ca and Na in BG network. The HR-TEM results **(Fig. 3.5(e-h))** are in good agreement with FE-SEM and corresponding SAED pattern of LBG_2.18 (**Fig**

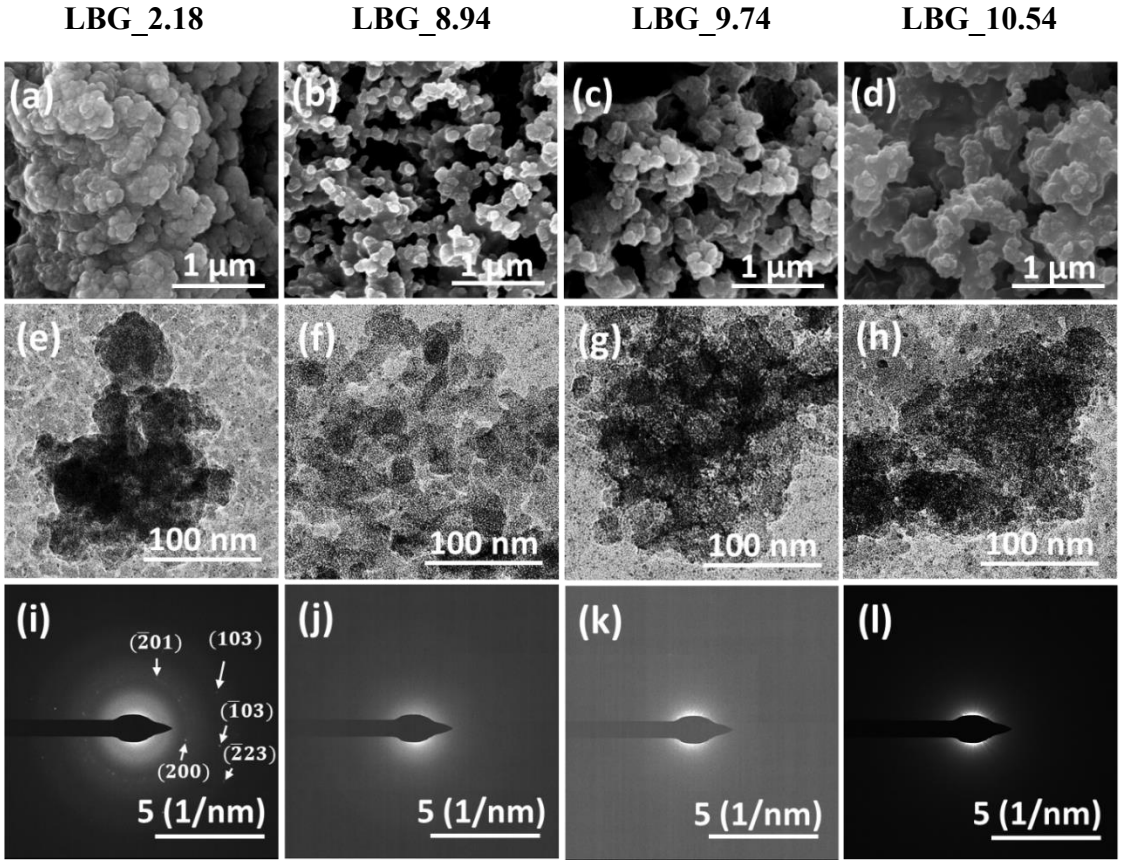

Fig. 3.5: (a-d) SEM micrographs, (e-h) HR-TEM micrographs and (i-l) showing TEM SAED pattern of various LBG xerogels.

3.5i) confirmed its crystalline nature. Whereas, LBG_8.94 **(Fig 3.5j)**, LBG_9.74 (**Fig 3.5k)** and LBG_10.54 (**Fig 3.5l)** xerogels revealed amorphous nature as evidenced by XRD **(Fig 3.3b)**.

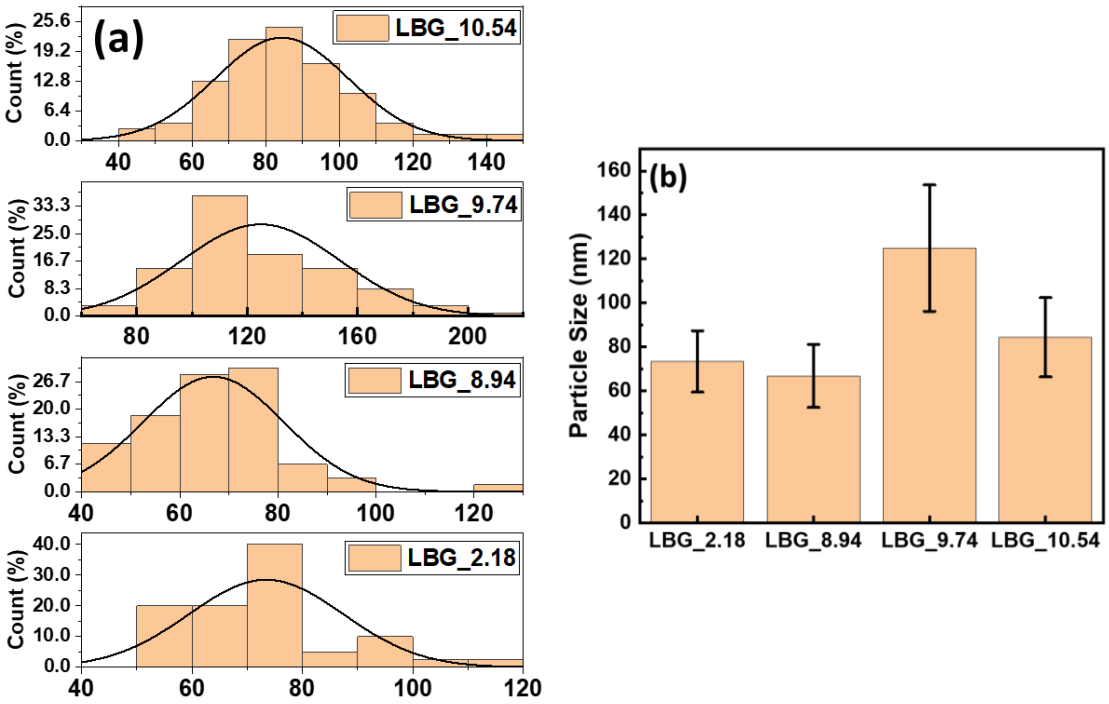

Fig 3.6: Average particle diameter of samples understudy through FE-SEM using ImageJ analysis software (ImageJ bundled with 64-bit Java 1.8.0_172).

3.3.6. Nitrogen sorption Analysis:

N_2 adsorption–desorption isotherms of various xerogels along with their pore size distribution is portrayed in **Fig 3.6(a-d).** Surface area, pore volume and pore size data are listed in **Table 3.3**. LBG_2.18 and LBG_10.54 showed type IV isotherm. The observations indicate that the xerogels formed at pKa_1 and pKa_3 are mesoporous in nature showing strong interaction. The hysteresis loop is of type H2 showing pores with narrow as well as wide section and interconnected region of pores. These findings confirm the existence of continuous BG network for LBG_2.18 and LBG_10.54. Type V isotherm was identified for LBG_8.94 and LBG_9.74, which indicate mesoporous nature of xerogels with weak interaction. The reported hysteresis loop belongs to type H1 showing

both xerogels contain mesopores without interconnected regions indicating discontinuity in BG network. The pore size distribution analysis carried out by BJH method further confirmed the existence of uniform sized mesopores of diameter 4.16 nm for LBG_2.18. On the other hand, multi sized mesopores with average diameter around 8 nm **(Table 3.3)** was reported for LBG_8.94, LBG_9.74 and LBG_10.54 xerogels. The calculated surface

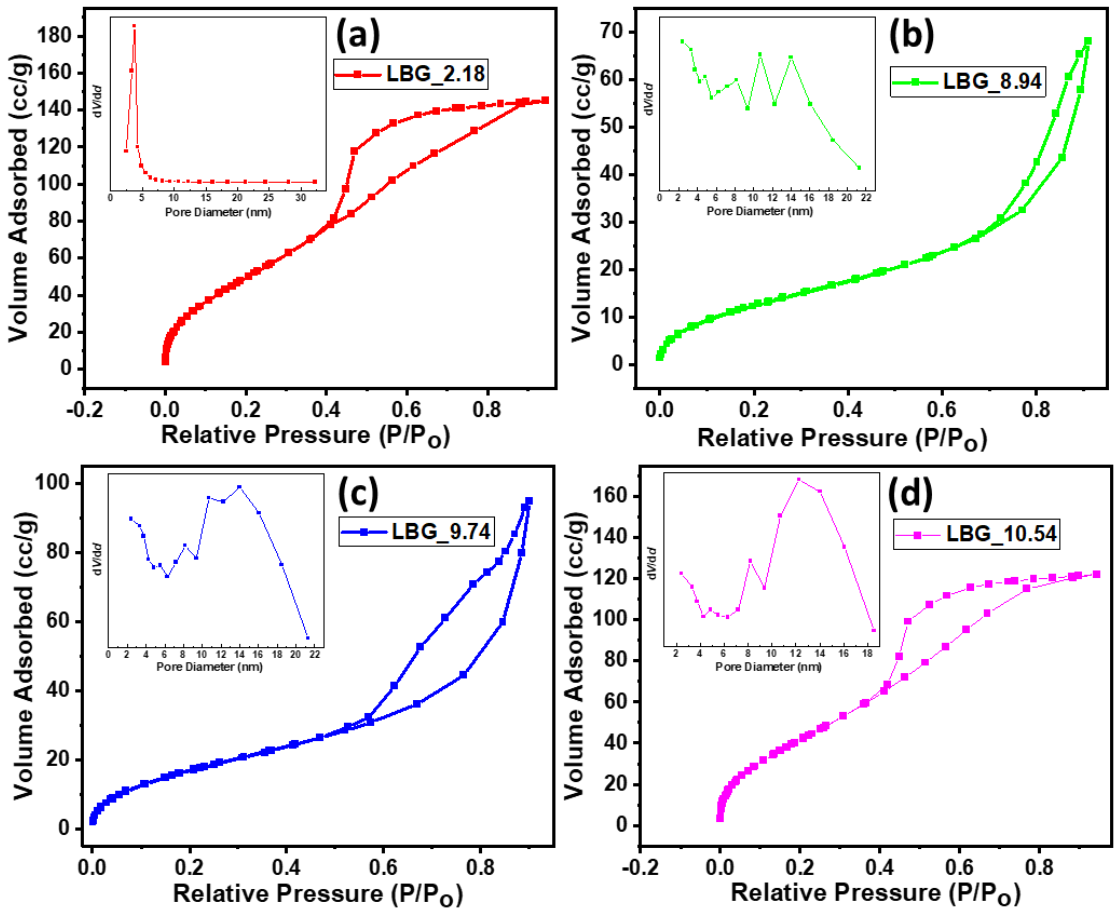

Fig. 3.7(a-d): Nitrogen adsorption-desorption isotherm and pore size distribution (inset) of xerogels.

Table 3.3: Surface area, pore volume and pore size data of xerogels.

	LBG_2.18	LBG_8.94	LBG_9.74	LBG_10.54
Total Surface Area ($a_{s,BET}$ [m^2 g^{-1}])	215.2	89.3	62.6	186.4
Total pore volume(p/p_0=0.944) [cm^3 g^{-1}]	0.2243	0.1052	0.1467	0.189
Mean pore diameter [nm]	4.1696	8.0054	8.4678	8.7554

area for LBG_2.18 and LBG_10.54 using BET was found higher (215.2 m^2/g and 186.4 m^2/g respectively) compared to LBG_8.94 and LBG_9.74 (89.3 m^2/g and 62.6 m^2/g respectively). These observations once again confirmed interconnected mesoporous continuous BG network for xerogels synthesized at pKa_1(2.18) and pKa_3(10.54) of L-lysine due to the rapid hydrolysis of silica precursor TEOS. Whereas, xerogels formed at pKa_2 (8.94) and PI (9.74) of L-lysine containing mesopores of without interconnection indicate the formation of clusters of BG network due to the slow hydrolysis of TEOS. Slightly higher surface area of LBG_8.94 compared to LBG_9.74 is due to its smallest particle size **(Fig 3.5b-c)**.

It is pertinent to mention that when dried blank gels, named BG_2.18 and BG_10.54 were subjected to FE-SEM, the corresponding surfaces were observed very smooth without any interesting morphological features. Also, the nitrogen sorption analysis revealed non-porous nature of the samples (data not shown).

3.3.7. Rheological Analysis:

The storage modulus (G') and loss modulus (G'') for freshly prepared LBG gels were examined as a function of shear strain **(Fig 3.8a-b)** and angular frequency **(Fig 3.8c-d)**. In general, for all gel samples storage modulus were reported to be independent to shear strain in the range of 0.01 % to 2.17 % **(Fig 3.8a)**. This is followed by a decrease in storage modulus with increase in shear strain beyond 2.17 % **(Fig 3.8a**) indicating breakage of BG network. On the other hand, storage modulus remains constant with increase in angular frequency for the chosen scan range 0.1 rad/sec to 100 rad/sec **(Fig 3.8c)**. Among all samples, LBG_2.18 shows highest value for G' evidencing its highest elastic nature with respect to shear strain as well as angular frequency due to the existence of continuous BG network. In contrast to this, observed lowest G' values indicate least

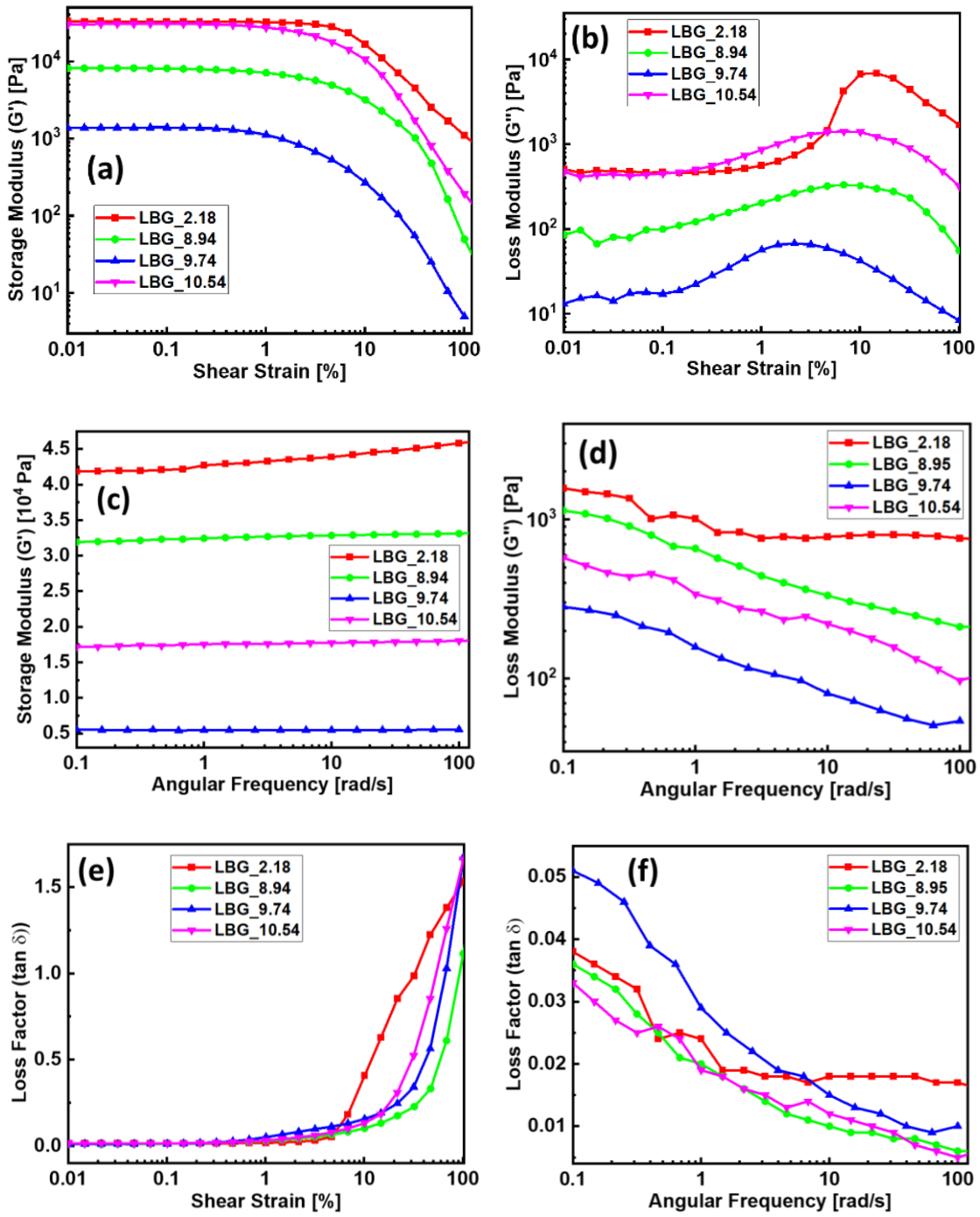

Fig. 3.8: (a-b) Amplitude sweep at constant frequency of 10 Hz, (c-d) Frequency sweep at constant strain of 1 Pa for storage modulus (G') and loss modulus (G") and (e) Loss factor v/s shear strain at constant frequency of 10 Hz (amplitude sweep), (f) Loss factor v/s angular frequency at constant shear strain of 1 Pa (Frequency sweep) of LBG xerogels by rheological analysis. of LBG xerogels by rheological analysis.

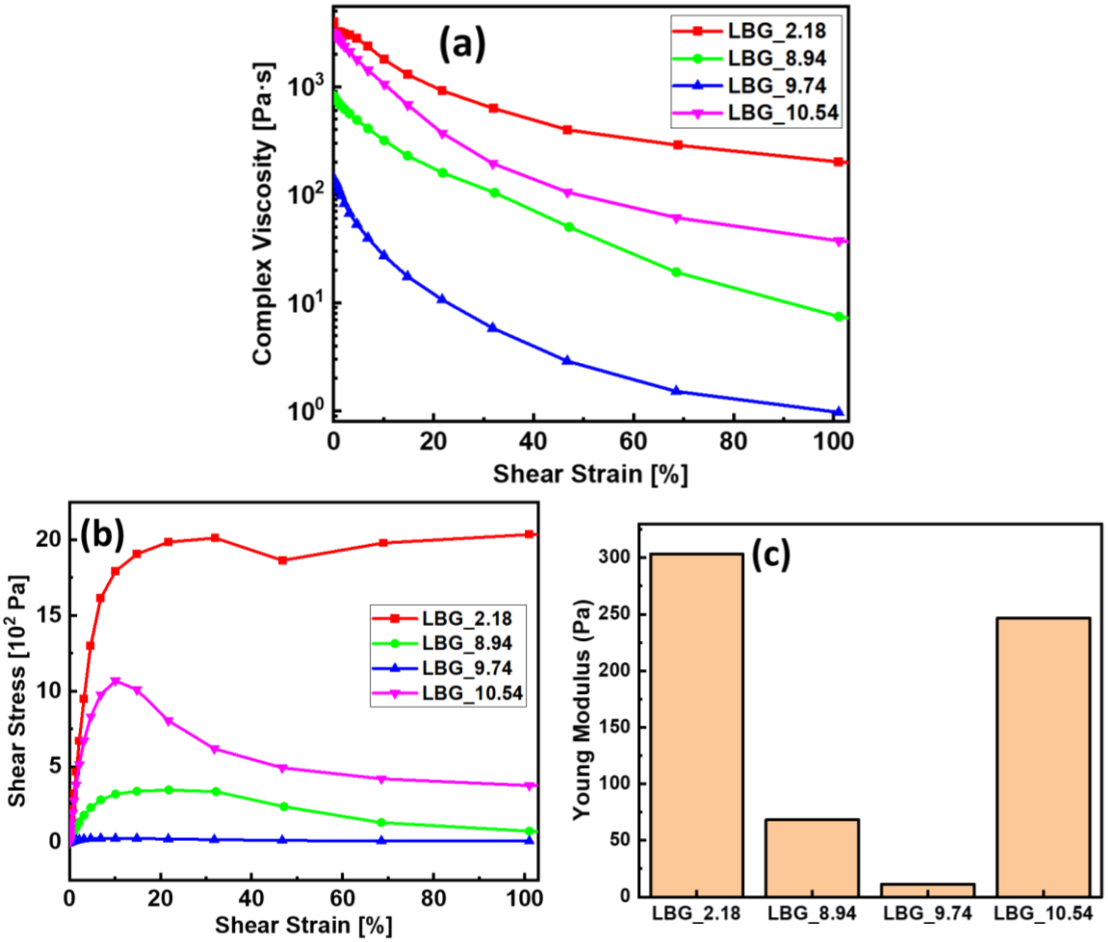

Fig. 3.9: (a) complex viscosity v/s shear strain, (b) shear stress v/s shear strain curve and (c) young modulus of LBG xerogels by rheological analysis.

elastic nature of LBG_9.74 resulting as a result of discontinuous BG network compared to other samples. The increasing elasticity of LBG samples can be arranged as: LBG_2.18 > LBG_10.54 > LBG_8.94 >> LBG_9.74. Herein, it is pertinent to recall findings of FE-SEM **(Fig. 3.5(a-d)**, where there exists continuous network morphology for LBG_2.18 and LBG_10.54. On the other hand, particles of size 65 nm and 120 nm were observed in the case of LBG_8.94 and LBG_9.74 respectively evidencing formation of BG gel clusters at pH 8.94 and pH 9.74 in the presence of L-lysine. Observed better elastic behaviour of LBG_8.94 compared to LBG_9.74 probably due to its nano-size compared to LBG_9.74. The reported storage modulus trends of LBG xerogels as a function of shear strain **(Fig 3.8a)** and angular frequency **(Fig 3.8c)** are also in good agreement with

complex viscosity data as a function of shear strain **(Fig. 3.9a)**. In **Fig 3.8b** loss modulus (G'') of LBG samples increases with increase in shear strain indicating increase in their fluidity nature and promise their applicability as injectable gels **(Fig 3.10).** In contrast, a slight decrease in G'' values were observed with increase angular frequency **(Fig 3.8d)**, which show an increase in the elastic nature of LBG sample evidencing intact BG network. Loss factor i.e., tan (δ) values were reported less than 1 with increase in angular

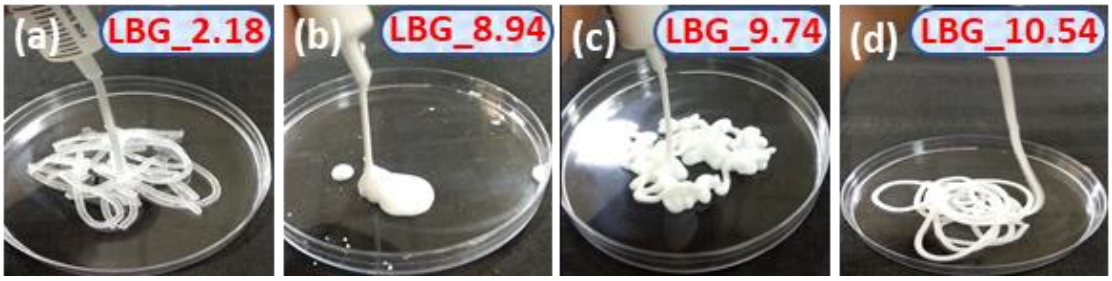

Fig. 3.10: Digital photographs showing injectable property of freshly formed xerogels.

frequency **(Fig 3.8f)** confirms the solid character of LBG. On the other hand, with increase shear strain tan (δ) values become greater than 1 once again proving the shear thinning behaviour of LBG samples **(Fig 3.8e)**. The stress-strain behaviour **(Fig 3.9b)** showcased LBG_2.18 and LBG_10.54 to be more mechanically robust (hard and tough) when compared to LBG_8.94 and LBG_9.74 (relatively softer and mechanically weaker). The corresponding young's modulus data **(Fig 3.9c)** were also in good agreement with the stress-strain behaviour of xerogels. The observed contrast in mechanical behaviour of LBG_2.18 and LBG_10.54 as well as LBG_8.94 and LBG_9.74 is due to the existence of continuous and discontinuous (gel clusters) BG network respectively.

3.3.8. *In-vitro* Bioactivity:

Apatite forming ability of various LBG xerogels was monitored in SBF by FTIR, XRD and FE-SEM analysis (**Fig 3.11**). FTIR spectrum of xerogels after 4 days, 9 days and 15 days interaction with SBF are portrayed in **Fig 3.11(a-c).** Interestingly, during the

interaction with SBF, the characteristic peaks of L-lysine in LBG samples (**Fig 3.3a)** were either become weak in intensity or disappeared with simultaneous appearance of HAP peaks. From **Fig. 3.11a** characteristic FTIR peaks for phosphate (1100 cm^{-1}, 1200 cm^{-1}, 963 cm^{-1} and 467 cm^{-1}), carbonate (1416 cm^{-1} and 800 cm^{-1}) and hydroxyl groups (1634 cm^{-1}) were seen. This is due to the deposition of HAP onto the surface of LBG xerogels after 4 days of interaction with SBF [15,33,34,36,37]. Further, these characteristic HAP peaks of xerogels after 4 days were increased in intensity as the interaction time increased with SBF for 9 days and 15 days. Similarly, after 4 days of immersion in SBF, XRD analysis (**Fig. 3.11d**) of LBG xerogels reported a few new diffraction maxima along with the broad hump, (2θ range of 15° to 30°). Post 15 days interaction of xerogels with SBF in case of LBG_2.18, LBG_8.94 and LBG_9.74. the intensity of the newly emerging diffraction maxima increases significantly along with many new diffraction maxima. These new XRD diffractions indicated interfacial activity on LBG surface when in contact with SBF. The observed reflections in the corresponding XRD pattern refer to ($Ca_5(PO_4)_3(OH)$) as per the JCPDS file no. 00-024-0033. This reveals that the formed microcrystals on the surface of the xerogels after interaction with SBF are of bone-like HAP. Slower deposition of HAP found in the case of LBG_2.18 validates its higher SiO_2 content (55.0 ± 1.1) compared to LBG_8.94 and LBG_9.74 (**Table 3.2)**. In case of LBG_10.54, on 15^{th} day, only the intensity of the peak at 31.77° increased very slightly. This shows slow dissolution of the xerogel, which hampers the deposition of HAP due to its higher SiO_2 content (59.4 ± 1.4 mole%) compared to other inorganic components **(Table 3.2)**. Due to the HAP deposition, FE-SEM micrographs of LBG xerogels **(Fig. 3.11f-i)** after 15 days interaction with SBF showed very different rough surface morphology compared to the corresponding bare surface morphology of xerogels due to HAP deposition (**Fig. 3.5a-d).** It is noteworthy that LBG_2.18 and LBG_10.54 showed

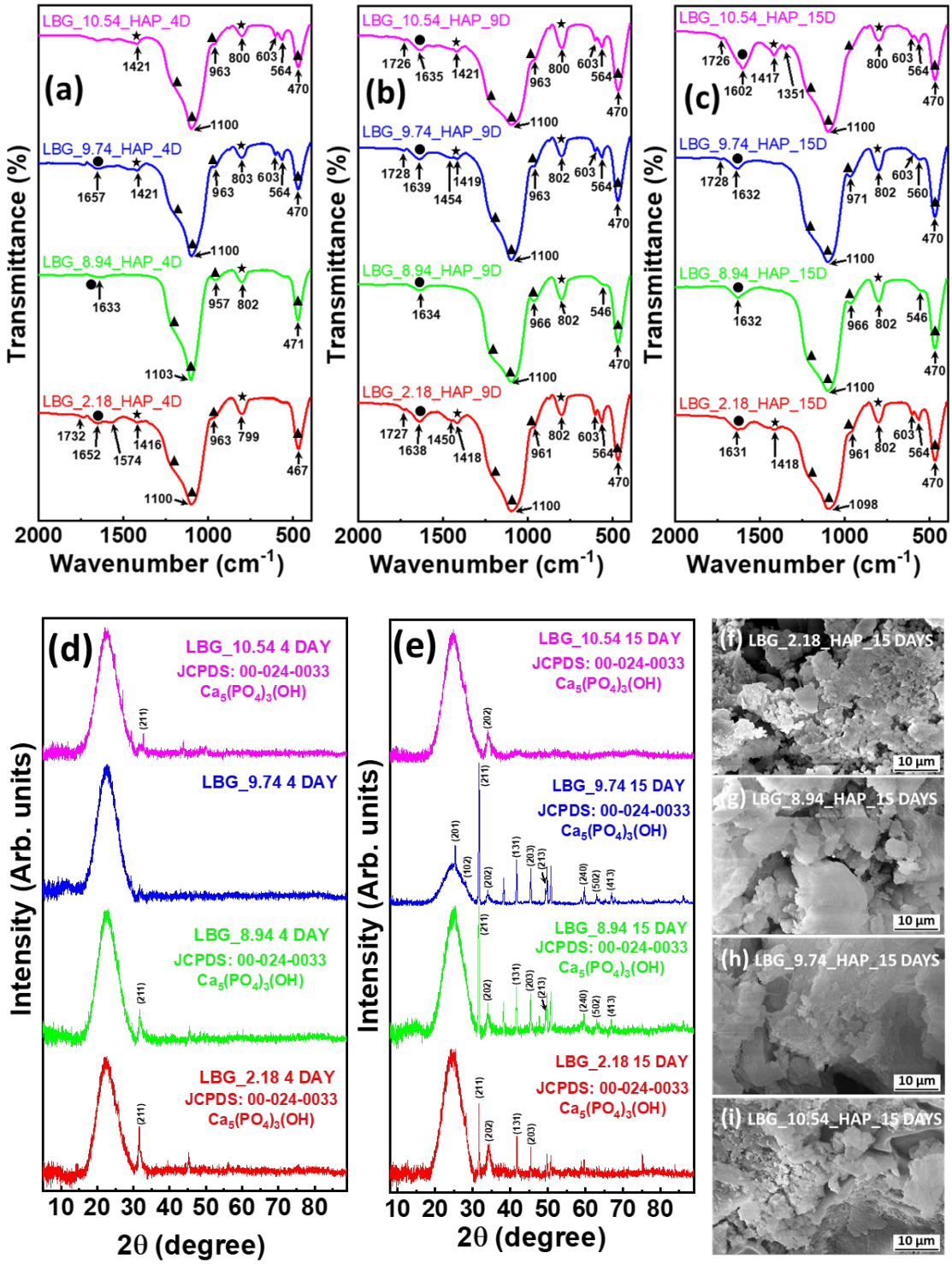

Fig. 3.11: Bioactivity analysis by FTIR spectra **(a – c)** (**(a)** 4 days, **(b)** 9 days and **(c)** 15 days) (●: OH^-; ★: CO_3^{2-}; ▲: PO_4^{3-}), XRD pattern **(d-e)** (**(d)** 4 days and **(e)** 9 days as well as SEM images **(f-i)** 15 days at 5 KX of LBG xerogels on interaction with SBF.

thin layer of HAP deposition compared to other xerogels and supported the findings of XRD results **(Fig. 3.11d-e)**. In general, rapid HAP deposition on LBG samples was

mainly due to their mesoporosity induced by L-lysine molecules. On the other hand, BG_2.18 and BG_10.54 (Blank samples) were shown feeble deposition of HAP even after interaction with SBF for 15 days (data not shown).

3.3.9. Drug release kinetics:

Encapsulation efficiency % of 7-dehydrocholesterol on LBG xerogels was reported as 95.6 % (LBG_2.18), 90.2% (LBG_10.54), 82.3 % (LBG_8.94) and 79.1 % (LBG_9.74) at 4 h and remained almost similar till 24 h. The observed 7-dehydrocholesterol encapsulation data are in good agreement with findings of nitrogen sorption analysis **(Table 3.3)**. The corresponding 7-dehydrocholesterol release was also observed from

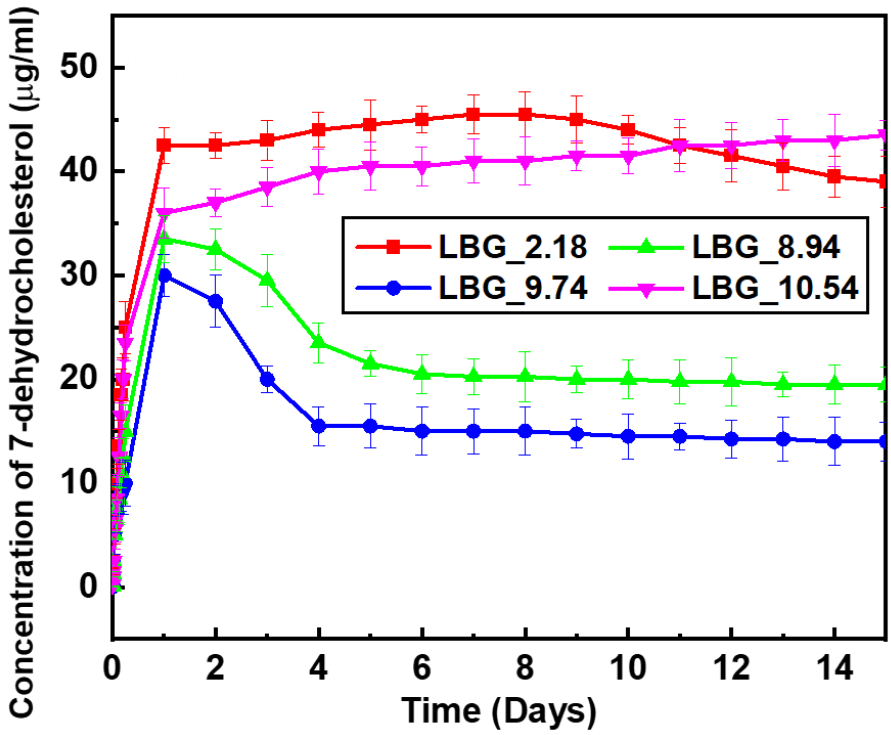

Fig. 3.12: Drug release profile of 7-dehydrocholesterol from LBG xerogels.

LBG xerogels **(Fig 3.12)** in SBF till 14 days. In general, LBG_2.18 and LBG_10.54 showed a burst release up to 24 h and continued more or less persistent up to 14 days. In comparison, though the drug release pattern of LBG_2.18 and LBG_10.54 are same,

amount of 7-dehydrocholesterol release was reported slightly higher for LBG_2.18 (42.5 ug/mL) compared to LBG_10.54 (36 ug/mL) for 24 h. Further, a slight dip in 7-dehydrocholesterol release from 45.5 ug/mL to 39 ug/mL was seen for LBG_2.18 after 7 days upto 14th day. These findings reveal higher rate of HAP deposition compared to LBG_10.54 leading to partial blockage of interconnected mesopores **(Fig 3.11)**. In the case of LBG_8.94 and LBG_9.74 also a burst release of vitamin D was reported up to 24 h. Thereafter a gradual decrease in drug release was seen up to 4 days for LBG_8.94 and LBG_9.74. This is once again due to the surface HAP formation **(Fig 3.11).** Beyond 4 days, drug release remained more or less constant up to 14 days. In general, the amount of drug released at 24 h and beyond by LBG xerogels can be arranged as LBG_2.18 > LBG_10.54 > LBG_8.94 > LBG_9.74. The reported trend in 7-dehydrocholesterol release is in good agreement with nitrogen sorption results **(Fig. 3.7).** It is pertinent to recall the interconnected mesoporous nature of LBG_2.18 and LBG_10.54 with high surface area compared to LBG_8.94 and LBG_9.74 as per the findings of nitrogen sorption. Hence, there results sustainable release of 7-dehydrocholesterol for a prolonged time upto 14 days in the case of LBG_2.18 and LBG_10.54 [31].

3.3.10. Interaction Mechanism:

In this study, the essential amino acid L-lysine is used as a structure directing molecule for BG xerogel network at various pH conditions. The pH conditions are maintained equal to pKa_1 (2.18), pKa_2 (8.94), pKa_3(10.54) and pI (9.74) values of L-lysine. At these pH conditions, L-lysine structure carries +2, +1, -1and 0 charges respectively **(Fig 3.1).** Based on the literature it is evidenced that the hydrolysis and condensation reactions of TEOS only depend on pH conditions [19]. Herein, hydrochloric acid (HCl) is used to maintain pH 2.18, which activate hydrolysis reaction of silica precursor very quickly

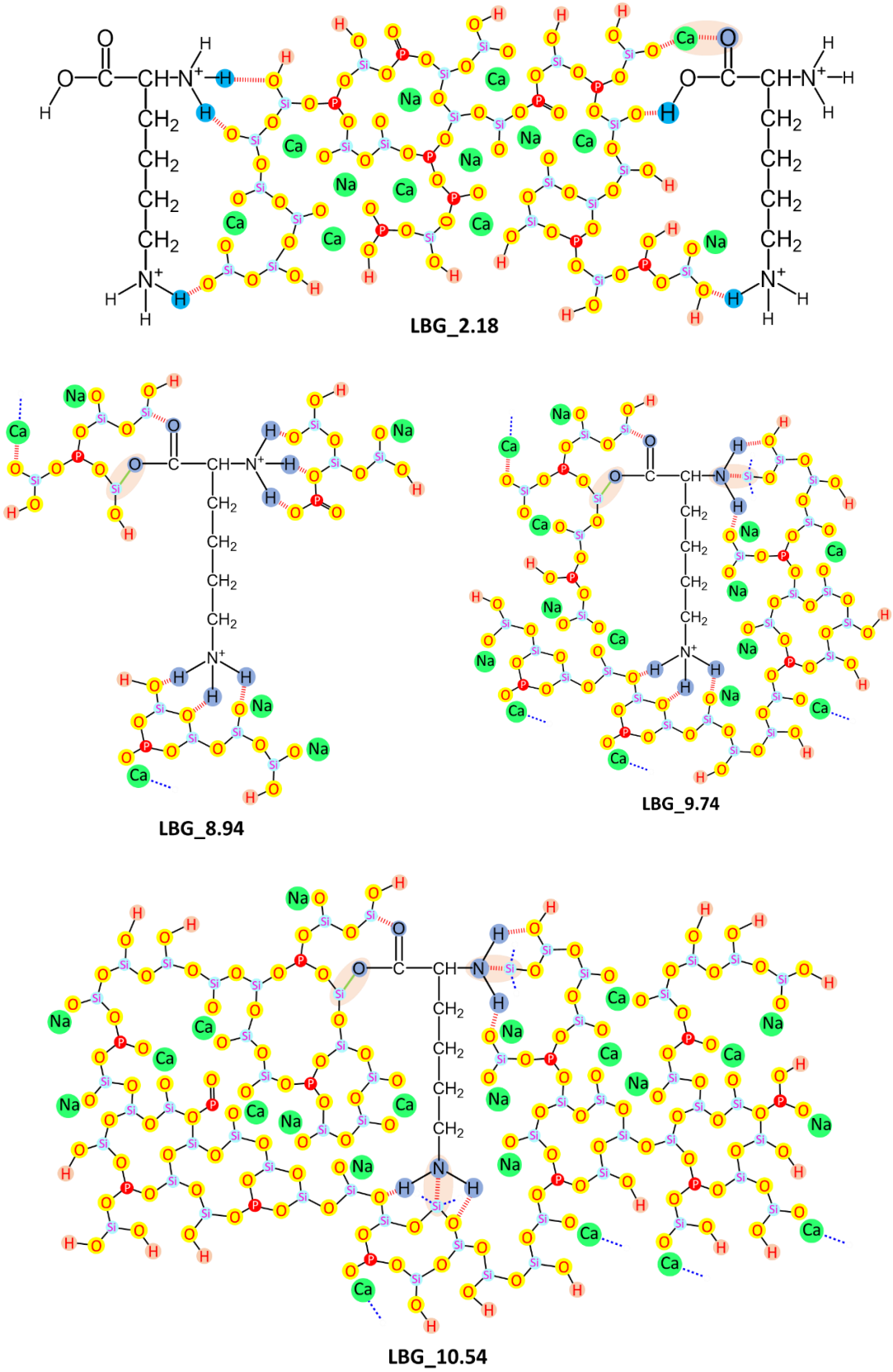

Fig. 3.13: Representative structures of LBG xerogels showing multi-centred interaction of L-lysine with bioglass network.

through interaction with positively charged L-lysine molecule as supported by FTIR studies **(Fig 3.3a)**. The observed heteronuclear interaction between BG network and L-lysine molecule regularized the orientation of the BG network by retaining organic molecules **(Fig 3.13).** As a result, a huge increase in surface area with interconnected mesopores was reported for LBG_2.18 as observed in BET analysis **(Fig. 3.7)**. Importantly, the retention of the L-lysine molecules in BG network induces highest viscoelasticity for LBG xerogel at pH 2.18 **(Fig 3.8 and Fig 3.9)**. Similarly, extreme alkaline pH condition (pH 10.54) maintained during the synthesis of LBG_10.54 using sodium hydroxide (NaOH) solution induces the formation of bulkier BG network through physicochemical interaction with L-lysine molecule. As a result the formation of viscoelastic mesoporous xerogel with high surface area was obtained at pH 10.54 **(Fig 3.8 and Fig 3.13).** In contrast, at pH 8.94, since hydrolysis of TEOS slowed down, nanosized BG clusters were formed around L-lysine molecule **(Fig 3.13)** as evidenced by FTIR, FE-SEM, nitrogen sorption and rheological analysis. This observation was almost similar for the xerogel prepared at pH condition 9.74 but with increase in the size of BG clusters **(Fig 3.13)**. In general, for all pH conditions maintained, LBG network/clusters were formed through chemical (complexation) and physical (electrostatic, hydrogen bonding and van der Waals) interactions with carboxylic (—COOH), carbonyl (—COO^{-}) and —NH_3^{+} groups of L-lysine and Si—O^{-}, Si—O—H and P—O groups of BG as shown by **Fig 3.13**.

3.4. Conclusion:

To the best of our knowledge a new class of degradable L-lysine-bioactive glass hybrid xerogels has been successfully synthesized at various pKa values and pI value of L-lysine through bioinspired method. The study showed that at each pKa and pI values of L-lysine the structural, thermal, morphological properties including elemental composition of

hybrid xerogels are unique. In detail, tailored mesoporosity of these LBG xerogels assures them as a suitable candidate for controlled drug delivery to regulate cellular behaviour. Further, the incorporation of L-lysine molecule through the interaction of the carboxylate as well as amine groups of L-lysine with the BG network induces viscoelastic property for LBG xerogels. The resulted viscoelastic nature of the LBG xerogels assures non-invasive injectable applications. The L-lysine content of the xerogels can also assist collagen formation by absorbing calcium during bone regeneration. Finally, the observed characteristic HAP forming ability of mesoporous LBG hybrid xerogels confirms their efficiency in bone regenerative applications. These findings on LBG xerogels promise for customizable biomaterials as per the requirement for bone engineering applications.

REFERENCE:

[1] S. Rößler, R. Unbehau, T. Gemming, B. Kruppke, H.P. Wiesmann, T. Hanke, Calcite incorporated in silica/collagen xerogels mediates calcium release and enhances osteoblast proliferation and differentiation, Sci. Rep. 10 (2020) 1–13. https://doi.org/10.1038/s41598-019-56023-8.

[2] M. Iafisco, N. Margiotta, Silica xerogels and hydroxyapatite nanocrystals for the local delivery of platinum-bisphosphonate complexes in the treatment of bone tumors: A mini-review, J. Inorg. Biochem. 117 (2012) 237–247. https://doi.org/10.1016/j.jinorgbio.2012.06.004.

[3] H. Maleki, L. Durães, C.A. García-González, P. del Gaudio, A. Portugal, M. Mahmoudi, Synthesis and biomedical applications of aerogels: Possibilities and challenges, Adv. Colloid Interface Sci. 236 (2016) 1–27. https://doi.org/10.1016/j.cis.2016.05.011.

[4] S. Heinemann, C. Heinemann, S. Wenisch, V. Alt, H. Worch, T. Hanke, Calcium phosphate phases integrated in silica/collagen nanocomposite xerogels enhance the bioactivity and ultimately manipulate the osteoblast/osteoclast ratio in a human co-culture model, Acta Biomater. 9 (2013) 4878–4888. https://doi.org/10.1016/j.actbio.2012.10.010.

[5] S. Heinemann, T. Coradin, H. Worch, H.P. Wiesmann, T. Hanke, Possibilities and limitations of preparing silica/collagen/hydroxyapatite composite xerogels as load-bearing biomaterials, Compos. Sci. Technol. 71 (2011) 1873–1880. https://doi.org/10.1016/j.compscitech.2011.08.023.

[6] L. Cianferotti, A.R. Gomes, S. Fabbri, A. Tanini, M.L. Brandi, The calcium-sensing receptor in bone metabolism: from bench to bedside and back, Osteoporos. Int. 26 (2015) 2055–2071. https://doi.org/10.1007/s00198-015-3203-1.

[7] J. Stergar, U. Maver, Review of aerogel-based materials in biomedical applications, J. Sol-Gel Sci. Technol. 77 (2016) 738–752. https://doi.org/10.1007/s10971-016-3968-5.

[8] D. Quintanar-Guerrero, A. Ganem-Quintanar, M.G. Nava-Arzaluz, E. Piñón-Segundo, Silica xerogels as pharmaceutical drug carriers, Expert Opin. Drug Deliv. 6 (2009) 485–498. https://doi.org/10.1517/17425240902902307.

[9] L. Albarran, T. López, P. Quintana, V. Chagoya, Controlled release of IFC-305 encapsulated in silica nanoparticles for liver cancer synthesized by sol-gel, Colloids Surfaces A Physicochem. Eng. Asp. 384 (2011) 131–136. https://doi.org/10.1016/j.colsurfa.2011.03.042.

[10] T. Sarkar, K. Rawat, P.R. Solanki, H.B. Bohidar, Carbon dots-embedded fluorescent silica xerogel, Colloids Surfaces A Physicochem. Eng. Asp. 583 (2019) 123844. https://doi.org/10.1016/j.colsurfa.2019.123844.

[11] S.H. Teng, P. Wang, J.Q. Dong, Bioactive hybrid coatings of poly(ε-caprolactone)-silica xerogel on titanium for biomedical applications, Mater. Lett. 129 (2014) 209–212. https://doi.org/10.1016/j.matlet.2014.05.068.

[12] A. Li, H. Shen, H. Ren, C. Wang, D. Wu, R.A. Martin, D. Qiu, Bioactive organic/inorganic hybrids with improved mechanical performance, J. Mater. Chem. B. 3 (2015) 1379–1390. https://doi.org/10.1039/c4tb01776e.

[13] C. Shuai, B. Peng, P. Feng, L. Yu, R. Lai, A. Min, In situ synthesis of hydroxyapatite nanorods on graphene oxide nanosheets and their reinforcement in biopolymer scaffold, J. Adv. Res. (2021). https://doi.org/10.1016/j.jare.2021.03.009.

[14] P. Feng, P. Wu, C. Gao, Y. Yang, W. Guo, W. Yang, C. Shuai, A Multimaterial Scaffold With Tunable Properties: Toward Bone Tissue Repair, Adv. Sci. 5 (2018) 1–15. https://doi.org/10.1002/advs.201700817.

[15] H. Goel, N. Gupta, D. Santhiya, N. Dey, H.B. Bohidar, A. Bhattacharya, Bioactivity reinforced surface patch bound collagen-pectin hydrogel, Int. J. Biol. Macromol. 174 (2021) 240–253. https://doi.org/10.1016/j.ijbiomac.2021.01.166.

[16] W. Liu, X. Wu, H. Zhan, F. Yan, Synthesis of bioactive poly(ethylene glycol)/SiO 2-CaO-P 2O 5 hybrids for bone regeneration, Mater. Sci. Eng. C. 32 (2012) 707–711. https://doi.org/10.1016/j.msec.2012.01.012.

[17] D. Ksouri, H. Khireddine, A. Aksas, Structure, Morphology and Bioactivity of Bioactive Glass Derived Xerogel and Aerogel, J. New Technol. Mater. 7 (2017) 30–37. https://doi.org/10.12816/0044600.

[18] B.R. Spirandeli, T.M.B. Campos, R.G. Ribas, G.P. Thim, E. de S. Trichês, Evaluation of colloidal and polymeric routes in sol-gel synthesis of a bioactive glass-ceramic derived from 45S5 bioglass, Ceram. Int. 46 (2020) 20264–20271. https://doi.org/10.1016/j.ceramint.2020.05.108.

[19] K. Deshmukh, T. Kovářík, T. Křenek, D. Docheva, T. Stich, J. Pola, Recent advances and future perspectives of sol-gel derived porous bioactive glasses: a

review, RSC Adv. 10 (2020) 33782–33835. https://doi.org/10.1039/d0ra04287k.

[20] S. Mann, Molecular tectonics in biomineralization and biomimetic materials chemistry, Nature. 365 (1993) 499–505. https://doi.org/10.1038/365499a0.

[21] K.A. Hudgins, A.K. Dillow, A.M. Lowman, Biomimetic Materials and Design: Biointerfacial Strategies, CRC Press, 2002. https://doi.org/10.1201/9780203908976.

[22] L.P. Bauermann, J. Bill, F. Aldinger, Bio-friendly synthesis of ZnO nanoparticles in aqueous solution at near-neutral pH and low temperature, J. Phys. Chem. B. 110 (2006) 5182–5185. https://doi.org/10.1021/jp056830m.

[23] L.P. Bauermann, A. Del Campo, J. Bill, F. Aldinger, Heterogeneous nucleation of ZnO using gelatin as the organic matrix, Chem. Mater. 18 (2006) 2016–2020. https://doi.org/10.1021/cm052317+.

[24] G. Pota, A. Zanfardino, M. Di Napoli, D. Cavasso, M. Varcamonti, G. D'Errico, A. Pezzella, G. Luciani, G. Vitiello, Bioinspired antibacterial PVA/Melanin-TiO2 hybrid nanoparticles: the role of poly-vinyl-alcohol on their self-assembly and biocide activity, Colloids Surfaces B Biointerfaces. 202 (2021) 111671. https://doi.org/10.1016/j.colsurfb.2021.111671.

[25] J.D. Bihuniak, K.L. Insogna, The effects of dietary protein and amino acids on skeletal metabolism, Mol. Cell. Endocrinol. 410 (2015) 78–86. https://doi.org/10.1016/j.mce.2015.03.024.

[26] J. Cihlář, Hydrolysis and polycondensation of ethyl silicates. 1. Effect of pH and catalyst on the hydrolysis and polycondensation of tetraethoxysilane (TEOS),

Colloids Surfaces A Physicochem. Eng. Asp. 70 (1993) 239–251. https://doi.org/10.1016/0927-7757(93)80298-S.

[27] G. De, B. Karmakar, D. Ganguli, Hydrolysis-condensation reactions of TEOS in the presence of acetic acid leading to the generation of glass-like silica microspheres in solution at room temperature, J. Mater. Chem. 10 (2000) 2289–2293. https://doi.org/10.1039/b003221m.

[28] D. Santhiya, H.K. Alajangi, F. Anjum, S. Murugavel, M. Ganguli, Bio-inspired synthesis of microporous bioactive glass-ceramic using CT-DNA as a template, J. Mater. Chem. B. 1 (2013) 6329–6338. https://doi.org/10.1039/c3tb21212b.

[29] N. Gupta, D. Santhiya, A. Aditya, K. Badra, Dendrimer templated bioactive glass-ceramic nanovehicle for gene delivery applications, RSC Adv. 5 (2015) 56794–56807. https://doi.org/10.1039/c5ra04441c.

[30] M. Gautam, D. Santhiya, N. Dey, Zein coated calcium carbonate nanoparticles for the targeted controlled release of model antibiotic and nutrient across the intestine, Mater. Today Commun. 25 (2020) 101394. https://doi.org/10.1016/j.mtcomm.2020.101394.

[31] N. Gupta, H. Goel, D. Santhiya, C.M. Srivastava, S. Mishra, P. Rai, Aqueous-Phased Electrospun Bioactive Glass Mineralized Gelatin-Pectin Hybrid Composite Fiber Matrix For 7-Dehydrocholesterol Delivery, ChemistrySelect. 5 (2020) 4364–4370. https://doi.org/10.1002/slct.202000264.

[32] T. Kokubo, H. Takadama, How useful is SBF in predicting in vivo bone bioactivity?, Biomaterials. 27 (2006) 2907–2915. https://doi.org/10.1016/j.

biomaterials.2006.01.017.

[33] N. Gupta, D. Santhiya, A. Aditya, Tailored smart bioactive glass nanoassembly for dual antibiotic in vitro sustained release against osteomyelitis, J. Mater. Chem. B. 4 (2016) 7605–7619. https://doi.org/10.1039/C6TB01528J.

[34] N. Gupta, D. Santhiya, Role of cellulose functionality in bio-inspired synthesis of nano bioactive glass, Mater. Sci. Eng. C. 75 (2017). https://doi.org/ 10.1016/j.msec.2017.03.026.

[35] N. Gupta, D. Santhiya, S. Murugavel, A. Kumar, A. Aditya, M. Ganguli, S. Gupta, Effects of transition metal ion dopants (Ag, Cu and Fe) on the structural, mechanical and antibacterial properties of bioactive glass, Colloids Surfaces A Physicochem. Eng. Asp. 538 (2018) 393–403. https://doi.org/10.1016/j.colsurfa. 2017.11.023.

[36] N. Gupta, A. Singh, N. Dey, S. Chattopadhyay, J.P. Joseph, D. Gupta, M. Ganguli, A. Pal, Pathway-Driven Peptide-Bioglass Nanocomposites as the Dynamic and Self-Healable Matrix, Chem. Mater. 33 (2021) 589–599. https://doi.org/10.1021 /acs.chemmater.0c03757.

[37] N. Gupta, D. Santhiya, In situ mineralization of bioactive glass in gelatin matrix, Mater. Lett. 188 (2017) 127–129. https://doi.org/10.1016/j.matlet.2016.11.045.

CHAPTER 4

Role of Trigonella foenum-graecum Leaf Extract in Tailoring the Synthesis and Properties of Bioactive Glass Nanoparticles

CHAPTER 4

Role of *Trigonella foenum-graecum* Leaf Extract in Tailoring the Synthesis and Properties of Bioactive Glass Nanoparticles

GRAPHICAL ABSTRACT

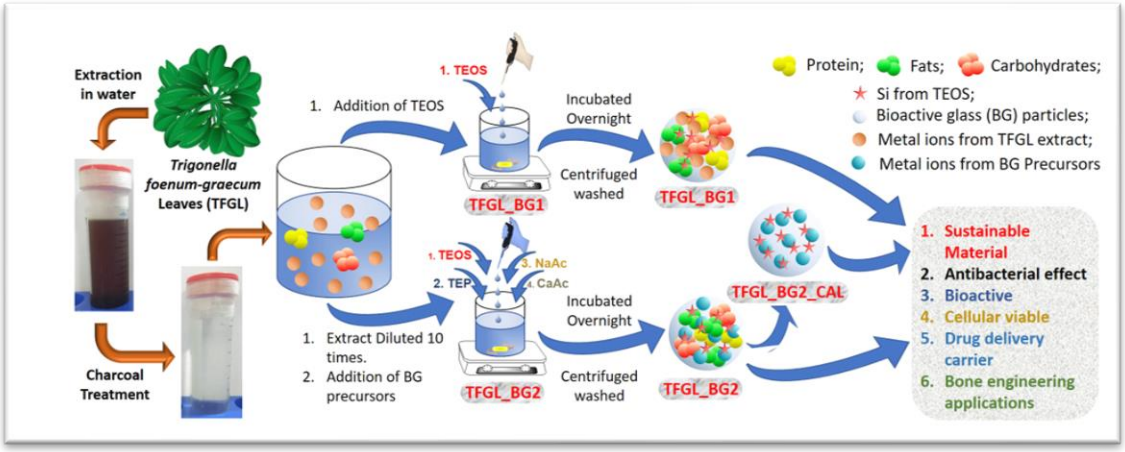

4.1. Introduction:

Green synthesis methods have attracted considerable attention in recent years in context of synthesis of various sustainable materials like metals, metal-oxides, inorganic-organic hybrids and different bio-inspired materials [1]. Biosynthesis is a class of green synthesis involving whole bacteria, fungi, yeast and plant extracts etc. and it serves as a magnificent source for synthesis of various metal oxide nanoparticles [2,3]. Most biomolecules applied in biosynthesis methods function both as reducing and capping agents under ambient conditions [4,5]. Biosynthesis methods reduce formation of environmentally toxic by-products due to application of green solvents [1,6]. Further, biosynthesis methods carried out using (or involving biological molecules have been

reported to provide precise control oversize, shape, morphology and physicochemical characteristics of synthesized nanoparticles [7,8]. However, most biosynthesis methods including microorganisms are time-consuming and require laborious cell culture procedures in addition to added risk of unwanted microbial contamination of the final product [1]. In contrast to this, plant extracts generally comprised of phytochemicals and biomolecules promise for sustainable industrial scale production of nanomaterials with desired properties and lesser chances of harmful contamination. Previously, magnesium oxide, zinc oxide, iron oxide, cerium oxide, cobalt oxide, nickel oxide, ruthenium oxide and manganous oxide nanoparticles have been synthesized using various plant extracts with distinct nanostructures and prolonged stability [7,8].

The purpose of the current work is to highlight the benefits of property-dependent green synthesis technique involved in bioprocess and medicinal applications. Herein, nanoparticles with biological components should help in improving characteristics like biocompatibility and antimicrobial activity, which may be utilized in several biomedical applications in future [9,10]. A recent literature review by S. Matussin *et al* covered previously reported plant extract mediated green synthesis of various SnO_2 nanoparticles with antioxidant, anti-bacterial and photocatalytic dye degradation properties. This is advantageous over traditional methods requiring toxic chemicals and harsh reaction conditions for generation of nano or microsized SnO_2 particles [7]. Silver nanoparticles obtained through green synthesis method using aqueous leaf extract of *Cucumis prophetarum* show antibacterial and antiproliferative activity against selected cancer cell lines [11]. A similar study by P. Roy *et al* demonstrated a facile green approach using ethanol extract of *Azadirachta indica* (neem) leaves for synthesizing nanostructured silver crystals which exhibit antimicrobial potential [12]. As bioactive glasses (BG) demonstrate attractive hard and soft tissue binding, it is frequently

reported as a bulk bioceramic material [13–15]. Apart from this, nanosized and mesoporous BG and BG-based materials have been long researched for therapeutic delivery applicable in treatment of multiple pathological conditions like osteoporosis, microbial infections, cancer and inflammatory diseases [16–18].

Current research suggests that environment-friendly techniques have been used in synthesis of diverse BG materials through water-based sol-gel method [19], application of organic acids as a catalyst [20] and various hydrothermal procedures [21–23]. Herein, we aim to obtain nanosized BG with inherent biomedical properties using aqueous *Trigonella foenum-graecum* (TFG) leaf extract (TFGL_EX). Previously, we had utilized bio-inspired routes for synthesis of nanosized BGNPs [24,25] where various organic biomolecules functioned as surface directing agents or templates. Use of organic solvents and high-temperature calcination during the synthesis process could be avoided through this method. The bio-inspired method developed in our lab generally requires template molecules dissolved in Trizma buffer at ambient conditions followed by sequential addition of bioglass precursors at room temperature [24,26–28]. In this study, aqueous TFGL EX was employed for the first time to synthesize nanosized mesoporous BG with built-in bioactivity and antimicrobial properties. Also known as fenugreek, TFG has been considered edible since ancient times due to its attractive medicinal properties [29–31]. Diets rich in TFG helps in balancing blood lipids while preventing hypercholesterolemia, diabetes and problems related to indigestion. Apart from this, TFG has reported antioxidant, antibacterial, anti-cancer and anti-inflammatory properties [30–33]. Initially, obtained TGFL extract (TFGL_EX) was subjected to detailed chemical analysis prior to utilization as template for synthesis of BGNPs. The template TFGL_EX was allowed to interact solely with tetraethyl orthosilicate (TEOS) in ambient conditions for generation of TFGL_EX-BG composite

(TFGL_BG1). Through previously reported bio-inspired method [26], the diluted leaf extract was subsequently combined with the necessary amounts of bioglass precursors for Ca, Na and P to synthesize BGNPs with 45S5 bioglass composition (TFGL_BG2) while a part of the product was subjected to calcination (TFGL_BG2_CAL). The three BG samples (TFGL_BG1, TFGL_BG2 and TFGL_BG2_CAL) were subjected to elemental analysis using Inductive Coupled Plasma-Mass spectrometry (ICP-MS) and CHNSO analyzer followed by other characterizations. In addition, a comparative analysis of *in-vitro* bone binding ability, biocompatibility, antibacterial property and drug releasing property of the materials were also carried out.

4.2. Experimental Section:

4.2.1. Materials:

Healthy fresh leaves of TFGL were collected from TFG crop fields located in the state of Uttar Pradesh in India. Various BG precursors namely tetraethyl orthosilicate (TEOS) (CAS No.: 78-10-4), triethyl phosphate (TEP) (CAS No.: 78-40-0), sodium acetate (NaAc) (CAS No.: 127-09-3) and calcium acetate hydrate (CaAc) (CAS No.: 114460-21-8) were obtained from Sigma-Aldrich, USA. Hank's Balanced Salt solution (HBSS) also addressed to as simulated body fluid (SBF) and gentamicin sulphate (CAS No.: 1405-41-0) were also purchased from Sigma-Aldrich, USA. Test microorganism strains, namely *Staphylococcus aureus* (*S. aureus* MCC 2408) (a gram-positive bacteria) and *Escherichia coli* (*E. coli* MCC 3144) (a gram-negative bacteria) were obtained from National Centre for Microbial Resource (NCMR), Pune, India. Cell studies were performed using U2OS, a human osteoblast-like osteosarcoma cell line procured from National Centre for Cell Science (NCCS), Pune, India. All other reagents used in these experiments were analytical reagents (AR) of high purity. Experiments

were performed using Milli-Q water at room temperature unless otherwise stated and in triplicates for error analysis using ANOVA from OriginLab 2021.

4.2.2. Aqueous TFGL Extraction:

Freshly collected leaves of TFG were washed under running water 2-3 times followed by careful rinsing in distilled water. The leaves were then dried for 10 days in dark and sterile environment. The dried leaves were ground in a kitchen blender into a fine powder and sieve with a mesh size of 1/16th of an inch. 10 g of the fine ground powder was soaked in 100 mL of Milli-Q water in an incubator for 24 h at 37 °C under continuous stirring. After incubation period, the mixture was centrifuged at 10000 rpm for 15 min in order to collect the supernatant. The collected supernatant was treated with activated charcoal to remove the color components of the extract **(Fig. 4.1).** The decolorized supernatant was filtered through sintered funnel (Grade 4) to remove the activated charcoal and insoluble precipitates if any **(Fig. 4.2)**. The filtrate was named TFGL_EX and preserved at 4 °C in sterile conditions for further experiments.

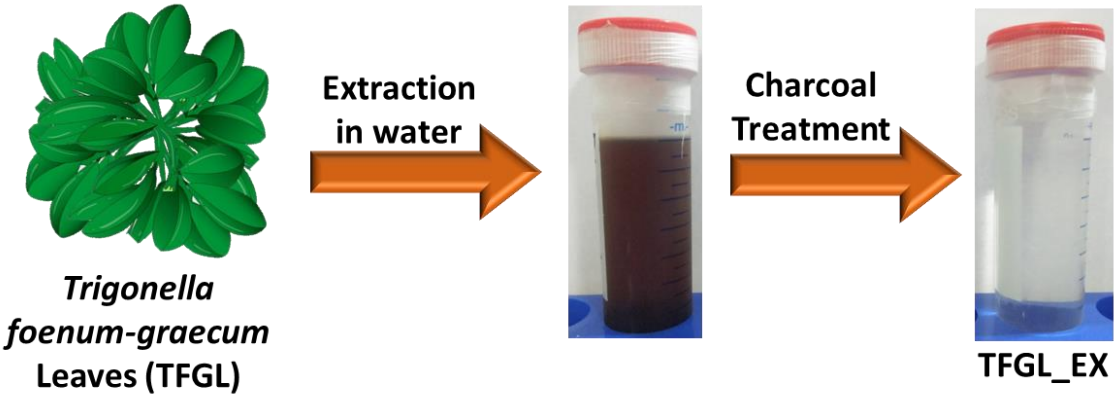

Fig. 4.1: Digital image of TFGL_EX before and after charcoal treatment.

4.2.3. Estimation of Nutritional Contents of TFGL_EX:

The protein, fat and carbohydrate contents of the leaf extract were estimated using

standard protocols as mentioned in IS:7219:1973 (for protein), AOAC 922.06 (for fat) and IS:1656:2007 (for carbohydrate). The detailed procedure for the above protocol is given in supplementary **(S1-S3)**. The mineral composition of the extract, i.e., calcium (Ca), potassium (K), sodium (Na), phosphorous (P), copper (Cu), magnesium (Mg) and iron (Fe) were determined using ICP-MS analysis **(Fig. 4.2)**.

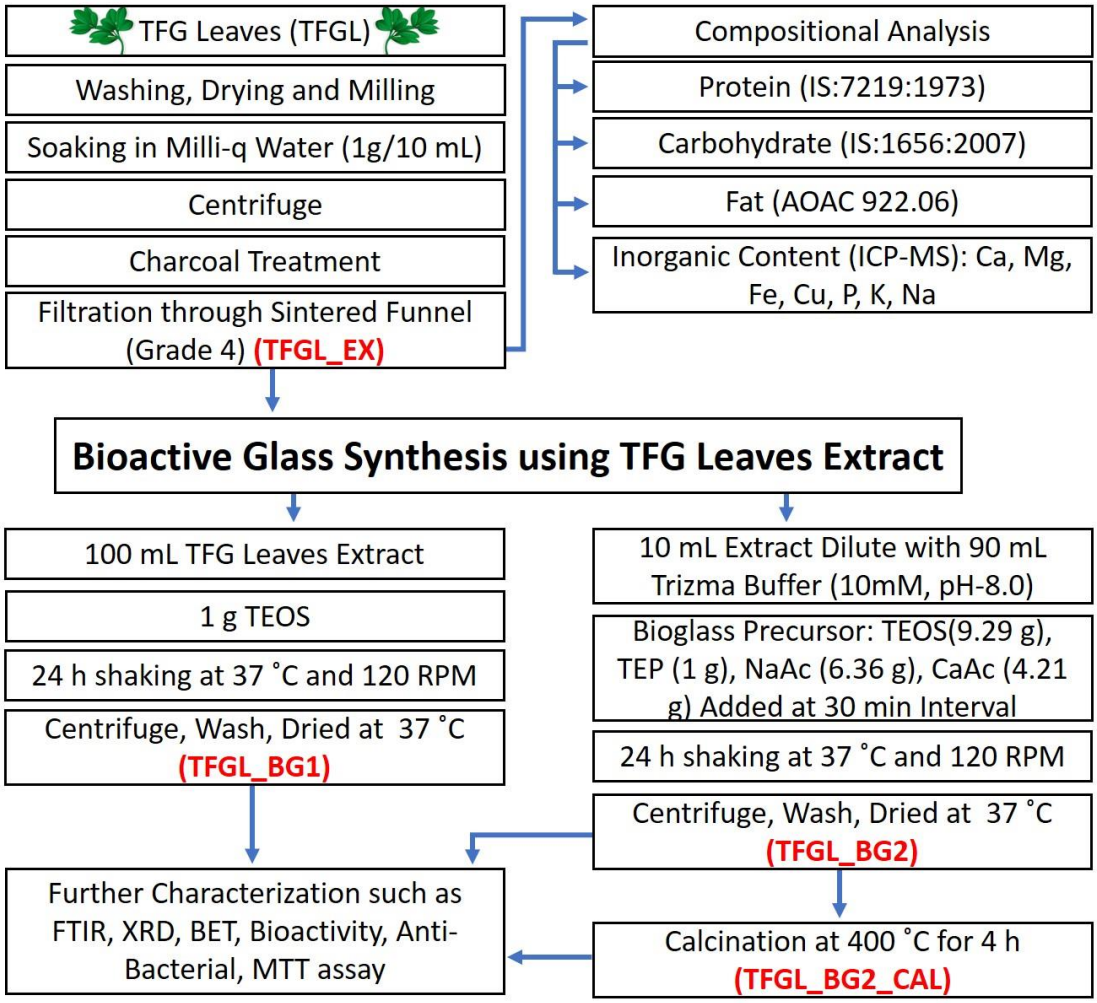

Fig. 4.2: Schematic illustration depicting TFGL_EX extraction and synthesis of TFGL_EX templated various BGNPs.

4.2.3.1. Estimation of Protein:

Amount of protein content in the TFGL_EX was determined using the Kjeldahl method by using standard test protocol IS: 7219:1973 adapted by the Indian standards. This

standard is based on ISO/TC 34 N 692 'Determination of total nitrogen protein in food and feeds by Kjeldahl method' issued by the International Organization for Standardization. Herein, the protein content was estimated by determining the total nitrogen content present in TFGL_EX. The total nitrogen concentration was then multiplied by the appropriate conversion factor. 6.25 is commonly employed as the conversion factor and is calculated based on the assumption that all proteins have nitrogen content of 16%.

In this method, 10 mL TFGL_EX was taken in 500 mL Kjeldahl flask. Further, mercury oxide (1 g), potassium sulphate (15 g) and conc. sulphuric acid (25 mL) have been added. The flask was heated slowly in an angled position on a heater until the foaming stopped. The content of the flask was aggressively heated until the solution became clear, and then boiled for 1 to 2 hours. The flask was then chilled, followed by the addition of 200 ml of distilled water. To avoid the formation of complexes, 25 ml of thiosulphate solution was added and stirred to precipitate the mercury followed by addition of zinc grains to avoid bumping. To make the solution extremely alkaline, the flask was tilted and 25 g of sodium hydroxide was added as solid. The flask was immediately attached to the condenser, with the tip of the condenser immersed in the receiver containing 0.1 N standard acid (50 mL). The flask was quickly heated until all of the ammonia had distilled over. Using methyl red as an indicator, the surplus acid was back titrated with standard 0.1 N sodium hydroxide. The experiment was carried out in triplicates to ascertain the standard deviation. A control experiment was also carried out using 1 g of glucose instead of TFG_EX.

4.2.3.1.*1. Calculation, Expression and Interpretation of Results:*

4.2.3.1.1.1. Calculation of Nitrogen Content:

$$Nitrogen\ Content\ (N)(g) = (A - B) - (C - D)\ X\ 0.0014$$

Where, **A** = volume of 0.1 N acid measured for primary distillation (mL), **B** = volume of 0.1 N alkali used for back-titrating A (mL), **C** = volume of 0.1 N acid measured for blank distillation (mL), **D** = volume of 0.1 N alkali used for back-titrating C (mL).

4.2.3.1.1.2. Calculation of Total Protein:

$$Protein, \%\ by\ mass = \frac{N\ X\ 100\ X\ C}{W}$$

Where, N = mass of nitrogen content (g) in TFGL_EX, C = Conversion Factor (6.25), W = mass of TFGL_EX(g).

4.2.3.2. Estimation of Fat:

Total fat content was determined by the acid hydrolysis method described in Association of Official Agricultural Chemists (AOAC) method 922.06. Total fat content refers to the sum of phospholipids, triglycerides, sterols, wax ester, and non-fatty materials. In this experiment, 10 mL of TFGL_EX was combined with 10 mL ethanol and 10 mL of 8 M HCL in a 50 mL beaker and heated to 80 °C with stirring for 1 hour. After cooling the solution, 10 mL additional ethanol was added. The mixture was transferred to Mojonnier fat extraction apparatus for total fat extraction followed by addition of 25 mL petroleum ether. After a thorough mixing, the Mojonnier flask was centrifuged at 1000 rpm followed by decanting the ether-containing supernatant. To remove any leftover ether content from the remaining solution, it was heated to 100 °C in a water bath. The remaining material was then dried out at 100 °C until a consistent weight was noted. The final weight of the obtained product is the total fat content in the TFGL_EX. The experiment was carried out in triplicates to ascertain the standard deviation.

4.2.3.3. Estimation of Carbohydrate:

Total carbohydrate content present in TFGL_EX was determined using standard test protocol IS: 1656:2007 adapted by the Indian standards. The total carbohydrate in this case comprises any polysaccharides, maltose, lactose, sucrose, dextrose, or dextrin present in the extract. The amount of total carbohydrates is calculated by deducting the combined contents of water, fat, protein, and dry ash from the total weight of TFGL_EX. The experiment was carried out in triplicates to ascertain the standard deviation.

$$\text{Total Carbohydrate} = X - (A + B + C + D)$$

Where, **X** = Total weight of the TFGL_EX used, **A** = Total content of water in it (determined by drying TFGL_EX at 100 °C until a consistent weight was observed), **B** = Total protein content, **C** = Total fat content, and **D** = Total ash weight (determined by burning TFGL_EX at 800 °C in muffle furnace).

Table 4.1: Nutritional composition of TFGL_EX.

Nutrition and Minerals	Amount
Protein	2200 ± 40 ppm
Carbohydrate	3800 ± 55 ppm
Fat	300 ± 5 ppm
Calcium	793.3 ± 13.2 ppm
Magnesium	190.8 ± 2.3 ppm
Potassium	629.8 ± 7.3 ppm
Sodium	1543.8 ± 24.7 ppm
Phosphorous	478.6 ± 6.4 ppm
Iron	13.6 ± 0.3 ppm
Copper	2.3 ± 0.1 ppm

4.2.4. Synthesis of TFGL-BGNPs:

4.2.4.1. Green Synthesis of TFGL-BGNPs using TEOS as precursor (TFGL_BG1):

1 g of TEOS was added to 100 mL of TFGL_EX with overnight stirring in an orbital shaking incubator set at stirring speed of 120 rpm and temperature of 37 °C. Quantity of TEOS (1 g) was decided based on required composition of the synthesized BG while keeping in mind the indigenous mineral concentrations of TFGL_EX that was expected to be retained in the final product **(Table 4.1).** Following day, the obtained precipitate was centrifuged and washed with Milli-Q water to remove unreacted components. Post washing, the sample was dried at 40 °C in a hot air oven for 48 h and preserved in a vacuum desiccator for further studies **(**TFGL_BG1, **Fig. 4.2).**

4.2.4.2. Bio-Inspired Synthesis of TFGL-BGNPs (TFGL_BG2):

10 mL of TFGL_EX was diluted to 100 mL solution using 10 mM Trizma buffer adjusted to pH-8.0. Pre-determined amount of bioglass precursors, namely TEOS (9.29 g), TEP (1.0 g), NaAc (6.36 g) and CaAc (4.21 g) were sequentially added into the TFGL_EX-Trizma solution each at an interval of 30 minutes from the other **(Fig. 4.2)**. The solution was kept under continuous stirring condition overnight as reported earlier [26]. Following incubation period, the precipitate was centrifuged and washed with Milli-Q water to remove presence of any unreacted components. The obtained precipitate was dried at 40 °C in a hot air oven for 48 h and preserved in a vacuum desiccator **(**TFGL_BG2 **Fig. 4.2)**.

4.2.4.3. Calcination of TFG_BG2 (TFGL_BG2_CAL):

The calcination of TFGL_BG2 was carried out in a muffle furnace at 400 °C for 5 h at 10 °C/min and was named as TFGL_BG2_CAL.

4.2.5. Characterization Studies:

A detailed explanation for sample preparation and instrument specification for characterization tools used for TFGL_EX and TFGL_EX templated BGNPs was already discussed in Chapter 2. The atomic % of various elements present in TFGL_BG1, TFGL_BG2 and TFGL_BG2_CAL (Si, P, Na, Ca, Fe, Mg, Cu and K) were estimated using ICP-MS analysis as described in section 2.2.3.1. The existence of organic contents in various BGNPs was estimated using CHNSO analyzer as described in section 2.2.3.2. Various BGNPs were further subjected to structural determination using XRD, FTIR, TGA and nitrogen sorption analysis as described in section 2.1.1, 2.1.2, 2.1.4 and 2.1.5. The surface morphologies were evaluated using FE-SEM and HR-TEM analysis as described in section 2.2.1.1 and 2.2.1.2. The particle size was calculated on FE-SEM and HR-TEM micrographs using ImageJ bundled with 64-bit Java 1.8.0_172 software.

4.2.5.1. Drug Loading:

TFGL_BG1, TFGL_BG2 and TFGL_BG2_CAL (25 mg/ml) were immersed in gentamicin sulphate solution (25 mg/ml) and incubated in an orbital shaker incubator set at 37 °C for 15 min with a stirring speed of 120 rpm. Post–incubation period, the drug-BG solution was centrifuged and dried at 40 °C. The supernatant was analyzed through an Ultraviolet-visible spectrophotometer (Agilent Technologies Carry 300 UV-Vis) at the wavelength (λmax) of 333 nm [34] to determine the quantity of unbound drug. The drug loaded BGNPs were named as TFGL_BG1_Gen, TFGL_BG2_Gen and TFGL_BG2_CAL_Gen. The experiment was performed in triplicates and the amount of loaded drug was calculated according to the equation given below:

$$Loaded\ Drug(\%) = \frac{Total\ Amount\ of\ Drug - Amount\ of\ Unbound\ Drug}{Total\ Amount\ of\ Drug}\ X\ 100$$

4.2.5.2. Drug Release Studies:

TFGL_BG1_Gen, TFGL_BG2_Gen and TFGL_BG2_CAL_Gen was dissolved in SBF solution (1 mg/mL) in a 50 ml flask and incubated in an orbital shaker incubator set at 80 rpm, 37 °C. After pre-determined intervals, 1 mL of suspension was taken out from each flask, centrifuged and subjected to quantitative analysis using Ultraviolet-visible Spectrophotometer (Agilent Technologies Carry 300 UV-Vis) to determine gentamicin sulphate release at 333 nm [34]. The amount of released drug was plotted against time. Experiments were conducted in triplicates with required volume corrections.

4.2.5.3. Bioactivity Test:

In-vitro bioactivity of TFGL_BG1, TFGL_BG2 and TFGL_BG2_CAL was carried out by monitoring the formation of bone-like hydroxyapatite on BG surface as per the procedure described by Kokubo *et al* [35]. BGNPs were immersed in SBF (1 mg/mL) and incubated at 37 °C under sterile conditions for pre-determined time interval. Here, the SBF solution was changed every 3rd day to prevent a drop in its cationic content, which otherwise may have decreased the ease of apatite formation. BG samples were separated from SBF solution after pre-determined time intervals, washed with Milli-Q water thrice and dried in air oven at 40 °C. The dried samples were subjected to FTIR, XRD and FE-SEM analysis for further characterization.

4.2.5.4. Antibacterial Susceptibility Tests:

The antibacterial properties of TFGL_BG1_Gen, TFGL_BG2_Gen and TFGL_BG2_CAL_Gen were studied against Gram-negative *E. coli* and Gram-positive

S. aureus. Pre-determined quantity of BGNPs were added to wells situated at the center of agar plates of chosen bacterial strains to carry out, disc diffusion test (AATCC-30). The plates were then incubated for 16 h at 37 °C and observed for zone of inhibition. Experiments were conducted in triplicates for various drug loaded BGNPs with appropriate positive (only gentamicin sulphate) and negative controls (only BGNPs).

4.2.5.5. Biocompatibility Studies: *MTT Assay:*

For 3-(4,5-dimethylthiazol-2-yl)-2,5-diphenyl-2H-tetrazolium bromide (MTT) analysis, TFGL_BG1, TFGL_BG2 and TFGL_BG2_CAL were placed in 96 well plates at concentrations of 10, 50, 100, 500 and 1000 μg/mL and seeded with the U2OS cells at a density of 1×10^4 cells per well. The plates were incubated at 37 °C with 5% CO_2 for 24 h in DMEM-F12 media with 5% FBS. After 24 h, 100 μL of 5% MTT reagent was added to each well and incubated for 2 h at 37 °C to allow the formation of formazan crystals. Crystal growth was confirmed by visualization through an optical microscope (Floid Cell Imaging Station). Once crystal formation could be observed, 100 μL dimethyl sulfoxide (DMSO) was added to each well for dissolving the formed formazan crystals. The absorbance of the resulting solution was determined using a TECAN multimode microplate reader at a wavelength of 570 nm. All experiments were performed thrice with appropriate control and the data have been represented as mean standard deviation.

4.3. Results and Discussion:

4.3.1. Nutritional Analysis of TFGL_EX:

Nutritional composition of TFGL_EX is shown in **Table 4.1**. TFGL_EX contain protein, carbohydrate, fat and metal ions like calcium, potassium, phosphorous and

sodium as macronutrients. In addition, the extract also contains inorganic micronutrients such as magnesium, iron and copper ions.

4.3.2. Elemental Analysis of BGNPs:

Elemental compositions of various BGNPs are given in **Table 4.2**. Based on the CHNSO analysis, the total organic content of TFGL_BG1, TFGL_BG2 and TFGL_BG2_CAL was reported as 16.9 ± 0.5 w/w%, 13.0 ± 0.2 w/w% and 2.8 ± 0.2 w/w% respectively. While TFGL_BG1 contains inorganic elements such as Si, P, Ca, Na, K, Mg and Fe, TFGL_BG2 and TFGL_BG2_CAL contains only Si, P, Ca and Na

Table 4.2: Elemental composition of TFGL_EX templated various BGNPs using ICP-MS (for Si, P, Ca, Na, Mg, Fe, K and Cu) and CHNSO (for C, N and H).

	Various Elements	Experimental Values (w/w %)		
		TFGL_BG1	**TFGL_BG2**	**TFGL_BG2_CAL**
CHNSO Analysis	**Carbon (C)**	13.1 ± 0.4	10.0 ± 0.2	2.8 ± 0.2
	Nitrogen (N)	1.6 ± 0.1	1.2 ± 0.0	0.0
	Hydrogen (H)	2.3 ± 0.0	1.7 ± 0.0	0.0
	Total Organic Content (Exclude Oxygen)	16.9 ± 0.5	13.0 ± 0.2	2.8 ± 0.2
ICP-MS Analysis	**Silicon (Si)**	22.3 ± 0.9	15.3 ± 0.8	19.2 ± 0.5
	Phosphorous (P)	4.0 ± 0.4	2.2 ± 0.2	2.4 ± 0.3
	Calcium (Ca)	6.6 ± 0.5	13.6 ± 0.7	16.8 ± 0.9
	Sodium (Na)	12.9 ± 0.2	14.1 ± 0.9	17.4 ± 0.6
	Magnesium (Mg)	1.6 ± 0.5	0.0	0.0
	Iron (Fe)	0.1 ± 0.0	0.0	0.0
	Potassium (K)	5.3 ± 0.6	0.0	0.0
	Copper (Cu)	0.0	0.0	0.0
	Total Inorganic Content (Exclude Oxygen)	52.9 ± 3.1	45.2 ± 2.6	55.9 ± 2.3

as representatives of the added precursors used in the synthesis process **(Section 4.2.4.2)**. It is pertinent to recall that TFGL_BG1 was synthesized using TFGL_EX and TEOS as received **(Section 4.2.4.1)**. As such, the other elements (P, Ca, Na, K, Mg and Fe) observed in case of TFGL_BG1 apart from Si may have possibly been incorporated from the leaf extract (TGFL-EX). A lower total organic content and absence of elements like K, Mg and Fe in TFGL_BG2 when compared to TFGL_BG1 can be due to the difference in synthesis methodology **(Section 4.2.4.2)** like using diluted TFGL_EX and standard BG precursors in case of the former. As expected, the lowest total organic content observed in case of TFGL_BG2_CAL among the three can be due to charring of the same during the calcination at 400 °C. Based on elemental analysis **(Table 4.2)**, calculated inorganic oxide composition (mole%) **(Table 4.3)** of TFGL_BG2 and TFGL_BG2_CAL nanoparticles are more or less similar to 45S5 bioglass. On the other hand, mole% of SiO_2 is higher for TFGL_BG1 (55.1 ± 1.1

Table 4.3: Comparative inorganic chemical composition in mole % of TFGL_EX templated various BGNPs with 45S5 bioglass.

	Calculated (mole %)	**Observed (mole %)**		
Units	**45S5**	**TFGL_BG1**	**TFGL_BG2**	**TFGL_BG2_CAL**
SiO_2	46.1	55.1 ± 1.1	44.4 ± 1.3	44.9 ± 1.2
P_2O_5	2.6	4.5 ± 0.1	2.9 ± 0.2	2.6 ± 0.3
CaO	26.9	11.5 ± 0.3	27.6 ± 0.6	27.6 ± 0.4
Na_2O	24.3	19.5 ± 1.1	25.0 ± 0.5	24.9 ± 0.2
MgO	0	4.6 ± 0.3	0	0
Fe_2O_3	0	0.1 ± 0.1	0	0
K_2O	0	4.7 ± 0.4	0	0
CuO	0	0	0	0
Total	100.0	100.0 ± 3.4	99.9 ± 2.6	100.0 ± 2.1

(Table 4.3) compared to TFGL_BG2 (44.4 ± 1.3 mole%). Other than P_2O_5, CaO and Na_2O, TFGL_BG1 was also reported to contain MgO (4.6 ± 0.3 mole%), Fe_2O_3 (0.1 ± 0.1 mole%) and K_2O (4.7 ± 0.4 mole%) **(Table 4.3)**. Although comparatively higher than TFGL_BG2 and TFGL_BG2_CAL, the measured mole% of SiO_2 in TFGL_BG1 is within the range needed for bioactivity of BG materials (SiO_2 45 mole% to 70 mole%) [36].

4.3.3. FTIR Analysis:

FTIR analysis was carried out to characterize the formation of BGNPs network in presence of TFGL_EX. FTIR Spectra of TFGL_EX, TGFL_BG1, TFGL_BG2 and TFGL_BG2_CAL are shown in **Fig. 4.3a**. Peaks at 1637 cm^{-1} (C=O stretching), 1412 cm^{-1} (C—C stretching) and a broad hump at 716 cm^{-1} (C—H out of plane) were observed in FTIR spectrum of TFGL_EX. The reported peaks must have originated from various organic contents of the leaf extract **(Table 4.1)**. Though phosphorous was reported by ICP-MS analysis (**Table 4.1**), the corresponding expected phosphate peaks could not be observed in the spectrum of TFGL_EX. The absence of expected characteristic phosphate group vibrations may be due to the appearance of a broad hump from 1000 cm^{-1} to 400 cm^{-1} which is generally considered to be the range of such vibrations. Appearance of a small peak at 1640 cm^{-1} for **TFGL_BG1** can be due to retention of —C=O group of TFGL_EX. Apart from this, few additional peaks at 1564 cm^{-1} (C—O stretching), 1477 cm^{-1} (C—N stretching), 1416 cm^{-1} (O—H bending and C—H wagging), 1341 cm^{-1} (C—H wagging) were also reported. These peaks might have originated due to interaction between Si—O^- groups of TEOS and the organic functional groups of TFGL_EX. Appearance of these peaks further accounts for the higher organic content observed for TFGL_BG1 compared to TFGL_BG2 as observed from CHNSO analysis (**Table 4.2**). Peaks due to silicate network were

observed at 1100 cm^{-1} (Si—O—Si, Si—O—C, Si—O^{-} stretching), 800 cm^{-1} (characteristic ring structures of the silicate network), 600 cm^{-1} (Si—O—Si) and 470

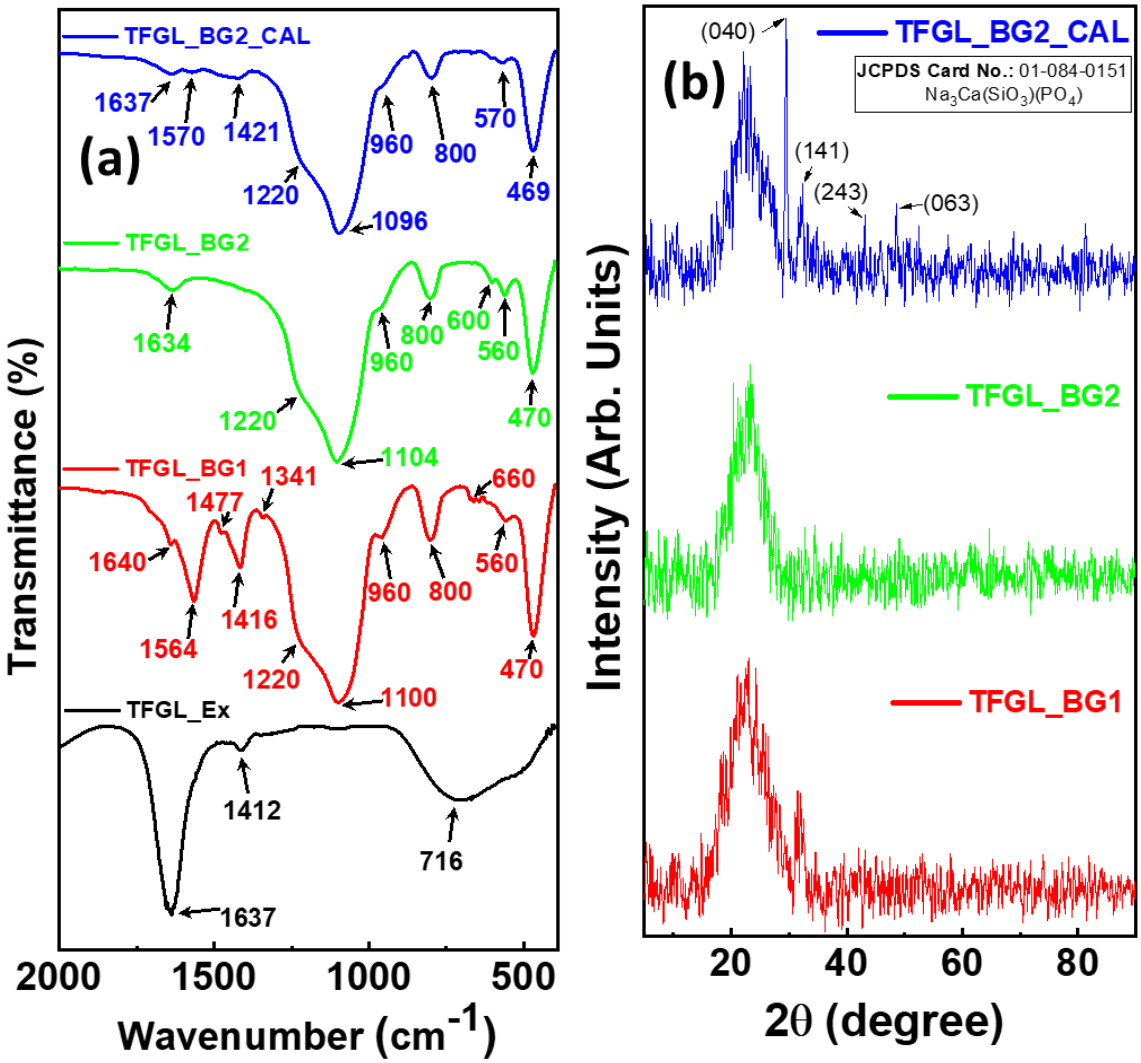

Fig. 4.3: (a) FTIR spectra of TFGL_EX and its templated various BGNPs. **(b)** XRD patterns of TFGL_EX templated various BGNPs.

cm^{-1} (Si—O^{-} bending) indicating successful generation of the BG structure. The shoulder at 1220 cm^{-1} corresponds to P—H bending, P=O and C—O stretching. In addition, shoulders at 960 cm^{-1} due to P—O—C, P—O—Si as well as P—H stretching at 623 cm^{-1} and 560 cm^{-1} due to PO_3^{2-} groups were also reported. These observations confirm the active participation of phosphorous **(Table 4.2)** in the silicate network as well as formation of TFGL_BG1.

In the FTIR spectrum of **TFGL_BG2** a small peak at 1634 cm^{-1} in the range of 2000 cm^{-1} to 1300 cm^{-1} was observed. Other than this, the spectrum appeared similar to TFGL_BG1 from 1300 cm^{-1} to 400 cm^{-1} thus supporting the development of BGNPs. In case of TFGL_BG2_CAL, no peaks could be observed in the range of 2000 cm^{-1} to 1400 cm^{-1} unlike TFGL_BG1 and TFGL_BG2. The observation may result from possible decomposition of organic content present within the BG network due to the calcination at 400 °C for 6 h. On the other hand, peaks in the range of 1400 cm^{-1} to 400 cm^{-1} are similar to TFGL_BG1 and TFGL_BG2 FTIR spectra, thereby leading to confirmation of the existence of the BG network.

4.3.4. XRD Diffraction Analysis:

XRD analysis was carried out to characterize the solid-state nature of the TFGL_BG1, TFGL_BG2 and TFGL_BG2_CAL nanoparticles and the results have been reported in **Fig 4.3b**. A large hump in the 2θ range of 15° to 30° was seen in the XRD pattern of TFGL_BG1 with the sole diffraction maximum occurring at 31.50°. The observation indicates that TFGL_BG1 has very little crystallinity which may sometimes be beyond the limit of detection of the instrument. Similar results were reported by Santhiya *et al* when doping BG particles with Ag, Cu and Fe using cetyltrimethylammonium bromide (CTAB) as a template [28]. Based on only one diffraction maximum, it is difficult to determine the exact crystal structure of TFGL_BG1. Additionally, according to the ICP-MS analysis (**Table 4.2)**, the BG network also contained other ions like Mg, K, and Fe. The presence of oxides of these metal ions may possibly be the source of observed diffraction maximum because their diffraction patterns show a similar diffraction maximum at 31.50º. The reported semi-crystalline nature of TFGL_BG1 is due to the interaction between the organic contents of the leaf extract and the inorganic contents of BGNPs network. Similar observation was reported by Santhiya *et al* for calf thymus-

DNA (CT-DNA) templated BG sample through bio-inspired method. Here, CT-DNA molecules led to the crystallization of BG particles in the solution phase under ambient conditions [26]. On the other hand, TFGL_BG2 showed only a broad hump in 2θ range of 15° to 30° confirming its amorphous nature. The lack of semi-crystalline nature of TFGL_BG2 is due to presence of insufficient organic content as a result of the dilution of the TFGL_EX template used for its synthesis **(Section 4.2.4.2)**. The semi-crystalline nature of TFGL_BG2_CAL observed probably due to the calcination step was indicated by a large hump in the 2θ range of 15° to 30° with a few diffracting domains at 2θ values of 29.54° (040), 32.34° (141), 43.16° (243), and 48.50° (063). The reported diffraction maxima correspond to JCPDS Card No.: 01-084-0151 (Na_3Ca (SiO_3) (PO_4)).

4.3.5. Thermogravimetric Analysis (TGA):

Fig. 4.4a portrays TGA thermograms of dried TFGL_EX and its templated BGNPs. For **TFGL_EX**, an initial weight loss percentage of 27.6 w/w% was observed up to 160 °C due to evaporation of sorbed water molecules. Further, from 225 °C to 380 °C, weight loss of 15.3 w/w% was observed which can be due to thermal decomposition of phytochemicals and biomolecules including amino acids, proteins, carbohydrates etc. 11.1 w/w% weight loss percentage observed from 510 °C to 590 °C can be attributed to degradation of phenolic acids and flavonoids present in the leaf extracts [37]. The total w/w% decomposition of the extract till 900 °C was calculated to be 67.9 w/w% indicating 32.1 w/w% of remnant inorganic content in the same. In the case of **TFGL_BG1,** initial weight loss percentage of 8.12 w/w% was seen up to 160 °C due to the evaporation of sorbed water molecules. Weight loss of 16.9 w/w% at higher temperature range (210 °C to 420 °C) can be due to the thermal decomposition of biomacromolecules as observed in case of TFGL_EX. Similarly, weight loss % of 3.6

w/w% corresponds to the phenolic acids and flavonoids present in the leaf extract can also be observed at higher temperature range from 575 °C to 650 °C [37]. Such observation may result from interactions between the organic components of the extract and the BG network and is well supported by observations from FTIR and XRD **(Fig. 4.3)**. At 900 °C, comparatively twice the amount of inorganic residues (66.1 w/w%) was left behind for TGFL_BG1 than TGFL_EX. In case of **TFGL_BG2**, 8.1 w/w% weight loss was observed at the lower temperature range (upto 63.3 °C) corresponding possibly to removal of adsorbed water from the surface of the particles. Further, 8.6 w/w% weight loss was observed from 315 °C to 430 °C which is at higher temperature range compared to TFGL_BG1. This is due to the interaction of proteins and carbohydrates from the leaf extract with the BG network. Herein, the absence of decomposition reported in the range of 500 °C to 650 °C can be due to the existence of phenolic acids and flavonoids below the detection limit when compared to TFGL_EX and TFGL_BG1. In this case, 71.2 w/w% (probably corresponding to inorganic residue content) in the TGFL_BG2 was observed to be remaining till the ultimate heating point at 900 °C.

In case of TFGL_BG2_CAL, a total weight loss of 4 w/w% was observed with 96 w/w% inorganic residue. The observed weight independent thermogram within the experimental temperature range is due to the calcination of TFGL_BG2_CAL at 400 °C which might have already resulted in removal of biomolecules, flavanoids and phenolic acids. The observations from the thermogravimetric analysis of the samples provided comparative estimation of organic and inorganic contents of various BGNPs. Further, size, shape and porosity of BGNPs were examined by nitrogen sorption and morphological analysis and results are discussed below.

4.3.6. Nitrogen Sorption Analysis:

N_2 adsorption–desorption isotherms of TFGL_EX templated BGNPs along with their pore size distribution is portrayed in **Fig. 4.4(b-d).** Surface area, pore volume and pore size data are listed in **Table 4.4**. The observations indicate that the BGNPs (TFGL_BG1, TFGL_BG2 and TFGL_BG2_CAL) followed type IV isotherm and type H3 hysteresis loop, indicating the samples to be mesoporous in nature, with slit like pores and demonstrating strong organic-inorganic interactions within the BG structure.

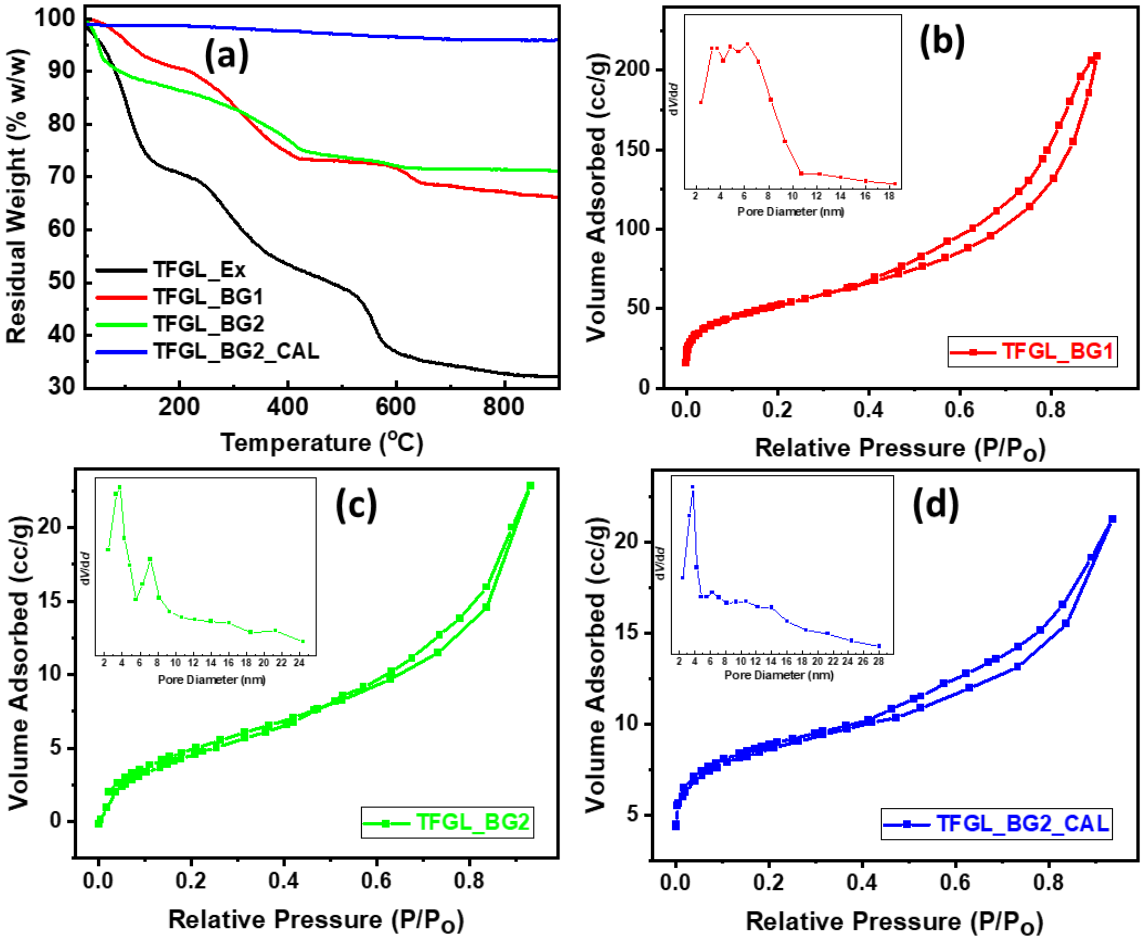

Fig. 4.4: (a) TGA thermogram, **(b-d)**: Nitrogen adsorption-desorption isotherm and pore size distribution **(inset)** of various TFGL_EX templated BGNPs.

It is noteworthy that BET isotherm of TFGL_BG1 **(Fig. 4.4b)** shows the highest volume of adsorbed N_2 (200 cm^3g^{-1}) at saturation point (P/Po ≈ 1) with a surface area of

184.12 m^2g^{-1} and total pore volume of 0.3229 cm^3g^{-1}. Its BJH plot shows a wide range of pore size distribution with an average pore diameter of 7.01 nm **(Fig. 4.4b insert)**.

In case of **TFGL_BG2 (Fig. 4.4c)** and **TFGL_BG2_CAL (Fig. 4.4d),** the highest volume adsorbed at saturation point and total pore volume remained more or less same, which shows that the calcination process did not deform the pore volume. However, decomposition of the organic materials due to calcinations may have led to the increase in the surface area of TFGL_BG2_CAL by ten units when compared to that of TFGL_BG2. In addition to this, the average pore diameter decreased to 4.31 nm from 7.24 nm (before calcination (TFGL_BG2)) indicating reformation of BG network in TFGL_BG2_CAL after calcination [38]. It is noteworthy that the BJH plot of TFGL_BG2 **(Fig. 4.4c insert)** showed bimodal distribution, whereas, in case of TFGL_BG2_CAL **(Fig. 4.4d insert),** mono model type distribution was observed.

Table 4.4: Surface area, pore volume and pore size data of TFGL_EX templated various BGNPs obtained via nitrogen adsorption-desorption isotherm.

	TFGL_BG1	**TFGL_BG2**	**TFGL_BG2_CAL**
Total Surface Area ($a_{s,BET}$ [m^2 g^{-1}])	184.12	19.524	30.505
Total pore volume(p/p_0=0.944) [cm^3 g^{-1}]	0.3229	0.03535	0.032894
Mean pore diameter [nm]	7.0146	7.2424	4.3132

4.3.7. Morphological Analysis:

FE-SEM and HR-TEM micrographs of TFGL_EX templated BGNPs (TFGL_BG1, TFGL_BG2 and TFGL_BG2_CAL) are shown in **Fig. 4.5(a-c)**. Based on FE-SEM micrographs, all three BG samples were of irregular spherical shapes with aggregated and dense morphology. HR-TEM (**Fig. 4.5d-f)** morphological features of BGNPs were also observed and were in accordance with the FE-SEM results. As per imageJ analysis

software on HR-TEM micrographs, TFGL_BG1 reported an average particle size of 8.8 ± 1.3 nm. On the other hand, the particle sizes of TFGL_BG2 (58.4 ± 11.6 nm) and TFGL_BG2_CAL (116.3 ± 6.2 nm) were observed to be greater than TFGL_BG1 **(Fig. 4.6)**. The observed differences in the particle sizes of BGNPs are due to high organic content of leaf extract (TFGL_EX) template **(Table 4.2)** of TFGL_BG1. The TFGL_EX offered more significant nucleation sites for BGNPs compared to TFGL_BG2. It is pertinent to recall that TFGL_EX has been diluted by ten times when used as template in case of TFGL_BG2 synthesis **(Section 4.2.4.2).** This must have

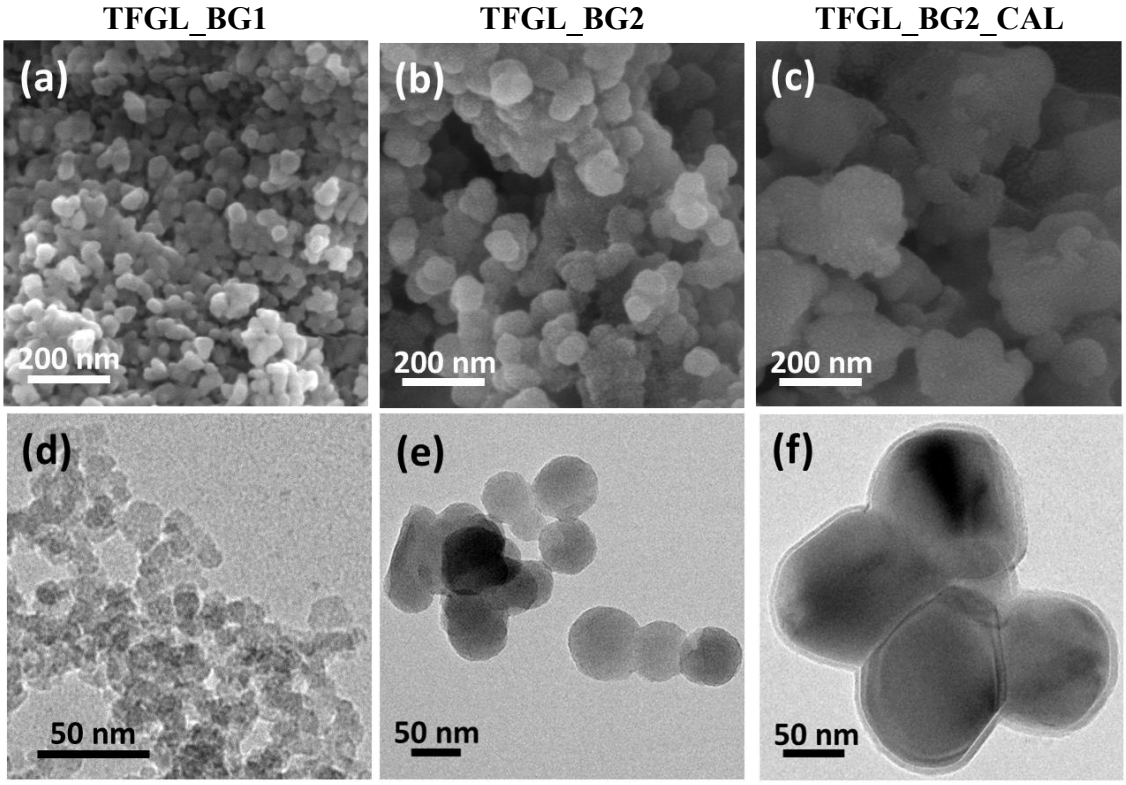

Fig. 4.5: (a-c) FE-SEM micrograph and **(d-f)** HR-TEM micrograph of TFGL_EX templated various BGNPs.

provided lesser number of organic molecules to be utilized as seeds for particle generation. Hence, reduced numbers of nucleation sites were available for the growth of TFGL_BG2 particles compared to TFGL_BG1 which in turn promoted growth of larger sized particles at limited available nucleation sites. In addition to the scarcely present

organic ingredients of the diluted leaf extract, the highest reported particle sizes for TFGL_BG2_CAL is probably due to BG network reformation as a result of crystal development following calcination.

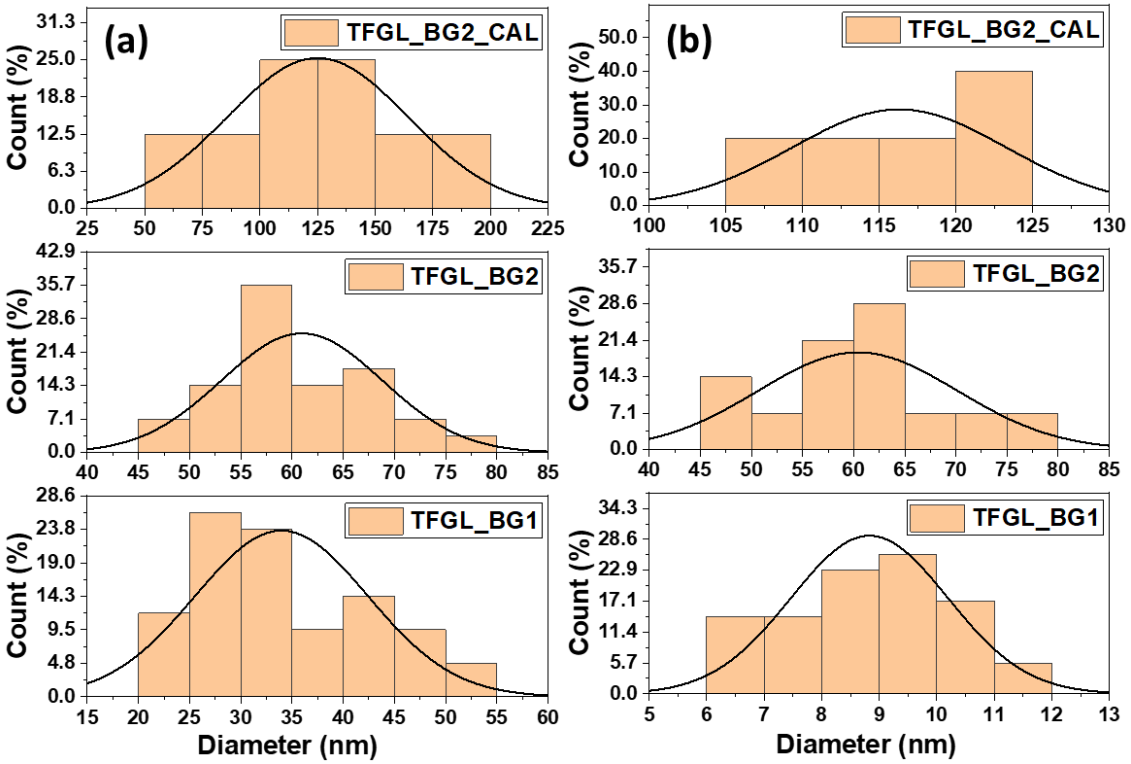

Fig. 4.6: Average pore diameter of various TFGL_EX templated BGNPs analysed through ImageJ analysis software for **(a)** FE-SEM and **(b)** HR-TEM micrographs.

4.3.8. *In-vitro* Bioactivity:

The formation of bone-like apatite on the surface of various BGNPs was monitored in SBF to understand the bone binding ability of the formed BGNPs [35]. The analysis of the bioactivity property was carried out through FTIR, XRD and FE-SEM for 15 days (**Fig. 4.7a-c**). In case of **TFGL_BG1**, a decrease in intensity of FTIR peaks was observed from 1350 cm^{-1} to 1650 cm^{-1} during this 15 day time period. This is due to the dissolution of organic contents into the SBF solution. Appearance of small shoulders at 1704 cm^{-1} and 1634 cm^{-1} due to C=O stretching indicate existence of the carbonate ions. Further, phosphate peaks at 800 cm^{-1}, 600 cm^{-1} and 560 cm^{-1} were observed to

have appeared gradually from 0 day to 15 days. It is pertinent to recall that the phosphate peaks on day 0 were from TFGL_EX **(Table 4.1 and Table 4.2)**. All these observations indicate deposition of apatite on surface of TFGL_BG1. After 15 days of interaction, appearance of new peaks with high intensity in the FTIR spectrum of **TFGL_BG2** could be observed in the range of 1300 cm^{-1} to 1720 cm^{-1} compared to TFGL_BG1, which could be due to the presence of carbonate ions. In addition, peaks in the range of 600 cm^{-1} to 700 cm^{-1} indicated deposition of calcium phosphate clusters along with PO_4^{3-} units and might be due to the deposition of Hydroxycarbonate apatite (HCA) [39,40]. Incubation of **TFGL_BG2_CAL** in SBF showed almost similar results as in the case of TFGL_BG1 and TFGL_BG2.

The apatite formation on the surface of virgin BGNPs was also analyzed using XRD **(Fig. 4.7d-f)** after immersing in SBF. In comparison to similar virgin BGNPs, additional diffraction maxima and a wide hump appeared for all three samples **(Fig. 4.7d-f)** indicating the surface deposition of apatite layer after 4 days of immersion in SBF. Further, the intensity of these diffraction maxima was observed to slightly increase from 4 days to 15 days on interaction with SBF. Interestingly, many new diffraction maxima could be noticed for TFGL_BG1 and TFGL_BG2_CAL compared to TFGL_BG2 as the immersion time of the nanoparticles increased from 7 days to 15 days.

In general, smaller particle sizes and high surface area of BGNPs helps in faster dissolution of Na^+, K^+, Mg^{2+}, Ca^{2+} as well as phosphate ions from the BGNPS into the surrounding SBF solution. As a result, faster deposition of apatite onto the surface of BGNPs can be seen within 4 days of incubation. However, if there is absence of the aforementioned ions on the surface of BGNPs, apatite formation would be deterred

even on prolonged immersion in SBF. It is due to this reason that bare SiO_2 surface on exposure to SBF normally lead to hampered deposition of apatite. In our study, an increase in intensity of a few diffracted domains along with emergence of new

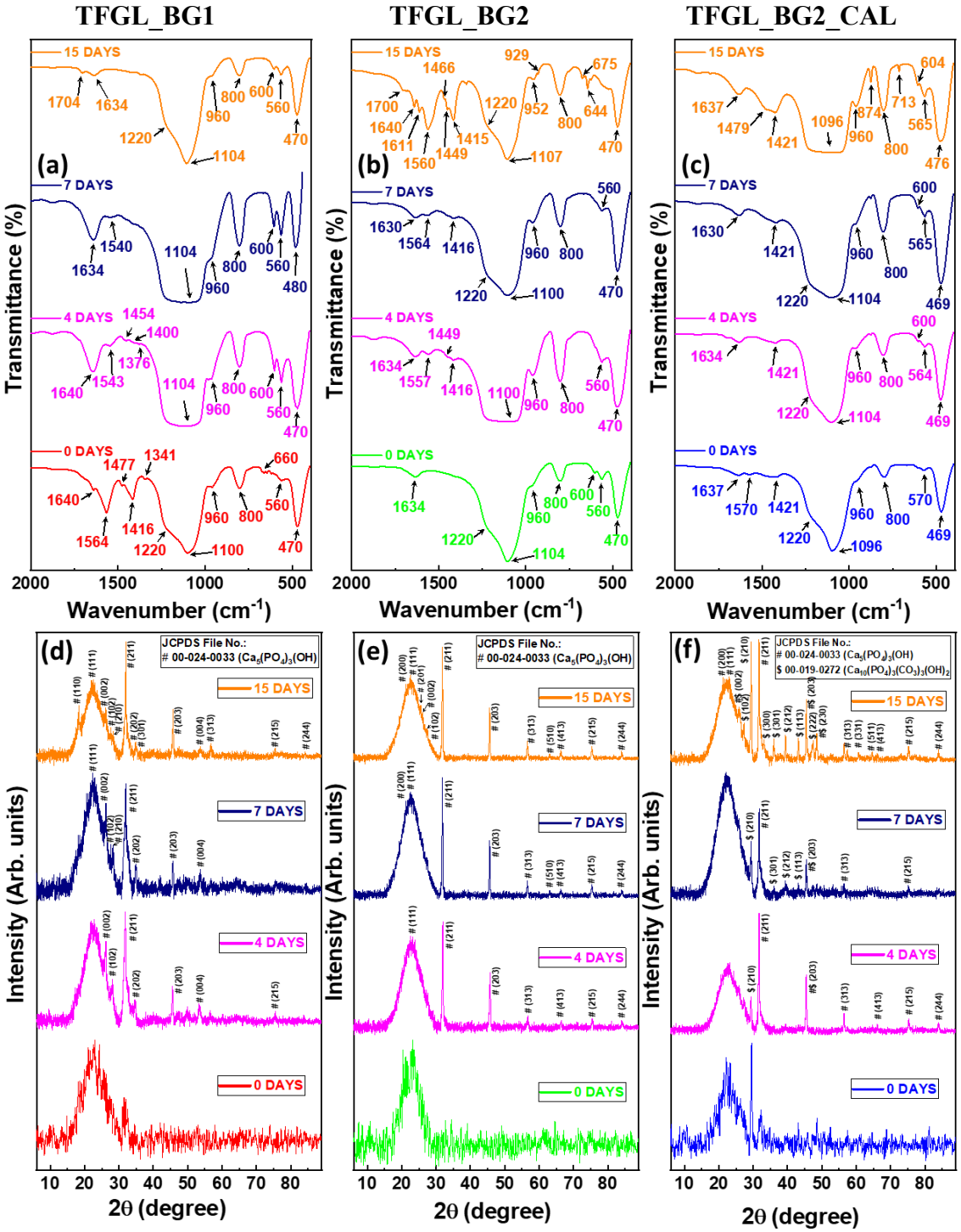

Fig. 4.7: (a-c) Bioactivity analysis by **(a-c)** FTIR spectra and **(d-f)** XRD pattern for 4 days, 7 days and 15 days of TFGL_EX templated various BGNPs on interaction with SBF.

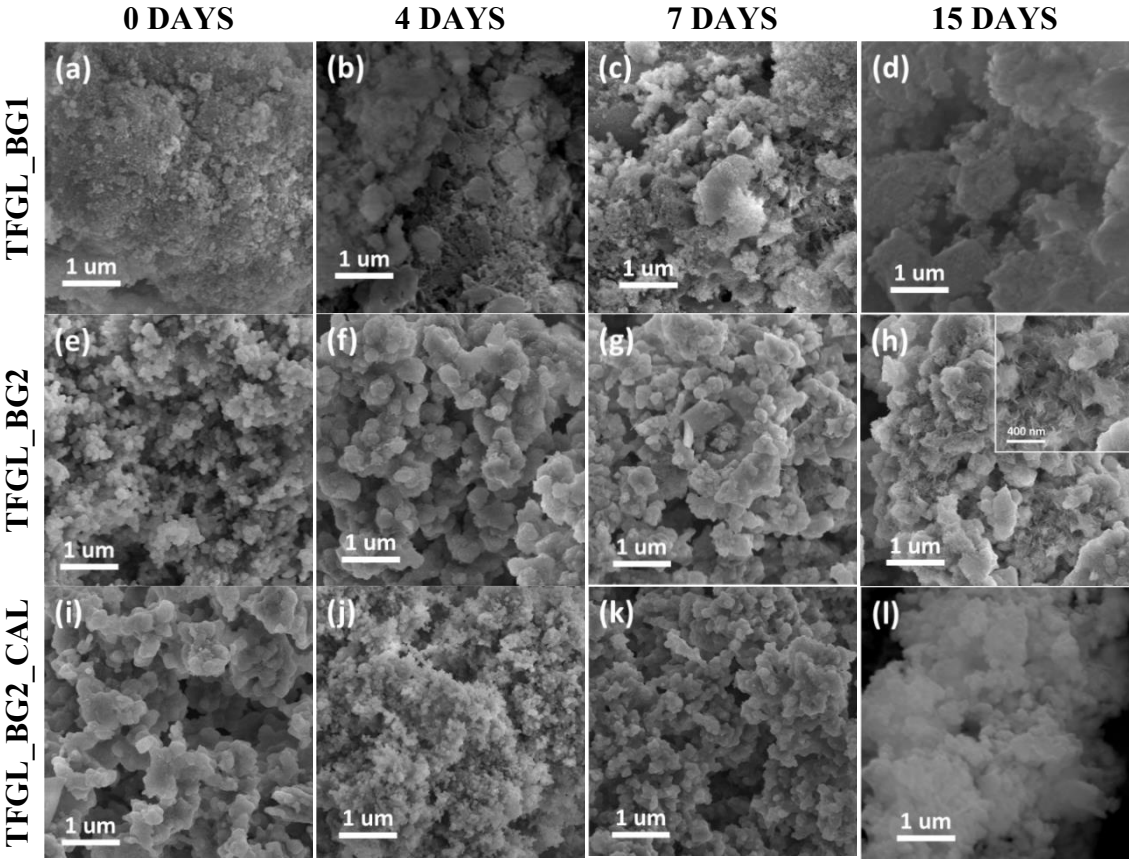

Fig. 4.8: (a-l) FE-SEM micrograph of TFGL_EX templated various BGNPs on interaction with SBF for 4 days, 7 days and 15 days.

diffraction maxima **(Fig.4.7d-f)** in case of TFGL_BG1 and TFGL_BG2_CAL are suggestive of dissolution of ions from core of the BGNPs. Apart from this, the crystallization of deposited amorphous apatite on surface of BGNPs can also cause the changes observed in the said XRD patterns **(Fig. 4.7d and 4.7f)** with increase in immersion time in SBF from day 7 to day 15.

In case of TFGL_BG1 and TFGL_BG2, the formation of hydroxyl apatite ($Ca_5(PO_4)_3(OH)$) (JCPDS file no.: 00-024-0033) was noticed. On the other hand, a combination of hydroxyl apatite ($Ca_5(PO_4)_3(OH)$) (JCPDS file no.: 00-024-0033) and carbonate hydroxyl apatite ($Ca_{10}(PO_4)_3(CO_3)_3(OH)_2$) (JCPDS file no.: 00-019-0272) was seen in case of TFGL_BG2_CAL. These observations are in good agreement with FTIR analysis of the said samples **(Fig. 4.7(a-c)).**

FE-SEM micrographs of various BGNPs after 4, 7 and 15 days of interaction with SBF are shown in **Fig. 4.8(a-l).** These micrographs display markedly distinct rough surface morphology compared to the bare surface morphology of untreated BGNPs possibly due to the deposition of apatite. In general, micrographs display increased apatite deposition from 7th day of SBF incubation for all BGNPs. The rapid apatite deposition on BG samples can be due to their mesoporous nature of the sample **(Fig. 4.5)**. The BGNPs were loaded with gentamicin sulphate as a model drug and subjected to drug release kinetics and antibacterial activity to understand their role in drug delivery applications.

4.3.9. Drug Release Kinetics:

The amount of drug loaded in various BGNPs was reported as 97.2 ± 2.1 w/v% (TFGL_BG1_Gen), 89.2 ± 1.2 w/v% (TFGL_BG2_Gen) and 93.3 ± 2.1 w/v% (TFGL_BG2_CAL_Gen) at 1 h and remained almost similar till 24 h. The drug loading w/v% data on BGNPs are in accordance with the findings of nitrogen sorption analysis **(Fig. 4.4(b-d) and Table 4.4)**.

Gentamicin sulphate release from the individual BGNPs in SBF was monitored **(Fig. 4.9a)** for 15 days. In general, all three samples showed a similar drug release pattern. A burst drug release was noticed up to 24 h for all three samples. This is because the adsorbed drug molecules on the surface of BGNPs dissolve more quickly when compared to the drug entrapped in the core of the nanoparticles. The initial burst release known to favor quick alleviation of microbial infection for initial wound healing treatments [41]. The amount of gentamicin sulphate released was highest for TFGL_BG1_Gen (66.5 w/v%) compared to TFGL_BG2_CAL_Gen (54.1 w/v%) and TFGL_BG2_Gen (42.3 w/v%) at 24 h. Further, the amount of drug released remained

more or less constant till 8 days, followed by a slight dip on 15th day for all three BGNPs. These findings corroborate with the rate of apatite deposition, which increased after 8 days leading to the partial blockage of interconnected mesopores **(Fig. 4.7 and Fig. 4.8)**. The amount of drug released at 24 h and beyond by BGNPs can be arranged as TFGL_BG1_Gen>TFGL_BG2_CAL_Gen>TFGL_BG2_Gen. The observed gentamicin sulphate release from BGNPs is in accordance with their reported surface area by nitrogen sorption analysis **(Fig. 4.4(b-d) and Table 4.4)** and thus can be established as sustained drug release.

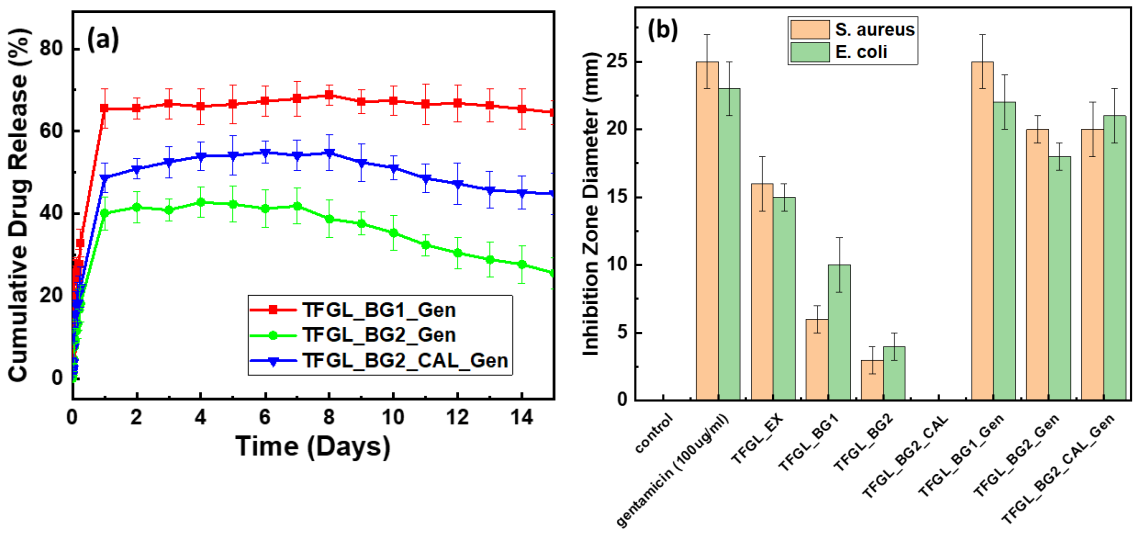

Fig. 4.9: (a) Cumulative drug release profile of gentamicin sulphate and **(b)** Disk diffusion assay of TFGL_EX templated various BGNPs.

4.3.10. Antibacterial Tests:

The antibacterial activities were examined by disk diffusion assay against *S. aureus* and *E. coli* and the results are portrayed as zone of inhibition (ZOI) in **Fig. 4.9(b) and Fig. 4.10**. TFGL_EX and its templated BGNPs demonstrated inherent antibacterial property due to the inorganic and organic contents **(Table 4.1 and Table 4.2)** of the leaf extract. No significant antibacterial activity against both strains of bacteria could be observed

for TGFL_BG2_CAL due to decomposition of the organic contents **(Table 4.2)** during calcination. As positive control, treatment of gentamicin sulphate (100 μg/mL) resulted in showed 25 ± 2 mm ZOI for *S. aureus* and 23 ± 2 mm ZOI for *E. coli*. TFGL_EX

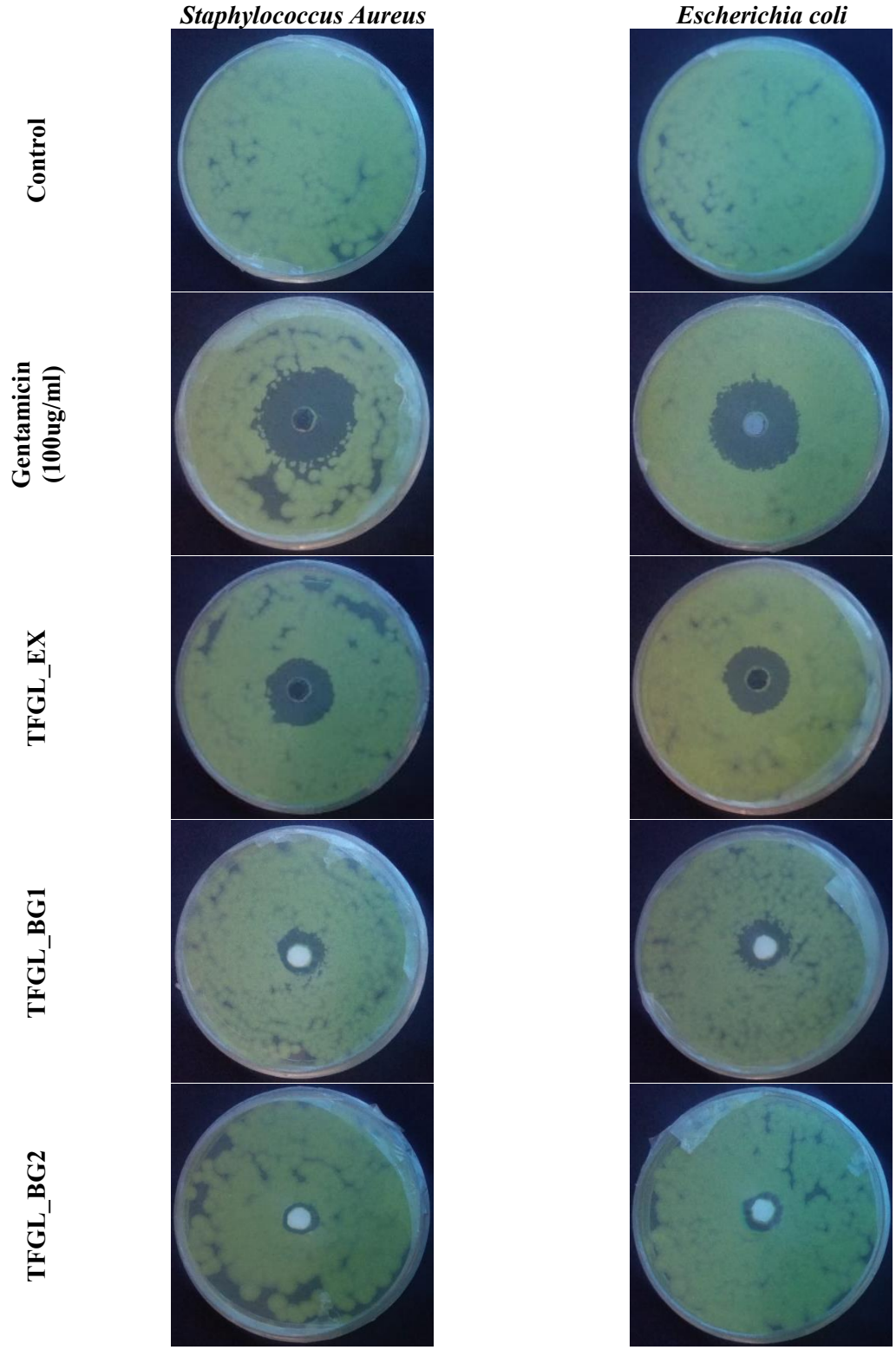

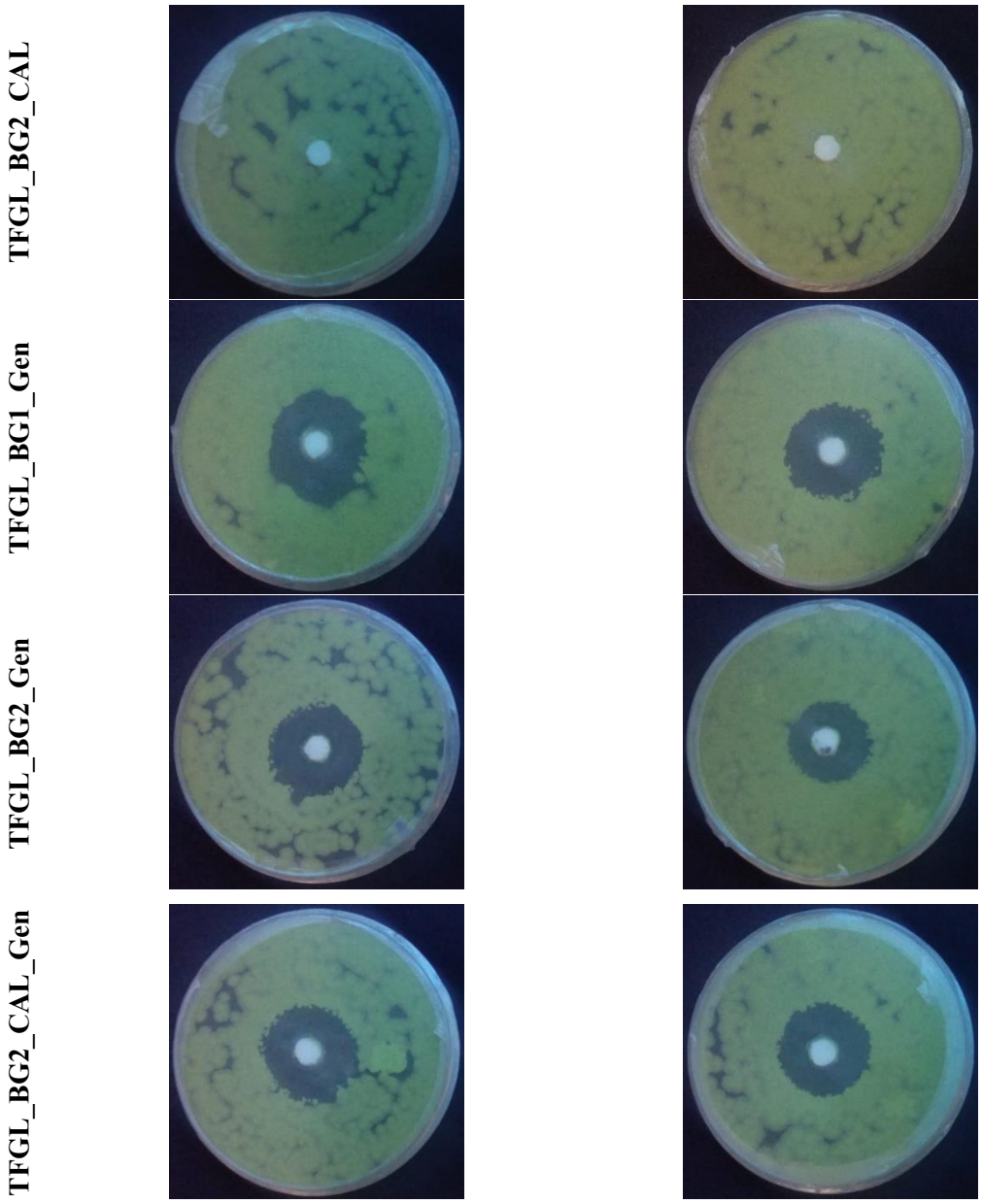

Fig. 4.10: Digital images for disk diffusion assay of TFGL_EX templated various BGNPs.

indicated antibacterial activity with 12 ± 2 mm ZOI for *S. aureus* and 15 ± 1 mm ZOI for *E. coli*. Naturally, ZOI for TFGL_BG1 (6 ± 1 mm ZOI for *S. aureus* and 10 ± 2 mm ZOI for *E. coli*) and TFGL_BG2 (3 ± 1 mm ZOI for *S. aureus* and 4 ± 1 mm ZOI for *E. coli*) were smaller compared to TFGL_EX due to possible hindrance in releasing the entrapped extract content from the BG network. Larger ZOI observed in case of TGFL_BG1 can be due to its comparatively higher extract content (**Table 4.2**), surface area (184.12 m^2g^{-1}) as well as pore volume (0.3229 cm^3g^{-1} **(Fig.2(b-d) and Table 4.4)**

than that of TFGL_BG2. Comparatively greater ZOI (>18 mm) could be observed for all drug loaded BGNPs than corresponding negative controls (TFGL_BG1, TFGL_BG2 and TFGL_BG2_CAL). Importantly, ZOI of all three-drug loaded BGNPs for the two different bacterial strains were consistent with its corresponding morphology **(Fig. 4.5),** the BET data (**Fig.2(b-d) and Table 4.4**) and cumulative drug release data respectively **(Fig.4.9a)**. Largest ZOI could be observed for TFGL_BG1_GEN when compared to all other BGNPs possibly due to the comparatively higher surface area and pore volume of TFGL_BG1 which results in maximum drug diffusion.

4.3.11. MTT Assay:

Cellular viability of various BGNPs was determined through MTT assay with increasing sample concentration (10 µg/mL, 50 µg/mL, 100 µg/mL, 500 µg/mL and 1000 µg/mL) against U2OS cell line **(Fig. 4.11)**. In general, cellular viability was

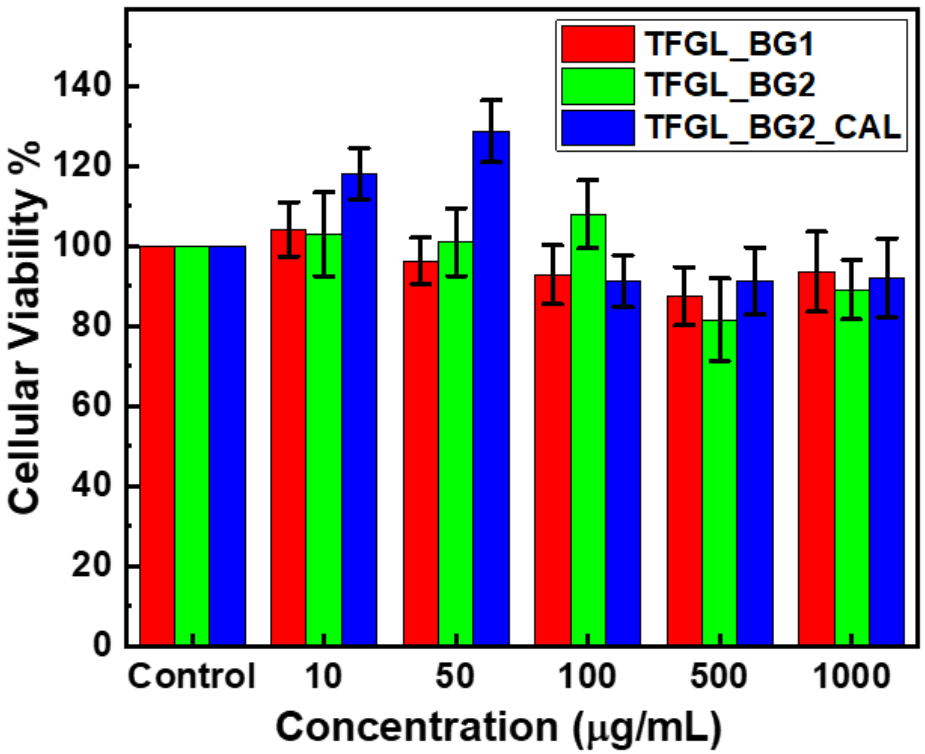

Fig. 4.11: Cellular viability assay for TFGL_EX templated various BGNPs.

observed to be above 80% for all BGNPs. This observation reveals that the content of various BGNPs does not influence viability of cells. The control untreated U2OS cells cultured in DMEM medium, are considered to have 100% cellular viability, while few cases of greater cellular viability than the control has been recorded. This is due to the uncertainty in cellular proliferation for longer duration [28]. These results prove cytocompatibility of BGNPs for U2OS cell lines and are in accordance with earlier reports [42,43]. The statistical analysis was carried out using one-way ANOVA for each material at different concentrations. No significant difference in toxicity was observed among different groups with varying concentrations.

4.3.12. Sustainability of Property Dependent TFGL_BG1:

In this study, TEOS and charcoal-treated aqueous *Trigonella foenum-graecum* leaf extract (TFGL_EX) was combined to create TFGL_BG1 under ambient conditions. The other inorganic elements (Ca, Na, and P) required for the synthesis of the BGNPs network were obtained directly from the TFGL_EX inorganic content. Additionally, the same TFGL_EX organic components (protein, fat, and carbohydrate) were also used as template molecules to synthesize BGNPs. As a result, nanosized, mesoporous TFGL_BG1 (Average pore diameter: 7.0146 nm) could be obtained with very high surface area (184.12 m^2g^{-1}). Interestingly, TFGL_BG1 was reported to have the highest gentamicin loading capacity (97.2 ± 2.1%) with sustained drug release. Mesoporous TFGL_BG1 interacted with SBF and displayed an excellent *in-vitro* bioactivity by depositing hydroxycarbonate apatite on its surface. The observation promises for the bone binding ability of TFGL_BG1. In addition, the remnants of the natural leaf extract in TFGL_BG1 induced its antibacterial property against *S. aureus* as well as *E. coli*. It is suggested that this substance is biocompatible for use in bone regeneration due to

observation of over 80% U2OS cellular viability even at concentrations as high as 1000 µg/mL. A detail comparison of TFGL_BG1 with other BGNPs (TFGL_BG2 and TFGL_BG2_CAL) synthesized by bio-inspired route thus confirms its efficient properties for biomedical applications. To our knowledge, only the sol-gel process, which uses organometallic precursors, organic solvents and synthetic polymer templates following high temperature calcination can produce such mesoporous BG materials [44–47]. In fact, the reported bio-inspired BG synthesis procedures require synthetic or biological molecules as structure-directing templates in addition to organometallic precursors [25,26,28,34]. Importantly, synthesizing such property-dependent BG samples for biological applications is difficult by utilizing the aforementioned procedures. Hence, there is no doubt that TFGL_BG1 is a sustainable property dependent BG material for biomedical applications.

4.4. Conclusion:

In summary, a simple and well-controlled sustainable synthesis of BGNPs has been established by employing aqueous leaf extract of TFGL. It is important to note that TFGL_EX serves as precursor for network formers and network modifiers in addition to working as a templating agent for the synthesis of BGNPs. Detailed elemental, FTIR and TGA analysis confirmed existence of extract contents in the BG network while maintaining BG composition required for demonstration of bioactive property. Nitrogen sorption analysis showed mesoporous nature of the BGNPs with high surface area, pore volume while HR-TEM confirmed its nanosize. On comparison of the three BGNPs, TFGL_BG1 outperformed TFGL_BG2 and its calcined counterpart (TFGL_BG2_CAL) in terms of bioactivity, biocompatibility, drug delivery and antibacterial susceptibility. This work provides a simple and sustainable strategy for large scale production of mesoporous BGNPs for a wide variety of biomedical applications.

REFERENCES:

[1] J. Singh, T. Dutta, K.H. Kim, M. Rawat, P. Samddar, P. Kumar, "Green" Synthesis of Metals and Their Oxide Nanoparticles: Applications for Environmental Remediation, Journal of Nanobiotechnology. 16 (2018) 1–24. https://doi.org/10.1186/s12951-018-0408-4.

[2] T.M. Abdelghany, A.M.H. Al-Rajhi, M.A. al Abboud, M.M. Alawlaqi, A. Ganash Magdah, E.A.M. Helmy, A.S. Mabrouk, Recent Advances in Green Synthesis of Silver Nanoparticles and Their Applications: About Future Directions. A review, Bionanoscience. 8 (2018) 5–16. https://doi.org/10.1007/s12668-017-0413-3.

[3] P. Malik, R. Shankar, V. Malik, N. Sharma, T.K. Mukherjee, Green Chemistry Based Benign Routes for Nanoparticle Synthesis, Journal of Nanoparticles. 2014 (2014). https://doi.org/10.1155/2014/302429.

[4] S.B. Ulaeto, G.M. Mathew, J.K. Pancrecious, J.B. Nair, T.P.D. Rajan, K.K. Maiti, B.C. Pai, Biogenic Ag Nanoparticles from Neem Extract: Their Structural Evaluation and Antimicrobial Effects against Pseudomonas nitroreducens and Aspergillus unguis (NII 08123), ACS Biomaterials Science and Engineering. 6 (2020) 235–245. https://doi.org/10.1021/acsbiomaterials.9b01257.

[5] S. Sukumar, A. Rudrasenan, D. Padmanabhan Nambiar, Green-Synthesized Rice-Shaped Copper Oxide Nanoparticles Using Caesalpinia bonducella Seed Extract and Their Applications, ACS Omega. 5 (2020) 1040–1051. https://doi.org/10.1021/acsomega.9b02857.

[6] F.G. Torres, O.P. Troncoso, L. Rodriguez, G.E. De-la-Torre, Sustainable Synthesis, Reduction and Applications of Graphene Obtained from Renewable

Resources, Sustainable Materials and Technologies. 29 (2021) e00310. https://doi.org/10.1016/j.susmat.2021.e00310.

[7] S. Matussin, M.H. Harunsani, A.L. Tan, M.M. Khan, Plant-Extract-Mediated SnO2 Nanoparticles: Synthesis and Applications, ACS Sustainable Chemistry and Engineering. 8 (2020) 3040–3054. https://doi.org/10.1021/acssuschemeng.9b06398.

[8] K.M. Metz, S.E. Sanders, J.P. Pender, M.R. Dix, D.T. Hinds, S.J. Quinn, A.D. Ward, P. Duffy, R.J. Cullen, P.E. Colavita, Green Synthesis of Metal Nanoparticles via Natural Extracts: The Biogenic Nanoparticle Corona and Its Effects on Reactivity, ACS Sustainable Chemistry and Engineering. 3 (2015) 1610–1617. https://doi.org/10.1021/acssuschemeng.5b00304.

[9] M. Rafique, I. Sadaf, M.S. Rafique, M.B. Tahir, A Review on Green Synthesis of Silver Nanoparticles and Their Applications, Artificial Cells, Nanomedicine and Biotechnology. 45 (2017) 1272–1291. https://doi.org/10.1080/21691401.2016.1241792.

[10] M. Shah, D. Fawcett, S. Sharma, S.K. Tripathy, G.E.J. Poinern, Green Synthesis of Metallic Nanoparticles Via Biological Entities, 2015. https://doi.org/10.3390/ma8115377.

[11] Hemlata, P.R. Meena, A.P. Singh, K.K. Tejavath, Biosynthesis of Silver Nanoparticles Using Cucumis prophetarum Aqueous Leaf Extract and Their Antibacterial and Antiproliferative Activity against Cancer Cell Lines, ACS Omega. 5 (2020) 5520–5528. https://doi.org/10.1021/acsomega.0c00155.

[12] P. Roy, B. Das, A. Mohanty, S. Mohapatra, Green Synthesis of Silver Nanoparticles Using Azadirachta Indica Leaf Extract and Its Antimicrobial Study, Applied Nanoscience (Switzerland). 7 (2017) 843–850. https://doi.org/10.1007/s13204-017-0621-8.

[13] E. Mazzoni, M.R. Iaquinta, C. Lanzillotti, C. Mazziotta, M. Maritati, M. Montesi, S. Sprio, A. Tampieri, M. Tognon, F. Martini, Bioactive Materials for Soft Tissue Repair, Front Bioeng Biotechnol. 9 (2021) 94. https://doi.org/10.3389/fbioe.2021.613787.

[14] M. Rizwan, M. Hamdi, W.J. Basirun, Bioglass® 45S5-Based Composites for Bone Tissue Engineering and Functional Applications, Journal of Biomedical Materials Research - Part A. (2017). https://doi.org/10.1002/jbm.a.36156.

[15] V. Miguez-Pacheco, L.L. Hench, A.R. Boccaccini, Bioactive Glasses Beyond Bone and Teeth: Emerging Applications in Contact with Soft Tissues, Acta Biomater. 13 (2015) 1–15. https://doi.org/10.1016/j.actbio.2014.11.004.

[16] Z. Cai, Y. Li, W. Song, Y. He, H. Li, X. Liu, Anti-Inflammatory and Prochondrogenic *In-situ* Formed Injectable Hydrogel Crosslinked by Strontium-Doped Bioglass for Cartilage Regeneration, ACS Applied Materials & Interfaces. 13 (2021) 59772–59786. https://doi.org/10.1021/acsami.1c20565.

[17] C. Pitta Kruize, S. Panahkhahi, N.E. Putra, P. Diaz-Payno, G. Van Osch, A.A. Zadpoor, M.J. Mirzaali, Biomimetic Approaches for the Design and Fabrication of Bone-to-Soft Tissue Interfaces, ACS Biomaterials Science & Engineering. (2021). https://doi.org/10.1021/acsbiomaterials.1c00620.

[18] E. Sharifi, A. Bigham, S. Yousefiasl, M. Trovato, M. Ghomi, Y. Esmaeili, P. Samadi, A. Zarrabi, M. Ashrafizadeh, S. Sharifi, R. Sartorius, F. Dabbagh Moghaddam, A. Maleki, H. Song, T. Agarwal, T.K. Maiti, N. Nikfarjam, C. Burvill, V. Mattoli, M.G. Raucci, K. Zheng, A.R. Boccaccini, L. Ambrosio, P. Makvandi, Mesoporous Bioactive Glasses in Cancer Diagnosis and Therapy: Stimuli-Responsive, Toxicity,

Immunogenicity, and Clinical Translation, Advanced Science. 9 (2022). https://doi.org/10.1002/advs.202102678.

[19] T.H. Dang, T.H. Bui, E. V. Guseva, A.T. Ta, A.T. Nguyen, T.T.H. Hoang, X.V. Bui, Characterization of Bioactive Glass Synthesized by Sol-Gel Process in Hot Water, Crystals (Basel). 10 (2020) 1–10. https://doi.org/10.3390/cryst10060529.

[20] B.A.E. Ben-Arfa, H.R. Fernandes, I.M.M. Salvado, J.M.F. Ferreira, R.C. Pullar, Effects of Catalysts on Polymerization and Microstructure of Sol-Gel Derived Bioglasses, Journal of the American Ceramic Society. 101 (2018) 2831–2839. https://doi.org/10.1111/jace.15450.

[21] T.A. Tuan, E. V. Guseva, L.H. Phuc, N.Q. Hien, N.V. Long, B.X. Vuong, Acid-free Hydrothermal Process for Synthesis of Bioactive Glasses 70SiO2–(30-x) CaO–xZnO (x = 1, 3, 5 mol.%), Proc West Mark Ed Assoc Conf. 62 (2020) 6. https://doi.org/10.3390/proceedings2020062006.

[22] B.T. Hoa, H.T.T. Hoa, N.A. Tien, N.H.D. Khang, E. V. Guseva, T.A. Tuan, B.X. Vuong, Green Synthesis of Bioactive Glass 70SiO2-30CaO by Hydrothermal Method, Materials Letters. 274 (2020) 128032. https://doi.org/10.1016/j.matlet.2020.128032.

[23] T.A. Tuan, E. V. Guseva, N.A. Tien, H.T. Dat, B.X. Vuong, Simple and Acid-Free Hydrothermal Synthesis of Bioactive Glass 58sio2-33cao-9p2o5 (Wt%), Crystals (Basel). 11 (2021) 1–11. https://doi.org/10.3390/cryst11030283.

[24] N. Gupta, D. Santhiya, A. Aditya, K. Badra, Dendrimer Templated Bioactive Glass-Ceramic Nanovehicle for Gene Delivery Applications, RSC Advances. 5 (2015) 56794–56807. https://doi.org/10.1039/c5ra04441c.

[25] H. Goel, D. Santhiya, Effect of Ph on Bio-Inspired Synthesis Of L-Lysine Templated Bioactive Glass Hybrid Xerogels for Tailored Textural and Rheological Properties, Materials Chemistry and Physics. 281 (2022) 125828. https://doi.org/10.1016/j.matchemphys.2022.125828.

[26] D. Santhiya, H.K. Alajangi, F. Anjum, S. Murugavel, M. Ganguli, Bio-inspired Synthesis of Microporous Bioactive Glass-Ceramic Using CT-DNA As a Template, Journal of Materials Chemistry B. 1 (2013) 6329–6338. https://doi.org/10.1039/c3tb21212b.

[27] N. Gupta, D. Santhiya, Role of Cellulose Functionality in Bio-Inspired Synthesis of Nano Bioactive Glass, Materials Science and Engineering C. 75 (2017). https://doi.org/10.1016/j.msec.2017.03.026.

[28] N. Gupta, D. Santhiya, S. Murugavel, A. Kumar, A. Aditya, M. Ganguli, S. Gupta, Effects of Transition Metal Ion Dopants (Ag, Cu and Fe) on the Structural, Mechanical and Antibacterial Properties of Bioactive Glass, Colloids and Surfaces A: Physicochemical and Engineering Aspects. 538 (2018) 393–403. https://doi.org/10.1016/j.colsurfa.2017.11.023.

[29] S.P. Lakshmanan, S.T. Jostar, G.J. Arputhavalli, S. Jebasingh, C.M.R. Josephine, Role of Green Synthesized CuO Nanoparticles of Trigonella Foenum-Graecum L. Leaves and their Impact on Structural, Optical and Antimicrobial Activity, International Journal of Nanoscience and Nanotechnology. 17 (2021) 109–121.

[30] H. Rizwana, M.S. Alwhibi, H.A. Aldarsone, M.A. Awad, D.A. Soliman, R.S. Bhat, Green Synthesis, Characterization, And Antimicrobial Activity of Silver Nanoparticles Prepared Using Trigonella foenum-graecum L. Leaves Grown in Saudi

Arabia, Green Processing and Synthesis. 10 (2021) 421–429. https://doi.org/10.1515/gps-2021-0043.

[31] M. Vergheese, S.K. Vishal, Green Synthesis of Magnesium Oxide Nanoparticles Using Trigonella foenum-graecum Leaf Extract and its Antibacterial Activity, J Pharmacogn Phytochem. 7 (2018) 1193–1200.

[32] M.A. Awad, A.A. Hendi, K.M. Ortashi, B. Alzahrani, D. Soliman, A. Alanazi, W. Alenazi, R.M. Taha, R. Ramadan, M. El-Tohamy, Biogenic Synthesis of Silver Nanoparticles Using Trigonella foenum-graecum Seed Extract: Characterization, photocatalytic and antibacterial activities, Sensors and Actuators A: Physical. 323 (2021) 112670. https://doi.org/10.1166/jctn.2018.7301.

[33] I. Zia, S. Mirza, R. Jolly, A. Rehman, R. Ullah, M. Shakir, Trigonella foenum-graecum seed Polysaccharide Coupled Nano Hydroxyapatite-Chitosan: A Ternary Nanocomposite for Bone Tissue Engineering, Int J Biol Macromol. 124 (2019) 88–101. https://doi.org/10.1016/j.ijbiomac.2018.11.059.

[34] N. Gupta, D. Santhiya, A. Aditya, Tailored Smart Bioactive Glass Nanoassembly for Dual Antibiotic: *In-vitro* Sustained Release Against Osteomyelitis, Journal of Materials Chemistry B. 4 (2016) 7605–7619. https://doi.org/10.1039/c6tb01528j.

[35] T. Kokubo, H. Takadama, How Useful is SBF in Predicting in Vivo Bone Bioactivity?, Biomaterials. 27 (2006) 2907–2915. https://doi.org/10.1016/j.biomaterials.2006.01.017.

[36] L.L. Hench, The story of Bioglass®, Journal of Materials Science: Materials in Medicine. 17 (2006) 967–978. https://doi.org/10.1007/s10856-006-0432-z.

[37] A.A. Alshehri, M.A. Malik, Facile One-Pot Biogenic Synthesis of Cu-Co-Ni Trimetallic Nanoparticles for Enhanced Photocatalytic Dye Degradation, Catalysts. 10 (2020) 1138. https://doi.org/10.3390/catal10101138.

[38] M. Oschatz, T.W. van Deelen, J.L. Weber, W.S. Lamme, G. Wang, B. Goderis, O. Verkinderen, A.I. Dugulan, K.P. De Jong, Effects of Calcination and Activation Conditions on Ordered Mesoporous Carbon Supported Iron Catalysts for Production of Lower Olefins from Synthesis Gas, Catal Sci Technol. 6 (2016) 8464–8473. https://doi.org/10.1039/C6CY01251E.

[39] A. Kumar, S. Murugavel, A. Aditya, A.R. Boccaccini, Mesoporous 45S5 Bioactive Glass: Synthesis, *In-vitro* Dissolution and Biomineralization Behavior, Journal of Materials Chemistry B. 5 (2017) 8786–8798. https://doi.org/10.1039/C7TB01738C.

[40] A. Kumar, S. Murugavel, Influence of Textural Characteristics on Biomineralization Behavior of Mesoporous SiO2-P2O5-CaO Bioactive Glass and Glass-Ceramics, Materials Chemistry and Physics. 242 (2020) 122511. https://doi.org/10.1016/j.matchemphys.2019.122511.

[41] N. Gupta, H. Goel, D. Santhiya, C.M. Srivastava, S. Mishra, P. Rai, Aqueous-Phased Electrospun Bioactive Glass Mineralized Gelatin-Pectin Hybrid Composite Fiber Matrix For 7-Dehydrocholesterol Delivery, ChemistrySelect. 5 (2020) 4364–4370. https://doi.org/10.1002/slct.202000264.

[42] T.E.L. Douglas, M. Dziadek, J. Schietse, M. Boone, H.A. Declercq, T. Coenye, V. Vanhoorne, C. Vervaet, L. Balcaen, M. Buchweitz, F. Vanhaecke, F. Van Assche, K. Cholewa-Kowalska, A.G. Skirtach, Pectin-Bioactive Glass Self-Gelling, Injectable

Composites with High Antibacterial Activity, Carbohydrate Polymers. 205 (2019) 427–436. https://doi.org/10.1016/j.carbpol.2018.10.061.

[43] G. Tommasi, S. Perni, P. Prokopovich, An Injectable Hydrogel as Bone Graft Material with Added Antimicrobial Properties, Tissue Engineering - Part A. 22 (2016) 862–872. https://doi.org/10.1089/ten.tea.2016.0014.

[44] G.J. Owens, R.K. Singh, F. Foroutan, M. Alqaysi, C.-M. Han, C. Mahapatra, H.-W. Kim, J.C. Knowles, Sol–gel Based Materials for Biomedical Applications, Prog Mater Sci. 77 (2016) 1–79. https://doi.org/10.1016/j.pmatsci.2015.12.001.

[45] C.H. Kong, C. Steffi, Z. Shi, W. Wang, Development of Mesoporous Bioactive Glass Nanoparticles and its Use in Bone Tissue Engineering, Journal of Biomedical Materials Research Part B: Applied Biomaterials. 106 (2018) 2878–2887. https://doi.org/10.1002/jbm.b.34143.

[46] H. Zhu, K. Zheng, A.R. Boccaccini, Multi-Functional Silica-Based Mesoporous Materials for Simultaneous Delivery of Biologically Active Ions and Therapeutic Biomolecules, Acta Biomaterialia. 129 (2021) 1–17. https://doi.org/10.1016/j.actbio.2021.05.007.

[47] S. Kaya, M. Cresswell, A.R. Boccaccini, Mesoporous Silica-Based Bioactive Glasses for Antibiotic-Free Antibacterial Applications, Materials Science and Engineering: C. 83 (2018) 99–107. https://doi.org/10.1016/j.msec.2017.11.003.

CHAPTER 5

Surface Patch Bound Collagen-Pectin Hydrogel Containing Bioactive Glass for Possible Tissue Regenerative Applications

CHAPTER 5

Surface Patch Bound Collagen-Pectin Hydrogel Containing Bioactive Glass for Possible Tissue Regenerative Applications

GRAPHICAL ABSTRACT

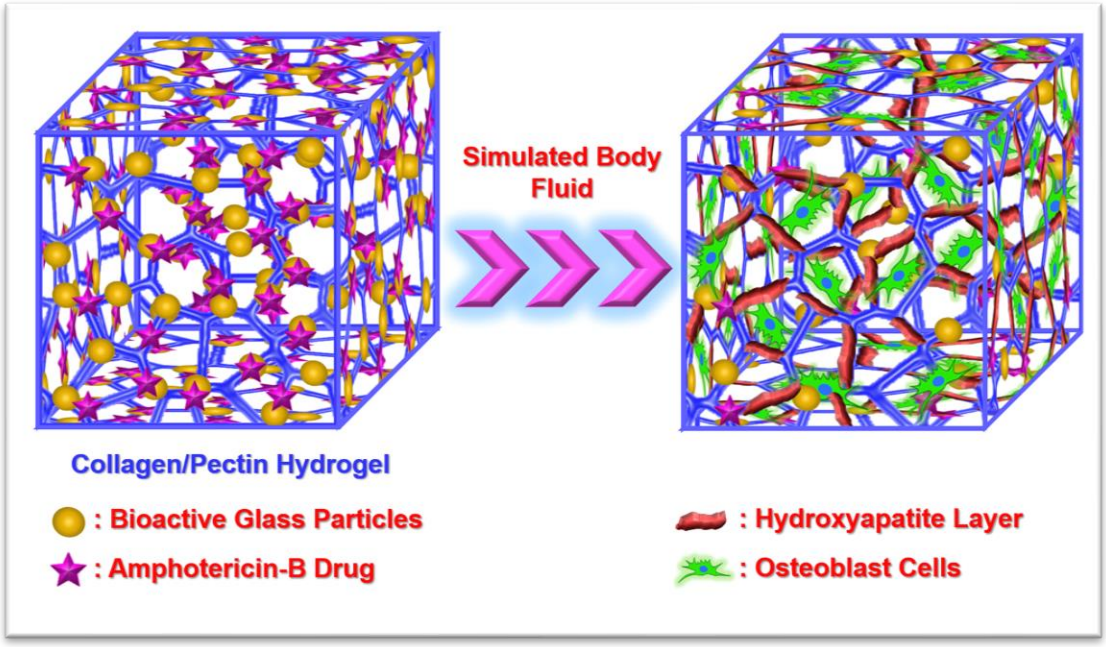

5.1. Introduction:

The architecture of native soft tissue to bone enthesis or interface is complicated due to its unique physiological composition and inherently poor healing capacity. Interface tissue engineering represents an attractive integrative strategy for functionally cementing soft and hard tissue and thereby improving the well-being of people exposed to its injuries.[1] Based on the numerous published reports, it is realized that future biomaterials must possess specific material properties in terms of design, composition, structure and functional features suitable for composite tissue graft.[1,2] One such type

of promising biomaterials are the hydrogels, three-dimensional cross-linked network possessing the capability of holding large amount of interstitial water while maintaining structural integrity. Hydrogels have excellent biological properties due to their ability to mimic the extracellular matrix. Their aqueous environment allows for the transport of substances such as nutrients and by-products of cell metabolism. Hydrogels have gained considerable attention in the past due to their widespread use in the medical field, particularly in various tissue regeneration applications.[3] They have an added advantage of positioning them at the target diseased site, thus enhancing the bioavailability of the incorporated drug. Many synthetic polymers have been explored in the fabrication of hydrogels;[4] however, the importance of natural biopolymers in the fabrication of biomaterials for tissue engineering has gained limited attention due to obvious reasons. Since the extracellular matrix (ECM) is mainly composed of collagen and proteoglycans, natural polymers have become popular candidate biomaterials for bone tissue engineering.[3] Pectin, a plant originated heterogeneous polysaccharide having a chemical structure similar to alginate, provides interesting properties as artificial ECM.[5] Importantly, easy to process pectin possesses anti-cancer and anti-inflammatory properties.[6,7] Collagen, an abundant protein of vertebrate, is not only the main component of bone ECM, but also is the load-bearing tissue of the muscles[8]. Due to these unique characteristics, both of these biopolymers are adequately placed for both soft and hard tissue engineering as well as for the formulations of tissue regenerative medicine in a variety of forms.[8,9]

Recently, the concept of design and applications of two polyelectrolyte based hybrid hydrogels has gained attention. In such systems, one polymer complements the other polymer, which results in the synergetic self-assembly of networks based on favourable surface charges. Interestingly, macromolecules possessing similar net charge can also

interact by an associative mechanism─through surface patch binding where the heterogeneous charge distribution on one of these allows for the surface selective associative interaction with its partner overcoming the same charge repulsion between segments.[10] Such interactions are predominantly noticed in polyampholyte-polyelectrolyte pairs. The persistence length of the polymer plays a key role in facilitating this type of binding.[11] A typical example is the development of dual gelling injectable hydrogel reported by Vo *et al*[12] and the bio-therapeutic pectin collagen composites[8] which suggests pectin as a compatible component for collagen in formulating scaffold with an increase in thermal stability of about 14 °C as compared to native collagen (62 °C). Moreover, pectin acts as an efficient inhibitor for resisting the action of collagenase on collagen, and in turn, increases its structural stability.[8] Pectin is also well known to interact with protein molecules through the freely available amino groups by lowering the effective glycation targets.[8] Apart from this, composites of polymers and bioglass particles have also been increasingly developed as both soft and hard tissue regenerating materials due to their superior bioactivity, biocompatibility, and biodegradability.[13] The inorganic particles can synergistically interact with the polymer network either through physical or chemical forces, which effectively improves the mechanical property and stability of the resultant composite hydrogels.[14] Different inorganic particles in the form of hydroxyapatite, calcium phosphate[15] and silica-based bioactive glass[14,16–20] have been explored in the past for bone tissue engineering applications. Of these, in the present report, we have utilized the bone regenerative ability of third-generation biomaterial i.e., bioactive glass as inorganic particles by *in-situ* mineralizing them in a dual-polymer based hybrid hydrogel system.

Highly cross-linked hydrogels were interacted with bioactive glass prepared previously

through photopolymerization of gelatin methacryloyl[14] and poly(ethylene glycol) dimethacrylate.[16] Applications of various formulations of bioglass for tissue engineering have been clearly shown in the literature. Recently, injectable and self-healing Au-based 4-arm thiol terminated poly(ethylene glycol) dynamic hydrogel containing bioactive glass nanoparticles for bone regeneration has been proposed.[17] Carbohydrate based hydrogel such as dextran[18] and β-chitin with the incorporation of bioactive glass has also been reported. Recently, stimuli-responsive thermo-gelling chitosan–collagen–bioactive glass hybrids[19] as well as chitosan-beta-glycerophosphate salt formulations combined with bioactive glass nanoparticles[20] have been developed as a potential injectable system for tissue engineering. It is pertinent to note that most of the reported procedures till date use the pre-prepared bioactive glass as a reinforcing agent in the composite hydrogel. In contrast, in the present work, *in-situ* mineralized bioactive glass was incorporated into the hybrid hydrogel, a protocol which imparts sufficient novelty to this work.

Microbial infection is a severe health issue concerning tissue regeneration, wound healing and recovery after surgery. Infection can prolong the healing process, leading to tissue morbidity and sepsis.[21] Candida species are the most common pathogen related to such type of infection[21,22] in various parts of the body including skin, mouth, gastrointestinal tract, vascular system and wounds related to both soft and hard tissues.[23] It may lead to serious complications or may even cause death.[23] Amphotericin-B (AmB) is a broad-spectrum antifungal drug effective against a wide range of most frequently occurring fungal infections including candida species.[23,24] To overcome its well-known side effects,[24] novel AmB delivery methods are being developed. For example, Shu *et al*[24] conjugated AmB with polypeptide hydrogel to increase its solubility in aqueous media. Demirci *et al*[23] synthesized levan based

hydrogel for controlled release of AmB. Sosa *et al*[22] reported AmB loaded pluronic (P407) thermo-reversible gel for the dermal and vaginal treatment of candidiasis.

To the best of our knowledge, first time an attempt has been made for the *in-situ* mineralization of bioactive glass in collagen-pectin based hybrid hydrogel matrix. The novelty of the work lies in the fact that one of the bioactive glass precursors namely calcium acetate, acts as the pseudo crosslinker and results in hydrogel formation, regardless of the fact that both biopolymers carried net charge of same polarity. This procedure excludes the need of any external crosslinker. It is postulated that the proposed hybrid composite hydrogel matrix not only would remain helpful in both soft and hard tissue engineering but also prevent microbial infections.

5.2. Experimental Section:

5.2.1. Materials:

For the fabrication of hydrogels, pectin with esterification 55 % to 70 % was purchased from Sigma-Aldrich, USA, and collagen was obtained from Sisco Research Laboratories (P) Ltd., Mumbai, India. Additionally, the precursors tetraethyl orthosilicate (TEOS), triethyl phosphate (TEP), sodium acetate and calcium acetate monohydrate, used for the *in-situ* mineralization of bioactive glass (BG) particles, were obtained from Sigma-Aldrich, USA. Hank's Balanced Salt solution (simulated body fluid (SBF)) purchased from Sigma-Aldrich; USA was used for *in-vitro* bioactivity test. Test microorganism, namely *Candida albicans* MCC1151, was obtained from National Centre for Microbial Resource, Pune, India. The broad-spectrum antifungal drug Amphotericin-B (AmB) was procured from Pharmaceutical and Research Laboratories (P) Ltd., Bangalore, India. Cell studies were carried out using U2OS, a human osteoblast-like osteosarcoma cell line and HaCaT, which is an adult keratinocyte cell

line and were obtained from National Institute of Immunology, Delhi and National Centre for Cell Science, Pune, India, respectively. For all the experimental work, Milli-Q water was used. All reagents used in these experiments were of analytical reagent (AR) grade of high purity. All procedures were performed at room temperature of 25 °C unless otherwise stated.

5.2.2. Synthesis of Hybrid Hydrogels:

5.2.2.1. Preparation of Collagen/Pectin Solution:

Initially, collagen and pectin solutions were prepared in 10 mM Trizma buffer at pH 8.0 by continuous stirring for 1 h at a desired concentration and composition ratio. The freshly prepared solutions were analyzed to study the best fit composition ratio for the synthesis of hydrogel. The identification code of the samples used in this study are represented as xC:yP which refers to a given sample containing x mg/mL of collagen

Table 5.1: Various concentrations of collagen (C) and pectin (P) solution mixtures used to determine the best fit composition for the hydrogel synthesis.

Coding	Concentration of collagen (mg/mL)	Concentration of Pectin (mg/mL)
C	50	0
P	0	50
20C:10P	20	10
10C:20P	10	20
10C:1P	10	1
1C:10P	1	10
5C:5P	5	5
10C:10P	10	10
20C:20P	20	20
50C:50P	50	50

and y mg/mL of pectin, respectively. (**Table 5.1**)

5.2.2.2. Control Hydrogels:

Initially, a homogenous 1:1 (v/v) solution of collagen and pectin, each having a concentration of 5 % (w/v) was prepared in 10 mM Trizma buffer at pH 8.0 by continuous stirring for 1 h. Thereafter, calcium acetate solution was added dropwise from its stock solution to obtain the desired concentrations (25 %, 50 % ,75 % and 100 % (w/v)) (**Table 5.2**). The concentration of stock calcium acetate solution was maintained at 63.6 % (w/v) based on our previous report on 45S5 bioglass composition.[25] Interestingly, gel formation was noticed during the dropwise addition of the required amount of calcium acetate solution to the collagen/pectin solution. Hydrogel synthesis was carried out in 3 mL glass vials and the total gel volume was maintained at 1 mL. The obtained gel was kept in a water bath at 37 °C for 24 h, lyophilized overnight and preserved in the desiccator. A control hydrogel series (CPCa)

Table 5.2: Various compositions of CPCa hydrogel series.

Various Compositions of CPCa Hydrogels	**Precursor**
	Calcium Acetate
CPCa_20	0.053 M
CPCa_25	0.066 M
CPCa_40	0.106 M
CPCa_50	0.133 M
CPCa_60	0.160 M
CPCa_75	0.199 M
CPCa_90	0.239 M
CPCa_100	0.266

using different concentrations of calcium acetate were made and named according to their respective Ca^{2+} content as CPCa_25, CPCa_50, CPCa_75, and CPCa_100.

5.2.2.3. Hydrogel Series Containing BG Particles:

Initially, a 1:1 homogenous solution of collagen/pectin was prepared as mentioned in the previous section. Then, BG precursors, namely TEOS, TEP, sodium acetate and calcium acetate were sequentially added dropwise, at an interval of 30 min while maintaining the required concentrations, to obtain the 45S5 composition (**Fig. 5.1**). Here again, during the dropwise addition of calcium acetate, gel formation was noticed, which was stored as mentioned earlier.

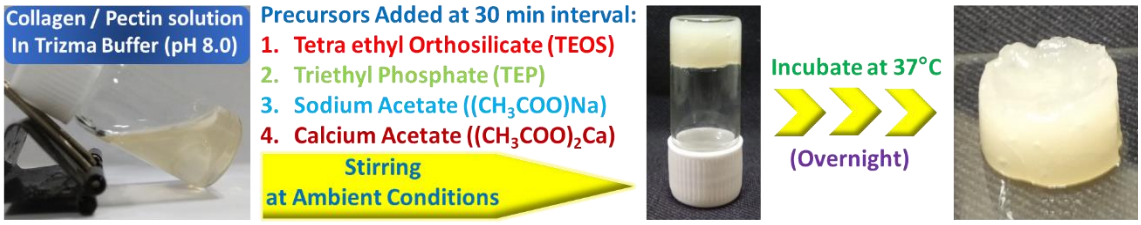

Fig. 5.1: Schematic illustration for the synthesis of collagen/pectin hybrid composite hydrogel containing *in-situ* mineralised bioactive glass particles.

It is pertinent to note that considering 45S5 composition as 100 %,[25] bioactive glass particles were also mineralized by varying the precursor concentration from 25 % to 100 % (w/v) (**Table 5.3**) in the hydrogel matrix. The obtained hydrogel series (CPBG) containing *in-situ* mineralized bioactive glass were named as CPBG_25, CPBG_50, CPBG_75, CPBG_100 as per the concentration of BG precursors used.

5.2.2.4. Drug Loading:

The broad-spectrum antifungal drug amphotericin-B(AmB) was loaded by soaking the as prepared lyophilized hydrogels (1 cm diameter and 1 cm thick (CPCa and CPBG series)) in 1000 µL (0.5 mg/mL) drug solution for 6 h. The obtained hydrogels were

named as CPCa_25_AmB, CPCa_50_AmB, CPCa_75_AmB, CPCa_100_AmB, CPBG_25_AmB, CPBG_50_AmB, CPBG_75_AmB and CPBG_100_AmB.

Table 5.3: Various compositions of bioactive glass precursors used in CPBG hydrogel series.

Various Compositions of CPBG Hydrogels	BG Precursors			
	Tetraethyl Orthosilicate	Triethyl Phosphate	Sodium Acetate	Calcium Acetate
CPBG_20	0.089 M	0.011 M	0.155 M	0.053 M
CPBG_25	0.111 M	0.014 M	0.194 M	0.066 M
CPBG_40	0.178 M	0.022 M	0.31 M	0.106 M
CPBG_50	0.222 M	0.027 M	0.387 M	0.133 M
CPBG_60	0.267 M	0.033 M	0.465 M	0.160 M
CPBG_75	0.333 M	0.041 M	0.581 M	0.199 M
CPBG_90	0.400 M	0.049 M	0.697 M	0.239 M
CPBG_100	0.445 M	0.055 M	0.775 M	0.266 M

5.2.3. Characterization of Hydrogels:

5.2.3.1. Turbidity Measurement:

Turbidity measurements of collagen/pectin solution at 10 times dilution (for various compositions reported in **Table 5.1** were performed on a UV-Vis spectrophotometer (Model CE7300, Cecil Instruments, UK) operating at 400 nm which was calibrated to 100 % transmittance (T) against deionized water. Turbidity was calculated as 100 - T%.

5.2.3.2. Zeta Potential Measurement:

Zeta potential measurement of collagen/pectin solution at 10 times dilution (for various compositions mentioned in **Table 5.1** were recorded using a Zetasizer (Model ZSP,

Malvern Instruments, UK). An average of three zeta potential readings was taken for each sample.

Further, a detailed explanation for sample preparation and instrument specification for characterization tools used for analysing lyophilized hydrogels was already discussed in Chapter 2. Structural determination of various lyophilized hydrogels was analyzed using XRD, FTIR, TGA and nitrogen sorption analysis as described in section 2.1.1, 2.1.2, 2.1.4 and 2.1.5.

5.2.3.3. Morphological Studies:

The surface morphology of various lyophilized samples was recorded using scanning electron microscopy SEM (ZEISS EVO MA15). The samples were gold coated and then observed in the SEM at accelerating voltage of 5 kV at 10,000 magnifications. The hydrogels were also subjected to Energy Dispersive X-Ray Analysis (EDAX) operated at the voltage of 20 kV using (ZEISS EVO MA15) to investigate the presence of Si, P, Na, Ca ions in various samples. Additionally, *in-situ* mineralized bioactive glass particles and the porosity of the hydrogel matrix were also characterized using a transmission electron microscope (TEM) (Tecnai G2 200 KV HRTEM SEI HOLLAND) operating at an accelerating voltage of 200 kV.

5.2.3.4. Swelling Studies and Kinetic Analysis:

The swelling measurement of the hydrogels (1 cm dia. and 1 cm thick) were examined

in simulated body fluid (SBF) buffer at 25 °C. At a pre-determined interval, the hydrogels were taken out, the excess surface liquid was wiped using a filter paper (Whatman filter paper grade, No. 2), and the weight of swollen hydrogel was measured using Sartorius BSA 2245 balance as per the standard procedure.[23] Thereafter, the

swelling ratio (S), equilibrium buffer content (EBC), swelling kinetic analysis (dS/dt) and buffer diffusion coefficient (D) was determined as follows:

The swelling ratio of the samples was determined using Eq. (5.1)[26]

$$S = \frac{Weight\ of\ swollen\ hydrogel\ at\ time\ t\ (W_t) - Weight\ of\ dry\ hydrogel\ (W_0)}{Weight\ of\ dry\ hydrogel\ (W_0)} \quad [5.1]$$

Further, the equilibrium buffer content (EBC) of the hydrogels was calculated from Eq. (5.2),

$$EBC\% = \frac{Weight\ of\ hydrogel\ at\ equillibrium\ (W_e) - Weight\ of\ dry\ hydrogel\ (W_0)}{Weight\ of\ dry\ hydrogel\ (W_0)} X100 \quad [5.2]$$

A simple kinetic analysis was performed using the second-order equation (i.e., phenomenal model, Eq. (5.3),

$$\frac{dS}{dt} = k_S \left(S_{eq} - S\right)^2 \quad [5.3]$$

where $\frac{dS}{dt}$ is the rehydration ratio, k_S is the rate of constant swelling, S_{eq} denotes the degree of swelling at equilibrium, and S is swelling ratio at t. After applying definite integration with the boundary conditions of S = 0 at t = 0 and S = S_{eq} at t = t, Eq. (5.3) becomes:

$$\frac{t}{S} = A + Bt \quad [5.4]$$

where A ($1/k_s\ S^2_{eq}$) is the inverse of the initial swelling rate ($1/r_0$) and B ($1/S_{eq}$) is the inverse of the degree of swelling equilibrium.[26]

The swelling mechanism of the samples was determined by Eq. (5.5):

$$F = \frac{M_t - M_0}{M_0} = kt^n \quad [5.5]$$

where M_t is the mass of the swollen hydrogels at time t, M_0 is the mass of the dry hydrogel at time 0, k is the swelling constant related to the structure of the network, and

n is the swelling exponent.

The diffusion coefficients of the cylindrical hydrogels were calculated from Eq. (5.6):

$$D = \pi r^2 (\frac{k}{4})^{\frac{1}{n}} \quad [5.6]$$

In this equation, D is in $cm^2\ s^{-1}$, n is the diffusional exponent, and r is the radius of cylindrical hydrogel samples.[26]

Additionally, disintegration of CPCa_25 and CPBG_25 hydrogels (1 cm dia. and 1 cm thick) were also monitored after swelling equilibrium in SBF overnight followed by determining the weight loss in the sample (% disintegration) at the end of each preset time point.

5.2.3.5. Rheological Analysis:

Pre-formed gels/hydrogels were used for the rheological characterization using a stress controlled AR-500 rheometer (TA Instruments, U.K.) equipped with cone -plate geometry (2^0, 25 mm). A constant stress of 1 Pa and truncation gap of 58 μm was maintained in all the measurements. Rheology experiments were performed with the objective to map the viscoelastic profiles of various concentrations of CP solution mixtures (**Table 5.1**), CPCa_25 and CPBG_25. In order to thermally equilibrate the sample with the instrument a waiting time of 10 min was used. The mechanical spectra were measured by isothermal temperature sweep experiments which yielded the storage (G′) and loss modulus (G″) as a function of angular frequency (ω) in the range of 1 to 100 rad/s.

5.2.3.6. Bioactivity Test:

In-vitro bioactivity of various hydrogel samples was performed by monitoring the

formation of bone-like hydroxyapatite on the surface of the bioglass as per the procedure described by Kokubo et al.[27]. The room dried hydrogel samples containing bioglass particles of size 1 cm dia. and 1 cm thick was immersed in simulated body fluid (SBF) of volume 10 mg/mL. The samples were incubated at 37 °C under sterile conditions by changing the SBF solution every 3 days in order to avoid the effect of a decrease in cationic concentration in the SBF solution, which otherwise may decrease the ease of hydroxyapatite formation. After the required interval of time, the samples were removed, washed with milli-Q water thrice and lyophilized. They were further characterized using FTIR, XRD, SEM and BET analysis.

5.2.3.7. Drug Entrapment Analysis:

To estimate the percentage AmB entrapment efficiency in CPCa and CPBG series, equal-sized hydrogel samples (1 cm dia. and 1 cm thick) were crushed, weighed, suspended in water for 24 h, centrifuged and subjected to quantitative analysis using UV-vis spectrophotometer (Agilent Technologies Carry 300 UV-vis) to determine the change in the absorbance at a characteristic wavelength of 320 nm as per the procedure described by Hudson *et al.*[28] Experiments were conducted in triplicates and the entrapment efficiency was calculated as follows:

$$\text{Drug entrapment efficiency (\%)} = \frac{\text{Actual drug content}}{\text{Total drug content}} \times 100 \qquad [5.7]$$

5.2.3.8. Drug Release Kinetics:

To determine the quantity and rate of drug release, the CPBG_25_AmB hydrogel sample was immersed in SBF at the concentration of 10 mg/mL. Further, at pre-determined intervals, 1 mL of solution was taken out and subjected to quantitative

analysis as described by Hudson *et al.*[28] Experiments were conducted with required volume corrections and in triplicates. Further, the drug release mechanism was analyzed for the samples along with kinetics using various drug diffusion models[29,30] as follows:

The mathematical modelling used are as follows:

Zero-order kinetic model: $\frac{M_t}{M_\infty} = kt$

First-order kinetic model: $ln\left(1 - \frac{M_t}{M_\infty}\right) = -kt$

Higuchi model: $\frac{M_t}{M_\infty} = kt^{1/2}$

Peppas model: $\ln\left(\frac{M_t}{M_\infty}\right) = nlnt + lnk$

where, $\mathbf{M_t}$ is the amount of drug released at time t,

$\mathbf{M_\infty}$ is the total amount of drug released,

$\frac{\boldsymbol{M_t}}{\boldsymbol{M_\infty}}$ is the fraction of drug released at time t,

k is a rate constant which depends on the geometrical and structural characteristics of the drug-loaded polymeric system,

n is the diffusion exponent which indicates the drug release kinetics mechanism. If, the value of release exponent $n \leq 0.5$, it corresponds to Fickian diffusion release during which the solvent penetration is the rate-limiting step, while if the value of n lies between $0.5 < n < 1$, it corresponds to non-Fickian diffusion or anomalous diffusion i.e. drug release follows both erosion mechanisms and diffusion and if, $n = 1$ corresponds to

the case, where the drug release is independent of time[29,31]

5.2.3.9. Cell Culture Studies:

Biocompatibility of the drug (AmB) loaded hydrogels under study were evaluated against both human osteoblast like osteosarcoma (U2OS) and keratinocyte (HaCaT) cell lines. The cellular viability was monitored through both 3-(4,5-dimethylthiazol-2-yl)-2,5-diphenyl tetrazolium bromide (MTT) and Lactate dehydrogenase (LDH) assay after 24 h. While the cellular proliferation ability of the U2OS cells were explored in the 3D cell culture construct of the CPBG_25 hydrogel. The detailed procedure for Cell culture studies and biocompatibility studies is as follows:

5.2.3.9.1. Cell Studies against U2OS and HaCaT Cell Lines:

The U2OS and HaCaT cell lines were maintained separately in Dulbecco's Modified Eagle's Medium (DMEM F12), purchased from Thermo Fisher Scientific supplemented with 10 % v/v fetal bovine serum and 0.1 % v/v streptomycin. The cells were incubated at 37 °C with 5 % CO_2 up to 80 % confluency, then washed thrice with 1X phosphate buffer saline and detached using trypsin. The cells were counted using Hemocytometer and diluted to a cell density of 10^4 cells/mL using a fresh DMEM F12 medium.

5.2.3.9.2. Biocompatibility Studies:

5.2.3.9.2.1. MTT Assay:

The MTT assay analysis was performed on the drug (AmB) loaded various hydrogel samples in powdered form. For the analysis, the samples were placed in 96 well plate at a concentration of 10, 50 and 100 μg/mL and seeded with the U2OS and HaCaT cell density of 1 X 10^4 cells per well. The plates were incubated at 37 °C with 5 % CO_2 for 24 h. After 24 h, 100 μL of 5 % MTT reagent was added in each well and incubated for

2 h at 37 °C, for the formation of formazan crystals. The crystal growth was also visualized using optical Microscope (Floid Cell Imaging Station). After the crystal formation, 100 µL dimethyl sulfoxide was added to dissolve the formed formazan crystals. Then, the absorbance of the sample was observed using a TECAN multimode microplate reader at a wavelength of 570 nm and 630 nm. Similarly, the positive control experiment was also performed simultaneously using the same cell density. All the experiments were performed thrice and the data were represented as mean standard deviation. The statistical difference was analyzed using Students' GraphPad and a P-value of > 0.05 was obtained.

5.2.3.9.2.2. Lactate Dehydrogenase Assay (LDH) Assay:

Percentage cellular toxicity for the sample CPCa_25_AmB and CPBG_25_AmB was also quantified using LDH Assay. Herein, the required sample (10 µg/mL) were checked for biocompatibility in both cell lines i.e., U2OS and HaCaT cell lines for 24 h separately. LDH assay was carried out as per the standard protocol mentioned by the manufacture (Sigma-Aldrich).

5.2.3.9.3. 3D Cell Culture Studies:

5.2.3.9.3.1. Seeding Method of U2OS Cells:

For 3D cell culture, hydrogels precursors (50 µl/well) were mixed with U2OS cells and cast in each well of the 96 well plate under the sterile condition and mixed with cross-linker and dried at 37 °C in incubators for 1-2 h. The incubated hydrogels were reconstituted in DMEM-F12 with 10 % FBS and kept in 37° C, 5% CO_2 incubators.

5.2.3.9.3.2. FDA/PI Assay:

Initially, the cellular morphology, attachment, spreading, visual proliferation and

stability of hydrogel in culture conditions were observed through an optical microscope (Floid Cell Imaging Station) on 1, 3 and 7 days for standardizing the cell growth. Followingly, fluorescence-based live-dead assays were carried out on hydrogels. Herein, the staining protocol (Ibidi web protocol)[32] comprised of fluorescein diacetate (FDA) (sigma, F7378) and propidium iodide (PI) (Sigma), which stain viable cells and dead cells, respectively.

Briefly, the FDA sock solution was prepared by dissolving 5 mg/mL FDA in acetone and stored at -20 ° C until further use. The PI stock solution was prepared by dissolving 2 mg/mL PI in PBS and stored at 4 °C. The staining solution was prepared as prescribed (8 µL in 5 mL of Opti-MeM (Invitrogen) for FDA and 10µL in 1mL of PBS for PI). For staining, media was removed from each well and 100 µL each of FDA and PI was added subsequently with 2 washes of PBS in between. The staining was done for 3-5 min in the cell culture incubators. Post staining, wells were washed with PBS, reconstituted in optimum and imaged using an inverted fluorescence microscope (Floid Cell Imaging Station).

5.2.3.10. Antifungal Susceptibility Tests:

The fungicidal properties of AmB loaded various hydrogels were studied against Candida albicans. Herein, disc diffusion assay (AATCC-30) was carried out by placing a drug-loaded hydrogel pellet into the well present in the middle of the agar plates of considered fungal strain culture. The plates were then incubated for 24 h at 37 °C and then observed for the zone of inhibition. Experiments were conducted in triplicates along with appropriate controls.

5.3. Results and Discussion:

5.3.1. Interaction Studies:

It is important to understand the interaction of collagen with pectin before discussing the details of hydrogel characterization. As we know, the relative biopolymer content is an important parameter that affects the complexation mechanism. Thus, the degree of associative interaction between the two biopolymers was evaluated as function of the biopolymer content through turbidity test. Turbidity is directly proportional to concentration (number density of particles) of solutes present in the solution, interparticle interaction, and their conformation. In a typical experiment, the turbidity value was found to increase with the concentration of collagen and pectin in 1:1 (v/v) mixing ratio sample (**Fig. 5.2a**). Higher turbidity value for samples at this mixing ratio indicated dominant interaction between the two biopolymers that promoted complexation. Corresponding zeta potential measurements (**Fig. 5.2b**) revealed least negative values for these samples.

As per the well-known protein-polysaccharide interaction phenomena, since collagen and pectin both carry the same net charge they are considered as non-interacting biopolymers.[33] However, interestingly, in the present investigation regardless of same charge polarity, these biopolymers formed a single phase by self-organizing in the medium with the help of existing physical forces in a milieu of electrostatic repulsion. Recently, there are reports of stable soft matter synthesized with biopolymers of same polarity,[10] which showed remarkable tenability in their physical properties. This is another case of same family. These physical forces could be any or a combination of the following: excluded volume, hydrogen bonding, hydrophobic, ion-bridging, van der Waals interactions etc as proposed by Dickinson[33]. A lesser known interaction, called

the surface selective patch binding, has been shown to be responsible in the formation of inter-polymer complexes.[34] A clear manifestation of this is noticed in the 50C:50P

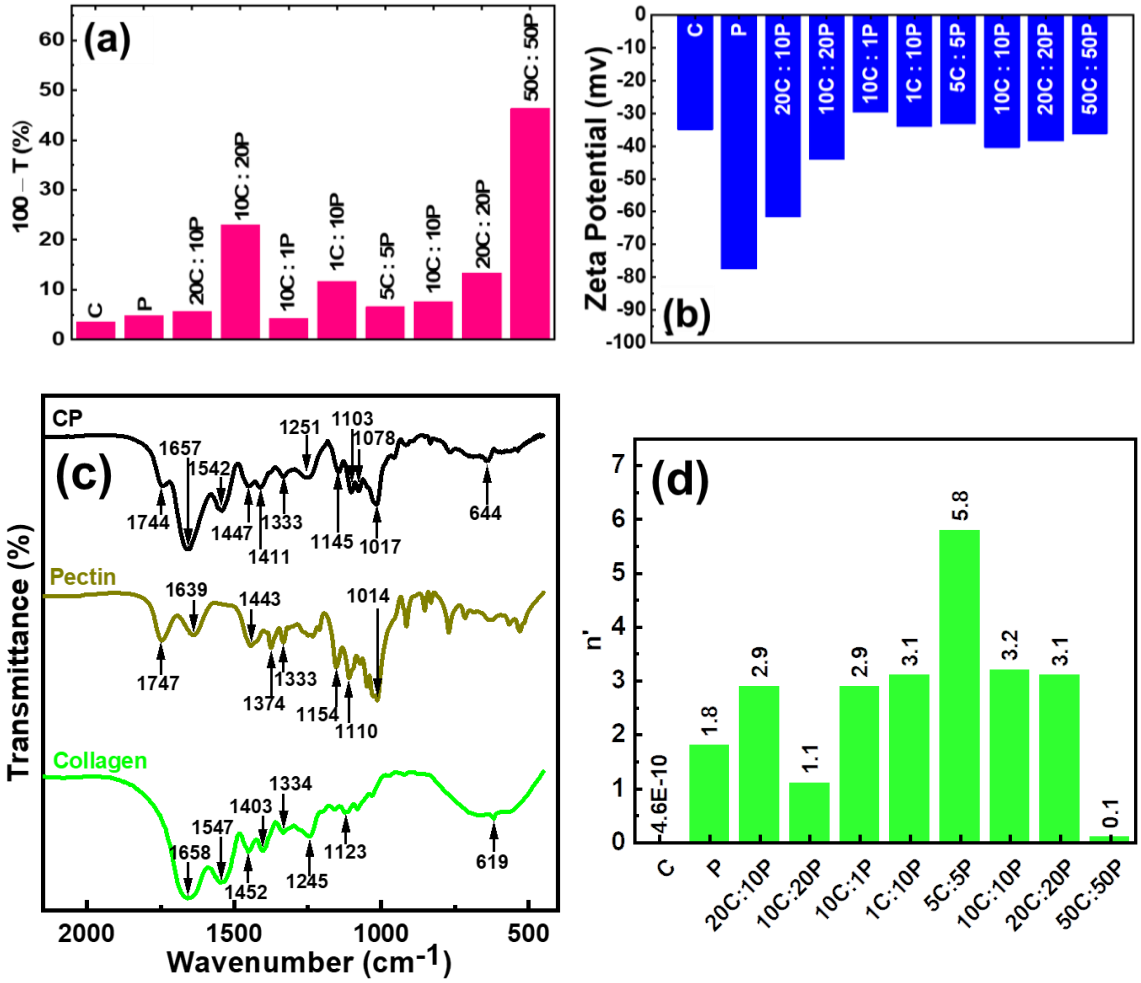

Fig. 5.2. (a) Turbidity measurement and **(b)** Zeta Potential measurement for various compositions of collagen/pectin mixture in trizma buffer (10mM, pH-8.0) **(c)** FTIR spectra for lyophilized collagen(C), pectin (P) and collagen/pectin (CP) blend. **(d)** The frequency dependence data fitted to the stress relaxation power law function, $G'(\omega) \approx \omega^{n'}$ where $0 < n' < 1$ reflects the gel behaviour. The value of n' close to 0 for the collagen and pectin in 1:1 ratio with 50 mg/mL each, implied the gel nature of the system.

sample that showed maximum turbidity and minimum zeta potential (**Fig. 5.2a and 5.2b**). Since pectin is a polyanionic biopolymer, and collagen is a polyampholyte, the positively charged patches on collagen will selectively bind to the negatively charged

segments of pectin overcoming the overcoming the inter-segment like-charge repulsion. This is facilitated by the heterogeneous charge distribution on collagen. Many proteins have shown binding with same polarity polyelectrolytes through this interaction protocol.[10] The recorded FTIR spectra (**Fig. 5.2c**) of collagen (C)[9] and pectin (P)[7] are consistent with the literature data. In the collagen-pectin (CP) sample, the characteristic —C=O stretching of pectin appeared as a small shoulder at 1744 cm^{-1} whereas, peaks ascribed to amide I of collagen at 1658 cm^{-1} and carboxylate group (—COO^{-}) of pectin at 1639 cm^{-1} overlapped at 1657 cm^{-1} as a strong and sharp peak in the spectrum. Amide II bond of collagen at 1547 cm^{-1} appeared at 1542 cm^{-1}. The —COO^{-} symmetrical stretching observed at 1442 cm^{-1} and 1403 cm^{-1} for collagen was noticed at 1411 cm^{-1} in the case of CP sample. Amide III of pure collagen was seen at 1245 cm^{-1}, which shifted to 1251 cm^{-1} for the CP sample. The above mentioned changes in FTIR footprint of the characteristic functional groups clearly indicate the existence of inter-polymer binding in the CP samples. These results confirmed collagen and pectin molecules existed as a hybrid complex prior to the formation of a stable hydrogel.

5.3.2. Rheological Studies on Collagen/Pectin Sol:

Rheology measurements were performed to probe the viscoelastic properties of the sol pre-formed biopolymer blends (**Table 5.1**) as a function of the mixing ratio. In the isothermal frequency sweep studies, the dispersion behaviour of the in-phase (G′, storage) and out-of-phase (G″, loss) modulus were observed at a constant oscillatory stress. This frequency dependence data was fitted to the stress relaxation power-law function given by $G'(\omega) \sim \omega^{n'}$, where $0 < n' < 1$ is considered as the reflection of the viscoelastic nature of the gel.[35] The variation in the value of n' with change in the mixing ratio of collagen and pectin depicted (**Fig. 5.2d**) that collagen and pectin in the ratio of 1:1 (50 mg/mL each) possessed the best gel forming ability. Hence, this

particular composition was used to make a series of following hydrogels. A control hydrogel series-I (CPCa) named after the respective Ca^{2+} crosslinker content as CPCa_25, CPCa_50, CPCa_75, CPCa_100 (**Table 5.2**), and a hydrogel series II (CPBG) containing bioactive glass (BG) designated as CPBG_25, CPBG_50, CPBG_75, and CPBG_100 (**Table 5.3**) as per the concentration of BG precursors, were prepared and used. The corresponding hydrogels loaded with Amphotericin-B (AmB) were named as CPCa_25_AmB, CPCa_50_AmB, CPCa_75_AmB, CPCa_100_AmB, CPBG_25_AmB, CPBG_50_AmB, CPBG_75_AmB and CPBG_100_AmB.

5.3.3. FTIR Analysis:

Functional group analysis on various control and composite hydrogels was performed using FTIR. Interestingly, in CPCa_100 (**Fig. 5.3a**) amide I peak appeared at the higher wavenumber of 1675 cm^{-1} compared to CP sol (1657 cm^{-1}) evidencing chemical interaction between C=O and Ca^{2+} ions,[36] whereas, the amide II of CP sol at 1542 cm^{-1} slightly shifted to the higher wavenumber at 1555 cm^{-1}. Peaks attributed to —COO^{-} symmetrical stretching at 1411 cm^{-1} and 1447 cm^{-1} of CP sample merged with higher intensity and appeared at 1420 cm^{-1} for CPCa_100. Amide III Peak of CP at 1251 cm^{-1} shifted to a lower wavelength at 1239 cm^{-1} in the case of CPCa_100. Here again, the changes observed in the characteristic frequencies of CPCa_100 is attributed to inter as well as intramolecular physical forces. In the case of CPBG_100, the intensity of amide I peak decreased and centred round 1652 cm^{-1} and the amide II band were seen at 1565 cm^{-1} compared to CPCa_100. —COO^{-} symmetrical stretching at 1420 cm^{-1} of CPCa got split as a triplet (1475 cm^{-1},1447 cm^{-1} and 1413 cm^{-1} respectively) indicating chemical interaction with the added inorganic components. It is pertinent to highlight that the existence of the characteristic bioglass peaks[37–39] such as P=O (1342 cm^{-1}),

1102 cm^{-1} (Si—O—C), 1024 cm^{-1} (P—O—C, Si—O, P=O, Si—O—Si), 470 cm^{-1} (Si—O—Si) in the FTIR spectrum of CPBG_100 confirm the *in-situ* mineralization of bioglass in the hydrogel matrix. In addition, it is interesting to note that with the increase in the concentration of crosslinker in the CP matrix, amide I band at 1655 cm^{-1} of CPCa_25 gradually shifted towards the higher wavenumber and finally appeared at 1675 cm^{-1} in the case of CPCa_100 sample (**Fig. 5.3a**).

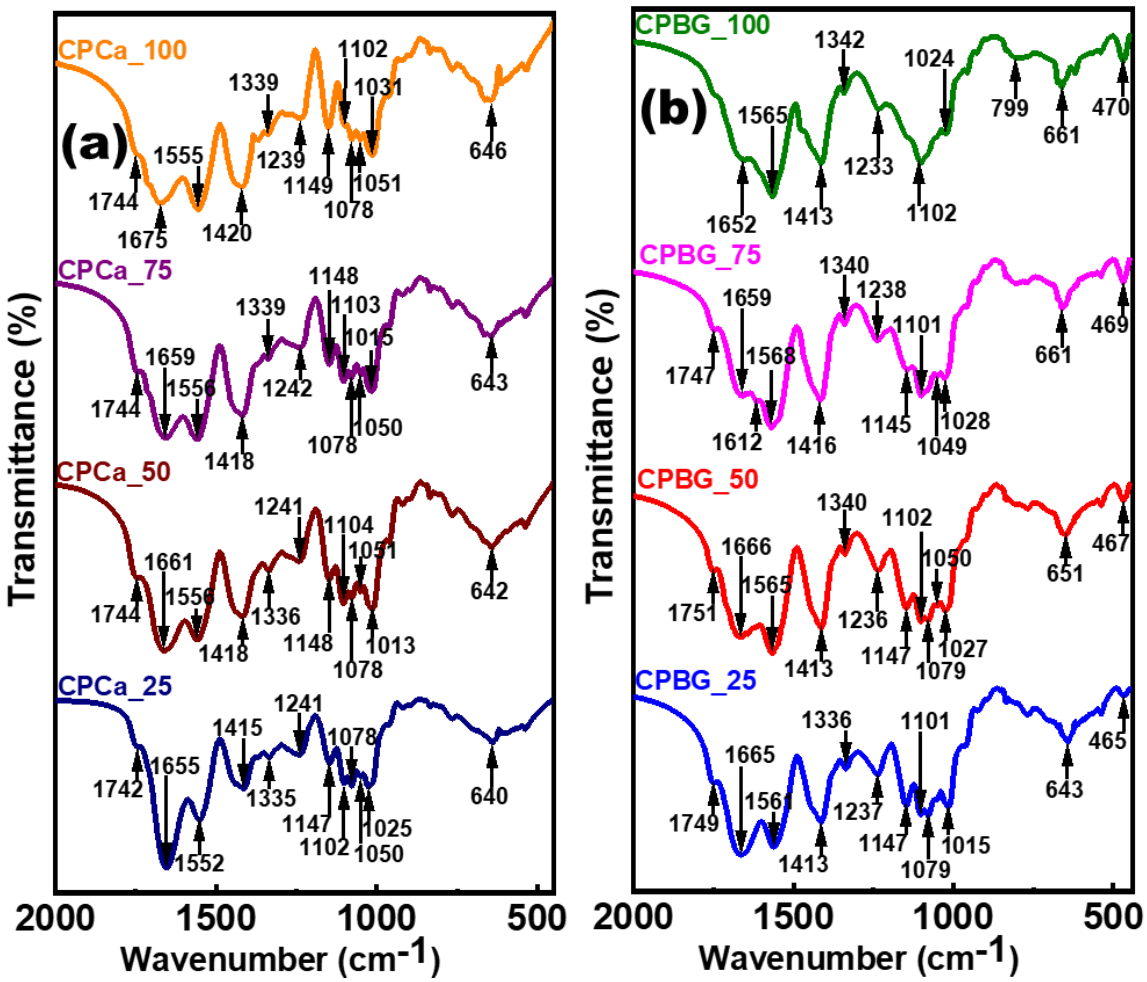

Fig. 5.3: FTIR Spectra in panel **(a)** CPCa_25 (—), CPCa_50 (—), CPCa_75 (—) as well as CPCa_100 (—) and panel **(b)** CPBG_25 (—), CPBG_50 (—), CPBG_75 (—) as well as CPBG_100 (—).

Similarly, in the case of CPBG (**Fig. 5.3b**) as bioglass precursor concentration increases, the peak corresponds to —COO^{-} symmetrical stretching observed at 1413

cm^{-1} in the case of CPBG_25 got split as a triplet namely at 1475 cm^{-1}, 1447 cm^{-1} and 1413 cm^{-1} for CPBG_100 signifying chemical interaction with the bioglass precursors. Once again, the intensity of the peak corresponding to Si—O—Si at 465 cm^{-1} increased with the concentration of bioglass precursors. It is noteworthy that peak corresponding to Si—O—C at 1102 cm^{-1} appeared uniquely in the CPBG_100 spectrum compared to samples made at other concentrations.

5.3.4. X-ray Diffraction (XRD):

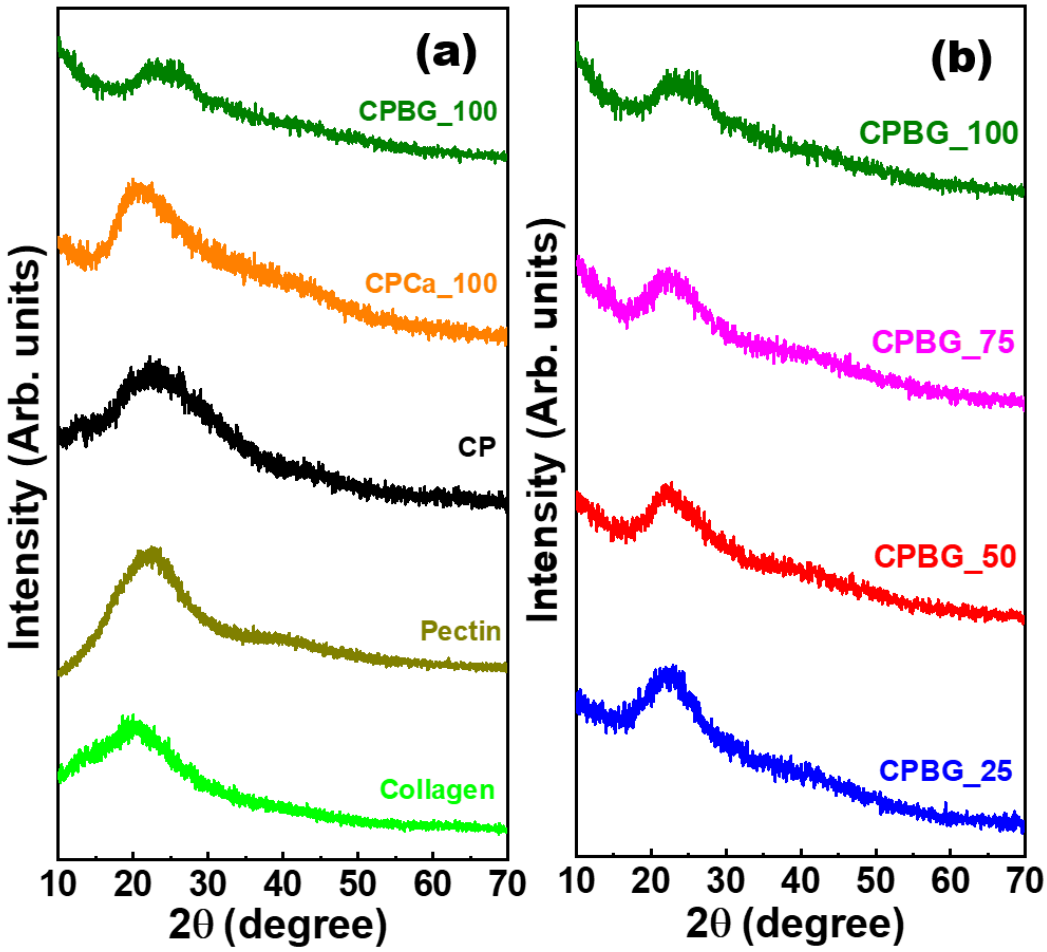

Fig. 5.4: XRD pattern of **(a)** pure collagen, pure pectin, collagen/pectin blend, **(b)** various hydrogels containing *in-situ* mineralized bioactive glass particles.

As prepared, collagen/pectin blend (CP) and hydrogels (CPCa and CPBG series) were subjected to XRD analysis and results were displayed in **Fig. 5.4**. It was observed that

the XRD pattern of various samples understudy were very similar. Only a broad peak at 2θ in the range of 15° to 30° was observed in the diffraction patterns. The observed broad peak in the case of pectin, collagen, CP, CPCa and CPBG samples represented their amorphous nature.

5.3.5. TGA Analysis:

A comparative study on the thermal stability examination of CP, CPCa and CPBG series (**Fig. 5.5**) demonstrated multiphase degradation behaviour of the samples under

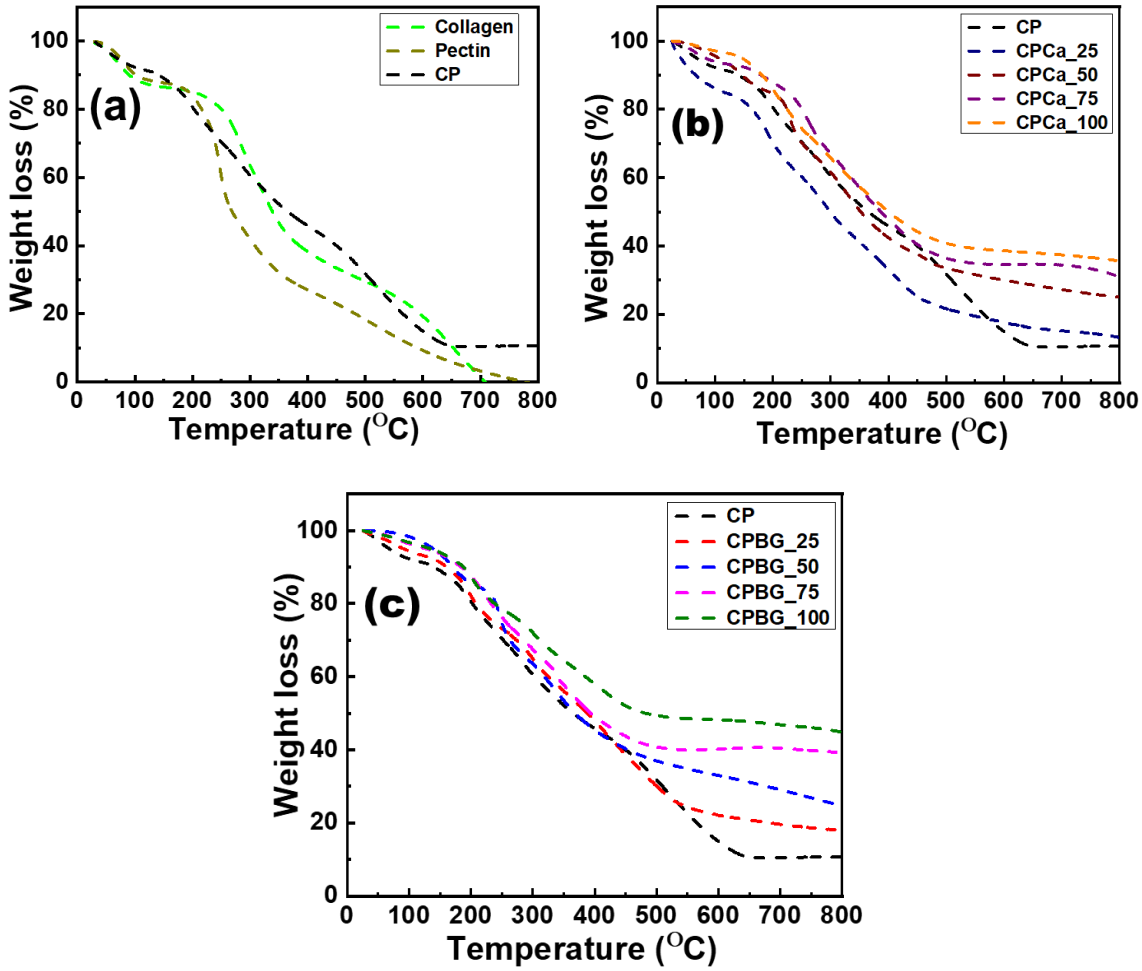

Fig. 5.5: Thermogravimetric analysis in panel **(a)** Collagen (- - -), Pectin (- - -), CP (- - -); panel **(b)** CP (- - -), CPCa_25 (- - -), CPCa_50 (- - -), CPCa_75 (- - -) as well as CPCa_100 (- - -); and panel **(c)** CP (- - -), CPBG_25 (- - -), CPBG_50 (- - -), CPBG_75 (- - -) as well as CPBG_100 (- - -).

investigation. In general, some initial weight loss occurred for all samples up to 135 °C due to the evaporation of bound water. The main decomposition of the backbone chains occurred above 135 °C due to breaking of protein chain and peptide bond.[40] CP blend starts to degrade at 152 °C and showed the lowest residual weight i.e., 10.8 wt% among various CPCa and CPBG samples. In summary, compared to CPCa series (CPCa_25 (13.5 wt%), CPCa_50 (25.1 wt%), CPCa_75 (31.4 wt%) and CPCa_100 (35.7 wt%)), CPBG series samples showed degradation above 195° C, and showed higher residual weights for CPBG_25, CPBG_50, CPBG_75, and CPBG_100 samples (i.e., 18 wt%, 24.7 wt%, 39.2 wt%, 44.8 wt% respectively, **(Fig. 5.5).** This result clearly indicates the improved thermal stability of the CP hydrogels after cross-linking with calcium ions (referred to as CPCa hydrogels) and *in-situ* mineralization of bioglass particles in the CPBG matrix. Therefore, it is necessary to realize that the bioglass particles played the role of (pseudo-) crosslinkers by strategically locating themselves at the junctions of the network, which reinforced the mechanical strength of the hydrogel.

5.3.6. Morphological Studies:

SEM micrographs of lyophilized hydrogel CPCa and CPBG series are depicted in **Fig. 5.6a-h**. In general, SEM images of both CPCa and CPBG samples show porous rough surface structure. Interestingly, pore size determination carried out on the SEM images of hydrogels using ImageJ analysis (**Fig. 5.7**) indicated a decrease in mean pore diameter from 31.3 to 10.2 μm for CPCa with an increase in Ca^{2+} concentration. Shrinkage in pore size could be attributed to the increase in the crosslinking density of Ca^{2+} ions within the matrix. A similar trend was also observed for CPBG samples, for which pore size decreased from 47.8 to 2.6 μm with increase in the concentration of the BG precursor. Importantly, the existence of the porous morphology indicated the presence of a large amount of water before lyophilization, which is the characteristic nature of a hydrogel. Further, at higher magnification (15 kX) assorted dense globular structures of various size embedded throughout the hydrogel matrix (**Fig. 5.6e-h inset**) were visualized. The mean pore size of CPCa hydrogels were smaller than those of

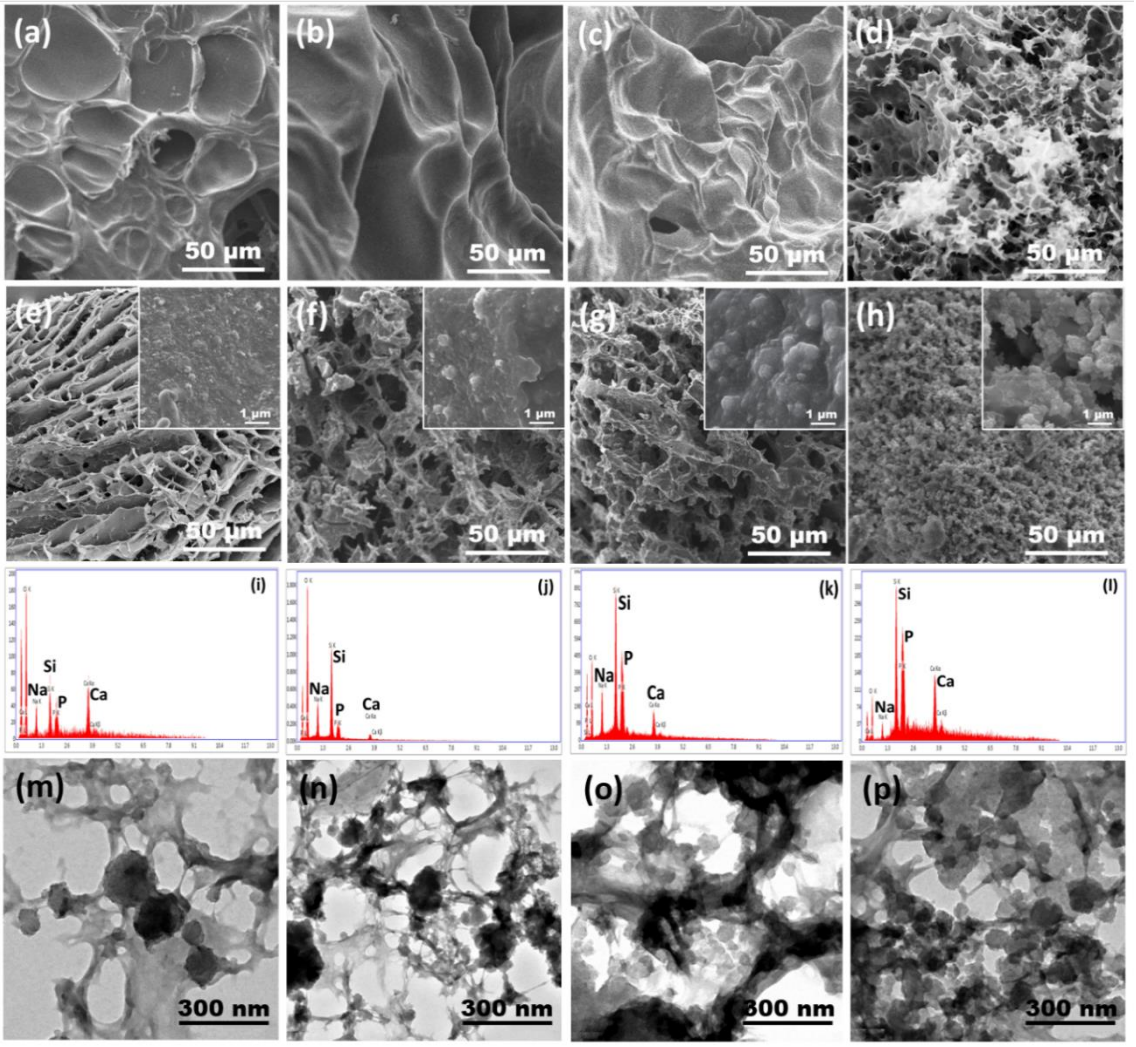

Fig. 5.6: SEM images of **(a)** CPCa_25, **(b)** CPCa_50, **(c)** CPCa_75, **(d)** CPCa_100, **(e)** CPBG_25, **(f)** CPBG_50, **(g)** CPBG_75 and **(h)** CPBG_100 at 250x (insert in figure **(e)-(h)** shows corresponding BG particles in hydrogel at 15 Kx). SEM-EDAX spectra of **(i)** CPBG_25, **(j)** CPBG_50, **(k)** CPBG_75 and **(l)** CPBG_100. TEM images of **(m)** CPBG_25, **(n)** CPBG_50, **(o)** CPBG_75 and **(p)** CPBG_100.

CPBG hydrogels except for CPCa_100 (10.2 µm) and CPBG_100 (2.6 µm) (**Fig. 5.7**) samples. In the case of CPCa, Ca^{2+} ions are crosslinkers whereas in CPBG series Ca^{2+} containing BG nano-particles are the cross-linkers, which function as a multiple inorganic binding sites in CP matrix and hence providing larger pore size to CPBG series. However, the reported smaller pore size of CPBG_100 compared to CPCa_100 is attributed to multiple crosslinking sites provided by the largest number of smallest BG particles mineralized in the hydrogel matrix (**Fig. 5.6h**). The pseudo-crosslinking

attribute of bioglass nanoparticles is clearly manifested here. Interestingly. EDAX spectra (**Fig. 5.6i-l**) revealed the existence of Si, P, Na, and Ca elements on these globular structures. These observations confirmed the mineralization of bioglass particles in the CP matrix due to the interaction between BG precursors and the CP

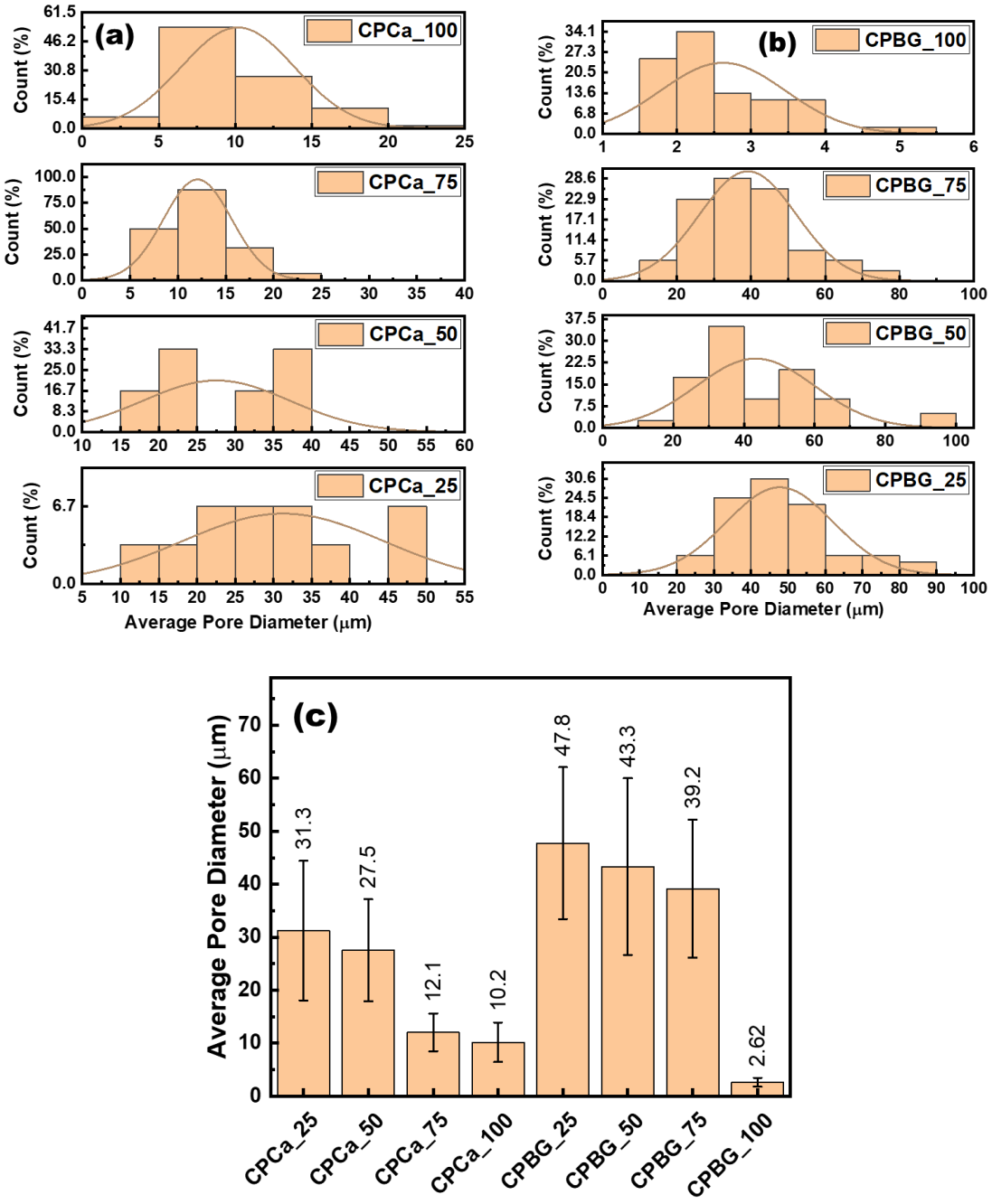

Fig. 5.7: Average pore diameter of various samples analysed through SEM using ImageJ analysis.

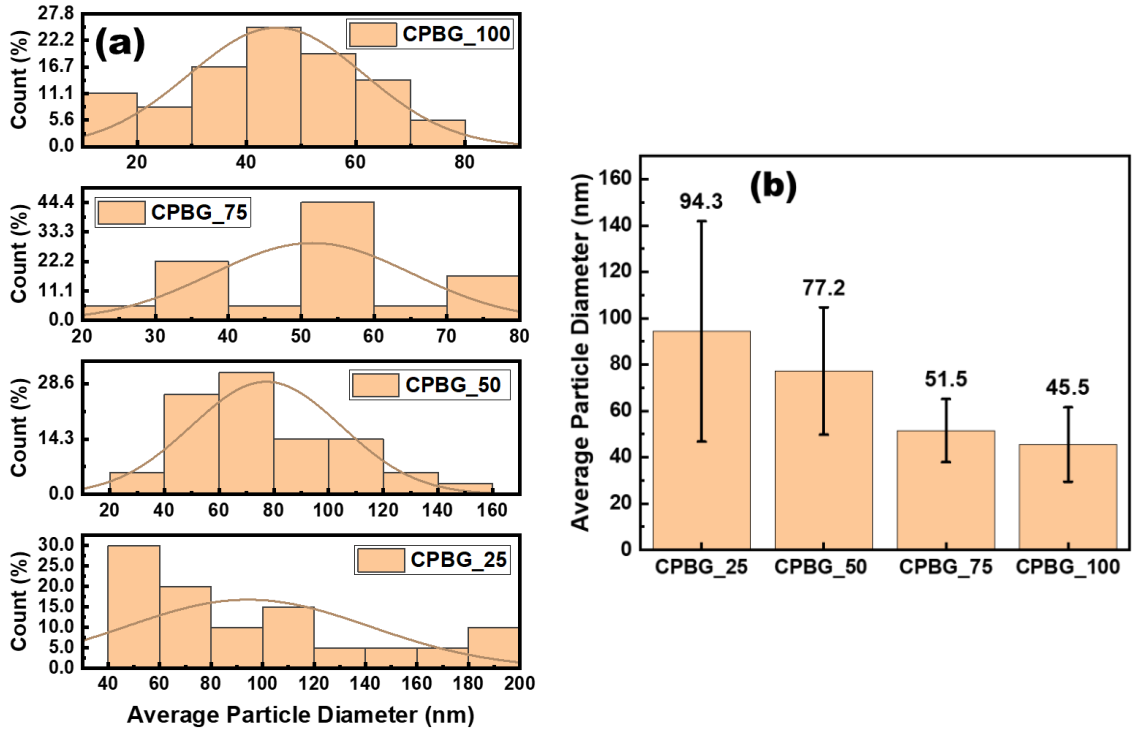

Fig. 5.8: Average particle diameter of samples understudy through TEM using ImageJ analysis.

matrix and is in good agreement with the findings of FTIR spectra (**Fig. 5.3b**). Due to the bioglass mineralization, the surface of CPBG hydrogel samples was rough in comparison to their corresponding control sample. It is also pertinent to note that with an increase in BG precursor concentration, the distribution of BG particles increased in the hydrogel matrix making these more homogeneous (**Fig. 5.6e-h inset**). Similar to SEM micrographs of CPBG hydrogels (**Fig. 5.6e-h**), TEM micrographs of CPBG hydrogels (**Fig. 5.6m-p**) confirmed the porous structure of the hydrogel containing higher number of bioglass particles for the CPBG_25 to CPBG_100. Interestingly, a decrease in BG particle size (94.3 to 45.5 nm) was reported by ImageJ analysis (**Fig. 5.8**) of TEM micrographs with increase in the amount of BG precursors. This observation indicates that as the concentration of BG precursors increases, a higher number of nucleation sites are generated and consequently, an increase in the number of BG particles with the corresponding decrease in their particle size was facilitated.

5.3.7. Swelling Studies and Kinetic Analysis:

The swelling ability of both CPCa and CPBG series of dried hydrogel samples were monitored in SBF buffer owing to evaluation of their application in tissue engineering (**Fig. 5.9, 5.10 and Table 5.4**). Significantly, Ca^{2+} ions act as a crosslinker for collagen and pectin molecules during the formation of both CPCa and CPBG hydrogel series. In CPBG series, Ca^{2+} ions also participate as one of the precursors for the *in-situ* bioactive glass mineralization in the hydrogel network in addition to crosslinking. Swelling ratio

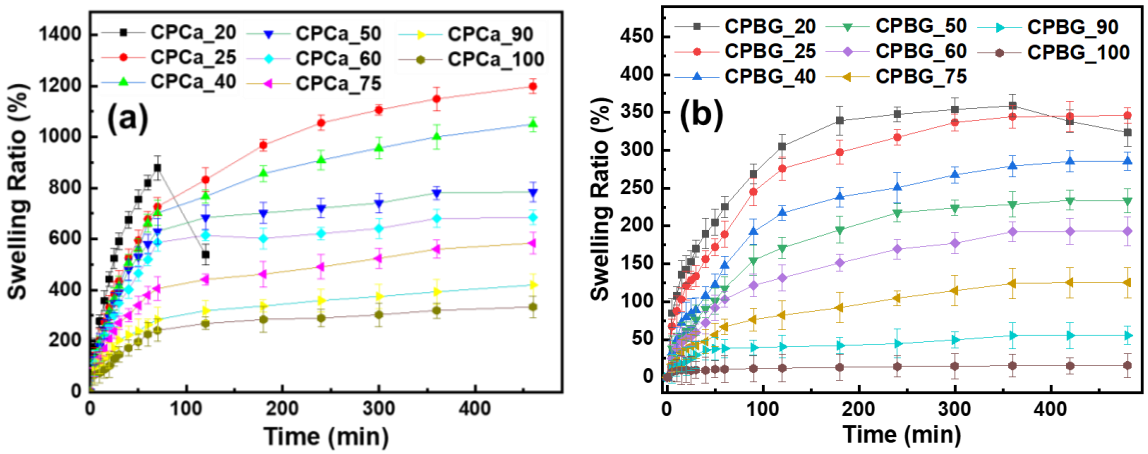

Fig. 5.9: Swelling Studies up to 8 h in Simulated Body Fluid on **(a)** control hydrogels, **(b)** hydrogels containing *in-situ* mineralized bioactive glass particles.

for both the hydrogel systems showed inverse proportionality to crosslinker density. Noticeably, crosslinking also influenced both the molecular structure and swelling properties of the hydrogel system. As the crosslinker density increases, the hydrogel network becomes stiffer and compact as well as the pore size becomes smaller, and a drop in swelling was recorded. These results are in line with the reported morphology studies (**Fig. 5.6**). Interestingly, highest swelling ratio of CPCa_25 (mean pore size 31.3 µm) was reported as compared to the CPBG_25 sample (mean pore size 47.8 µm).

It might be attributed to the mineralization induced stiffness in the CPBG_25 that hindered the polymeric chain mobilization and stretching enough to hold greater amount of buffer thereby, decreasing the swelling capacity. In addition, the decrease in

the swelling capacity of CPCa hydrogels in SBF with increasing crosslinker concentration could also be due to development of osmotic pressure caused by the unequal distribution of various ions in the SBF medium and the hydrogel network. It may be noted that ions attached to the hydrogel network are partly immobile and considered to be separated from the external solution through a semi-permeable membrane.[41] Within the polymeric gel network, the development of osmotic pressure is much lower , when the difference of counter ions in the gel phase and SBF solution increases. On the other hand, with the increase in concentration of crosslinker in the hydrogel matrix, the difference between the concentration of counter ions in the gel phase and solution phase decreases, thus causing a decrease in the equilibrium solvent uptake of hydrogel sample (**Table 5.4**). For the CPBG series, comprised of polymeric network and *in-situ* mineralized BG that consist of various inorganic ions. Here, difference in the concentration of counter ions in the gel phase and solution phase is relatively less, therefore, a drastic decrease in equilibrium buffer content (EBC %) is observed in comparison to CPCa sample series. It also accounted for the drastic reduction in the swelling ability, as observed through the swelling kinetics analysis of the hydrogel (CPBG) using second-order equation (Phenomenological model, **Eq 5.3**). The t/S_{eq} versus t graph reflected the decrease in the values of initial swelling rate (r_0), the swelling rate (k_s), and degree of swelling equilibrium (S_{eq}) with the increase in crosslinker concentration (**Table 5.4** and **Fig. 5.10**). Based on previous findings,[41] analysis of swelling ability mechanisms of both the hydrogel series could be characterized either by Fick's second law or by a more advanced equation of anomalous diffusion. Power-law (**Eq.5.5**) was used to determine the nature of solvent diffusion into the hydrogel and a straight line was obtained by plotting ln(F) versus ln(t) for the initial stages of swelling (60 %), shown in **Fig. 5.10 a, c**. The slope of this line displays

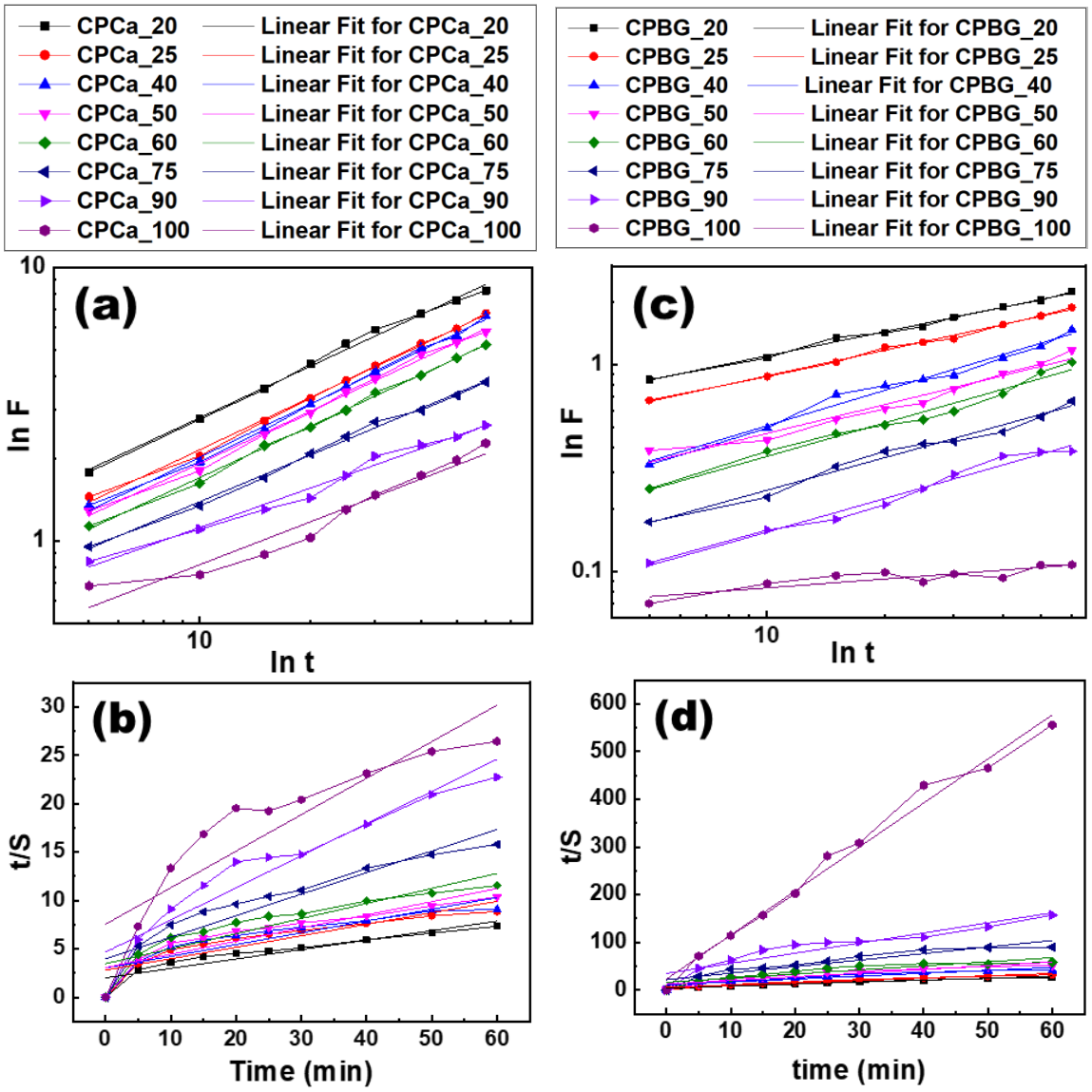

Fig. 5.10: Swelling kinetics model fitting for various hydrogels of (a-b) CPCa and (c-d) CPBG series.

swelling exponent 'n' and its intercept gives swelling constant 'k', tabulated in **Table 5.4**. The 'n' value is correlated with mechanism that drives the diffusion process and its values for CPCa and CPBG series, was found between 0.44 and 0.55 close to what is expected for Fickian diffusion. In the case of Fickian diffusion, the polymer chains have a higher mobility and the solvent penetrates easily into the gel matrix, and the solvent diffusion rate is clearly slower than the polymer chain relaxation rate. Here equilibrium is attained linearly with the square-root of time (t). For anomalous diffusion, the polymer chains are not sufficiently mobile to permit diffusion of solvent into the gel

Table 5.4: Discusses about various coefficients and variables of swelling kinetic models on CPCa and CPBG hydrogel series. According to R^2 values, it can be noted R^2 value for CPBG_100 was less to comment on its release mechanism.

S. No.	Sample Code	EBC (%)	R^2	K (s^{-1})	Release Exponent (n)	Mechanism of Release	r_0	S_{eq}	k_s	D (x 10^{-5}) (cm^2s^{-1})
1	CPCa_20	84.33	0.994	0.66	0.63	Non-Fickian	0.50	10.24	0.004	2860
2	CPCa_25	89.27	0.997	0.49	0.63	Non-Fickian	0.36	8.43	0.005	1890
3	CPCa_40	88.46	0.996	0.45	0.65	Non-Fickian	0.33	8.23	0.004	1750
4	CPCa_50	87.25	0.995	0.44	0.63	Non-Fickian	0.32	7.3	0.006	1570
5	CPCa_60	86.00	0.997	0.40	0.62	Non-Fickian	0.29	6.42	0.007	1280
6	CPCa_75	81.52	0.995	0.37	0.57	Non-Fickian	0.25	4.49	0.012	780
7	CPCa_90	76.15	0.982	0.37	0.50	Non-Fickian	0.21	3.01	0.023	440
8	CPCa_100	72.90	0.934	0.24	0.52	Non-Fickian	0.13	2.65	0.018	240
9	CPBG_20	77.50	0.993	0.45	0.39	Fickian	0.24	2.42	0.041	184
10	CPBG_25	76.03	0.995	0.34	0.41	Fickian	0.19	2.05	0.044	129
11	CPBG_40	71.23	0.981	0.13	0.57	Non-Fickian	0.09	1.66	0.033	135
12	CPBG_50	68.51	0.954	0.16	0.50	Non-Fickian	0.08	1.30	0.048	80
13	CPBG_60	62.88	0.973	0.10	0.53	Non-Fickian	0.06	1.16	0.045	58
14	CPBG_75	46.08	0.979	0.07	0.52	Non-Fickian	0.05	0.73	0.086	25
15	CPBG_90	29.82	0.977	0.04	0.54	Non-Fickian	0.03	0.47	0.129	12
16	CPBG_100	12.45	0.730	-	-	-	-	-	-	-

core since both diffusion and polymer chain relaxation rate are comparable with equilibrium approaching with t^{n-1} time-dependence.[42] The diffusion constant 'k' decay markedly from 0.66 to 0.37 in CPCa, and 0.45 to 0.045 in CPBG series with increasing crosslinker concentration. The diffusion coefficients (D) given in **Table 5.4** were calculated from **Eqs. 5.6.** For the same measurement conditions in all hydrogel

systems, yield remarkably consistent D values in the range of 10^{-5} to 10^{-6} cm^2/s, an optimum range for the biomedical application of the hydrogel system.[43] It is accepted that the physical entanglement of the collagen-pectin hybrid chains with the inorganic silica network of bioactive glass provided the cohesive nature to the hydrogel system and significantly improved the structural integrity of the hydrogel and decreased stress relaxation, which helped enhancing its ability to withstand the osmotic pressure for longer duration (**Fig. 5.10**) particularly, in the case of CPBG_25 gel. The hydrogel disintegration studies carried out on CPCa_25 and CPBG_25 (**Fig. 5.11**) revealed a steep rise in percentage dispersion of CPCa_25. Whereas, dispersion of CPBG_25 is slow compared to CPCa_25 due to the multi-centered crosslinking nature of BG particles. The maximum disintegration of CPCa_25 (100 %) and CPBG_25 (80 %) was observed on day 7 and day 15 respectively.

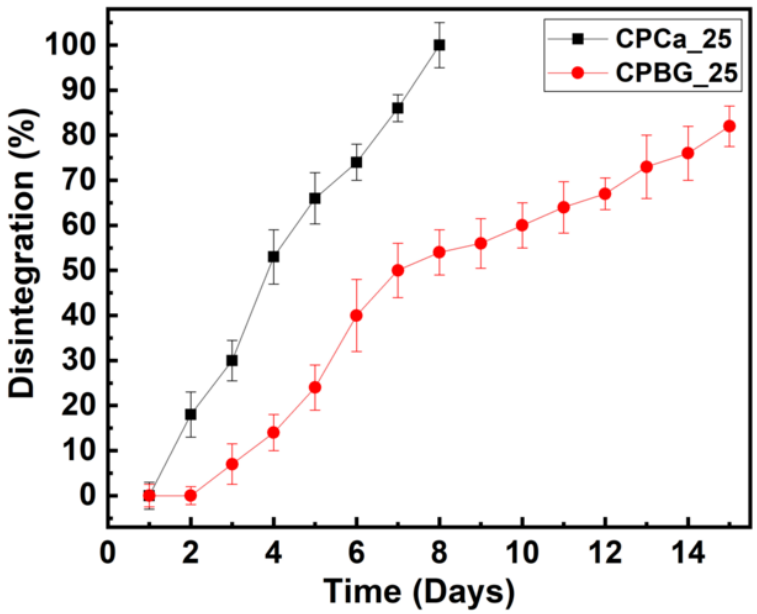

Fig. 5.11: Disintegration studies up to 15 days in Simulated Body Fluid for CPCa_25 and CPBG_25.

5.3.8. Rheological Analysis:

Although the value of G′ (ω) and G″ (ω) was found to be quite low reflecting the fragile

nature of the collagen/pectin blend in 1:1 ratio at 50 mg/mL each however, it possessed gel forming ability among others (**Fig. 5.2d**). These were considered further for evaluating the effect of calcium crosslinker and as a template for the *in-situ* mineralization of bioactive glass. Evidence of the formation of solid like network (CPCa_25) was observed which showed G′ > G″ over the entire frequency range (**Fig. 5.12**) confirming elastic response of the CP hydrogel with high storage modulus. The increase in mechanical strength of the gel phase after crosslinking in the CP hydrogel implied the existence of a well-formed network structure. The value of *n′* for CPBG_25 after the *in-situ* mineralization of bioactive glass revealed gain in elasticity corresponding to control CPCa_25 hydrogel, thus suitable for the load bearing applications. Therefore, bioglass particles do play the role of pseudo-crosslinkers by positioning them at the junction zones. It could be justified on the basis of the presence of silica inorganic polymeric structure incorporation into biopolymeric hydrogel network of CPBG_25.

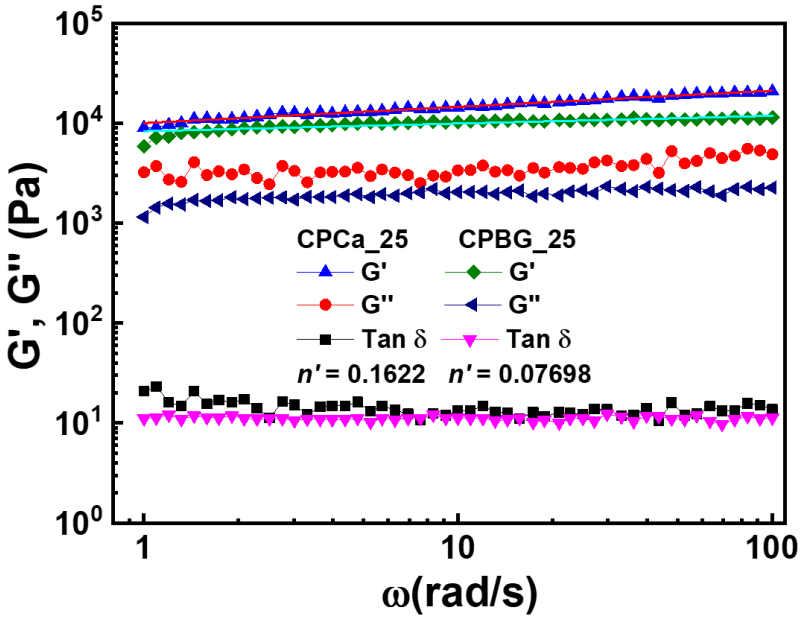

Fig. 5.12: Frequency sweep oscillatory rheology at constant oscillation stress of 1 Pa for the hydrogels CPCa_25 and CPBG_25 obtained by ionic crosslinking with calcium

ions. The fitting lines in the data points are power law fit $G'(\omega) \approx \omega^{n'}$ where $0 < n' < 1$ reflects the gel nature.

5.3.9. Hydrogel Formation Mechanisms:

Unlike the usual attraction of opposite charges, interaction between selective portions of two different macromolecules carrying similar net polarity is gaining momentum in the synthesis of potential novel materials. Herein, the formation of such inter-macromolecular aggregates purely depends on various physical environments around these polymer chains in the solution such as solution pH, ionic strength, temperature, polymer charge density and polymer mixing ratio. In the present work, we report one such type of interaction between collagen and pectin (**Fig. 5.13d**) that regardless of similar net negative charges, bind to each other and forms complex gel. The complexation of pectin and collagen was noted at 1:1 mixing ratio at pH 7 as evidenced by highest turbidity (50 %) and least zeta potential values (-39 mV) (**Fig. 5.2a and 5.2b**) compared to respective individual solutions. Precisely, interaction of these macromolecules is evidenced by FTIR (**Fig. 5.2c**) through amide I, amide II and amide III of collagen and —COO^{-} and —OH groups of pectin by physical forces (**Fig. 5.13a-b**). In detail, pectin (**Fig. 5.13a**), a polysaccharide is a strong polyelectrolyte, whereas collagen **(Fig. 5.13b**), a protein is polyampholyte. When two of these biopolymers are associating, regardless of similar charge/polarity, the protein partner collagen being a polyampholyte containing positive and negative patches expose its positively charged patches and associates with pectin molecules. Although there is a same polarity repulsion while the positive surface patches will attract the negatively charged segment of its binding partner and then result in localized contact and localized electrostatic attraction. The resulted phenomenon is called as Surface Patch Binding (SPB) as demonstrated by Bohidar *et al*.[10] Further, the addition of crosslinker (Ca^{2+}) to the

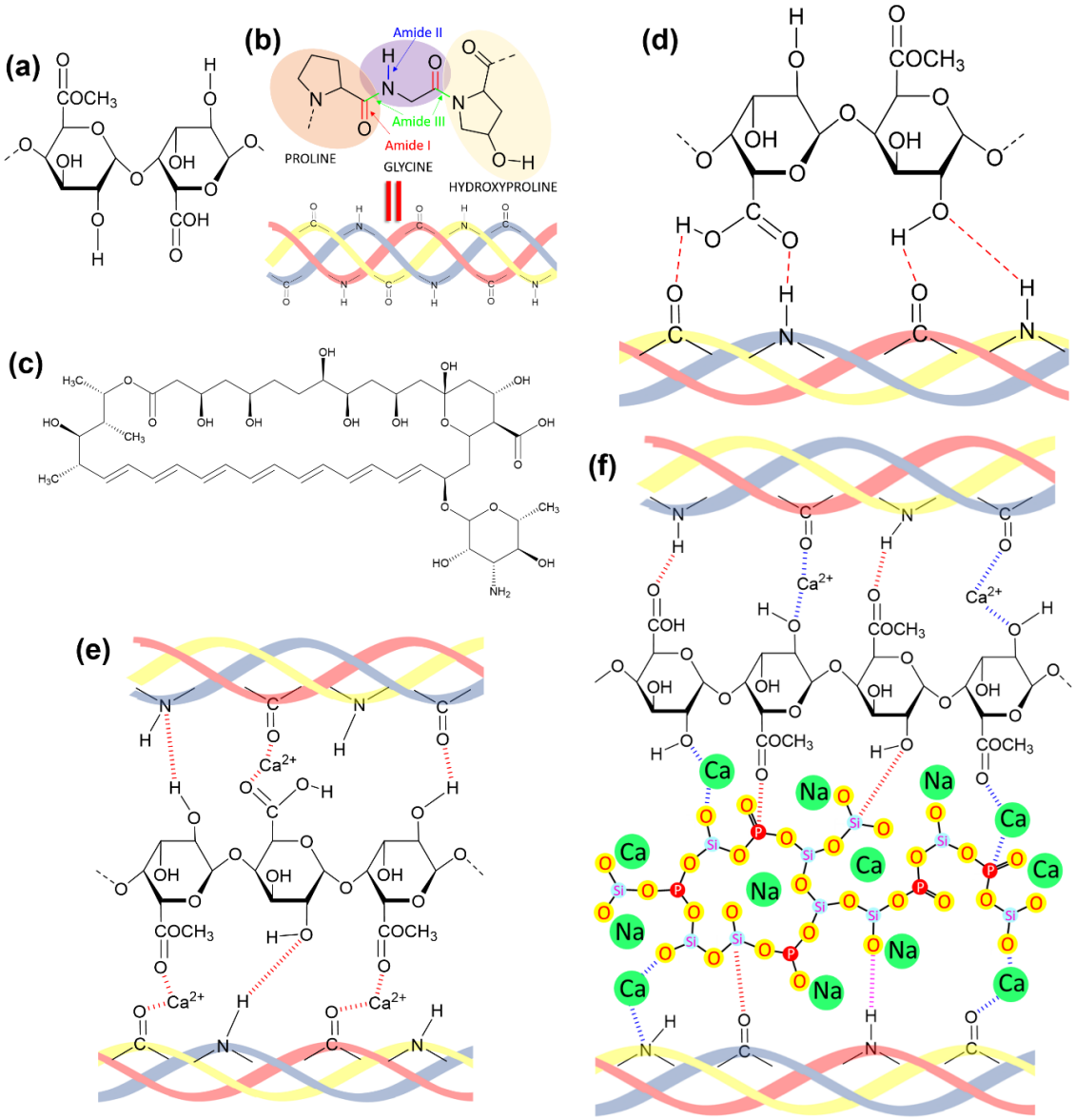

Fig. 5.13: Schematic representation of representative structure of **(a)** pectin, **(b)** collagen and **(c)** Amphotericin-B (AmB), **(d)** Surface Patch Binding of collagen and pectin, **(e)** Calcium crosslinked interaction between collagen and pectin (CPCa) and **(f)** i*n-situ* mineralization of bioglass particles showing multicentered crosslinking between collagen and pectin.

collagen-pectin (CP) system strengthens their association through chemical interaction between —C=O as well as —COO^{-} groups of CP system and Ca^{2+} ions (**Fig. 5.13e**) in addition to the physical forces. As a result, the growth of insoluble macromolecular aggregates (complex coacervation) increases with entrapping water molecules leading

to hydrogel (CPCa) formation. It is worthy to note that in another class of soft matter (coacervation) interpolymer complex formation is shown to be governed by surface patch binding mechanism in polymers of same polarity. To this end, in CPBG system, addition of BG precursors in CP system not only enhances complex formation through chemical interaction, but also result in *in-situ* mineralization of BG nanoparticles as evidenced ~~by~~ from the FTIR spectra of CPBG_100 (**Fig. 5.13f**). It is worth mentioning that network former precursors of bioglass i.e. tetraethyl orthosilicate and triethyl phosphate are also negatively charged[38] so, surface patch binding phenomena facilitate in forming nucleation sites on the CP aggregates. The process further leads to tightened complexation between collagen and pectin by entrapping water molecules in the interstitial space favouring the formation of an all pervading network structure.

5.3.10. Bioactivity Test:

Detailed structural analysis revealed that CPBG_25 possessed an adequate mechanical strength and pore size for cell attachment as well as oxygen and nutrient transport, therefore chosen for the biological response studies. Bioactivity of CPBG_25 in SBF was monitored over 30 days by XRD, FTIR and SEM (**Fig. 5.14a-f**). Interestingly, on immersion in SBF, (**Fig. 5.14a**) broad hump in the XRD pattern in the 2θ range of 15° to 30° disappeared along with the emergence of two new peaks at 31.7° and 45.5°. These new XRD diffractions signalled for an interfacial activity on the hydrogel surface in contact with SBF. As the interaction time of the hydrogel with SBF prolonged to 7 days, the intensity of the above newly emerged peaks at 24 h increased and further, many new peaks were noticed after 30 days. The observed reflections in the corresponding spectra are in good agreement with the JCPDS file no. 01-072-1243, which reveals that the formed microcrystals on the surface of CPBG_25 after

interaction with SBF are of bone-like hydroxyapatite ($Ca_{10}(PO_4)_6(OH)_2$). Literature evidences a similar type of bioactive behaviour in BG embedded hydrogels.[44,45]

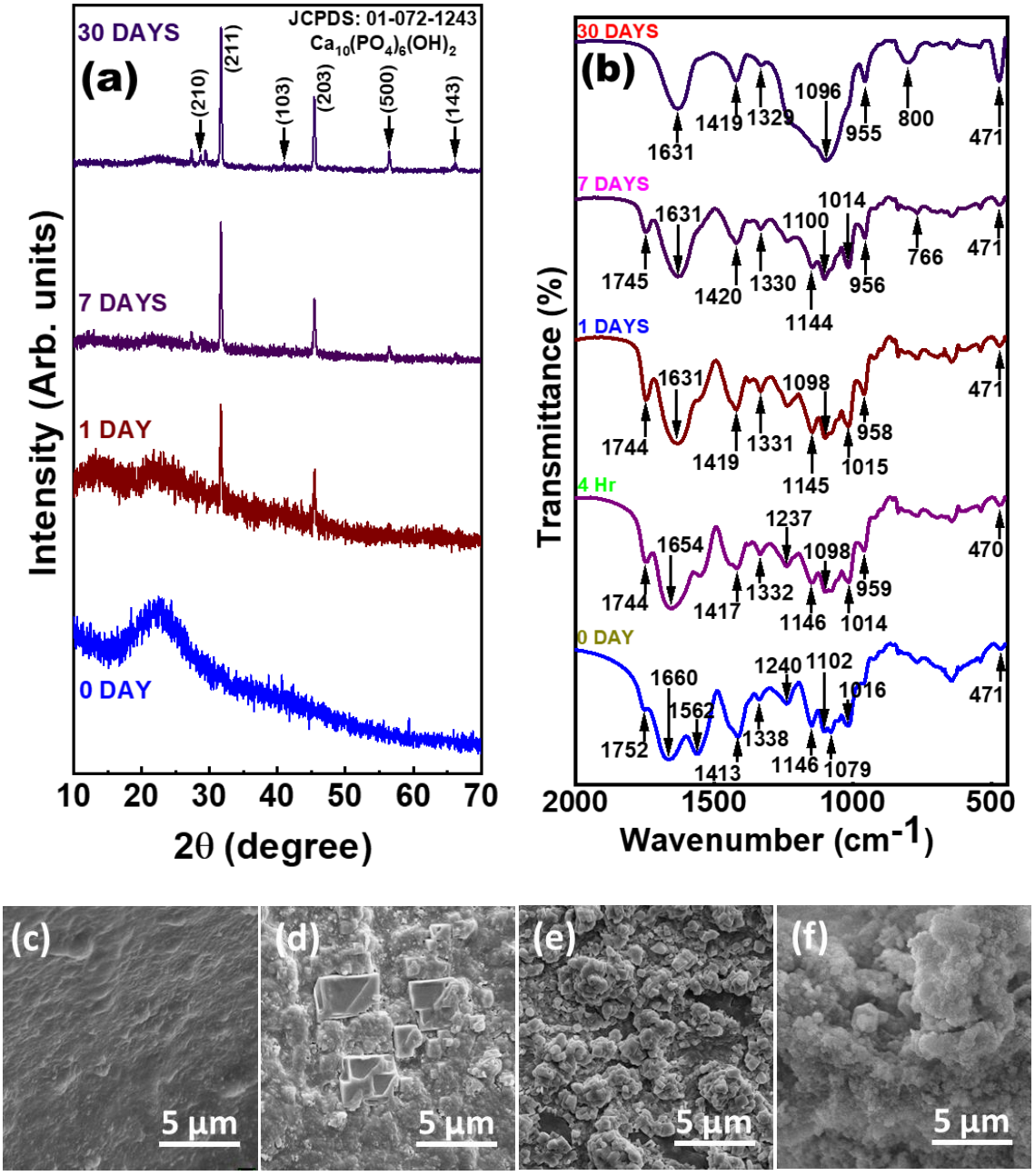

Fig. 5.14: (a) XRD pattern, **(b)** FTIR spectra and **(c-f)** SEM images (at 5 Kx) for CPBG_25 on interaction with SBF for **(c)** 0, **(d)** 1, **(e)** 7 and **(f)** 30 days. FTIR spectrum of CPBG_25 after 4 h interaction with SBF is also shown in **Fig. 5.14(b).**

FTIR data (**Fig. 5.14b**) also supports the bioactivity of the hydrogel sample by indicating the disappearance of characteristic polymer peaks and appearance of

characteristic peaks corresponding to hydroxyapatite during the period of 30 days of interaction with SBF. In fact, after 30 days of interaction with SBF, FTIR spectrum of CPBG_25 sample demonstrated the absence of the — C=O stretching peak at 1745 cm^{-1} and reduced intensity of the peak at 1419 cm^{-1} due to COO^{-} symmetrical stretching of the polymer matrix (**Fig. 5.3b and 5.14b**). Further, a small peak corresponding to P=O at 1329 cm^{-1}; a broad peak at 1096 cm^{-1} masked region of Si—O—C, P—O, and Si—O and small characteristic peak at 800 cm^{-1} due to the ring structure of silicate network appeared.[25,37–39] Importantly, a reported intensive peak at 471 cm^{-1} after 30 days interaction with SBF represents the phosphate ion[25,37–39] compared to 0 to 7 days interaction with SBF. These observations strongly support the XRD pattern obtained after 30 days of interaction of CPBG_25 sample with SBF solution and confirmed the hydroxyapatite formation. Further, SEM micrographs (**Fig. 5.14c-f**) showed the appearance of a few hydroxyapatite crystals on the hydrogel surface after 1 day of interaction with SBF (**Fig. 5.14d**). Interestingly, further soaking the hydrogel for 7 days and 30 days showed an increase in the aggregation of the microcrystals covering a larger surface area (**Fig. 5.14e-f**). These morphological analyses are in line with XRD and FTIR data[46,47] and confirm the bioactivity of the CPBG hydrogels.

5.3.11. Nitrogen Sorption Analysis:

Nitrogen Sorption Analysis or Brunauer–Emmett–Teller (BET) analysis was carried out on CPCa_25, CPBG_25 and CPBG_25 after interaction with SBF for 7 days, as shown in **Fig. 5.15**. From the figure, it is evident that the obtained BET isotherm of CPCa_25 belongs to type III with the H2 hysteresis loop. Whereas, CPBG_25 sample shows isotherm of type V with similar hysteresis loop (H2) compared to CPCa_25. These results revealed that the hydrogel cross-linked with only Ca^{2+} ions were of narrow and wide sectional interconnected macropores. On the other hand, the hydrogel obtained

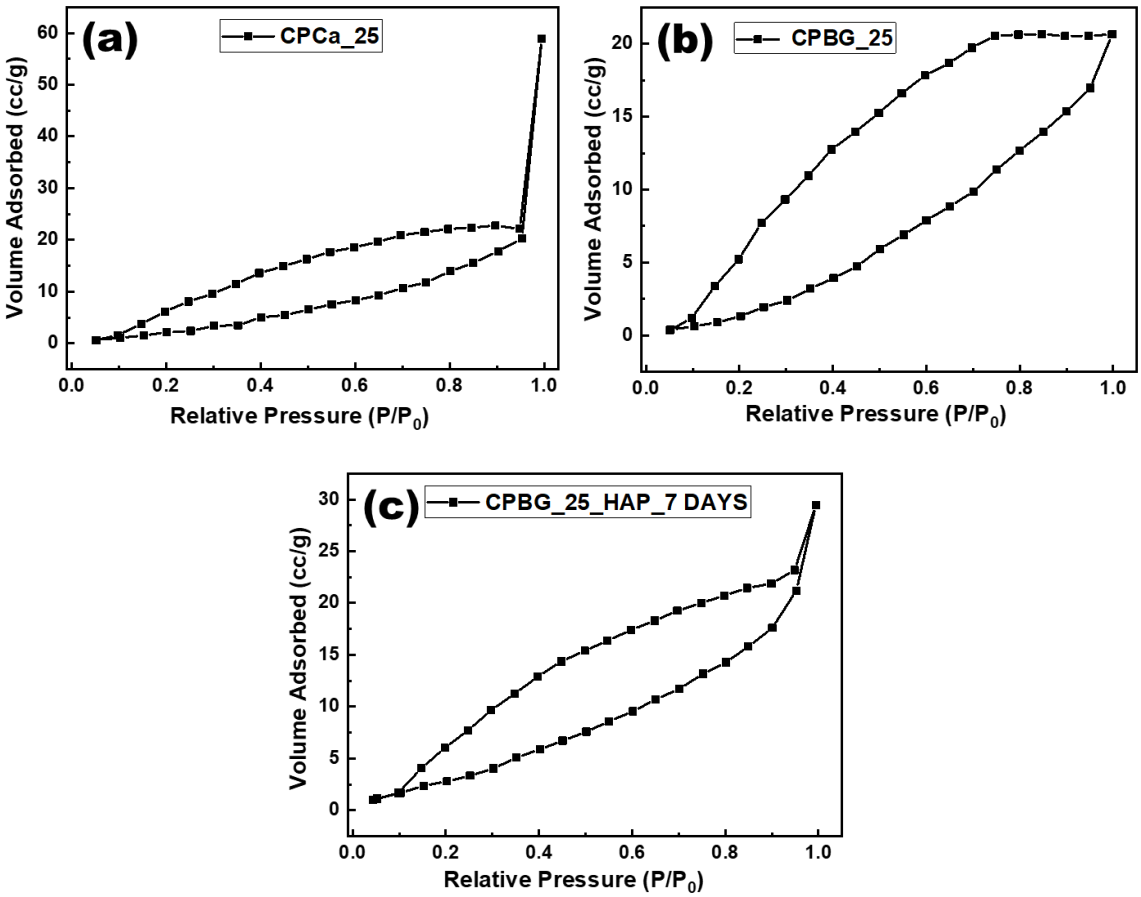

Fig. 5.15: BET analysis of **(a)** CPCa_25, **(b)** CPBG_25 (before bioactivity) and **(c)** PCBG_25(after interaction with SBF for 7 days).

Table 5.5: Showing pore diameter, pore volume and surface area of hydrogels obtained through nitrogen adsorption-desorption analysis.

Sample	Pore Diameter (nm)	Pore Volume (ccg^{-1})	BET Surface Area (m^2g^{-1})
CPCa_25	18.8	0.091	19.44
CPBG_25	5.6	0.032	22.84
CPBG_25_ HAP_7 DAYS	9.8	0.045	18.65

after the *in-situ* mineralization of bioglass (CPBG_25) contained interconnected mesopores. Herein, the observed difference in porosity of CPCa_25 and CPBG_25 is mainly due to the BG nanoparticle content of CPBG_25. Interestingly, a reported

decrease in BET pore volume (**Table 5.5**) and pore diameter with an increase in surface area of CPBG_25 compared to CPCa_25 is due to the BG mineralization in collagen/pectin hydrogel matrix. These observations are also consistent with FTIR, SEM and TEM results (**Fig. 5.3 and 5.6**). In the case of CPBG_25 after interaction with SBF for 7 days, the pore volume and pore diameter increase whereas the surface area decreases. This is due to the bioactivity of BG particles present in the CP matrix as well as its simultaneous swelling activity in SBF solution as evidenced by SEM (**Fig. 5.14c-f**).

5.3.12. Drug Release Studies:

The Amphotericin-B (AmB) encapsulation efficiency of the hydrogel CPBG_25 was found to be 81.2 % and the corresponding drug release profile was analyzed based on the reported encapsulation efficiency. The initial phase of AmB release (**Fig. 5.16a**) showed a burst release of 32.5 % in the first 10 min due to drug dissolution from the hydrogel surface. Such type of reported AmB release behaviour from CPBG_25 is

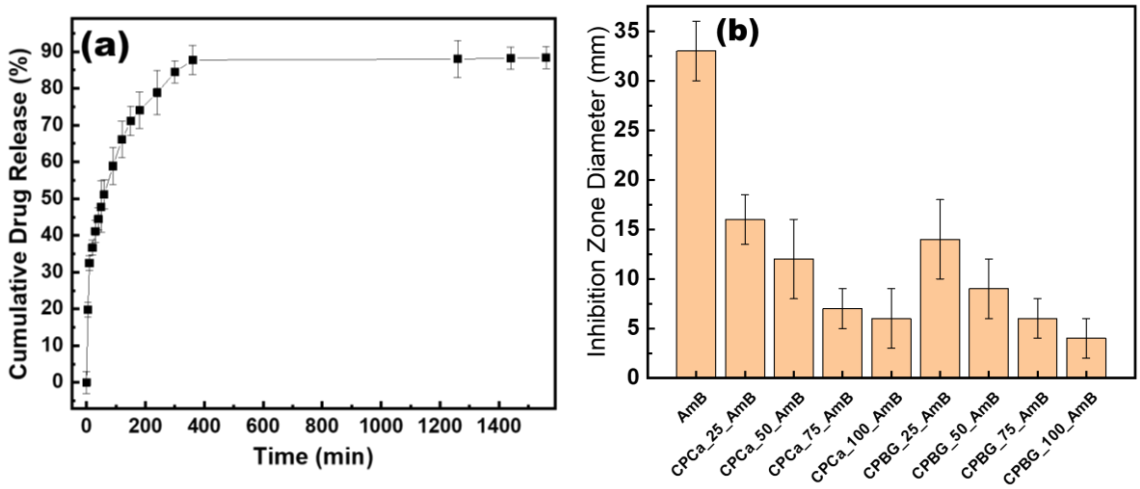

Fig. 5.16: (a) Cumulative drug release of Amphotericin-B (AmB) from the hydrogel CPBG_25_AmB. **(b)** Disk diffusion assay for pure AmB (500µg), CPCa_25_AmB, CPCa_50_AmB, CPCa_75_AmB, CPCa_100_AmB, CPBG_25_AmB, CPBG_50_AmB, CPBG_75_AmB and CPBG_100_AmB.

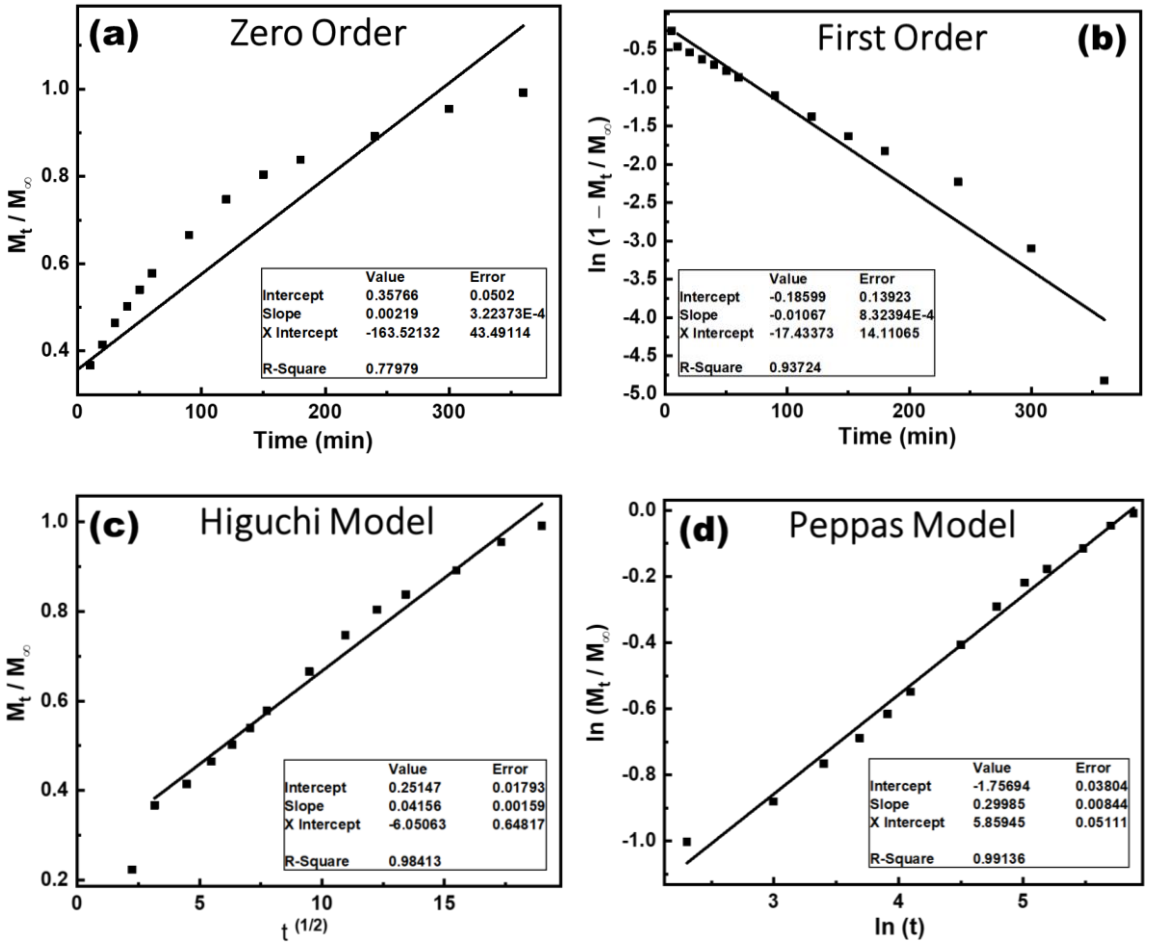

Fig. 5.17: Release Kinetics of Amphotericin-B from CPBG_25_AmB Hydrogel.

known to provide immediate relief at the initial stages of healing treatment due to the high content of drug release.[6] After 10 min, the drug release profile becomes gradual up to 360 min. Here, the duration of gradual drug release was observed to be equal to the time taken for complete swelling of the hydrogel (**Fig. 5.9b**). After 360 min the AmB release becomes constant (88 %) for 24 h. The reported drug release behaviour shows that the release of AmB from the hydrogel is proportional to the swelling behaviour of the hydrogel and favours the Fickian diffusion release mechanism. Further, the drug release mechanism and its kinetics were analyzed by fitting the obtained drug release data with various existing mathematical modelling as shown in **Fig. 5.17**. Out of various correlation coefficients (r^2) obtained, the highest correlation value was observed in the case of Peppas model, which describes the drug release from

a polymeric system. The observed n value in our case is 0.29 which is lower than 0.5 and corresponds to the Fickian diffusion release mechanism in which solvent penetration is the rate-limiting step.[31]

5.3.13. Antifungal Studies:

Antifungal activity of various hydrogels was evaluated by disk diffusion assay against *Candida albicans* and the zone of inhibition (**Fig. 5.16b**) was monitored. Interestingly, in all the hydrogel samples (CPCa and CPBG) containing AmB, anti-microbial activity was reported. A positive control, pure AmB and negative controls, hydrogels (CPCa and CPBG) without AmB were used. Positive control showed 32.5 mm as a zone of inhibition and negative does not give any zone of inhibition (data not shown). In the case of hydrogel samples with AmB, the reported minimum zone of inhibition was less as compared to the positive control. It can be justified based on the drug release profile of the hydrogel. Further, the minimum zone of inhibition for CPCa and CPBG decreases with an increase in the crosslinker concentration and reported zone of inhibitions for various CPCa samples were slightly higher than the corresponding CPBG hydrogels. As the network connectivity for various hydrogel samples increases (as observed in SEM images (**Fig. 5.6**), the pore size decreases and lesser content of drug diffuse out and show lesser anti-microbial activity.[48,49] In brief, the lesser the content of BG particles or calcium the diffusion of the drug is higher and consequently resulting in a higher antifungal property. Noticeably, higher the bioglass mineralization, proportionally the crystalline hydroxyapatite formation is high that acts as a barrier in the release of drug from the hydrogel system.[39] In addition, the crosslinking ability of BG particles with the CP matrix is more substantial in comparison with Ca^{2+}, as explained in section 3.5.

5.3.14. Cell Culture Studies; Cellular Viability Assay:

The cellular viability of hydrogel powder samples was evaluated through MTT assay with increasing sample concentration (10 µg/mL, 50 µg/mL and 100 µg/mL) against U2OS and HaCaT cell lines for 24 h (**Fig. 5.18a-b**). In general, the cellular viability was observed above 80 % for all the hydrogel samples. Importantly, the MTT assay results exhibited that the concentration of crosslinker or the content of the BG particle does not influence the viability of both the cells. Herein, untreated U2OS and HaCaT cells grown in DMEM media were considered as control with 100 % cellular viability.

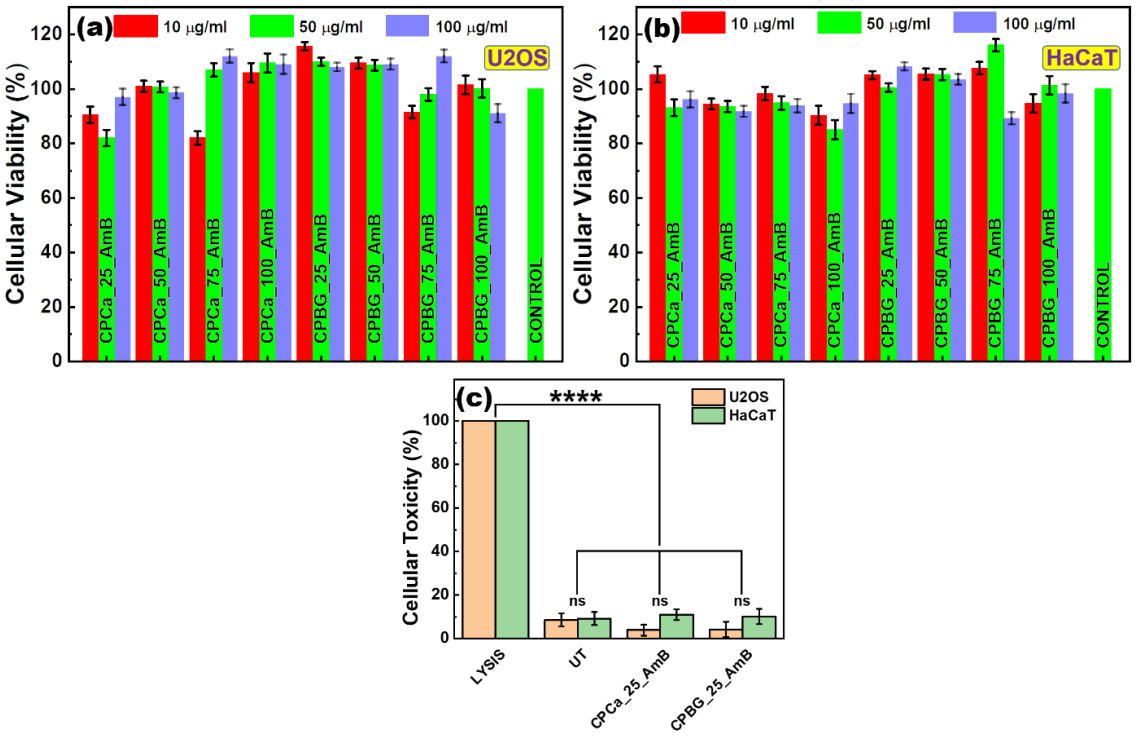

Fig. 5.18: Demonstration of biocompatibility for various hydrogels by **(a and b)** MTT assay and **(c)** LDH assay against U2OS and HaCaT cell lines. The statistical analysis was carried out through graph pad prism 8.4.3 software using two-way ANOVA followed by Turkey's multiplicative comparison test. MTT assay of different samples on HaCaT and U2OS cell lines shows no significant cytotoxicity below or at sample concentration of 100 µg/ml. ($p>0.05$). In LDH release for various samples signifficant difference was assumed for $p<0.05$, ****$p<0.0001$.

It is pertinent to mention that the reported cellular viability by MTT assay is greater than the control (untreated), which is due to the uncertainty in the cellular proliferation for longer duration.[48] Additionally, as shown in **Fig. 5.18c**, MTT assay results are in good agreement with the LDH assay on the representative hydrogel CPBG_25_AmB and its corresponding control CPCa_25_AmB using U2OS and HaCaT cell lines for 24 h respectively. Importantly, LDH assay results confirm that there is no considerable cytotoxicity imposed by both the samples i.e CPCa_25_AmB and CPBG_25_AmB. These findings validate the cytocompatibility of the hydrogel samples with both U2OS and HaCaT cell lines and are in good agreement with earlier reports.[47,50]

5.3.15. FDA/PI Assay:

Cell viability for U2OS cells on interaction with hydrogels CPCa_25_AmB and CPBG_25_AmB was investigated by fluorescence images of FDA/PI staining for 1, 3 and 7 days (**Fig. 5.19 and Fig. 5.20**). Initially, on day 1, most of the cells exhibited viability indicating low cytotoxicity for both the hydrogels. These results are in good agreement with MTT assay and LDH assay (**Fig. 5.18**). However, on 3rd day, only CPBG_25 showed more cell viability as compared to CPCa_25. The presence of viable cells and well-spread morphology of CPBG_25 indicates that the hydrogel can support cell adhesion due to the hydroxyapatite formation (**Fig. 5.14**)**.** In the case of CPCa_25, more inferior cell adhesion and lower cell viability might be due to relatively lower stiffness of the sample and the absence of bioactivity as compared to CPBG_25 (**Fig. 5.19, 5.20**).[47] Further, at 7th day, in CPBG_25 the morphology of the cells was highly branched due to cytoplasmic extensions, showing adhesion on the hydrogel. Whereas, in the case of CPCa_25, the cell viability decreases. The cytoplasmic extensions

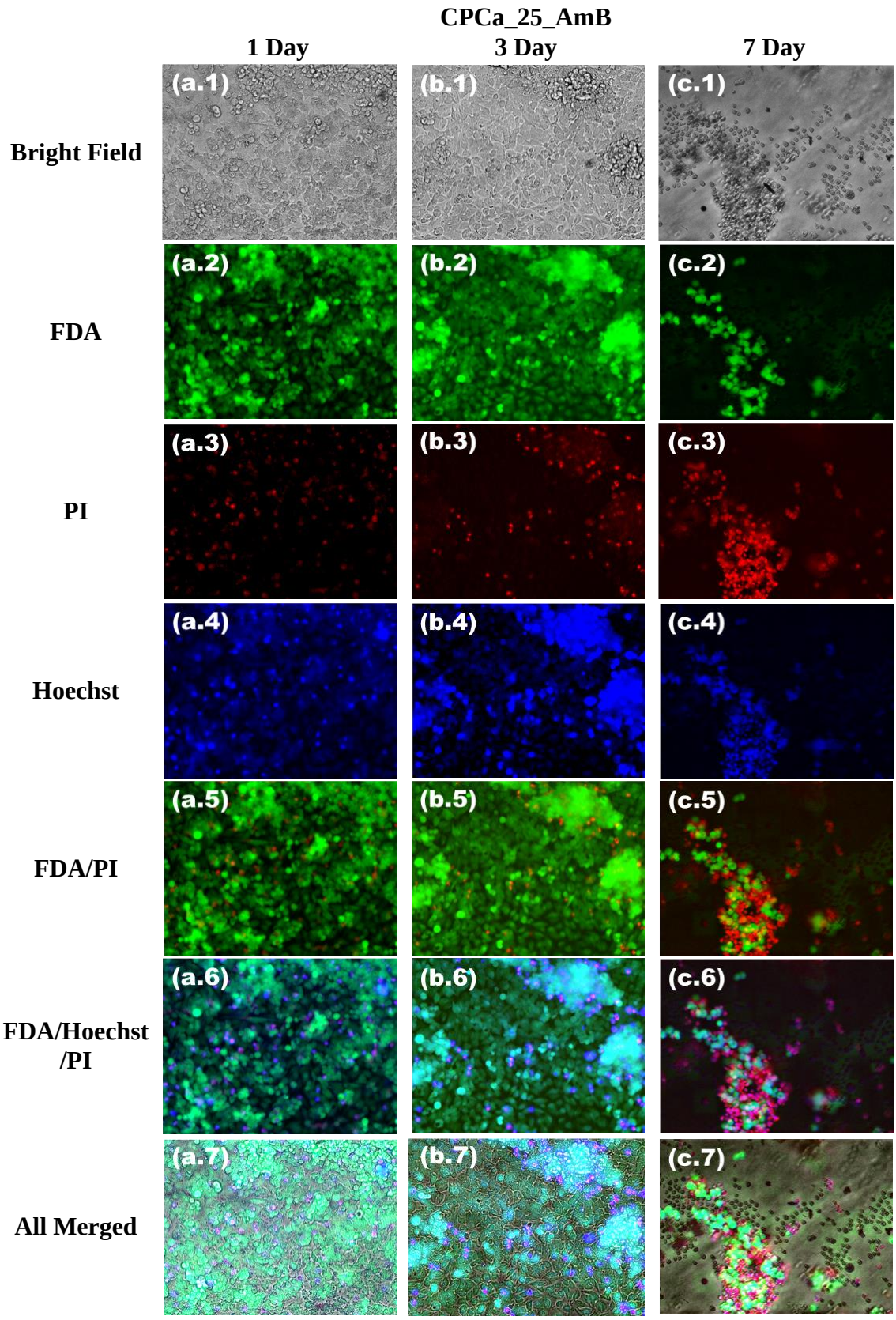

Fig. 5.19: Fluorescence images for cell viability analysis using Fluorescein diacetate (FDA) (green), propidium iodide (PI) (red) and Hoechst (blue)) staining of U2OS cell cultured for 1,3 and 7 days with (a-c) CPCa_25_AmB.

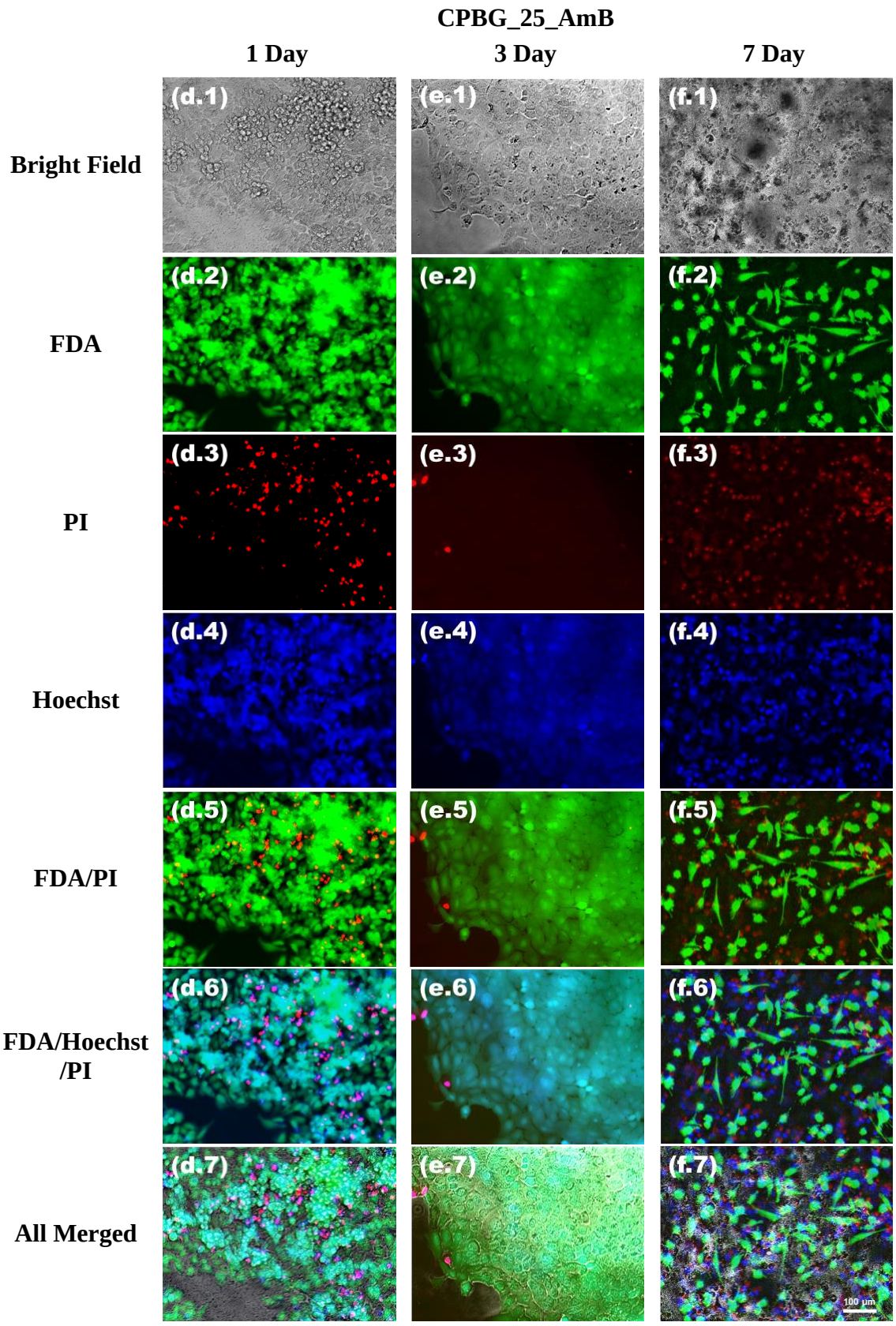

Fig. 5.20: Fluorescence images for cell viability analysis using Fluorescein diacetate (FDA) (green), propidium iodide (PI) (red) and Hoechst (blue)) staining of U2OS cell cultured for 1,3 and 7 days with (d-f) CPBG_25_AmB hydrogels.

observed in CPBG_25 at the 7th day concludes that the presence of bioglass particles and the corresponding bioactivity profoundly influence the cell morphology. The observed higher U2OS cell adherence on hydrophobic hydroxyapatite layer compared to hydrophilic surfaces is well reported in literature.[47,51–53] Further in line with the *in-vitro* disintegration study (**Fig. 5.11**), the lower number of cells observed on day 7 can be attributed to the disintegration of the hydrogel in media by day 7. Most cells might have dispersed and removed from wells when media was replaced every 2 days.

5.4.Conclusion:

In this investigation, collagen-pectin based hybrid composite hydrogel containing BG nanoparticles was synthesized successfully without any external crosslinkers. The fact that, at the molecular level surface patch binding interaction between collagen and pectin, irrespective of both carrying similar net charge, favoured multi-centred crosslinking that was synergetic with the additional crosslinking provided by the *in-situ* mineralized BG nanoparticles, is one of the unique features of the hybrid composite hydrogel containing interconnected macropores. The Fickian swelling behaviour of the macroporous hydrogel (sample CPBG_25) combined with its high mechanical strength not only favored free solvent mobility but also acted as controlled release of its drug cargo. Importantly, the macroporous hydrogel exhibited *in-vitro* bioactivity in SBF solution by the formation of bone like hydroxyapatite ($Ca_{10}(PO_4)_6(OH)_2$) microcrystals. In addition, the hydrogel was also biocompatible with U2OS and HaCaT cell lines showing higher U2OS cell adherence on hydroxyapatite layer. The observed characteristic bone bonding ability and excellent biocompatibility of the macroporous hybrid composite hydrogel promises as a suitable candidate for tissue regeneration in future.

REFERENCES:

[1] A. Seidi, M. Ramalingam, I. Elloumi-Hannachi, S. Ostrovidov, A. Khademhosseini, Gradient biomaterials for soft-to-hard interface tissue engineering, Acta Biomater. 7 (2011) 1441–1451.

[2] Y.J. No, M. Castilho, Y. Ramaswamy, H. Zreiqat, Role of Biomaterials and Controlled Architecture on Tendon/Ligament Repair and Regeneration, Adv. Mater. 32 (2020) 1904511.

[3] L.R. Feksa, E.A. Troian, C.D. Muller, F. Viegas, A.B. Machado, V.C. Rech, Hydrogels for biomedical applications, in: Nanostructures Eng. Cells, Tissues Organs, Elsevier, 2018: pp. 403–438.

[4] H. B. Bohidar, P. Dubin, Y. Osada, Fundamentals and Applications, ed. HB Bohidar, P. Dubin and Y. Osada, (2002).

[5] F. Munarin, S.G. Guerreiro, M.A. Grellier, M.C. Tanzi, M.A. Barbosa, P. Petrini, P.L. Granja, Pectin-Based Injectable Biomaterials for Bone Tissue Engineering, Biomacromolecules. 12 (2011) 568–577.

[6] N. Gupta, H. Goel, D. Santhiya, C.M. Srivastava, S. Mishra, P. Rai, Aqueous- Phased Electrospun Bioactive Glass Mineralized Gelatin- Pectin Hybrid Composite Fiber Matrix For 7- Dehydrocholesterol Delivery, ChemistrySelect. 5 (2020) 4364–4370. https://doi.org/10.1002/slct.202000264.

[7] S. Cui, B. Yao, M. Gao, X. Sun, D. Gou, J. Hu, Y. Zhou, Y. Liu, Effects of pectin structure and crosslinking method on the properties of crosslinked pectin nanofibers, Carbohydr. Polym. 157 (2017) 766–774. https://doi.org/10.1016/j. carbpol.2016.10.052.

[8] G.C. Jayakumar, N. Usharani, K. Kawakami, J.R. Rao, B.U. Nair, Studies on the Physico-Chemical Characteristics of Collagen-Pectin Composites, RSC Adv. 4 (2014) 63840–63849. https://doi.org/10.1039/C4RA10368H.

[9] F. Wenpo, L. Gaofeng, F. Shuying, Q. Yuanming, T. Keyong, Preparation and characterization of collagen-hydroxyapatite/pectin composite, Int. J. Biol. Macromol. 74 (2015) 218–223. https://doi.org/10.1016/j.ijbiomac.2014.11.031.

[10] J. Pathak, E. Priyadarshini, K. Rawat, H.B. Bohidar, Complex coacervation in charge complementary biopolymers: Electrostatic versus surface patch binding, Adv. Colloid Interface Sci. 250 (2017) 40–53.

[11] J. Pathak, K. Rawat, H.B. Bohidar, Surface patch binding and mesophase separation in biopolymeric polyelectrolyte–polyampholyte solutions, Int. J. Biol. Macromol. 63 (2014) 29–37.

[12] T.N. Vo, S.R. Shah, S. Lu, A.M. Tatara, E.J. Lee, T.T. Roh, Y. Tabata, A.G. Mikos, Injectable dual-gelling cell-laden composite hydrogels for bone tissue engineering, Biomaterials. 83 (2016) 1–11. https://doi.org/10.1016/j.biomaterials.2015.12.026.

[13] M. Erol-Taygun, I. Unalan, M.I.B. Idris, J.F. Mano, A.R. Boccaccini, Bioactıve Glass-Polymer Nanocomposites for Bone Tıssue Regeneration Applicatıons: A Revıew, Adv. Eng. Mater. 21 (2019) 1900287.

[14] J. Zheng, F. Zhao, W. Zhang, Y. Mo, L. Zeng, X. Li, X. Chen, Sequentially-crosslinked biomimetic bioactive glass/gelatin methacryloyl composites hydrogels for bone regeneration, Mater. Sci. Eng. C. 89 (2018) 119–127.

[15] M.H. Kim, B.S. Kim, H. Park, J. Lee, W.H. Park, Injectable methylcellulose

hydrogel containing calcium phosphate nanoparticles for bone regeneration, Int. J. Biol. Macromol. 109 (2018) 57–64.

[16] J.A. Killion, S. Kehoe, L.M. Geever, D.M. Devine, E. Sheehan, D. Boyd, C.L. Higginbotham, Hydrogel/bioactive glass composites for bone regeneration applications: Synthesis and characterisation, Mater. Sci. Eng. C. 33 (2013) 4203–4212. https://doi.org/10.1016/j.msec.2013.06.013.

[17] A. Gantar, N. Drnovšek, P. Casuso, A. Pérez-San Vicente, J. Rodriguez, D. Dupin, S. Novak, I. Loinaz, Injectable and self-healing dynamic hydrogel containing bioactive glass nanoparticles as a potential biomaterial for bone regeneration, RSC Adv. 6 (2016) 69156–69166. https://doi.org/10.1039/c6ra17327f.

[18] P. Nikpour, H. Salimi-Kenari, F. Fahimipour, S.M. Rabiee, M. Imani, E. Dashtimoghadam, L. Tayebi, Dextran hydrogels incorporated with bioactive glass-ceramic: Nanocomposite scaffolds for bone tissue engineering, Carbohydr. Polym. 190 (2018) 281–294. https://doi.org/10.1016/j.carbpol.2018.02.083.

[19] C.D.F. Moreira, S.M. Carvalho, H.S. Mansur, M.M. Pereira, Thermogelling chitosan–collagen–bioactive glass nanoparticle hybrids as potential injectable systems for tissue engineering, Mater. Sci. Eng. C. 58 (2016) 1207–1216.

[20] D.S. Couto, Z. Hong, J.F. Mano, Development of bioactive and biodegradable chitosan-based injectable systems containing bioactive glass nanoparticles, Acta Biomater. 5 (2009) 115–123.

[21] A.S. Veiga, J.P. Schneider, Antimicrobial hydrogels for the treatment of infection, Biopolymers. 100 (2013) 637–644. https://doi.org/10.1002/bip.22412.

[22] L. Sosa, A.C. Calpena, M. Silva-Abreu, L.C. Espinoza, M. Rincón, N. Bozal, O. Domenech, M.J. Rodríguez-Lagunas, B. Clares, Thermoreversible gel-loaded amphotericin B for the treatment of dermal and vaginal candidiasis, Pharmaceutics. 11 (2019) 1–18. https://doi.org/10.3390/pharmaceutics11070312.

[23] T. Demirci, M.E. Hasköylü, M.S. Eroğlu, J. Hemberger, E. Toksoy Öner, Levan-based hydrogels for controlled release of Amphotericin B for dermal local antifungal therapy of Candidiasis, Eur. J. Pharm. Sci. 145 (2020). https://doi.org/10.1016/j.ejps.2020.105255.

[24] C. Shu, T. Li, W. Yang, D. Li, S. Ji, L. Ding, Amphotericin B-conjugated polypeptide hydrogels as a novel innovative strategy for fungal infections, R. Soc. Open Sci. 5 (2018) 171814. https://doi.org/10.1098/rsos.171814.

[25] D. Santhiya, H.K. Alajangi, F. Anjum, S. Murugavel, M. Ganguli, Bio-inspired synthesis of microporous bioactive glass-ceramic using CT-DNA as a template, J. Mater. Chem. B. 1 (2013) 6329–6338. https://doi.org/10.1039/c3tb21212b.

[26] C. Boztepe, M. Solener, M. Yuceer, A. Kunkul, O.S. Kabasakal, Modeling of swelling behaviors of acrylamide-based polymeric hydrogels by intelligent system, J. Dispers. Sci. Technol. 36 (2015) 1647–1656.

[27] T. Kokubo, Bioactive glass ceramics: properties and applications, Biomaterials. 12 (1991) 155–163.

[28] S.P. Hudson, R. Langer, G.R. Fink, D.S. Kohane, Injectable in situ cross-linking hydrogels for local antifungal therapy, Biomaterials. 31 (2010) 1444–1452. https://doi.org/10.1016/j.biomaterials.2009.11.016.

[29] A.I. Rezk, F.O. Obiweluozor, G. Choukrani, C.H. Park, C.S. Kim, Drug release

and kinetic models of anticancer drug (BTZ) from a pH-responsive alginate polydopamine hydrogel: Towards cancer chemotherapy, Int. J. Biol. Macromol. 141 (2019) 388–400. https://doi.org/10.1016/j.ijbiomac.2019.09.013.

[30] M. Gautam, D. Santhiya, Pectin/PEG food grade hydrogel blend for the targeted oral co-delivery of nutrients, Colloids Surfaces A Physicochem. Eng. Asp. 577 (2019) 637–644.

[31] J. Hernandez-Montelongo, N. Naveas, S. Degoutin, N. Tabary, F. Chai, V. Spampinato, G. Ceccone, F. Rossi, V. Torres-Costa, M. Manso-Silvan, B. Martel, Porous silicon-cyclodextrin based polymer composites for drug delivery applications, Carbohydr. Polym. 110 (2014) 238–252. https://doi.org/10.1016/j.carbpol.2014.04.002.

[32] © ibidi GmbH, Live / dead staining with FDA and PI 1 General information, Ibidi GmbH. (2015) 1–4. http://ibidi.com/fileadmin/support/application_notes/AN33_Live_Dead_staining_with_FDA_and_PI.pdf.

[33] E. Dickinson, Stability and rheological implications of electrostatic milk protein–polysaccharide interactions, Trends Food Sci. Technol. 9 (1998) 347–354.

[34] Y. Xu, M. Mazzawi, K. Chen, L. Sun, P.L. Dubin, Protein purification by polyelectrolyte coacervation: influence of protein charge anisotropy on selectivity, Biomacromolecules. 12 (2011) 1512–1522.

[35] H.A. Barnes, A handbook of elementary rheology, (2000).

[36] I. Fraeye, T. Duvetter, E. Doungla, A. Van Loey, M. Hendrickx, Fine-tuning the properties of pectin-calcium gels by control of pectin fine structure, gel composition and environmental conditions, Trends Food Sci. Technol. 21 (2010)

219–228. https://doi.org/10.1016/j.tifs.2010.02.001.

[37] N. Gupta, D. Santhiya, Role of cellulose functionality in bio-inspired synthesis of nano bioactive glass, Mater. Sci. Eng. C. 75 (2017) 1206–1213. https://doi.org/10.1016/j.msec.2017.03.026.

[38] N. Gupta, D. Santhiya, A. Aditya, K. Badra, Dendrimer templated bioactive glass-ceramic nanovehicle for gene delivery applications, RSC Adv. 5 (2015) 56794–56807. https://doi.org/10.1039/c5ra04441c.

[39] N. Gupta, D. Santhiya, A. Aditya, Tailored smart bioactive glass nanoassembly for dual antibiotic: In vitro sustained release against osteomyelitis, J. Mater. Chem. B. 4 (2016) 7605–7619. https://doi.org/10.1039/c6tb01528j.

[40] B.H. León-Mancilla, M.A. Araiza-Téllez, J.O. Flores-Flores, M.C. Piña-Barba, Physico-chemical characterization of collagen scaffolds for tissue engineering, J. Appl. Res. Technol. 14 (2016) 77–85. https://doi.org/10.1016/j.jart.2016.01.001.

[41] N.V. Gupta, H.G. Shivakumar, Investigation of swelling behavior and mechanical properties of a pH-sensitive superporous hydrogel composite, Iran. J. Pharm. Res. IJPR. 11 (2012) 481.

[42] F. Ganji, S. Vasheghani-Farahani, E. Vasheghani-Farahani, Theoretical description of hydrogel swelling: A review, Iran. Polym. J. (English Ed. 19 (2010) 375–398.

[43] A. Martinez-Ruvalcaba, J.C. Sánchez-Díaz, F. Becerra, L.E. Cruz-Barba, A. González-Álvarez, Swelling characterization and drug delivery kinetics of polyacrylamide-co-itaconic acid/chitosan hydrogels, Express Polym Lett. 3 (2009) 25–32.

[44] M.H. Misbah, M. Santos, L. Quintanilla, C. Günter, M. Alonso, A. Taubert, J.C. Rodríguez-Cabello, Recombinant DNA technology and click chemistry: A powerful combination for generating a hybrid elastin-like-statherin hydrogel to control calcium phosphate mineralization, Beilstein J. Nanotechnol. 8 (2017) 80. https://doi.org/10.3762/bjnano.8.80.

[45] R. Lakshmi, S. Sasikumar, Influence of needle-like morphology on the bioactivity of nanocrystalline wollastonite – An in vitro study, Int. J. Nanomedicine. 10 (2015) 129–136. https://doi.org/10.2147/IJN.S79986.

[46] T.E.L. Douglas, W. Piwowarczyk, E. Pamula, J. Liskova, D. Schaubroeck, S.C.G. Leeuwenburgh, G. Brackman, L. Balcaen, R. Detsch, H. Declercq, K. Cholewa-Kowalska, A. Dokupil, V.M.J.I. Cuijpers, F. Vanhaecke, R. Cornelissen, T. Coenye, A.R. Boccaccini, P. Dubruel, Injectable self-gelling composites for bone tissue engineering based on gellan gum hydrogel enriched with different bioglasses, Biomed. Mater. 9 (2014). https://doi.org/10.1088/1748-6041/9/4/045014.

[47] T.E.L. Douglas, M. Dziadek, J. Schietse, M. Boone, H.A. Declercq, T. Coenye, V. Vanhoorne, C. Vervaet, L. Balcaen, M. Buchweitz, F. Vanhaecke, F. Van Assche, K. Cholewa-Kowalska, A.G. Skirtach, Pectin-bioactive glass self-gelling, injectable composites with high antibacterial activity, Carbohydr. Polym. 205 (2019) 427–436. https://doi.org/10.1016/j.carbpol.2018.10.061.

[48] N. Gupta, D. Santhiya, S. Murugavel, A. Kumar, A. Aditya, M. Ganguli, S. Gupta, Effects of transition metal ion dopants (Ag, Cu and Fe) on the structural, mechanical and antibacterial properties of bioactive glass, Colloids Surfaces A Physicochem. Eng. Asp. 538 (2018) 393–403.

[49] F. Wahid, C. Zhong, H.-S. Wang, X.-H. Hu, L.-Q. Chu, Recent advances in antimicrobial hydrogels containing metal ions and metals/metal oxide nanoparticles, Polymers (Basel). 9 (2017) 636.

[50] G. Tommasi, S. Perni, P. Prokopovich, An Injectable Hydrogel as Bone Graft Material with Added Antimicrobial Properties, Tissue Eng. - Part A. 22 (2016) 862–872. https://doi.org/10.1089/ten.tea.2016.0014.

[51] R. Goldshmid, D. Seliktar, Hydrogel Modulus Affects Proliferation Rate and Pluripotency of Human Mesenchymal Stem Cells Grown in Three-Dimensional Culture, ACS Biomater. Sci. Eng. 3 (2017) 3433–3446. https://doi.org/ 10.1021/acsbiomaterials.7b00266.

[52] W.S. Huang, I.M. Chu, Injectable polypeptide hydrogel/inorganic nanoparticle composites for bone tissue engineering, PLoS One. 14 (2019) 1–17. https://doi. org/10.1371/journal.pone.0210285.

[53] T. Jiang, G. Xu, X. Chen, X. Huang, J. Zhao, L. Zheng, Impact of Hydrogel Elasticity and Adherence on Osteosarcoma Cells and Osteoblasts, Adv. Healthc. Mater. 8 (2019) 1–11. https://doi.org/10.1002/adhm.201801587.

CHAPTER 6

Aqueous Phased Electrospun Bioactive Glass Incorporated Gelatin-Pectin Composite Fiber Matrix For 7-Dehydrocholesterol Delivery

CHAPTER 6

Aqueous Phased Electrospun Bioactive Glass Incorporated Gelatin-Pectin Composite Fiber Matrix For 7-Dehydrocholesterol Delivery

GRAPHICAL ABSTRACT

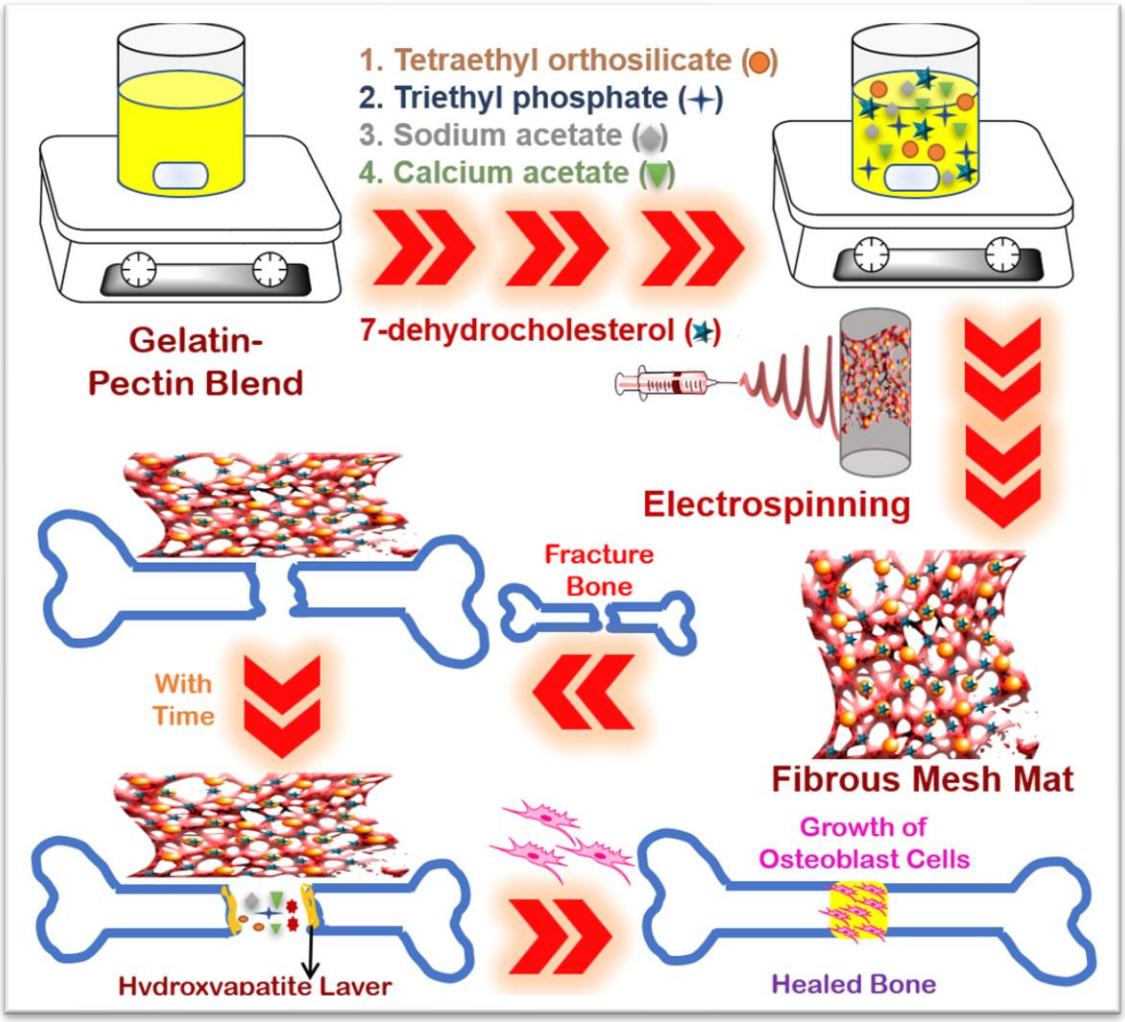

6.1. Introduction:

Gelatin based electrospun fibers are making advances in the medical community for their therapeutic importance [1,2]. To improve the mechanical property of gelatin, a blend with pectin is required owing to its importance in bone regenerative medicine [3–9]. Recently, pectin - a plant-derived diet has gained the attention of the medical community owing to its health-promoting ability [10] such as anti-inflammatory property [11] and anti-cancer ability [12] by inducing apoptosis in cancer cells [13]. Pectin also serves to be a promising cell injectable [14] and drug delivery system [15]. Biomedical applications of pectin have been explored in the form of the composites, scaffolds or injectable gel [16]. Moving towards green processing techniques, using an aqueous blend of natural biopolymers, ultrafine fibers are electrospun. Particularly, in the considered gelatin-pectin blend solution a higher percentage of gelatin is used to overcome challenges associated with the pectin processing (solubility and charge issues) [3,17,18]. Compounding the advantages of these biopolymers, the resulting ultrafine fibers mat containing bioactive glass particles, and 7-dehydrocholesterol could potentially give synergistic mechanical and biological responses. In addition to our previous contribution of films [19], the present investigation focuses on the nanofibrous mat, with the increase in aspect ratio, as well as the presence of pores in the mat, helps to enhance the biological response in the form of cellular proliferation and loaded therapeutic molecule release profile [20,21].

Literature shows that calcium phosphate loaded gelatin-pectin scaffold is known to serve as a promising biomaterial for bone tissue engineering [6]. Rationales for the use of polymer-ceramic composites for bone regeneration arise from the natural composition of the bone [22]. Here, the novelty lies in the *in-situ* mineralization of bioactive glass particles into aqueous phased gelatin-pectin electrospun ultrafine hybrid composite

fibrous mat following bioinspired approach [23]. Pertinently, nanosized fibers possess remarkable importance owing to their superior interfacial reactions with higher physiological (bioactivity), biological and mechanical properties. It is noteworthy that the bioactive glass electrospun fibers reported till date were synthetic polymer-based requiring calcination [24] and inorganic sol-gel solutions. They were also electrospun to produce bioactive glass structure like cotton-wool in ethanol [25].

Interestingly, in the present investigation, an engineered hybrid composite fiber construct has been proposed for synergistically efficient bone regeneration after incorporating 7-dehydrocholesterol along with bioactive glass particles. 7-dehydrocholesterol acts as a precursor to vitamin D, a vital bone-strengthening vitamin. Vitamin-D is a significant ingredient factor in maintaining calcium as well as phosphate homeostasis by modulating their intestinal absorption and henceforth, plays a crucial role in bone health [26,27]. Nutritional deficiency of vitamin D, successively of calcium and phosphate can result in the formation of weak and poorly mineralized bone [28].

6.2. Experimental Section:

6.2.1. Materials:

Pectin (esterified 60% to 70%), gelatin, 7-dehydrocholesterol (MW 384.64) as well as bioactive glass precursors (tetraethyl orthosilicate (TEOS), triethyl phosphate (TEP), sodium acetate and calcium acetate) were obtained from Sigma-Aldrich. Milli-Q water was used for all the experimental work. All the other chemicals used were of analytical reagent (AR) grade.

6.2.2. Methods:

6.2.2.1. Fiber preparation:

For electrospinning (Royal Enterprises, India) of gelatin-pectin fiber (GP), 20 w/v % gelatin (G) was blended with 0.4 w/v % pectin (P) in 12.5 v/v % formic acid solution. The GP blended solution was electrospun at the voltage of 18 kV with a flow rate of 1 mL/h. In order to fabricate gelatin-pectin hybrid composite fibers containing *in-situ* mineralized bioactive glass particles (GPBG), bioactive glass precursors namely 0.44 M TEOS, 0.05 M TEP, 5 M aq. sodium acetate and 2.5 M aq. calcium acetate were added into the GP spinning solution sequentially at an interval of 15 min as per our earlier procedure [1]. The obtained spinning mixture of GP along with BG precursors was electrospun at the voltage of 19.5 kV with a flow rate of 1 mL/h. Further, 7-dehydrocholesterol solution in dimethylformamide (0.5 mg/mL) was added after the addition of bioactive glass precursors as explained above and electrospun at the voltage of 19.5 kV and 0.8mL/h flow rate. The resulting vitamin-D containing bioglass incorporated hybrid composite fibers are named as GPBGD. For all the experiments, tip to collector distance was maintained at 13 cm. The final product was washed with milli-Q water.

6.2.3. Characterization:

To evaluate the structural properties of the samples, XRD, FTIR and TGA experiments were performed as described in section 2.1.1, 2.1.2 and 2.1.4. The surface morphology of GP and GPBGD before and after interaction with SBF was characterized by SEM (JEOL 6610LV) described in section 2.2.1.1. The surface morphology along with Raman spectra was also recorded through atomic force microscope (AFM) to understand internal structural details described in section 2.1.3 and 2.2.2. Mechanical properties of various fibers were determined through Instron universal testing machine (ASTM D882) at a strain rate of 1 mm/min in triplicates and averaged described in section 2.4.2. The contact

angle measurements were carried out using SURFTENS universal (OEG GmbH Germany) in triplicates and averaged.

6.2.4. Bioactivity test:

Bioactivity test for the GPBGD was evaluated through an *in-vitro* test using simulated body fluid (SBF). The fibrous mat of size 1×1 cm^2 was immersed in 10 mL of SBF solution for different duration of time. After each interval, fibrous mat was observed for the formation of hydroxyapatite through FTIR, XRD and SEM as explained in section 2.2.2. Besides this, the corresponding SBF solutions after interaction with fibrous samples were subjected to ICP-AES for elemental analysis. Similar control experiments were also performed for GP fibers.

6.2.5. 7-dehydrocholesterol release test:

7-dehydrocholesterol release from GPBGD was evaluated in phosphate buffer saline (PBS). The release profile of the drug was recorded for 7 days using UV-Vis (Agilent Technologies Carry 300 UV-Vis) spectrophotometer at the wavelength (λ_{max}) of 285 nm [2]. After a specific interval of time, the solution was taken out and UV-Vis spectra were recorded. Required volume correction was carried out during the analysis.

6.2.6. MTT ((3-(4,5-Dimethylthiazol-2-yl)-2,5- diphenyltetrazolium bromide) assay after 24 h and cell proliferation Studies:

The cytocompatibility for the different fibrous mat, namely, GP, GPBG and GPBGD were carried out using MTT assay. The electrospun matrices of size 1×1 cm^2 were washed with 70 % ethanol and then thrice washed with DMEM culture medium before seeding with U2OS (human osteoblast-like osteosarcoma cells) at a seeding density of 2,00,000 cells/well in 6-well plate. A blank coverslip was added to the well on which cells were

seeded to be used as a control. The experiment was done thrice and the cellular viability was calculated through formazan absorbance at 570 nm considering control cells as 100% viable.

The cellular growth and morphology of U2OS cells on the sterilized GPBGD electrospun samples was analyzed using SEM. The cells were seeded at a density of 90,000 cells/well and were replenished with complete media every 24 hrs. At the end of 3 and 5 days, respectively, the samples were washed with PBS, followed by washing with sodium cacodylate. The samples were then fixed using a mixture of 2.5% glutaraldehyde and 4% paraformaldehyde overnight at 4°C. The cells were then dehydrated using a series of graded ethanol washes. The samples were then gold-coated and observed by SEM (JEOL 6610LV) at 15 KeV.

6.3.Results and Discussion:

6.3.1. Material Characterization:

It was worth observing that polymer concentration plays a vital role in defining the fiber diameter. For gelatin concentration below 20 w/v % in the GP blend solution, it was not possible to obtain the fibers. However, at the 20 w/v % nanosized fibers **(Fig. 6.1a)** (20-40 nm diameter measured through ImageJ software) were obtained. Interestingly, the addition of bioactive glass precursors into the GP blend resulted in the *in-situ* mineralization of bioactive glass in the natural polymer blend matrix as visualized by SEM **(Fig. 6.1b).** Further, the fibers were also well visualized through AFM **(Fig. 6.1c-f).** It was interesting to note that the fibrous mat was denser in case of GPBGD **(Fig. 6.1e-f)**. It could be validated by the fact that both vitamin D [28] and silica [29] are the vital elements for the promotion of bone mineralization. Hence, a synergistic response is observed, which results in a denser fibrous mat. More importantly, the presence of

bioactive glass along with 7-dehydrocholesterol, was validated through integrated Raman spectroscopy with AFM **(Fig. 6.1g-h)**. For GPBG, a prominent peak at 1098 cm^{-1} and 1240 cm^{-1} was observed in raman spectra **(Fig. 6.1g)** corresponding to Q^4 state of the siliceous network based bioactive glass. Other Q^n states (where, n refers to number of bridging oxygen) raman peaks were beyond the detection limit of the instrument. While in Raman spectra for GPBGD, a prominent peak at 2944 cm^{-1} and a broad hump at 3293 cm^{-1} corresponding to -CH and -OH group of the organic molecules namely, gelatin, pectin and vitamin D were observed along with Si—O—Si, a characteristic peak of silica-based bioactive glass. Peaks centred at 407 cm^{-1} and 520 cm^{-1} corresponds to the siliceous vibrational modes were observed. In addition to Q^4 state peak at 1240 cm^{-1}, further peaks from 810 cm^{-1} to 1010 cm^{-1} attributed to the Si—O—Si bond in silica tetrahedra with a different number of non-bridging oxygen (NBO) was recorded. Notably, the 860 cm^{-1} and 975 cm^{-1} peaks can be ascribed to monomers SiO^{4-} (Q^0;4 NBO), dimers $Si_2O_7^{6-}$ (Q^1;3 NBO), rings and chains $Si_2O_6^{4-}$ (Q^2;2 NBO), respectively. A peak at 1008 cm^{-1} is also

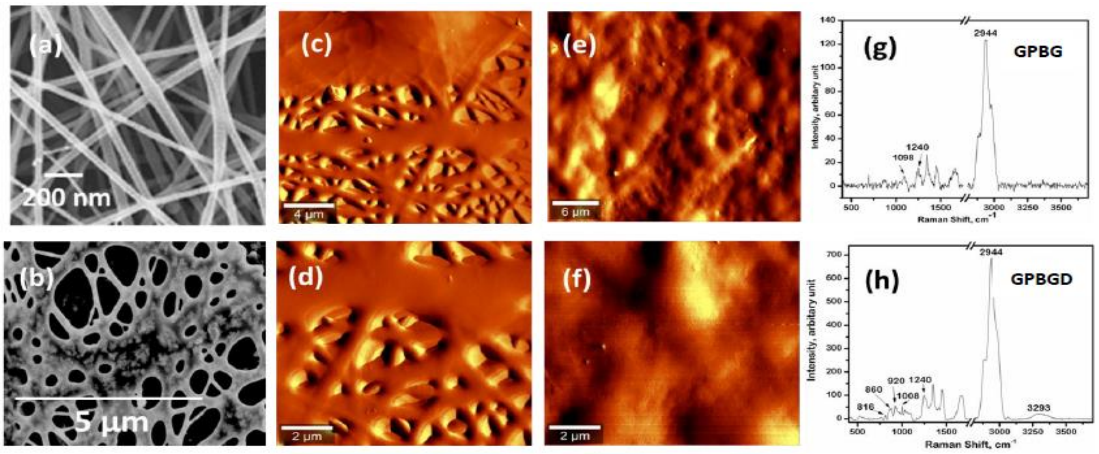

Fig. 6.1: SEM images of **(a)** GP and **(b)** GPBG. AFM images of **(c-d)** GPBG and **(e-f)** GPBGD. Raman Spectra of **(g)** GPBG and **(h)** GPBGD.

associated with the Si-O-Si stretching vibration mode. Interestingly, the peak at 920 cm^{-1} ascribed to P–O bond is also observed in the Raman spectra. It is pertinent to note that

the introduction of 7-dehydrocholesterol during the GPBGD fibers fabrication, distorts the silica network as evidenced by the reduced Q^4 state to lower Q^n states, namely Q^2, Q^1 and Q^0 states **(Fig. 6.1h).**

Fig. 6.2 shows the thermogravimetric analysis of GP, GPBG and GPBGD. Herein, TGA of GP showed initial degradation at ~90 °C due to the loss of water, followed by depolymerization of gelatin and pectin chains at ~250 °C and finally ~98.8 % weight loss was noticed at 800 °C. In the case of GPBG and GPBGD, TGA pattern appeared nearly the same but showing an increase in stability compared to GP. It is worth mentioning that the final weight loss of 85% at 800 °C was observed for GPBG and GPBGD, confirming the inorganic bioglass content.

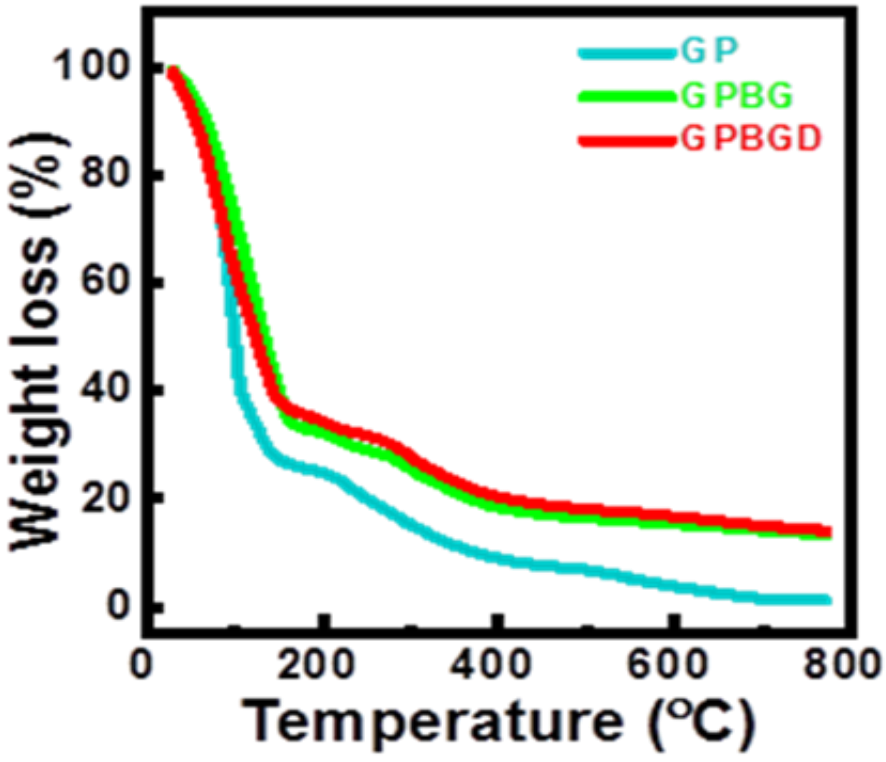

Fig. 6.2: Thermogravimetric analysis of GP, GPBG and GPBGD.

XRD pattern of as prepared GP, GPBG and GPBGD are depicted in **Fig. 6.3a**. XRD pattern showed a broad peak in the 2θ range of 20° to 30° for GP, GPBG and GPBGD.

The observation indicates the amorphous and nanosized nature of GP fibers as well as fibrous mats GPBG and GPBGD containing mineralized bioactive glass particles in consistent with literature [30].

Fig. 6.3b portrays FTIR spectra of GP, GPBG and GPBGD. FTIR spectrum of GP reveals the existence of esterified –C=O stretching at 1714 cm^{-1} as well as symmetric –COO° stretching originated from pectin molecules at 1446 cm^{-1}. Besides, amide I (–C=O, 1635 cm^{-1}), amide II (–N–H, 1531 cm^{-1}) and amide III (–C–N, 1191 cm^{-1}) peaks of gelatin were also observed in GP. Interestingly, characteristic bioglass peaks were observed in FTIR spectra of GPBG. Peak corresponds to –P=O and –P–O appeared at 1367 cm^{-1} and 1215 cm^{-1}, respectively. Also, the ring structure of the silicate network was reported at 734 cm^{-1}, and Si-O–Si vibration was observed at 472 cm^{-1}. It is noteworthy that in the case of GPBG, the peak corresponding to esterified –C=O stretching and amide II were noticeably shifted to higher wavenumber in comparison with GP revealing the

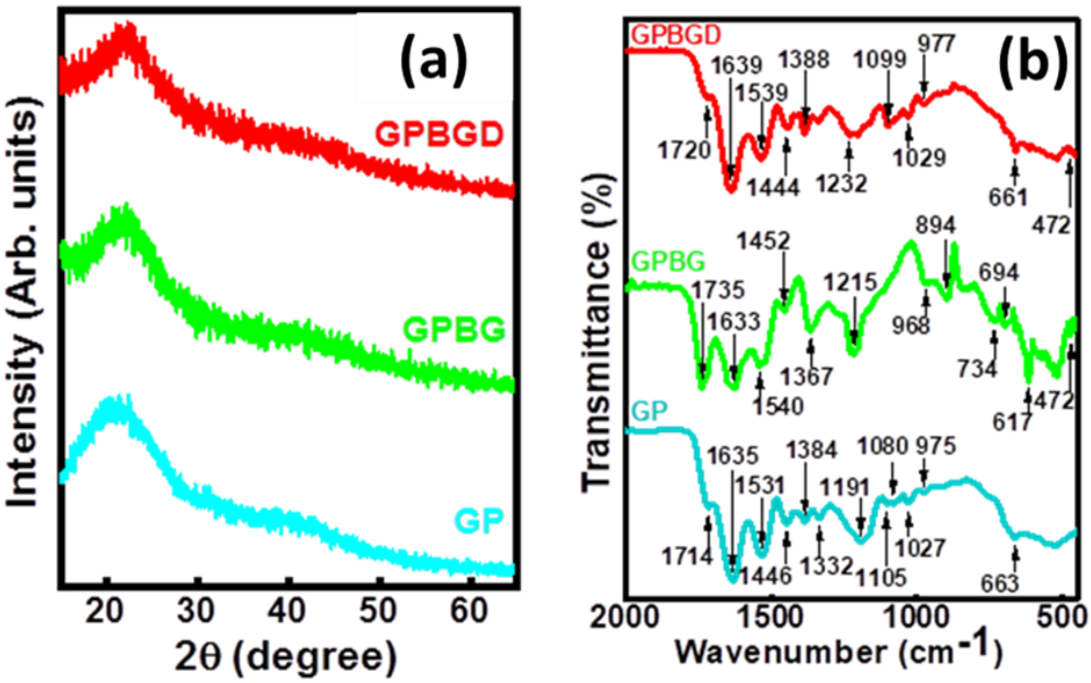

Fig. 6.3: (a) XRD pattern and **(b)** FTIR Spectra of GP, GPBG and GPBGD.

interaction between GP and bioglass precursors during electrospinning. FTIR spectrum of GPBGD after incorporation of 7-dehydrocholesterol also exhibited similar to GPBG containing characteristic peak of bioglass as well as GP. It is worth mentioning that characteristic peaks correspond to esterified –C=O stretching was observed at slightly lower wavenumber (1720 cm^{-1}) and the intensity of amide I peak was intensified. In addition, the characteristic peak of bioglass (–Si–O) was shifted to higher wavenumber and appeared at 1232 cm^{-1} in comparison to GPBG. These observations validate the interaction of 7-dehydrocholesterol with the polymer matrix as well as with the mineralized bioglass particles. The reported FTIR results are in good agreement with SEM, AFM images and Raman spectra **(Fig. 6.1).**

6.3.2. Bioactivity:

After interaction of GPBG and GPBGD with SBF solution, *in-vitro* bioactivity of the fiber mat was determined by SEM, **(Fig. 6.4a-b)**, FTIR **(Fig. 6.4e)** and XRD **(Fig. 6.4d)**. The corresponding supernatants of the SBF solutions at various time points were subjected to elemental analysis using ICP-AES **(Fig. 6.4c)**. It is pertinent to note that after 4 h interaction of GPBGD in SBF solution **(Fig. 6.4a)** a surface deposition is visualized by SEM, indicating an inherent bioactive nature of *in-situ* mineralized bioactive glass particles in the hybrid composite fibers **(Fig. 6.1b)**. As the interaction time increased to 24 h, the enhancement in the bioactivity of the fiber mat (GPBGD) was justified by an increase in the surface deposit **(Fig. 6.4b)**.

Noticeably, holding of GP matrix for GPBG and GPBGD after 24 h interaction with SBF solution was observed through the retention of broad hump from 20° to 30° in the XRD pattern **(Fig. 6.4d)**. Similar XRD pattern for GP, GPBG and GPBGD was obtained before SBF immersion **(Fig. 6.3a)**. Pertinently, emergence of new typical reflections at 32° and

45° with hkl plane of 112 and 203, respectively were also observed after SBF immersion corresponding to carbonate hydroxyapatite ($Ca_{10}(PO_4)_3(CO_3)_3(OH)_2$) phase (JCPDS: 00-019-0272).

FTIR studies on GPBG and GPBGD after interaction with SBF solution for 24 h is shown in **Fig. 6.4e**. Interestingly, in the case of GPBG after 24 h interaction with SBF, new peaks appear at 1079 cm^{-1} and 964 cm^{-1} corresponding to phosphate and at 794 cm^{-1} for carbonate groups compared to GPBG before immersion in SBF **(Fig. 6.3b)**. Herein, it is worth mentioning that peak corresponding to –H–O bending expected from

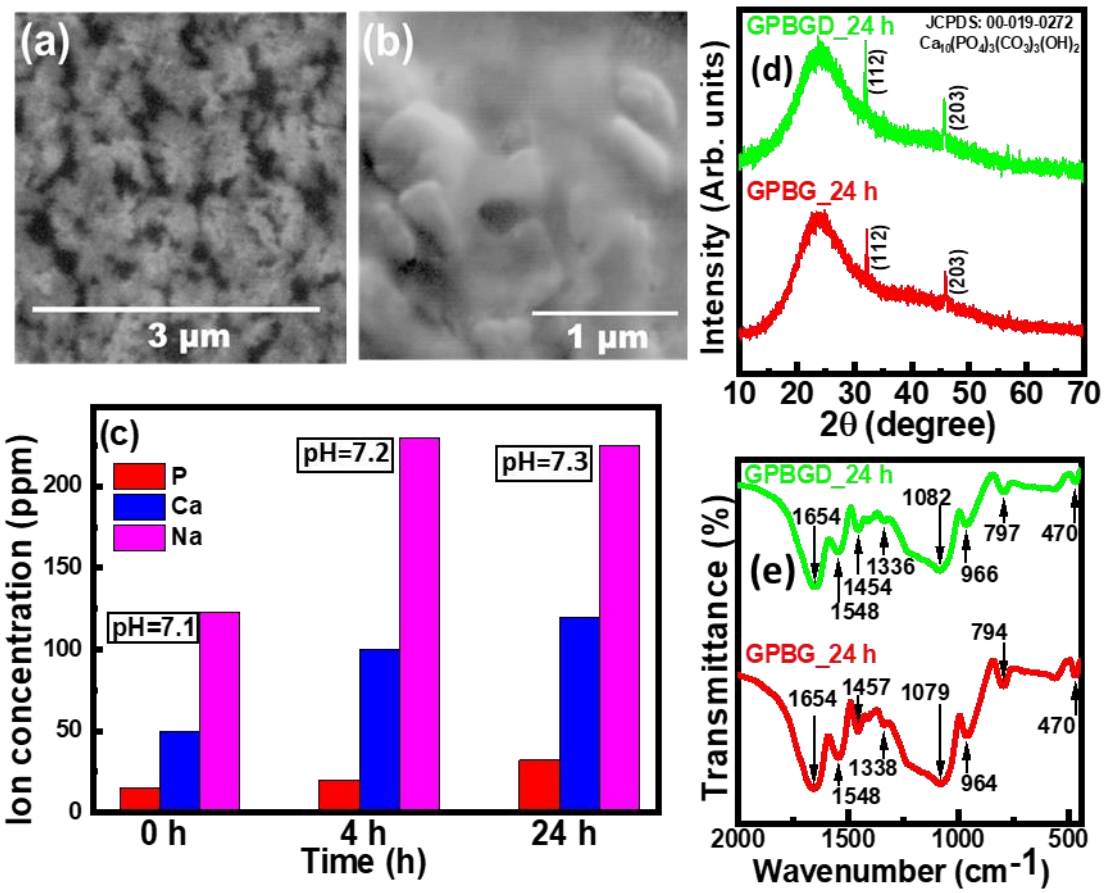

Fig. 6.4: SEM images of GPBGD after interaction with SBF for **(a)** 4 h and **(b)** 24 h, **(c)** Elemental analysis of P, Ca and Na ion concentrations before and after interaction of GPBGD with SBF at different intervals of time along with pH variation, **(d)** XRD pattern and **(e)** FTIR spectra for GPBG and GPBGD for 24 h.

hydroxyapatite might be overlapped with amide I peak at 1654 cm^{-1}. Considering together, FTIR results further confirm the formation of carbonated hydroxyapatite. GPBGD showed the similar emergence of characteristic peaks of phosphate, carbonate and hydroxyl groups confirming that the surface deposition **(Fig. 6.4a-b)** was attributed to carbonate hydroxyapatite. ICP-AES analysis **(Fig. 6.4c)** indicated the release of elements P, Ca and Na from the surface of fibrous mat (GPBGD) to SBF solution and further supported the bioactive nature of the fiber material. It is also noticed that as interaction time increased from 0 h to 24 h, the pH of the SBF solution increased from 7.1 (0 h) to 7.3 (24 h). The observed pH increases from pH 7.1 to 7.3 after 24 h is attributed to the release of sodium and calcium ions to the surrounding medium via exchange with hydronium ions H_3O^+ or H+ in the simulated body fluid and is in good agreement with our earlier results [31].

6.3.3. Mechanical Studies:

Mechanical properties namely tensile strength and young's modulus of various samples were evaluated **(Fig. 6.5).** The shape of the tensile curve for fiber G indicates its soft and weak nature, with the lowest tensile strength and young's modulus. Addition of pectin (0.4 wt. %) to the gelatin solution slightly enhances the tensile response of fiber GP from 8.3 MPa to 11 MPa. Interestingly, on the addition of bioactive glass precursors to the polymer blend resulted in the striking increase in the tensile strength of the fibrous mat GPBG to 27.9 MPa as reported earlier [32]. This could be attributed to the fact that the *in-situ* mineralized bioactive glass particles within polymer chains acted as a reinforcing filler, thereby enhancing the stiffness of G and GP mat.

Additionally, it was found that *in-situ* mineralized BG particles in GP fibrous mat showed slightly lower elasticity. This may be attributed to the presence of BG particles

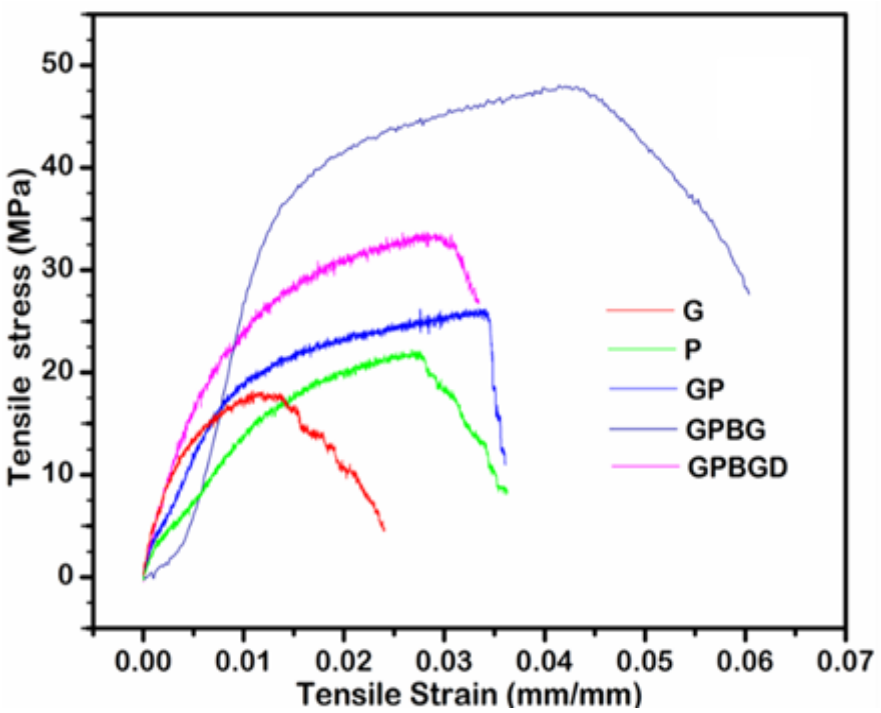

Fig. 6.5: UTM results for various samples.

that reduces chain to chain entanglement which results in limited uncoiling and slippage of chains. As expected, incorporation of a small organic molecule, i.e., a vitamin D precursor slightly decreases the polymeric entanglement as well as tensile strength to 26.7 MPa. Further, it is pertinent to recall the fact that a dense fibrous matrix with limited pores was visualized through AFM **(Fig. 6.1e-f)**. So, it could be validated through this observation **(Fig. 6.1e-f)** that stress transfer was hindered which in turn decreased the tensile response as well as stiffness of GPBGD.

6.3.4. Drug Release:

The release profile **(Fig. 6.6a)** of vitamin D from GPBGD shows the initial burst release upto 30 min of vitamin D precursor followed by the gradual decrease up to 240 min which is then followed by the sustained release of vitamin D. The observed initial bust release profile of vitamin D from GPBGD indicates that mostly small molecules of vitamin D exist on the fiber surface. Such type of release behaviour favours the bone healing

treatment as an initial high amount of drug release provides immediate relief followed by prolonged release to promote gradual healing. It is well known that bioactive glass materials induce apatite formation at the surface in the physiological condition that delays the release payload [30,33]. The resulting decrease in drug release profile could be attributed to the formation of hydroxyapatite crystalline planes with the progression of HA formation (as observed in **Fig. 6.4d**), that do not completely resist the drug release however, regularize the prolonged drug release upto 7 days in line with the reported literature [33]. Such phenomena have been considered as a primary impetus for the sustained drug release.

6.3.5. Contact Angle and Degradation Studies:

Wetting of surface can easily be tuned through the deposition or incorporation of various organic and inorganic materials. The hydrophilicity of materials, is analyzed by water contact angle measurement [34]. The water contact angle of GP, GPBG & GPBGD is recorded as 51°, 49°, & 54° respectively as shown in **Fig. 6.6b**. A significant reduction in contact angle after *in-situ* mineralization of silica based bioactive glass particles in

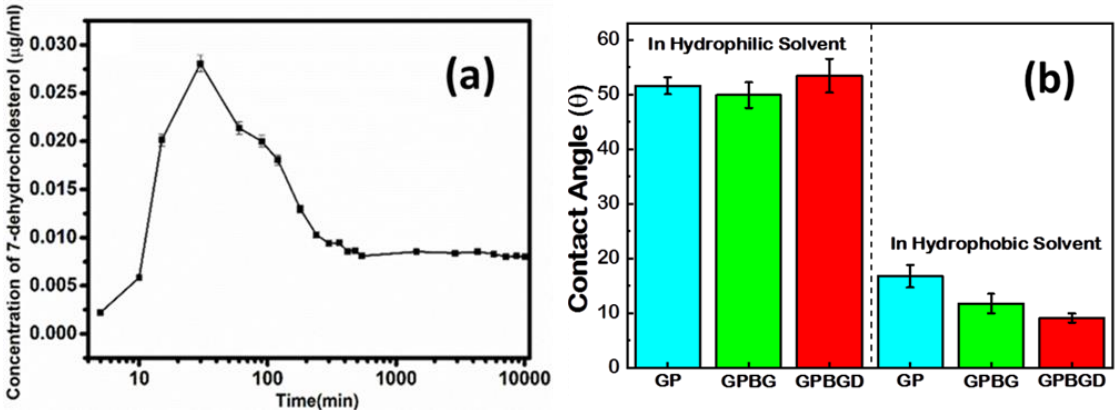

Fig. 6.6: (a) Drug Release profile of 7-dehtydrocholesterol from GPBGD. **(b)** Contact angle measurement of GP, GPBG and GPBGD in hydrophobic as well as hydrophilic solvents.

GPBG sample shows that GPBG surface is more hydrophilic as compared to GP [35]. However, after incorporation of 7-dehydrocholesterol, there must be slight decrease in surface energy that tunes to increase the contact angle for GPBGD but it remains certainly below 90° to maintain the surface wettability. Contact angle with hydrophobic solvent was also determined. Contact angle with hydrophobic solvent is focused on being lower than that of water. The contact angle in GP was found to be higher, which is followed by GPBG and GPBGD respectively. The decrease in contact angle is due to an increase in hydrophilicity, which would favor the adherence, growth and proliferation of cells seeded on the materials. In addition, the disintegration of the fibers GP, and fiber mat GPBG as well as GPBGD was monitored up to 24 h in milli-Q water. It is noteworthy that the fiber GP disintegrated within 4 h whereas, in the case of GPBG as well as GPBGD it was difficult to follow the disintegration due to the hydroxyapatite formation onto the surface of the fiber mat.

6.3.6. Cell cytotoxicity and proliferation:

The cell cytotoxicity for all the different fibrous mat was evaluated using MTT assay after 24 h interaction with the human osteoblast-like osteosarcoma (U2OS) cells and the results are shown in **Fig. 6.7a**. Interestingly, all the electrospun fibrous mat were found to be cytocompatible as in the presence of GP, GPBG and GPBGD mats, approximately 100% of the cells were alive. This was calculated considering the % viability of control cells as 100%.

SEM micrographs **(Fig. 6.7b-c)** revealed the attachment of the normal morphological phenotype of U2OS cells on the surface of the GPBGD fibrous mat with an increase in the cell adherence from 3 days to 5 days, further supporting the cytocompatibility of the proposed biomaterial. It is worth to mention that surface properties such as contact angle,

surface area and charge plays an essential role in cell adherence and proliferation. Pertinently formation of an osteoconductive hydroxyapatite layer on the surface of GPBGD and favourable contact angle formation on immersion in DMEM media mediates cells in sensing fibrous mat as a proper attachment surface as visualized by the formation of cellular protrusion surrounding them **(Fig. 6.7b)**.

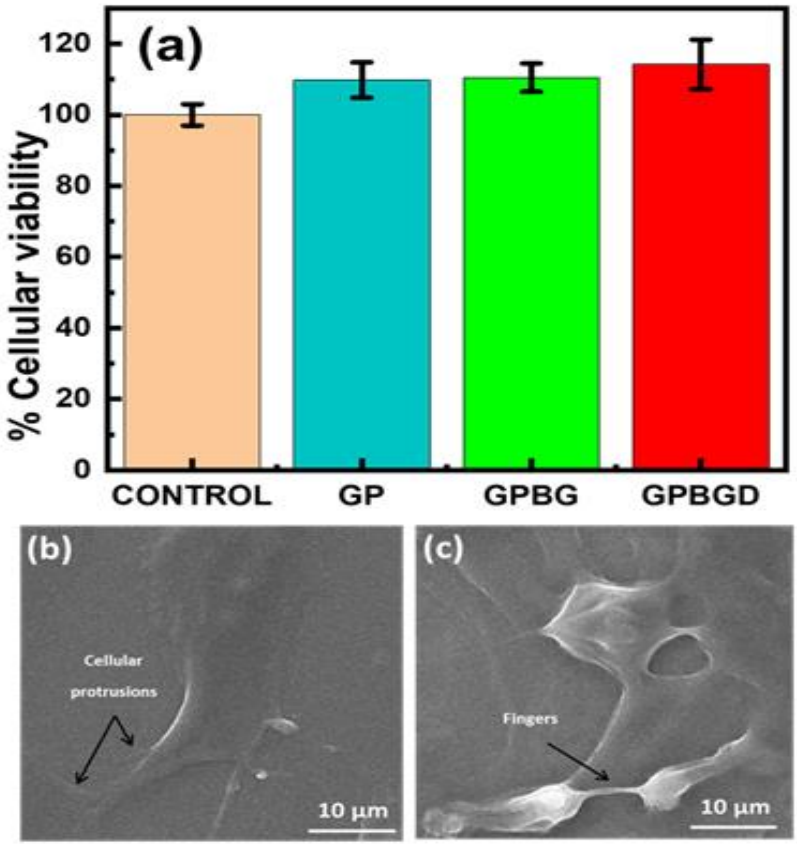

Fig. 6.7: (a) MTT assay (after 24 h) to determine the percentage cellular viability for GP, GPBG and GPBGD and SEM images of GPBGD after interaction with U2OS cells for **(b)** 3 days and **(c)** 5 days.

This contributed to cell proliferation as witnessed by the formation of cell fingers on 5 days interaction with cells **(Fig. 6.7c)**. It is evident through such a visualization of the active attachment of cells to the sample surface by membranous processes that the synthesized material is cytocompatible and could lead to proper tissue growth.

6.4.Conclusion:

The 7-dehydrocholesterol incorporated bioactive glass hybrid composite fibrous mat has been processed in the aqueous phase. This designed fibrous mat proved to be an efficient, sustainable payload release for 7-dehydrocholesterol, a precursor to vitamin D. Further, hydroxyapatite formation behaviour would lead to excellent bone-bonding nature along with bone-strengthening vitamin.

REFERENCES:

[1] A. A. Nada, A. S. Montaser, R. A. Abdel Azeem, M. M. Mounier, *Fibers Polym.* **2016**, *17*, 1985–1994.

[2] Y. Gao, Y. Wang, Y. Wang, W.- Cui, *Mar. Drugs* **2016**, *14*, DOI 10.3390/md14100192.

[3] K. Y. Lee, L. Jeong, Y. O. Kang, S. J. Lee, W. H. Park, *Adv. Drug Deliv. Rev.* **2009**, *61*, 1020–1032.

[4] F. Munarin, M. C. Tanzi, P. Petrini, *Int. J. Biol. Macromol.* **2012**, *51*, 681–689.

[5] A. Noreen, Z. i. H. Nazli, J. Akram, I. Rasul, A. Mansha, N. Yaqoob, R. Iqbal, S. Tabasum, M. Zuber, K. M. Zia, *Int. J. Biol. Macromol.* **2017**, *101*, 254–272.

[6] T. B. L. Nguyen, Y. K. Min, B.-T. Lee, *Tissue Eng. Part A* **2015**, *21*, 1376–1387.

[7] F. Munarin, S. G. Guerreiro, M. A. Grellier, M. C. Tanzi, M. A. Barbosa, P. Petrini, P. L. Granja, *Biomacromolecules* **2011**, *12*, 568–577.

[8] E. M. Varoni, M. Iriti, L. Rimondini, *Coatings* **2012**, *2*, 179–194.

[9] H. E. Kokkonen, J. M. Ilvesaro, M. Morra, H. A. Schols, J. Tuukkanen, *Biomacromolecules* **2007**, *8*, 509–515.

[10] A. Wikiera, M. Irla, M. Mika, *Postep. Hig Med Dosw* **2014**, *68*, 590–596.

[11] C. H. Chen, M. T. Sheu, T. F. Chen, Y. C. Wang, W. C. Hou, D. Z. Liu, T. C. Chung, Y. C. Liang, *Biochem. Pharmacol.* **2006**, *72*, 1001–1009.

[12] V. V. Glinsky, A. Raz, *Carbohydr. Res.* **2009**, *344*, 1788–1791.

[13] C. L. Jackson, T. M. Dreaden, L. K. Theobald, N. M. Tran, T. L. Beal, M. Eid, M.

Y. Gao, R. B. Shirley, M. T. Stoffel, M. V. Kumar, D. Mohnen, *Glycobiology* **2007**, *17*, 805–819.

[14] F. Munarin, P. Petrini, M. C. Tanzi, M. A. Barbosa, P. L. Granja, *Soft Matter* **2012**, *8*, 4731–4739.

[15] R. K. Mishra, M. Datt, K. Pal, A. K. Banthia, *J. Mater. Sci. Mater. Med.* **2008**, *19*, 2275–2280.

[16] L. S. Liu, Y. J. Won, P. H. Cooke, D. R. Coffin, M. L. Fishman, K. B. Hicks, P. X. Ma, *Biomaterials* **2004**, *25*, 3201–3210.

[17] P. L. Rockwell, M. A. Kiechel, J. S. Atchison, L. J. Toth, C. L. Schauer, *Carbohydr. Polym.* **2014**, *107*, 110–118.

[18] S. Alborzi, L. T. Lim, Y. Kakuda, *J. Food Sci.* **2010**, *75*, 100–107.

[19] N. Gupta, D. Santhiya, *Mater. Lett.* **2017**, *188*, 127–129.

[20] F. Zeighampour, F. Alihosseini, M. Morshed, A. A. Rahimi, *J. Appl. Polym. Sci.* **2018**, DOI 10.1002/app.45794.

[21] H. Liao, Y. Wu, M. Wu, H. Liu, *Polym. Compos.* **2011**, DOI 10.1002/pc.21107.

[22] A. Nandakumar, C. Cruz, A. Mentink, Z. Tahmasebi, L. Moroni, C. Van Blitterswijk, P. Habibovic, *Acta Biomater.* **2013**, *9*, 5708–5717.

[23] F. Nudelman, N. A. J. M. Sommerdijk, *Angew. Chemie - Int. Ed.* **2012**, *51*, 6582–6596.

[24] S. Huang, X. Kang, Z. Cheng, Ma Pingan, Y. Jia, J. Lin, *J. Colloid Interface Sci.* **2012**, *387*, 285–291.

[25] G. Poologasundarampillai, D. Wang, S. Li, J. Nakamura, R. Bradley, P. D. Lee, M. M. Stevens, D. S. McPhail, T. Kasuga, J. R. Jones, *Acta Biomater.* **2014**, *10*, 3733–3746.

[26] S. Christakos, P. Dhawan, A. Porta, L. J. Mady, T. Seth, *Mol. Cell. Endocrinol.* **2011**, *347*, 25–29.

[27] S. Fukumoto, *BoneKEy Reports 3* **2014**, DOI 10.1038/bonekey.2013.231.

[28] J. P. van Leeuwen, M. van Driel, G. J. van den Bemd, H. a Pols, *Crit. Rev. Eukaryot. Gene Expr.* **2001**, *11*, 199–226.

[29] J. R., *J Nut Heath Aging* **2007**, *11*, 99–110.

[30] N. Gupta, D. Santhiya, A. Aditya, *J. Mater. Chem. B* **2016**, *4*, 7605–7619.

[31] D. Santhiya, H. K. Alajangi, F. Anjum, S. Murugavel, M. Ganguli, *J. Mater. Chem. B* **2013**, *1*, 6329.

[32] S. G. Caridade, E. G. Merino, N. M. Alves, V. de Z. Bermudez, A. R. Boccaccini, J. F. Mano, *J. Mech. Behav. Biomed. Mater.* **2013**, *20*, 173–183.

[33] S. Shruti, A. J. Salinas, E. Ferrari, G. Malavasi, G. Lusvardi, A. L. Doadrio, L. Menabue and M. V. Regi, Microporous Mesoporous Mater., **2013**, 180, 92–101.

[34] R. Förch, H. Schönherr, A. T. A. Jenkins, *Surface Design: Applications in Biosceicne and Nanotechnology*, **2009**.

[35] B. Kobrin, T. Zhang, J. Chinn, in *209th ECS Meet.*, **2006,** 781-78.

FUTURE PROSPECTS

Over the past decades, research work on bone tissue engineering has surfaced the way towards the innovative designing of new materials with new manufacturing techniques, better performances and wider applications. Since, bioactive glass discovery, although tremendous work continues with a significant progress in this field, still scope for improvements in terms of its **processing, functionality and targeted delivery exists**. The reported methods are more green than those reported previously, but TEOS were still in use, which is inherently not green, so there is still work to do.

New frontiers of research are the need of the hour for **the feasibility of the bioactive glass in steroids, vaccine, hormones and therapeutic protein delivery, along with validation of growth factors and gene delivery**. In future, it would be great if bioactive glass materials could be delivered non-invasively **through skin/oral rout**. In this context, the route of delivery plays a vital role. It could be carried out **by tagging the biomaterial with an efficient skin penetrating peptides/functional food**.

Practical major challenge remains in front of the medical community is the way of **molding the bioactive glass into the desired defect shape** during operation times. Further, its application **in the field of connective tissue engineering is limited**; bioactive glass needs to be explored for it too. In addition, **the research activity is significantly growing for major future developments in the field of cancer through the advent of magnetic bioactive glass-ceramics.** Most importantly, as like any other biomaterial requirement of carrying out clinical studies before launching in the market, similarly for bioinspired bioactive glass ***in-vivo*** clinical test is yet to be performed.